FIELD MONITORING AND MODELING OF PAVEMENT RESPONSE AND SERVICE LIFE CONSUMPTION DUE TO OVERWEIGHT TRUCK TRAFFIC

A Dissertation

by

JEONG HO OH

Submitted to the Office of Graduate Studies of
Texas A&M University
in partial fulfillment of the requirements for the degree of

DOCTOR OF PHILOSOPHY

August 2004

Major Subject: Civil Engineering

FIELD MONITORING AND MODELING OF PAVEMENT RESPONSE AND SERVICE LIFE CONSUMPTION DUE TO OVERWEIGHT TRUCK TRAFFIC

A Dissertation

by

JEONG HO OH

Submitted to Texas A&M University
in partial fulfillment of the requirements
for the degree of

DOCTOR OF PHILOSOPHY

Approved as to style and content by:

Robert L. Lytton (Chair of Committee)	Dallas N. Little (Member)
Jose M. Roesset (Member)	Christopher C. Mathewson (Member)

Paul Roschke
(Head of Department)

August 2004

Major Subject: Civil Engineering

ABSTRACT

Field Monitoring and Modeling of Pavement Response and Service Life Consumption due to Overweight Truck Traffic. (August 2004)

Jeong Ho Oh, B.S., Korea University;

M.S., Korea University

Chair of Advisory Committee: Dr. Robert L. Lytton

A number of pavement structures experience deterioration due to high traffic volume and growing weights. Recently, the Texas Legislatures passed bills allowing trucks of gross vehicle weight (GVW) up to 556 kN routinely to use a route in south Texas along the Mexican border. Thus, there is a need to model pavement responses due to various types of overweight truck traffic (OTT) by taking into account axle loads, configuration, and pavement layer material characterizations in order to provide a guideline to assess the existing pavement performance and expected service life. It is for this purpose that the nonlinear cross-anisotropic pavement analysis finite element program (NCPA) has been developed. Stress dependent and directionally different resilient modulus and Poisson's ratios are incorporated into the finite element formulation to model the pavement response. As a tool to assess the performance of the pavement, the procedure to calculate the overall rutting and the cracked area was included in the formulation

Intensive nondestructive testing has been performed to identify the existing pavement test section geometry and layer properties. In addition, a fiber optic based

Weigh-in Motion (WIM) sensor was developed and tested. It is expected to be a promising device to monitor traffic by showing a reliable response. Sampled materials from the test section were tested to characterize their stress-dependent, cross-anisotropic and permanent deformation properties.

Constitutive models are verified by comparing the predicted displacements with field displacements measured with the Multi-Depth Deflectometer (MDD). The result was that the least error between predicted and measured displacements is generated by the nonlinear cross-anisotropic model. In addition, the cross-anisotropic characteristic of the asphalt concrete material is introduced and evaluated based on the relationship between the backcalculated static and dynamic modulus. This addition improves the accuracy of the assessment of pavement performance with respect to both rutting and fatigue cracking. Charts to evaluate the service life of the existing pavement subjected to OTTs are established in terms of the unit service life consumed due to the rutting and fatigue cracking with the various observed combinations of pavement geometry, traffic load, and material properties.

ACKNOWLEDGMENTS

The effort and good will of many people have enabled completion of this dissertation. First, I would like to express deepest gratitude to my advisor, Dr. Robert Lytton, for the encouragement and valuable detailed comments and suggestions on this work. He showed me the right way to go as a civil engineer.

I would like to also thank Dr. Dallas Little, Dr. Joes M Roesset, and Dr. Christopher Mathewson for serving as the advisory committee and Dr. Charles Aubeny for serving as a substitute committee member at the final exam.

Sincere thanks and appreciation are also due Dr. Emmanuel Fernando of the Texas Transportation Institute for his support and enthusiasm in this study. As a mentor, he never failed to share valuable opinions to complete this work.

Thanks should also be given to Dr. Woo-Jin Lee, my advisor during my master's degree at Korea University, for his guidance and motivation to pursue a Ph.D.

I also thank my many friends in this town for providing me wonderful times and refreshment. I sincerely wish you all successful and happy lives.

In addition, I greatly acknowledge the support and endless encouragement of my family. They always showed open hearts and unconditional love over the past several years of this work. Especially, this dissertation is dedicated to my parents, Se-Wang Oh and Ok-Hee Jun.

Finally, I take this opportunity to thank my wife, Seong-Jin Hong, and lovely son, Seung-Yoon Oh, for their trust, understanding, and patience during this demanding part of my life.

TABLE OF CONTENTS

Page

ABSTRACT iii

ACKNOWLEDGMENTS v

TABLE OF CONTENTS vi

LIST OF FIGURES ix

LIST OF TABLES xix

CHAPTER

I INTRODUCTION 1

1.1. Problem Statement 3
1.2. Research Objectives 5
1.3. Layout of Dissertation 6

II FIELD INSTRUMENTS AND DATA ANALYSIS 8

2.1. General 8
2.2. Introduction of the WIM System 8
2.3. Types of WIM Systems 9
2.3.1. Bending Plate 9
2.3.2. Piezoelectric Sensor 10
2.3.3. Load Cell 10
2.3.4. Load Cell 10
2.4. Review of WIM Research 12
2.4.1. WAVE Project 12
2.4.2. Low Speed WIM System (LS-WIM) 14
2.4.3. Development of a Fiber-Optic Dynamic WIM System 15
2.3.4. Load Cell 10
2.5. Application of Fiber Optic WIM 17
2.6. Falling Weight Deflectometer 18
2.7. Dynamic Cone Penetrometer 21
2.8. Ground Penetrating Radar 22
2.9. Multi Depth Deflectometer 25
2.10. Time Domain Reflectometry 27
2.11. Thermocouple 32
2.12. Weather Station 33

CHAPTER Page

III CHARACTERIZATION OF MATERIALS 39

3.1. Particle Size Analysis 40
3.2. Moisture – Density Characteristics 42
3.3. Stress Dependent Resilient Property 44
3.4. Cross-Anisotropy Property 46
3.4.1. Application of Cross-Anisotropy in Granular Materials 46
3.4.2. Tests for Cross-Anisotropy Property 49
3.5. Permanent Deformation Test 60

IV COMPARISON AND VERIFICATION OF RESPONSE MODELS 67

4.1. Finite Element Model 67
4.1.1. FEM Formulation on Two-Dimensional Axisymmetric Solid 68
4.1.2. Cross-Anisotropy under Axisymmetric Condition 71
4.2. Verification of Cross-Anisotropy Model 72
4.3. Model Comparison with Field Measurement 78
4.4. Sensitivity Analysis 91
4.4.1. Sensitivity Analysis of Stress-Dependent Property 93
4.4.2. Sensitivity Analysis of Cross-Anisotropy Properties 99

V EVALUATION OF DAMAGE POTENTIAL 109

5.1. General 109
5.2. Evaluation of Damage Potential Using MDD 109
5.3. Pavement Performance Measurement 118
5.3.1. Analysis of Rut Bar Data 120
5.3.2. Analysis of Roughness Data 125
5.3.3. Analysis of Cracking Data 130
5.4. Performance Prediction of NCPA 131
5.4.1. Verification of Performance Prediction of NCPA 137
5.4.2. Comparison of Performance with NCPA and Field Measurement 142

CHAPTER Page

VI DEVELOPMENT OF CHARTS TO EVALUATE SERVICE LIFE OF EXISTING PAVEMENT DUE TO OVERWEIGHT TRUCK LOADS 152

6.1. General 152
6.2. Chart Establishment 153
6.2.1. Overweight Truck Route Analysis (OTRA) Program 153
6.2.2. Determination of Standard Material Property 154
6.2.3. Separation of Cases 158
6.2.4. Procedure to Develop Charts 161
6.3. Application of Cross-Anisotropy in Charts 175
6.4. Application of Charts in Practice 188

VII SUMMARY AND CONCLUSIONS 189

REFERENCES 194

APPENDIX A DEVELOPMENT OF FIBER OPTIC BASED WIM SYSTEM 200

APPENDIX B MATERIAL PROPERTY OF INTACT SOILS 212

APPENDIX C PLOTS OF VARIATION IN FATIGUE CRACKING AND PAVEMENT SCORE FROM VISUAL SURVEY 219

VITA 228

LIST OF FIGURES

FIGURE		Page
1.1.	SH 4/48 in Brownsville, Texas	4
2.1.	Typical Bending Plate System Layout (McCall and Vodrazka, 1997)	11
2.2.	Typical Piezoelectric WIM System Layout (McCall and Vodrazka, 1997)	11
2.3.	Relative Errors Based on GVW (Jehaes, 1999)	14
2.4.	Components of Fiber-Optic Sensor Signal (Cosentino and Grossman, 1997)	17
2.5.	Comparison of Static Scale Weight with WIM Weight	18
2.6.	Dynatest 8000 Falling Weight Deflectometer	20
2.7.	General Scheme of South African DCP	21
2.8.	Air-Launched Antenna in Ground Penetrating Radar System (TTI, 2001)	24
2.9.	Installed Multi-Depth Deflectometer	26
2.10.	TDR Probe	28
2.11.	Sample Preparation for Calibration Test	30
2.12.	TDR Trace with Time Variation	30
2.13.	Layout of TDR at the Field Test Section	31
2.14.	Layout of Thermocouple Sensors	33
2.15.	Scheme of Weather Station	35
2.16.	Variation of Temperature	35
2.17.	Variation of Moisture Content of Flexible Base	37
2.18.	Variation of Moisture Content of Salvage Base	38
2.19.	Variation of Moisture Content of Lime Treated Subbase and Subgrade	38

FIGURE Page

3.1. Particle Size Distribution for Base Materials 42

3.2a. Molded Sample before Load Application 52

3.2b. Molded Sample during Load Application 53

3.3. Stress States for Flexible Base 53

3.4. Stress States for Salvage Base 54

3.5. Stress States for Lime Treated Subbase 54

3.6. Stress States for Subgrade 55

3.7. Plastic Strain versus Number of Load Cycles of Flexible Base 62

3.8. Plastic Strain versus Number of Load Cycles of Salvage Base 62

3.9. Plastic Strain versus Number of Load Cycles of Lime Treated Subbase 63

3.10. Plastic Strain versus Number of Load Cycles of Subgrade 63

3.11. Plastic Strain versus Number of Load Cycles of K6 Intact Soils 64

3.12. Plastic Strain versus Number of Load Cycles of K7 Intact Soils 64

4.1. Comparison of Vertical Stress Computed by the Theoretical Solution and NCPA 75

4.2. Comparison of Radial Stress Computed by the Theoretical Solution and NCPA 76

4.3. Comparison of Vertical Stress by CIRCLY and NCPA 77

4.4. Comparison of Radial Stress by CIRCLY and NCPA 78

4.5. Layout of MDD Installation 81

FIGURE Page

4.6a. MDD Response of OTT in August 83

4.6b. MDD Response of OTT in December..... 83

4.7. Comparison of Displacements due to FWD Loading 84

4.8. Comparison of Displacements due to No. 215 OTT (K7 Lane, August 2002)..... 85

4.9. Comparison of Displacements due to No. 342 OTT (K6 Lane, August 2002)..... 85

4.10. Comparison of Displacements due to No. 403 OTT (K7 Lane, October 2002)..... 86

4.11. Comparison of Displacements due to No. 418 OTT (K6 Lane, October 2002)..... 86

4.12. Comparison of Displacements due to No. 486 OTT (K7 Lane, December 2002) 87

4.13. Comparison of Displacements due to No. 553 OTT (K6 Lane, December 2002) 87

4.14. Comparison of Displacements due to No. 609 OTT (K7 Lane, February 2002) 88

4.15. Comparison of Displacements due to No. 638 OTT (K6 Lane, February 2002) 88

4.16a. Model Verification Using OTT Collected in August 2002..... 90

4.16b. Model Verification Using OTT Collected in December 2002..... 90

4.17. Pavement Structure with Standard Material Property..... 92

4.18. Sensitivity Evaluation Points 92

4.19. Sensitivity of the Displacement to Changes in Parameters in Flexible Base 94

FIGURE Page

4.20. Sensitivity of the Displacement to Changes in Parameters in Lime Treated Subbase 95

4.21. Sensitivity of the Displacement to Changes in Parameters in the Subgrade 95

4.22. Sensitivity of the Displacement to Changes K_1 in the Subgrade 96

4.23. Sensitivity of the Displacement to Changes K_2 in the Subgrade 96

4.24. Sensitivity of the Displacement to Changes K_3 in the Subgrade 97

4.25. Sensitivity of the Strain to Changes K_1 in Flexible Base 97

4.26. Sensitivity of the Strain to Changes K_2 in Flexible Base 98

4.27. Sensitivity of the Strain to Changes K_3 in Flexible Base 98

4.28. Sensitivity of the Displacement to Changes in Parameters in Flexible Base 101

4.29. Sensitivity of the Displacement to Changes in Parameters in Lime Treated Subbase 101

4.30. Sensitivity of the Displacement to Changes in Parameters in Subgrade 102

4.31. Sensitivity of the Displacements to Changes in the n Value in Subgrade 102

4.32. Sensitivity of the Displacements to Changes in the m Value in Subgrade 103

4.33. Sensitivity of the Displacements to Changes in the p Value in Subgrade 103

4.34. Sensitivity of the Strains to Changes in the n Value in Subgrade 104

4.35. Sensitivity of the Strains to Changes in the m Value in Subgrade 104

FIGURE Page

4.36. Sensitivity of the Strains to Changes in the p Value in Subgrade 105

4.37. Resilient Vertical Modulus (MPa) Variation within Flexible Base due to the Change of the n Value in Subgrade 105

4.38. Resilient Radial Modulus (MPa) Variation within Flexible Base due to the Change of the n Value in Subgrade 106

4.39. Resilient Vertical Modulus (MPa) Variation within Lime Treated Subbase due to the Change of the n Value in Subgrade 106

4.40. Resilient Radial Modulus (MPa) Variation within Lime Treated Subbase due to the Change of the n Value in Subgrade 107

4.41. Resilient Vertical Modulus (MPa) Variation within Subgrade due to the Change of the n Value in Subgrade 107

4.42. Resilient Radial Modulus (MPa) Variation within the Subgrade due to the Change of the n Value in Subgrade 108

5.1. MDD Response under Legal Truck 110

5.2. MDD Response under Permitted Overweight Truck 111

5.3. Evidence of Damage of Pavement Group 1A of SH4/48 (after Ramos, 2003) 118

5.4. Average Rut Depth Variation in Group 1A 121

5.5. Average Rut Depth Variation in Group 1 121

5.6. Average Rut Depth Variation in Group 2 122

5.7. Average Rut Depth Variation in Group 3 122

5.8. Average Rut Depth Variation in Group 4 123

5.9 Average Rut Depth Variation in Group 5 123

5.10 Average Rut Depth Variation in Group 6 124

FIGURE Page

5.11. Average Rut Depth Variation in Group 7 124

5.12. The International Roughness Index (IRI) Scale of Road Roughness (Sayers et al., 1986) 126

5.13. Average IRI Variation in Group 1A 126

5.14. Average IRI Variation in Group 1 127

5.15. Average IRI Variation in Group 2 127

5.16. Average IRI Variation in Group 3 128

5.17. Average IRI Variation in Group 4 128

5.18. Average IRI Variation in Group 5 129

5.19. Average IRI Variation in Group 6 129

5.20. Average IRI Variation in Group 7 130

5.21. Schematic Illustration of Shift Factor (after Balbissi, 1983) 136

5.22. Comparison of Rut Depth Using 3 Parameter Model 139

5.23. Comparison of Rut Depth Using VESYS Model 139

5.24. Comparison of Fatigue Cracking 141

5.25. Comparison of Rut Depth from Measurement and Prediction at K6-4 Station 147

5.26. Comparison of Rut Depth by Measurement and Prediction at K7-3 Station 147

5.27. Variation of mc Values over Time at the K6 Lane (after Ramos, 2003) 148

5.28. Variation of mc Values over Time at the K7 Lane (after Ramos, 2003) 149

5.29. Comparison of Fatigue Cracking from Measurement and Prediction at K6-4 150

FIGURE Page

5.30. Comparison of Fatigue Cracking from Measurement and Prediction at K7-3 151

6.1. Establishing Pavement Layering Using DCP Data 161

6.2. Permitted Overweight Truck Class and Configuration 162

6.3. Comparison of AC Thickness in Fatigue Cracking Criteria for Case 1.. 166

6.4. Comparison of AC Thickness in Rutting Criteria for Case 1 167

6.5. Comparison of AC Thickness in Fatigue Cracking Criteria for Case 4.. 167

6.6. Comparison of AC Thickness in Rutting Criteria for Case 4 168

6.7. Variation of Service Life with $1/N_f$ and Traffic for Fatigue Cracking.... 168

6.8. Variation of Service Life with $1/N_f$ and Traffic for Rutting 169

6.9. Variation of $1/N_f$ with AC and Base Thickness for Fatigue Cracking in Case 1..... 169

6.10. Variation of $1/N_f$ with AC and Base Thickness for Fatigue Cracking in Case 2..... 170

6.11. Variation of $1/N_f$ with AC and Base Thickness for Fatigue Cracking in Case 3..... 170

6.12. Variation of $1/N_f$ with AC and Base Thickness for Fatigue Cracking in Case 4..... 171

6.13. Variation of $1/N_f$ with AC and Base Thickness for Rutting Case 1 (50/50)..... 171

6.14. Variation of $1/N_f$ with AC and Base Thickness for Rutting Case 1 (80/20)..... 172

6.15. Variation of $1/N_f$ with AC and Base Thickness for Rutting Case 2 (50/50)..... 172

FIGURE Page

6.16. Variation of $1/N_f$ with AC and Base Thickness for Rutting Case 2 (80/20) 173

6.17. Variation of $1/N_f$ with AC and Base Thickness for Rutting Case 3 (50/50) 173

6.18. Variation of $1/N_f$ with AC and Base Thickness for Rutting Case 3 (80/20) 174

6.19. Variation of $1/N_f$ with AC and Base Thickness for Rutting Case 4 (50/50) 174

6.20. Variation of $1/N_f$ with AC and Base Thickness for Rutting Case 4 (80/20) 175

6.21. Shift of Critical Strain at the Top of the Subgrade in Case 1 176

6.22. Shift of Critical Strain at the Top of the Subgrade in Case 2 177

6.23. Shift of Critical Strain at the Top of the Subgrade in Case 3 177

6.24. Shift of Critical Strain at the Top of the Subgrade in Case 4 178

6.25. Comparison of $1/N_f$ Calculated between the NNA and NI Models for Rutting in Case 1 (80/20) 180

6.26. Comparison of $1/N_f$ Calculated between the NNA and NI Models for Rutting in Case 1 (50/50) 180

6.27. Comparison of $1/N_f$ Calculated between the NNA and NI Models for Rutting in Case 2 (80/20) 181

6.28. Comparison of $1/N_f$ Calculated between the NNA and NI Models for Rutting in Case 2 (50/50) 181

6.29. Comparison of $1/N_f$ Calculated between the NNA and NI Models for Rutting in Case 3 (80/20) 182

6.30. Comparison of $1/N_f$ Calculated between the NNA and NI Models for Rutting in Case 3 (50/50) 182

FIGURE Page

6.31. Shift of AC Strain at the Bottom of the AC in Case 1 184

6.32. Shift of AC Strain at the Bottom of the AC in Case 2 184

6.33. Shift of AC Strain at the Bottom of the AC in Case 3 185

6.34. Shift of AC Strain at the Bottom of the AC in Case 4 185

6.35. Comparison of $1/N_f$ Calculated between the NA and NI Models for Fatigue Cracking in Case 1 (50/50) 186

6.36. Comparison of $1/N_f$ Calculated between the NA and NI Models for Fatigue Cracking in Case 2 (50/50) 187

6.37. Comparison of $1/N_f$ Calculated between the NA and NI Models for Fatigue Cracking in Case 3 (50/50) 187

A1. Components of Fiber Optic Cable 202

A2. Fiber Fabry-Perot Interferometer 203

A3. Steel Bar Response of MTS 206

A4. Aluminum Bar Response of MTS 206

A5. Dependence of Peak Response on Axial Displacement 207

A6. FFPI Installation Procedure 208

A7. Location of Sensors 209

A8. Response of Five FFPI Sensors Embedded in a Steel Bar on a Class 10 Truck 210

B1. Particle Size Distribution Curve of BE Clay 213

B2. Particle Size Distribution Curve of BU Clay 214

B3. Particle Size Distribution Curve of HA Clay 215

B4. Particle Size Distribution Curve of HE Clay 216

FIGURE Page

B5. Particle Size Distribution Curve of OM Clay 217

B6. Particle Size Distribution Curve of ON Clay 218

C1. Variation of Longitudinal Crack in Group 1A 220

C2. Variation of Longitudinal Crack in Group 1 220

C3. Variation of Longitudinal Crack in Group 2 221

C4. Variation of Longitudinal Crack in Group 3 221

C5. Variation of Longitudinal Crack in Group 4 222

C6. Variation of Longitudinal Crack in Group 5 222

C7. Variation of Longitudinal Crack in Group 6 223

C8. Variation of Longitudinal Crack in Group 7 223

C9. Variation of Pavement Score in Group 1A 224

C10. Variation of Pavement Score in Group 1 224

C11. Variation of Pavement Score in Group 2 225

C12. Variation of Pavement Score in Group 3 225

C13. Variation of Pavement Score in Group 4 226

C14. Variation of Pavement Score in Group 5 226

C15. Variation of Pavement Score in Group 6 227

C16. Variation of Pavement Score in Group 7 227

LIST OF TABLES

TABLE		Page
1.1.	Axle Weight Limits	5
2.1.	Molded Sample Information	29
2.2.	Calibration Equation for Six TDR Probes	31
2.3.	Average Temperature (°F) for Seasons	36
3.1.	Soil Classification for Intact Soil	40
3.2.	Sieve Analysis of Base Materials (Based on Percent Passing)	41
3.3.	Moisture Content and Dry Density Obtained from Field and Laboratory	43
3.4.	Cross-Anisotropy Property of Flexible Base	58
3.5.	Cross-Anisotropy Property of Salvage Base	58
3.6.	Cross-Anisotropy Property of Lime Treated Subbase	59
3.7.	Cross-Anisotropy Property of Subgrade	59
3.8.	Nonlinear Cross-Anisotropy Properties	60
3.9.	Level of Test Loads for Materials	61
3.10.	Permanent Deformation Parameters for Stress Levels 1 and 2	66
3.11.	Permanent Deformation Parameters for Intact Soils	66
4.1.	Input Used in Theoretical Solution	74
4.2.	Backcalculated Modulus and Monitored Number of Traffic	80
4.3.	Stress Dependent and Cross-Anisotropy Parameters	82
4.4.	Variation of Resilient Parameters in Sensitivity Analysis	93
4.5.	Variation of Cross-Anisotropy Parameters in the Sensitivity Analysis	99
5.1.	Equations for Predicting Vertical Strain at the Top of Subgrade	113

TABLE Page

5.2. Prediction of Damage Effects of Overweight vs. Legal Trucks by Rutting in K6 & K7 Lanes 115

5.3. Equations for Predicting Horizontal Strain at the Bottom of the AC Layer 116

5.4. Prediction of Damage Effects of Overweight vs. Legal Truck Weight by Fatigue Cracking in K6 & K7 Lanes 117

5.5. Permanent Deformation Property used in Analysis 138

5.6. Creep Compliance Parameters of the K6-4 FWD Station (after Ramos, 2003) 141

5.7. Cumulative 80 kN ESAL by Year and by Pavement Groups (after Ramos, 2003) 143

5.8. Cumulative 80 kN ESAL by Lanes and by Pavement Groups (after Ramos, 2003) 144

5.9. Permanent Deformation Property of Materials Based on 3-Parameter Model 146

5.10. Used m Values and Parameters in Fatigue Cracking Evaluation 149

6.1. Material Parameters Used in Design Charts 155

6.2. Typical CBR Ranges of Soils (U.S. Army Engineer, 1960) 160

6.3. Classification of Pavement Materials Based on DCP Penetration Rate.. 161

6.4. Used Axle Weight Limit (kN) in Charts 163

6.5. Shift Factor of the Subgrade Strain for Each Case 179

6.6. Shift Factor of the AC Strain for Each Case 183

B1. Physical Soil Property of BE Clay 213

B2. Cross-Anisotropy Test Result of BE Clay 213

TABLE Page

B3. Physical Soil Property of BU Clay 214
B4. Cross-Anisotropy Test Result of BU Clay 214
B5. Physical Soil Property of HA Clay 215
B6. Cross-Anisotropy Test Result of HA Clay 215
B7. Physical Soil Property of HE Clay 216
B8. Cross-Anisotropy Test Result of HE Clay 216
B9. Physical Soil Property of OM Clay 217
B10. Cross-Anisotropy Test Result of OM Clay 217
B11. Physical Soil Property of ON Clay 218
B12. Cross-Anisotropy Test Result of ON Clay 218

CHAPTER I

INTRODUCTION

The impact of increasing overweight truck traffic (OTT) on highways due to economic growth is a growing concern within the Texas Department of Transportation (TxDOT). Eventually, the 75th and 76th Texas Legislatures passed bills allowing trucks of gross vehicle weights (GVW) up to 556 kN to routinely use a route in south Texas, along the Mexico border. Since pavement performance under OTT is influenced greatly by truck traffic loadings rather than the number of repetition, it is essential that the proper design procedure be used to build a pavement that will provide the desired performance for the expected service conditions. As an approach to develop a design procedure that uses a specific pavement condition, as a criterion, the maximum allowable wheel load that can be sustained by a given pavement structure was determined on the basis of the well known Mohr-Coulomb criterion (Jooste and Fernando, 1995). The primary factor to characterize pavement response under OTT is highly dependent on being able to model the pavement structure realistically close to field conditions. To serve this purpose, there has been extensive application of theory of elasticity to the analysis of layered pavement systems (Brown, 1996). Burmister (1943) developed the essential equations and various computer programs were developed to simplify the steps.

This dissertation follows the style and format of the *Journal of Geotechnical and Geoenviromental Engineering*.

Today the most widely used isotropic linear-elastic layered computer programs are the BISAR and ELSYM 5 programs. These programs were originally developed by researchers in the Shell and Chevron oil companies respectively. Typically, an area influenced by OTT loading is expected to broaden and deepen into the supporting unbound granular materials and subgrade soils. In order to take into account the behavior of granular materials, non-linear elastic theory has been applied to explain the stress-strain relationship of the material. Recently, finite element programs considering cross-anisotropic theory were developed by Tutumluer (1995) and Adu-Osei (2000) resulting in the elimination of tensile radial stress at the bottom of the base layer that is generated by the isotropic elastic approach.

Accurate modeling requires an appropriate material property and pavement structure geometry condition. The use of nondestructive testing (NDT) has become an integral part of the structural evaluation and rehabilitation process of pavements in recent years. The procedure using NDT to assess the characteristic of pavement can be done through three stages: (1) determination of layer thickness using dynamic cone penetrometer (DCP), ground penetrating radar (GPR); (2) determination of layer modulus by falling weight deflectometer (FWD) deflection basin; (3) measurement of pavement response due to traffic load by multi depth deflectometer (MDD); and (4) monitoring traffic using weigh-in-motion (WIM). As an attractive tool, the fiber optic technique is widely used to monitor civil structure condition called ‘health monitoring’. Cosentino and Grossman (1997) made an effort to analyze fiber optic sensor behavior embedded in flexible pavement and found satisfying performance of the sensor.

1.1. PROBLEM STATEMENT

There are two routes (SH 4 and SH 48 shown in Figure 1.1) in south Texas along the border with Mexico where trucks of gross vehicle weights (GVWs) up to 556kN lbs are permitted. Table 1.1 presents the limits of axle weight for different axle types used in Texas. During the first year of operation, about 30,000 permits were issued. The payloads carried by the permitted trucks are mostly coiled metal sheets, oil, and powder mineral (fluorite), which are transported from the Port of Brownsville to Mexico and vice versa. The route was established in response to the need expressed by truckers to haul cargo at their trucks' operating capacities to improve operational efficiency. Since TxDOT is concerned about the impact of the overweight truck traffic on the routes, a piezoelectric WIM system has been installed to characterize truck traffic. The NDTs including FWD, MDD, and GPR were carried out to figure out the existing pavement structure. In addition, instrumented weather station equipment monitors seasonal variation due to the weather effects. Thermocouples and time domain reflectometers (TDR) measured temperature and moisture variation respectively during the test period.

Prior to this research, TxDOT had a procedure for assessing the potential for pavement damage prior to the movement of a super-heavy load. It appears that this procedure can be used to the estimate allowable wheel load based on Mohr-Coulomb criterion under representative pavement structures with various asphalt concrete and base thicknesses. However, the directional dependency related to cross-anisotropy was not taken into account in this procedure. This study hypothesize that the effects of non-linearity and cross-anisotropic behavior are likely to be significant under the heavy axle

loads. Thus research is needed to evaluate and improve the previously developed procedure. This research will provide a cost-effective means for assessing pavement performance combining all information obtained from field and laboratory tests and the mechanistic approach using finite element method.

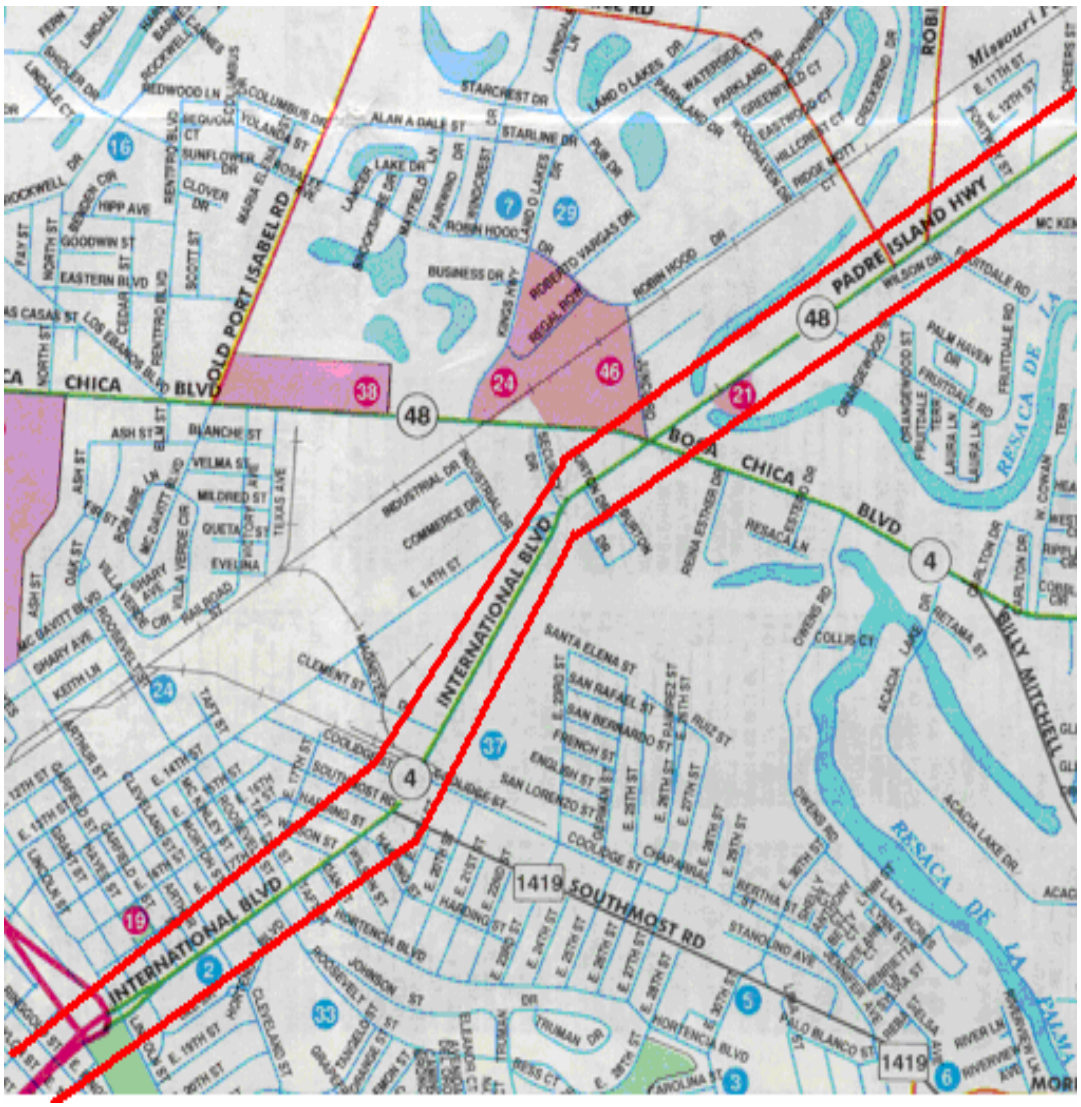

Figure 1.1. SH 4/48 in Brownsville, Texas

Table 1.1. Axle Weight Limits

Axle Type	Weight Limit (kN)
Single	111
Tandem	205
Tridem	267
4-Axle Group	311
5-Axle Group	362

1.2. RESEARCH OBJECTIVES

The general objective of this research is to develop a procedure whereby pavement engineers can assess potential damage of pavement that experiences OTT. It needs to take into account in a realistic way the complex interaction between pavement performance and the factors related to traffic, weather, pavement structure, and material characteristics. To deal with this situation, the following tasks need to be accomplished:

1) Assessment of pavement condition by NDT tests and the development of fiber optic WIM;
2) Material characterization by laboratory tests especially for nonlinear cross-anisotropy;
3) Development of a finite element program to handle nonlinear cross-anisotropy and performance prediction with respect to rut depth and fatigue cracking;

4) Nonlinear cross-anisotropy model verification by comparing calculated critical strains field measurements;
5) Sensitivity analysis to determine the interaction between nonlinear cross-anisotropic parameters with pavement response;
6) Damage analysis based on MDD measurements using the developed program; and
7) Establish charts to characterize a route under OTT.

1.3. LAYOUT OF DISSERTATION

This dissertation consists of seven chapters. An intensive literature review on the field instruments used in this study and the analysis of data is included in Chapter II.

The characterization of unbound granular materials and subgrade soils through various laboratory tests to determine the nonlinear cross anisotropy and permanent deformation properties is presented in Chapter III.

Chapter IV presents description of a developed finite element program. The program handles nonlinear stress dependent cross-anisotropic condition to evaluate the behavior of layers subjected to the repeated traffic loading. In addition, performance prediction tool is incorporated to assess rutting and fatigue cracking. Different constitutive models are used to compare with field displacements and verified.

Performance prediction of tested pavement section are covered in Chapter V. The installed MDD is used to estimate the damage potential between overweight truck and

legal truck loading. Using the program, an attempt is made to predict and match with field measurement using verified constitutive models.

Based on the finding of this study, charts are established to determine service life under various pavement geometry conditions, traffic configurations and two constitutive models such as nonlinear isotropic and anisotropic theory in Chapter VI.

Chapter VII concludes this dissertation and summarizes findings of this study.

CHAPTER II

FIELD INSTRUMENTS AND DATA ANALYIS

2.1. GENERAL

To estimate the effects of overweight truck traffic on pavement performance, researchers have conducted a comprehensive field test and monitored selected pavement test sections along SH 4/48 in Brownsville. For this purpose, TxDOT installed a WIM system based on piezoelectric sensor. The traffic information such as wheel loads, axle weighs, tire spacing, and axle spacing is very valuable to conduct the current research. In addition, various field equipments were used in order to measure the pavement structure condition. In this chapter, the basic principles of equipment operations and relevant previous work on the applications in current research will be introduced.

2.2. INTRODUCTION OF THE WIM SYSTEM

One of the first efforts to develop a WIM system was undertaken in 1951 by Normann and Hopkins of the Bureau of Public Roads (Lee and Garner, 1996). The first system constructed in Virginia consisted of a floating reinforced concrete slab supported by four strain-gage load cells used for aircraft weighing. Similar systems were installed throughout the United States, Europe, and Japan through the early 1960s. An inherent problem with the platform WIM system was that the inertia of the reinforced concrete slab prevented response to rapid changes as required for measuring multiple axles and closely following vehicles. Other problems included lateral movement, moisture damage,

and the expense of construction and maintenance (Cunagin, 1986). Smaller, more portable WIM systems began to be developed soon after the large platform-type scales. Lee and Garner (1996) developed a system composed of steel plates supported by strain gage load cells, first at Mississippi State University, and later at The University of Texas at Austin. In Germany, a bending plate system was developed that had strain gages embedded in grooves in the bottom surface of a steel plate.

2.3. TYPES OF WIM SYSTEMS

2.3.1. Bending Plate

Bending plate WIM systems utilize plates with strain gages bonded to the underside (McCall and Vodrazka, 1997). As a vehicle passes over the bending plate, the system records the strain measured by the strain gage and calculates the dynamic load. The static load is estimated using the measured dynamic load and calibration parameters that account for the influence of factors such as vehicle speed and pavement/suspension dynamics on the measurement of static weight. Bending plate WIM systems consist of either one or two scales. The scale or pair of scales is placed in the travel lane perpendicular to the direction of travel. The pair of scales is placed in the lane either side-by-side or staggered by five meters (16 ft). There are two types of bending plate systems, permanent and portable. Bending plate WIM systems consist of at least one scale and two inductive loops. The inductive loops are placed upstream and downstream from scales. The upstream loop is used to detect vehicles and alert the system of an approaching vehicle. If an axle sensor is used to determine the vehicle speed, it is placed

downstream of the weigh pad. Figure 2.1 shows an example layout for a bending plate WIM system.

2.3.2. Piezoelectric Sensor

Piezoelectric WIM systems utilize piezo sensors to detect a change in voltage caused by pressure exerted on the sensor by an axle and measure the axle's weight (McCall and Vodrazka, 1997). As a vehicle passes over the piezo sensor, the system records the electrical charge created by the sensor and calculates the dynamic load. The static load is estimated using the measured dynamic load and calibration parameters. Piezoelectric WIM systems consist of one or more sensors, which are placed across the traffic lane. Piezo-sensors may or may not be encapsulated in an epoxy-filled metal channel that is usually made of aluminum. Figure 2.2 illustrates a typical layout of a piezoelectric WIM system.

2.3.3. Load Cell

Load cell WIM systems utilize a single load cell with two scales to detect an axle and weigh both the right and left side of the axle simultaneously (McCall and Vodrazka, 1997). As a vehicle passes over the load cell, the system records the weights measured by each scale and sums them to obtain the axle weight. The typical load cell WIM systems consist of a single load cell placed across the traffic lane. The single load cell has two in-line scales that operate independently. Off-scale detectors are integrated into the scale assembly to sense any vehicles off the weighing surface. The typical system

consists of the load cell and at least one inductive loop and one axle sensor. The schematic of the load cell is similar to Figure 2.1.

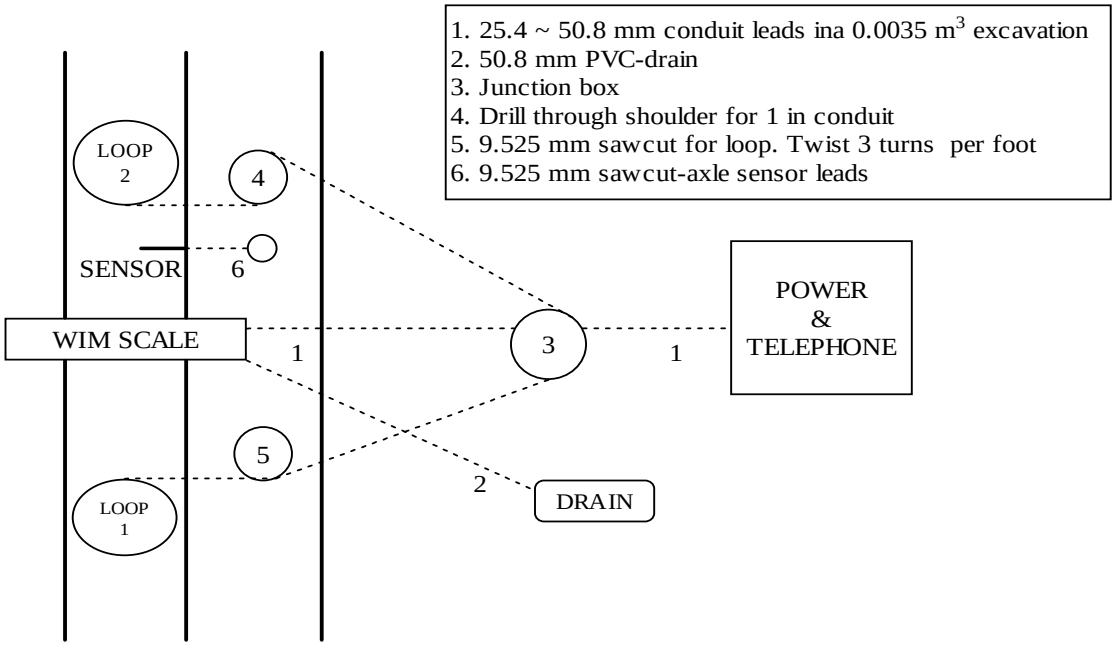

Figure 2.1. Typical Bending Plate System Layout (McCall and Vodrazka, 1997)

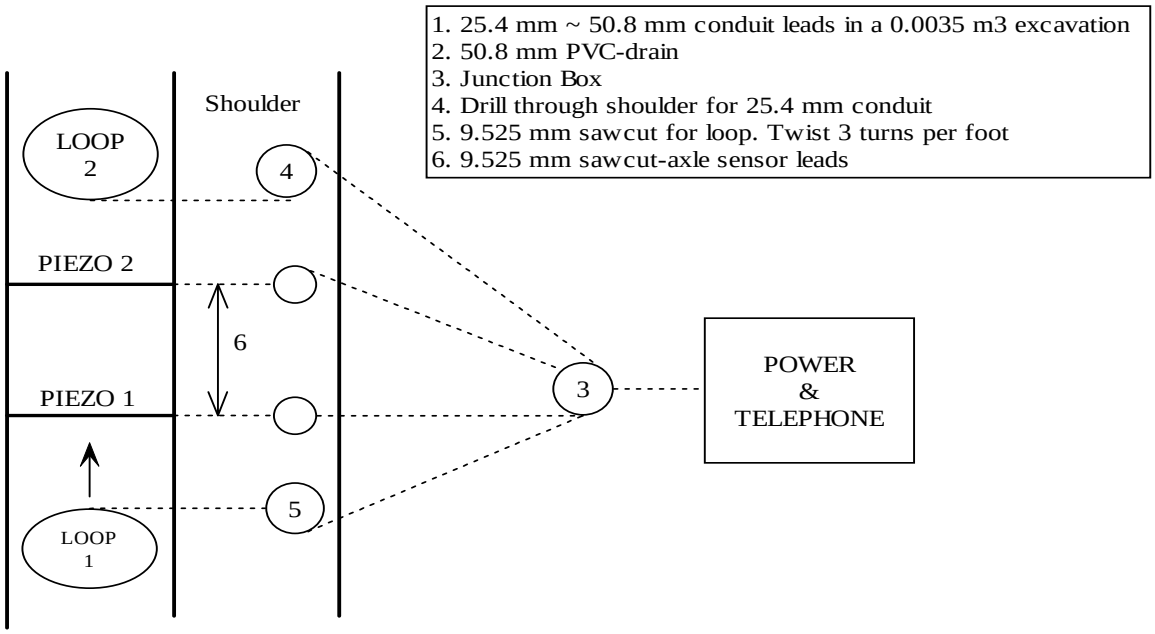

Figure 2.2. Typical Piezoelectric WIM System Layout (McCall and Vodrazka, 1997)

2.4. REVIEW OF WIM RESEARCH

2.4.1. WAVE Project

Jacob (1999) conducted a comprehensive research program called Weighing in motion of Axles and Vehicles for Europe (WAVE) began in September 1996 and was scheduled to run until June 1999. The objective of the project was to develop WIM through various measures such as improving the accuracy of conventional WIM systems; developing and improving the function and accuracy of Bridge Weigh In Motion (B-WIM) systems through more sophisticated vehicle interaction modeling and data processing; and developing common data structures. The project was divided into four main tasks.

(1) Accurate estimation of static weights using WIM systems - two techniques were investigated: multiple-sensor weigh-in-motion (MS-WIM), using an array of several WIM sensors; and B-WIM (using a structure instrumented with strain gages as a weighing plate). The work program intended to provide final specifications to implement both systems.

(2) Quality, management and exchange of WIM data – a quality assurance (QA) system was developed in order to classify and verify WIM information. The QA system was implemented and validated with a European WIM database that was produced by the COST323 project. This project was initiated in 1992 in response to a proposal from the Forum of European Highway Research Laboratories (FEHRI).

(3) Consistency of accuracy and durability - the third package is split into two parts: a Cold Environment Test (CET); and calibration procedures for WIM systems. The CET was organized by the Swedish National Road Administration (SNRA). It ran over one year and involved five WIM systems installed on a 0.5 km stretch of roadway in June 1997.

(4) Optical WIM systems - the fourth package was mainly supported by Alcatel CIT in a partnership with LCPC. A new sensor design was achieved at the beginning of the project and its performance was assessed by a number of successful laboratory tests.

Test results were analyzed based on the COST323 European specification (Jahaes, 1999). In the analysis, the relative error of the WIM measurement was determined as the difference between corresponding WIM and static measurements, expressed as a percentage of the static weight. The relative errors were calculated for the following four criteria: single axle, axle of group, group of axles and gross vehicle weight (GVW). Figure 2.3 shows the trends in the means and standard deviations of the relative errors over a one year period for the systems tested. A negative mean indicates that the WIM system tends to underestimate the measured static weights. The closer the mean relative error is to zero, the lesser is the bias in the WIM measurements relative to the static weights. Likewise, a smaller standard deviation indicates better consistency in the WIM data from a particular system. Note that a given system may indicate good reproducibility (small standard deviation) but large bias (a large mean relative error) and

vice versa. Thus, it is desirable that WIM systems exhibit mean relative errors close to zero and small standard deviations.

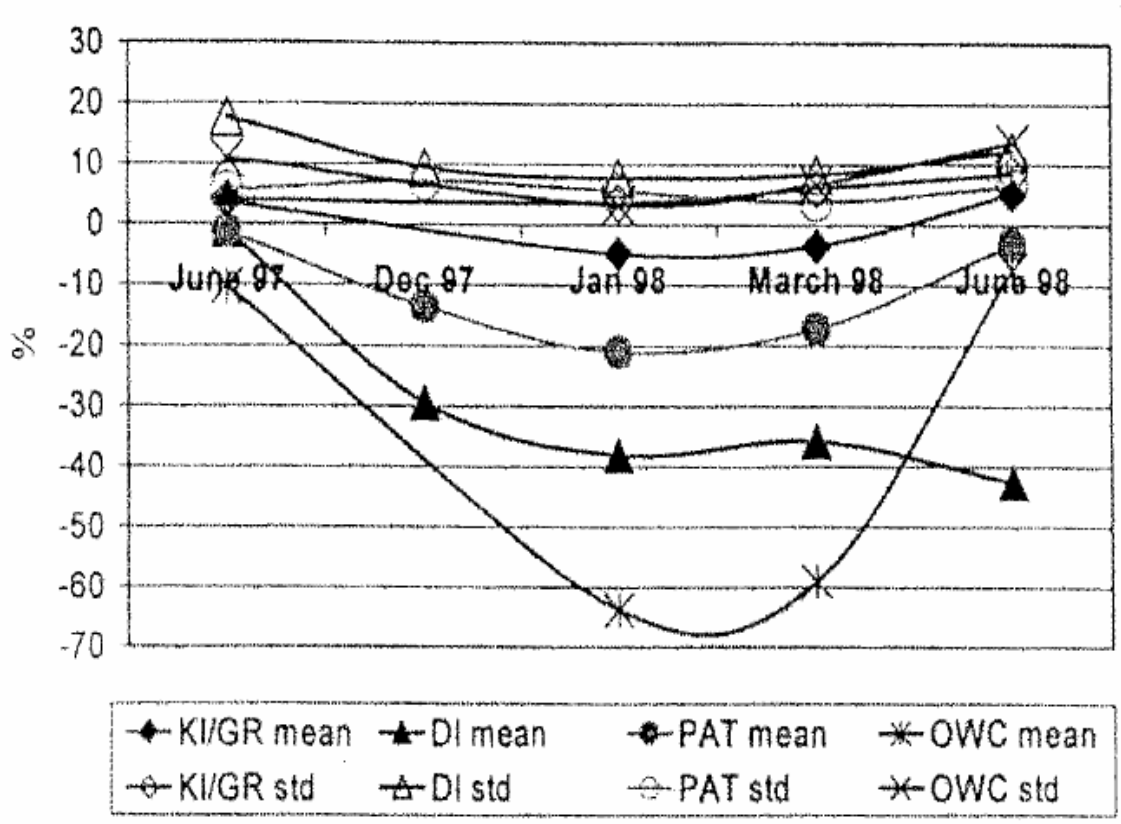

Figure 2.3. Relative Errors Based on GVW (Jehaes, 1999)

2.4.2. Low Speed WIM System (LS-WIM)

CAPTELS, a French company specialized in static weighing, developed a LS-WIM system in 1992 to 1994 (Dolcemascolo et al.1998). The principle of low speed WIM is similar to that of static weighing. It is mainly concentrated in designated areas situated beside the roadside, under the control of the police, who stop heavy vehicles and instruct them to pass over the LS-WIM system at a speed of about 10 km/h. The main advantage of low speed weighing, in comparison with static weighing, is the significant

increase of the number of vehicles weighed (typically, by a factor 10). A LS-WIM system was tested on three different sites in repeatability and reproducibility conditions, both in the laboratory and on operational sites.

The first test was carried out in August 1995 over two days. The objective was to make an initial estimation of the accuracy in full and extended repeatability conditions. Each truck made about ten passages at each of the following speeds: 4.5, 9 and 13.5 km/h. The axle loads and gross weights were recorded in motion. In the second test, trucks were first weighed by the LS-WIM system and then the static load was measured on the weigh-bridge. Due to the lack of space, trucks had some difficulties crossing the LS-WIM system at uniform speed. The test was carried out over 3 days and 207 trucks were weighed. Only gross weights were measured in static. Test results showed that the gross weights accuracy is lower for light trucks than for the heavier vehicles. The influenced of the speed was pointed out in this test. The other finding was that the ramp approach should be long enough, to avoid the dynamic effects induced by the axle climbing it up or down during the weighing operation. A total length of 30 to 35 m was recommended. To allow installation of the metallic approach ramps and to help drivers maintain a uniform speed during measurement, the site should be at least 70 to 80 m long. In addition, the weighing area must be flat and horizontal.

2.4.3. Development of a Fiber-Optic Dynamic WIM System

Cosentino and Grossman (1997) deployed flexible fiber optic sensors in both flexible and rigid pavements subjected to heavy truck traffic. Vehicles were classified

and weighed in both pavement types. The sensors, manufactured in any desirable lengths, are about 6.35 mm wide by 1.588 mm thick. For vehicle classification and WIM, sensors were typically constructed 1.83 to 2.13 m long. The sensors were epoxied into pavement grooves covered with a flexible filler material, with the leads connected to a specially designed optical electronic box. Field installations of the fiber optic sensor were conducted on the access road to a hot mix asphalt plant. The sensors in the rigid pavement have been subjected to approximately 10,000 loaded trucks weighing about 267 kN each while the sensors in the flexible pavements were subjected to about 3000 loaded hot mix asphalt trucks. The information obtained from a fiber optic sensor requires that the wave resulting from the passage of a tire be analyzed. A waveform produced from a tire rolling on a fiber optic sensor is depicted in Figure 2.4. The two main components of the fiber optic sensor waveform are the intensity loss and the pulse width. The pulse width is the time the tire contacts the sensor, which can be multiplied by the velocity of the vehicle to determine tire contact length. A method of using the contact length measured from the output waveform, along with constant values of tire pressure and tire width for each class of vehicle, resulted in the successful prediction of half axle loads within 20 percent of the static half axle weights. A portable data acquisition system was developed for use with the fiber optic sensors.

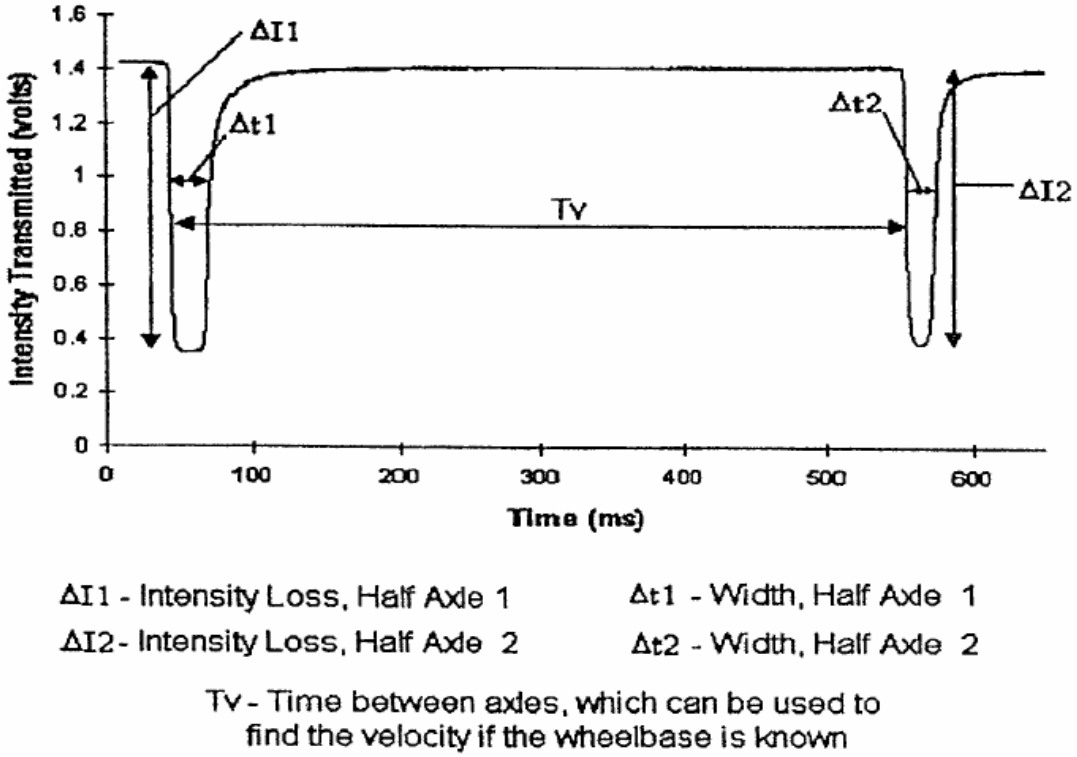

Figure 2.4. Components of Fiber-Optic Sensor Signal (Cosentino and Grossman, 1997)

2.5. APPLICATION OF FIBER OPTIC WIM

One of objects of this research is to develop WIM device based on the fiber optic technique. As mentioned, piezoelectric WIM system has monitored traffic in test section. When it comes to axle weight, permitted trucks are weighed by a static scale in Brownsville port to check their axle weight and gross weight. However there exists some discrepancy between the static scale weight and the WIM scale as shown in Figure 2.5. This discrepancy may be due to the dynamic effect or improper sensor workability. To minimize this error, a promising tool using the fiber optic technique is proposed and

applied in the current research. A detailed description of the test and results is presented in Appendix A.

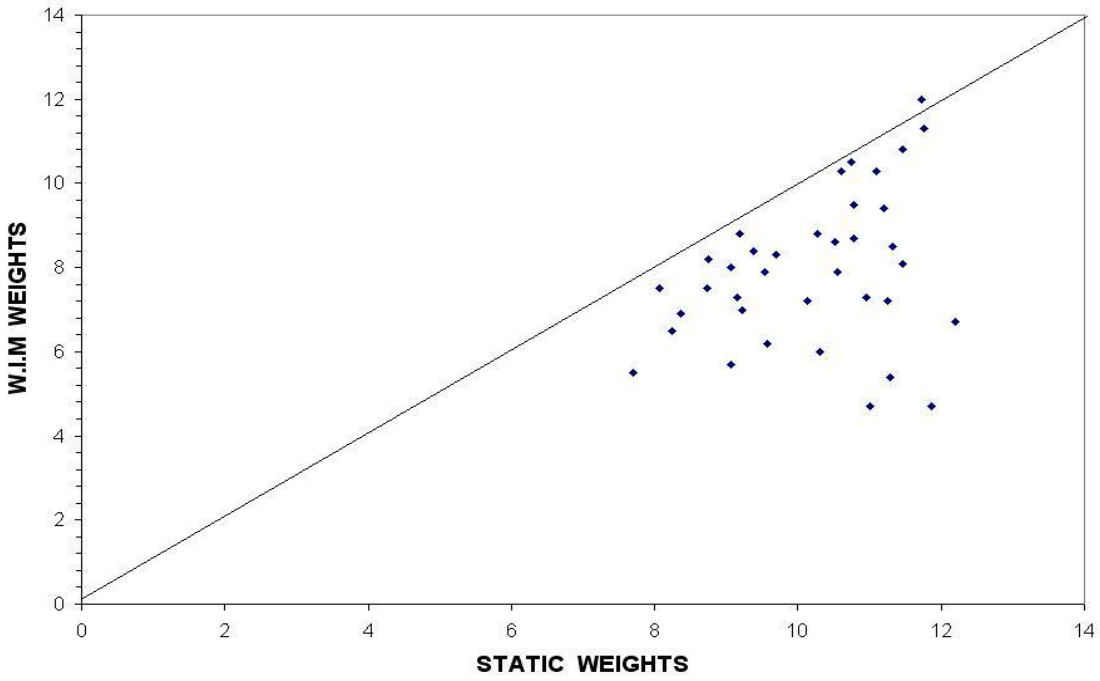

Figure 2.5. Comparison of Static Scale Weight with WIM Weight

2.6. FALLING WEIGHT DEFLECTOMETER

The Falling Weight Deflectometer (FWD) has been widely used to provide periodic non-destructive evaluations of the structural capacity and integrity of the test sections in many states. The FWD consists of a drop weight mounted on a vertical shaft and housed in a trailer that can be towed by most conventional vehicles. The FWD is a pavement NDT apparatus, which simulates the load pulse from traffic loadings. Usually the load range is 6.7 kN to 155.7 kN. Variation in the applied load levels is achieved by varying the magnitude of the dropping mass and the height of the drop. The vertical

deflections of the pavement are measured through a series of geophones at various distances from the loading plate as described in Figure 2.6. The idea of backcalculation stems from that fact that a complete analysis of the FWD field data may provide estimates of the linear-elastic response of the individual layers comprising the pavement structure and its supporting medium. A considerable knowledge of the materials comprising each layer (elastic modulus, Poisson's ratio, and layer thickness) and of the complete pavement system (linear and isotropic elasticity full interlayer friction, infinite or finite bottom conditions) is required in the analysis.

However, this is rather close to an art than a science because even with the same deflection data and given pavement structures there are no unique moduli to be determined by the backcalculation (Park, 2000). The backcalculation procedure involves calculation of theoretical deflections under the applied load using assumed pavement moduli. These theoretical deflections are compared with measured deflections and the assumed moduli are then adjusted in an iterative procedure until the theoretical and measured deflection basins reach an acceptable match. The moduli derived in this way are considered representative of the pavement response to load and can be used to calculate stresses or strains in the pavement structure.

In this study, the FWD test was conducted at several stations along the outside and inside southbound lanes of SH4/48 corresponding, respectively, to the K6 and K7 lanes. Based on the GPR measurements, FWD stations along the K6 and K7 lanes of the permitted truck route were determined. Altogether, there were 56 FWD stations established on the K6 lane, and 50 stations on the K7 lane.

Figure 2.6. Dynatest 8000 Falling Weight Deflectometer

2.7. DYNAMIC CONE PENETROMETER

The Dynamic Cone Penetrometer (DCP) has become one of the most useful testing equipment in pavement evaluation. The DCP was developed in South Africa (Kleyn and Savage, 1982) and consists of a steel rod with a cone at one end. It is driven into the pavement or the subgrade with a sliding hammer, and the material resistance to penetration is measured in terms of millimeters per blow. The cone is angled at 30 degrees, with the larger diameter of the cone being 20 mm. The hammer weights 8 kg, and the dropping sliding height is 575 mm as shown in Figure 2.7.

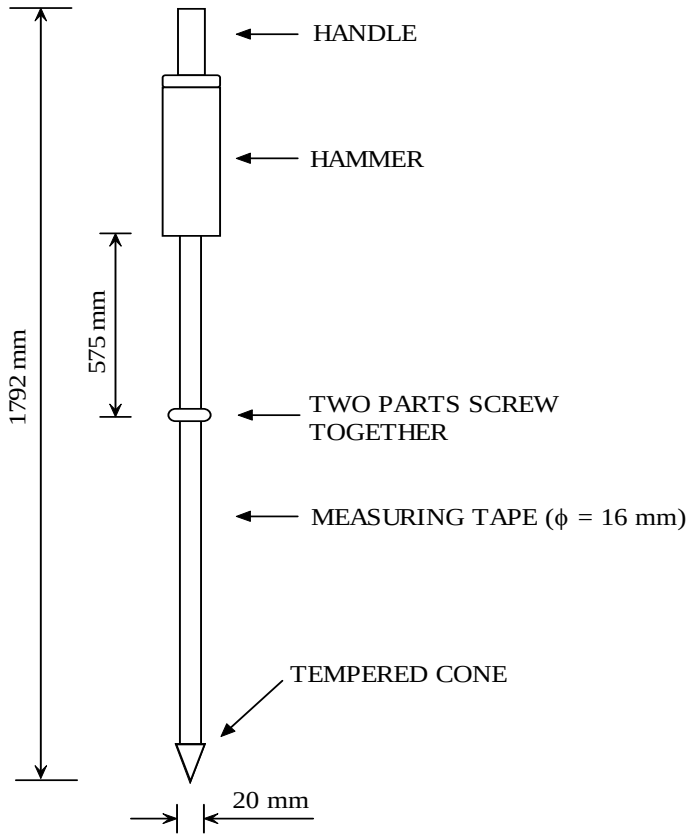

Figure 2.7. General Scheme of South African DCP

2.8. GROUND PENETRATING RADAR

The Ground Penetrating Radar (GPR) uses electromagnetic wave propagation to identify changes in electrical and magnetic properties due to reflection in the ground. The GPR has the highest resolution in subsurface imaging of any geophysical method, approaching centimeters under the right conditions. The high frequency and short time duration electromagnetic signals from 100 to 1000 MHz are transmitted through an antenna system into the subsurface (Park, 2000).

The GPR utilized for the measurement of subsurface conditions normally consists of a radar control unit, transmitter and receiver antennas, and suitable data storage and/or display devices. The radar control unit generates synchronized trigger pulses to the transmitter and receiver electronics in the antennas. These pulses control the transmitter and receiver electronics in order to generate a sampled waveform of the reflected radar pulses. Antennas are transducers that convert electrical currents on the metallic antenna elements to transmit electromagnetic waves that propagate into a material. Antennas radiate electromagnetic energy when there is a change in the acceleration of the current on the antenna. Radiation occurs along a curved path, and radiation occurs anytime that the current changes direction (e.g. at the end of the antenna element). Controlling and directing the electromagnetic energy from an antenna is the purpose of antenna design. Antennas also convert electromagnetic waves to currents on an antenna element, acting as a receiver of the electromagnetic energy by capturing part of the electromagnetic wave. GPR systems are digitally controlled, and data are usually recorded digitally for post-survey processing and display. The digital control and display

part of a GPR system generally consists of a microprocessor, memory, and a mass storage medium to store the field measurements. A small microcomputer and standard operating system is often utilized to control the measurement process, store the data, and serve as a user interface. Data may be filtered in the field to remove noise, or the raw data may be recorded and the data processed for noise removal at a later time. Field filtering for noise removal may consist of electronic filtering and/or digital filtering prior to recording the data on the mass data storage medium. Field filtering should be normally minimized except in those cases where the data are to be interpreted immediately after recording (http://fate.clu-in.org/gpr.asp?techtypeid=41).

In the application of pavement, air-launched applications have aided in determining pavement thickness and locating trapped moisture and air voids as shown in Figure 2.8. In this system, it is possible to calculate layer dielectric constants and layer thickness by automatically monitoring the amplitudes and time delays between peaks. The surface layer is calculated using the dielectric constants as following.

$$\varepsilon_a = \left[\frac{1 + A_0 / A_m}{1 - A_0 / A_m} \right]^2 \tag{2.1}$$

where

ε_a = the dielectric constant of the asphalt concrete surfacing layer,

A_0 = the amplitude of reflection from the surface in volts, and

A_m = the amplitude of reflection from a large metal plate in volts representing the 100% reflection case.

Using a dielectric constant, the thickness of the asphalt concrete layer can be calculated:

$$h_{asphalt} = \frac{C \times \Delta t_1}{\sqrt{\varepsilon_a}} \tag{2.2}$$

where

C = the velocity of electromagnetic waves in free space, which is the speed of light and,

Δt_1 = the time delay, usually recorded in nanoseconds (10^{-9} seconds)

Figure 2.8. Air-Launched Antenna in Ground Penetrating Radar System (TTI, 2001)

2.9. MULTI-DEPTH DEFLECTOMETER

The Multi-Depth Deflectometer (MDD) is used to measure "in-situ" elastic deflections and/or permanent deformations in the various pavement layers of a test section. The basis of the patented MDD system is a series of Linear Variable Differential Transducer (LVDT) modules that are mounted on a rod in a 39mm diameter hole in the test section. The modules are anchored to the soil by way of small steel balls that are forced against of the walls of hole as shown in Figure 2.9. The reference rod is anchored into the subgrade at approximately 3 m below the pavement surface. The top of the hole is sealed with a cap that contains the connector cable to the data acquisition system. The reference rod is connected to the anchor rod using a snap head connector so that the MDD modules can be removed for re-use. The MDD is designed for use with the Heavy Vehicle Simulator (HVS). Generally, two of three MDDs with modules at each layer interface are normally installed in each HVS section. During testing, the permanent deformation at each module is recorded, as are the elastic deformation basins under the test wheel loads. The plastic deformation data is used to develop transfer functions relating load repetition to plastic strain in the road building materials. (http://www.dynatest.com/hardware/CSIR/mdd.htm). The deflection data can be used to determine the effective elastic moduli for each pavement layer. One of the advantages of MDD is that, it is feasible to check the validity of backcalculation of layer moduli by comparing calculated pavement responses against the values measured by the MDD. In addition, the layer strain can be calculated by dividing the difference of displacement between two adjacent modules by the gap length. It allows not only estimating layer rut

depth with the layer strain approach but also predicting the service life using the vertical strain at the top of the subgrade. Actually, the MDD was used to measure axial displacement due to OTT loads in order to compare with predicted measurements and evaluate damage potential in this study. The layout of the MDD installation and test results are presented in Chapter IV.

Figure 2.9. Installed Multi-Depth Deflectometer

2.10. TIME DOMAIN REFLECTOMETRY

The Time Domain Reflectometry (TDR) equipment was originally developed to detect breaks in communication cables. In the 1950s, it was adopted by the agricultural community to measure soil moisture. The principle of the TDR system is similar to that of a radar system. An electromagnetic waveform is transmitted through a medium, and any obstruction or change in impedance sends a portion of the reflected waveform back to the source (Klemunes, 1998). The soil or unbound granular materials comprising the pavement structure is composed of a three-phase system: soil solids, air and water. The dielectric constant for air is 1. For most soils, the dielectric constant typically varies between 3 and 5, while the dielectric constant of water is typically near 80. The presence of water in a mixture is the primary determinant of the dielectric constant of the mixture by the TDR probe. As moisture is added to the soil, the composite dielectric constant increases due to the large dielectric constant of water. The TDR probe used in this research is depicted schematically in Figure 2.10.

Once the emitted pulse reaches the end of the probe, a portion of the signal is reflected back through the shielding of the coaxial cable to the Tektronix unit. The reflected voltage versus time is displayed on the PC monitor by software. The horizontal distance between the initial and final inflection points of the TDR trace response is the travel time of the signal called the apparent length (L_a). The apparent dielectric constant (K_a) of soil can be obtained as:

$$K_a = \left[\frac{L_a}{L \times V_p} \right]^2 \qquad (2.3)$$

where L is the actual length of the probe, and Vp is the ratio of the actual propagation velocity to the speed of light. Volumetric water content θ may be estimated from the dielectric constant as (Topp et al., 1980) :

$$\theta = -5.3\times10^{-2} + 2.92\times10^{-2} K_a - 5.5\times10^{-4} K_a{}^2 + 4.3\times10^{-6} K_a{}^3 \qquad (2.4)$$

However, this model does not show accuracy for all tested soils, especially fine grained soils. A more suitable equation for a granular material is given by Scott et al. (1983):

$$K_a = 3.91 + 30.1\theta + 198.8\theta^2 - 417.3\theta^3 \qquad (2.5)$$

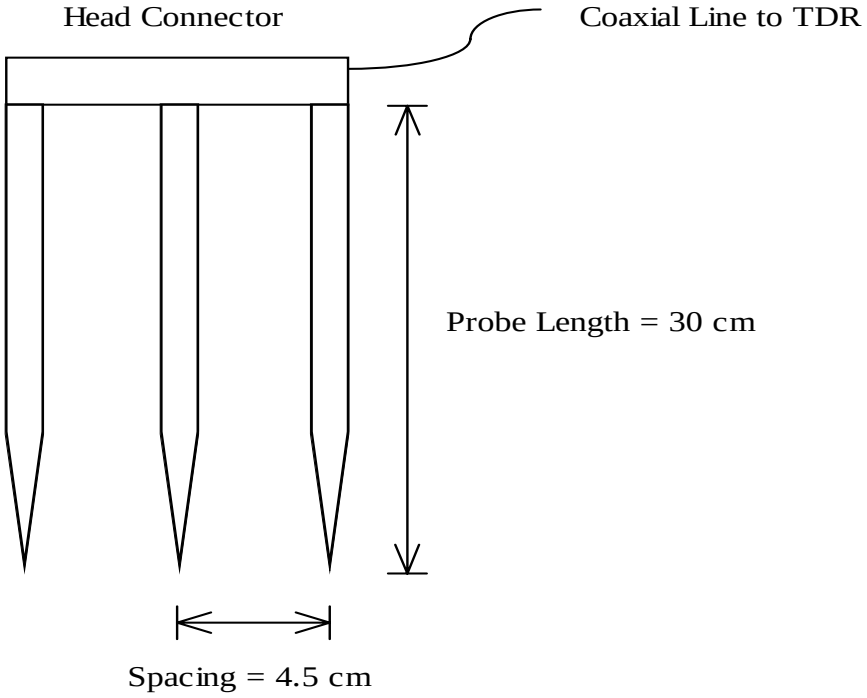

Figure 2.10. TDR probe

The accuracy of TDR measurements depends on precise measurement of time and precise calibration with the relative volumetric content of water around the probe (http://www.sowacs.com/sensors/tdr.html). The laboratory test was conducted to obtain

an empirical calibration equation that has a good agreement between TDR measurements and laboratory test results. Soil samples taken from field test section were compacted. Whenever each compacted sample was completed, the level of moisture and compaction was recorded. Soil samples consisted of base and subgrade material was moisturized at three different water contents and compacted at two levels of compaction efforts. Table 2.1 summarizes the test combinations.

Table 2.1. Molded Sample Information

Soil Type	Base	Subgrade
Moisture content (%)	3, 9, 15	5, 15, 25
Compaction Level	Low density	Low/High density

After completion of molded samples, the TDR probe was inserted vertically and perpendicularly to the surface of sample. During the test, samples were covered by a vinyl membrane to prevent moisture from evaporating as shown in Figure 2.11. Measurements were taken every 15 minutes using 6 TDR probes simultaneously. Although traces of the TDR from the soil were distorted after the TDR probes were inserted, all traces reached an equilibrium stage after around 30 minutes as shown in Figure 2.12. The calibration equation for the six TDR probes were obtained and tabulated in Table 2.2.

Figure 2.11. Sample Preparation for Calibration Test

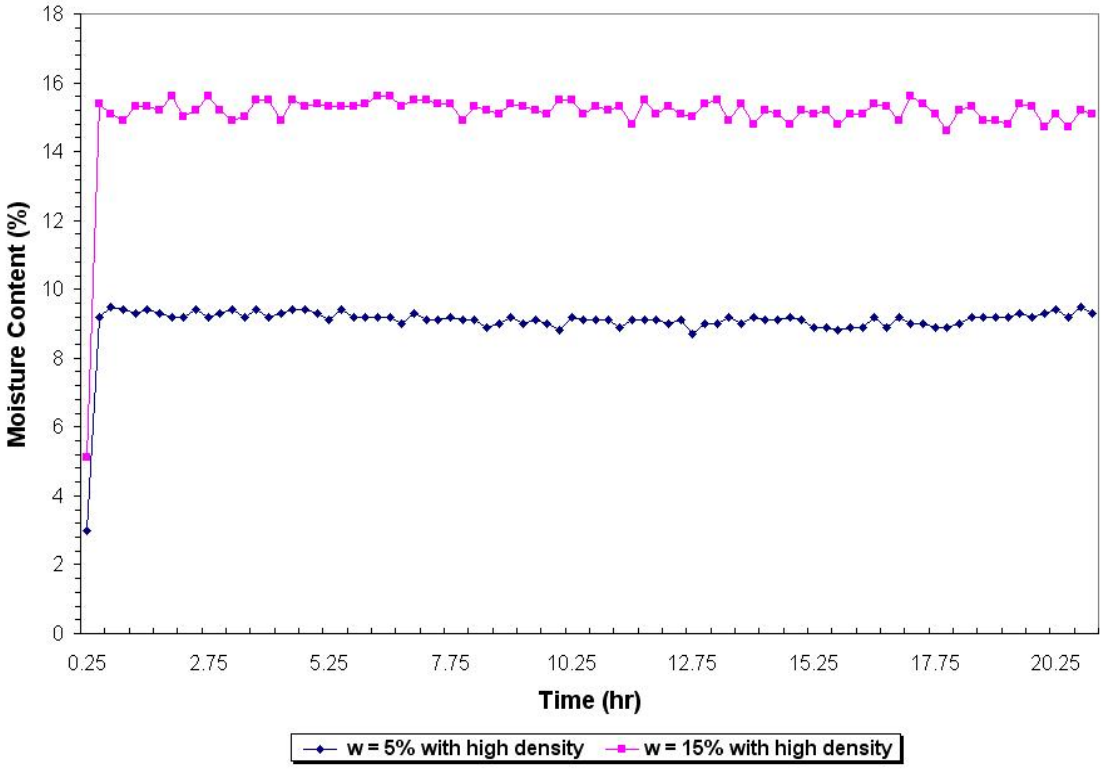

Figure 2.12. TDR Trace with Time Variation

Table 2.2. Calibration Equation for Six TDR Probes

No. of Probe	Equation	R-square
1	$w_{lab} = 0.8433 \times w_{TDR} + 0.9957$	0.95
2	$w_{lab} = 0.1098 \times w_{TDR} + 18.261$	0.98
3	$w_{lab} = 0.1000 \times w_{TDR} + 18.56$	0.99
4	$w_{lab} = 0.0743 \times w_{TDR} + 6.4869$	0.97
5	$w_{lab} = 1.3000 \times w_{TDR} + 0.09$	0.93
6	$w_{lab} = 1.4965 \times w_{TDR} - 2.6594$	0.90

The TDR was installed at the field test section as illustrated in Figure 2.13. Six TDR probes were embedded within the base and subgrade layers to monitor the variation of moisture during the test period.

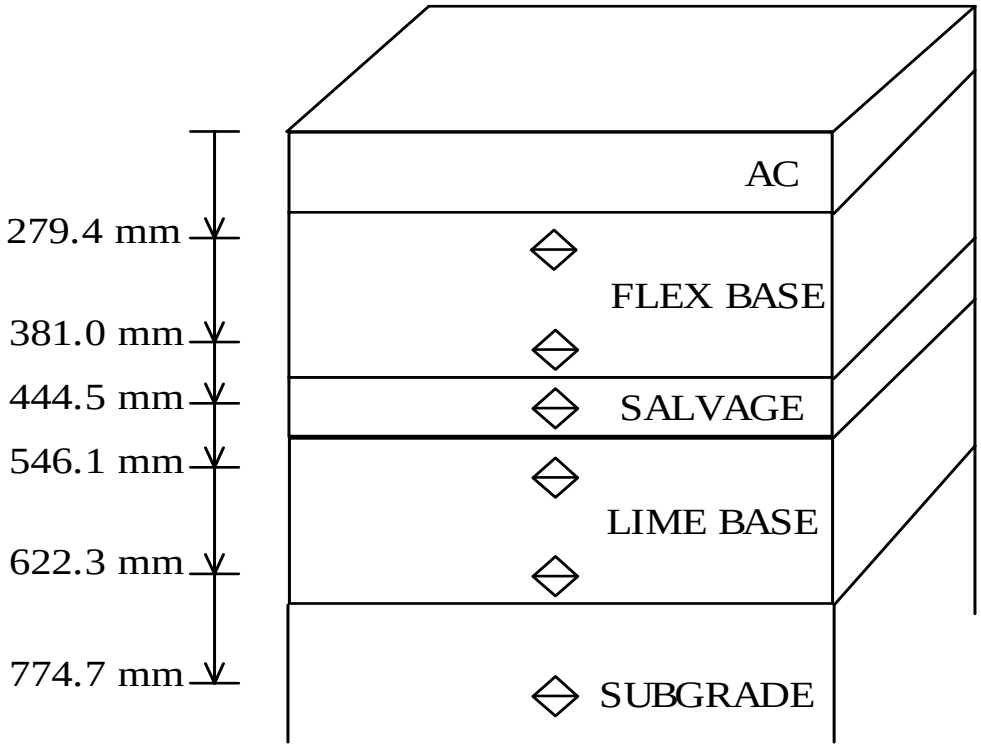

Figure 2.13. Layout of TDR at the Field Test Section

2.11. THERMOCOUPLE

A thermocouple is a sensor for measuring temperature. It consists of two dissimilar metals, joined together at one end, which produce a small unique voltage at a given temperature. This voltage is measured and interpreted by a thermocouple thermometer. It is essential to measure pavement temperature to obtain temperature corrected modulus. Fernando (2001) recommended that pavement temperature measurements be made on homogeneous segments at specified depths. At the very least, the temperature at the mid-depth of each layer should be taken. However, additional measurements near the surface and bottom of the layer may be necessary to characterize the temperature profile for establishing the pavement temperature at the time of test. In this study, eight thermocouples were installed in the asphalt concrete layer and base layers to investigate the variation of temperature during the test as shown in Figure 2.14.

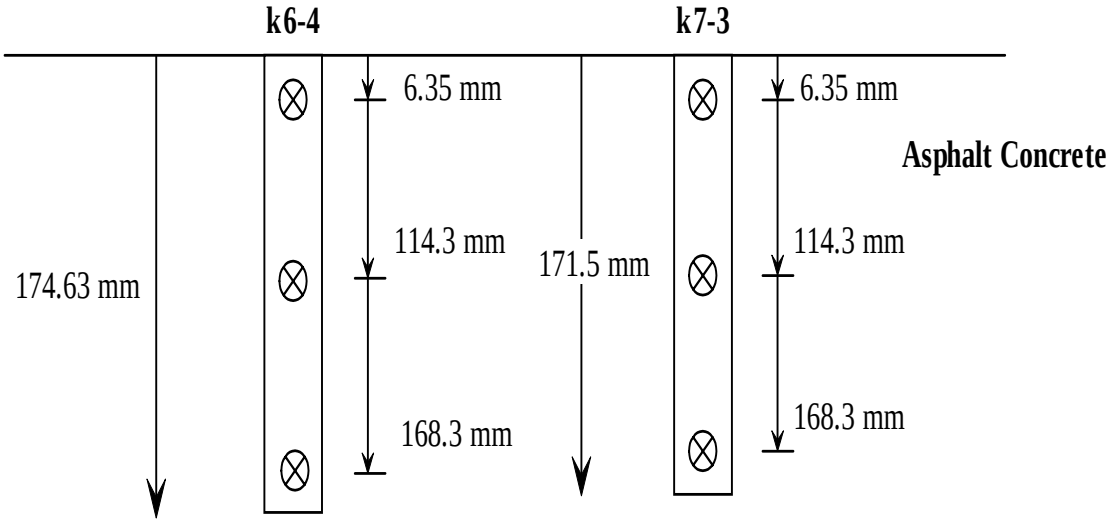

(a) On the Lane.

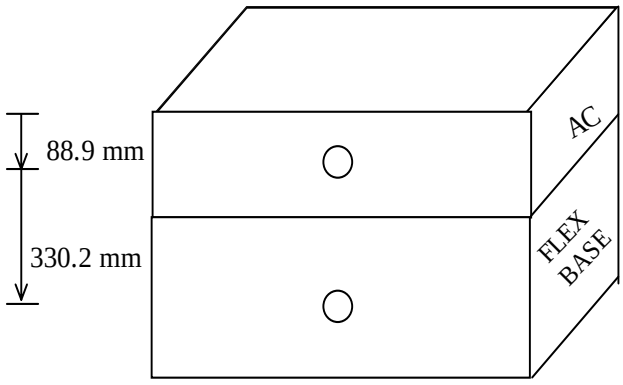

(b) At shoulder.

Figure 2.14. Layout of Thermocouple Sensors

2.12. WEATHER STATION

In this research, the weather station was installed near the weigh in motion station as depicted in Figure 2.15. The weather station was used to collect weather data during the test period in order to characterize seasonal variation. The following data are collected using this equipment:

(1) Average Air Temperature (F)

(2) Relatively Humidity (%RH)

(3) Average Solar Flux Density (W/m^2)

(4) Average Wind Speed (mph)

(5) Average Unit Vector Wind Direction (degrees)

(6) Total Rain (inches)

(7) Average Thermocouple Temperature (F)

(8) Volumetric Water Content by TDR Probe (%)

Thermocouples and the TDR described in previous sections are linked to the weather station data logging system and the data is stored automatically as a type of electronic file. The weather station collected data from June/02 to March/03. The main concern was focused on moisture and temperature variation to investigate seasonal variation. It may permit a verification of the correlation between those variations with the property of materials making up the pavement structures. Every data set was collected every 15 minutes. To check the seasonal variation, the data were averaged each month because most of the trends per day were similar. In case of the TDR, the data collected by six probes was corrected using the calibration equations presented in Table 2.2. Unfortunately, several probes that were embedded within subgrade did not work well during the test. It may be attributed to the electrical or mechanical problem of probes. Figure 2.16 shows the variation of average temperature measured at the middle depth of the asphalt concrete and base layers. The corresponding sensor location to the number of sensor is as below:

- #2 : At the middle of the AC on the K7 Lane,
- #5 : At the middle of the AC on the K6 Lane,
- #7 : At the middle of the AC on the Shoulder,
- #8 : At the middle of the Flexible base.

Figure 2.15. Scheme of Weather Station

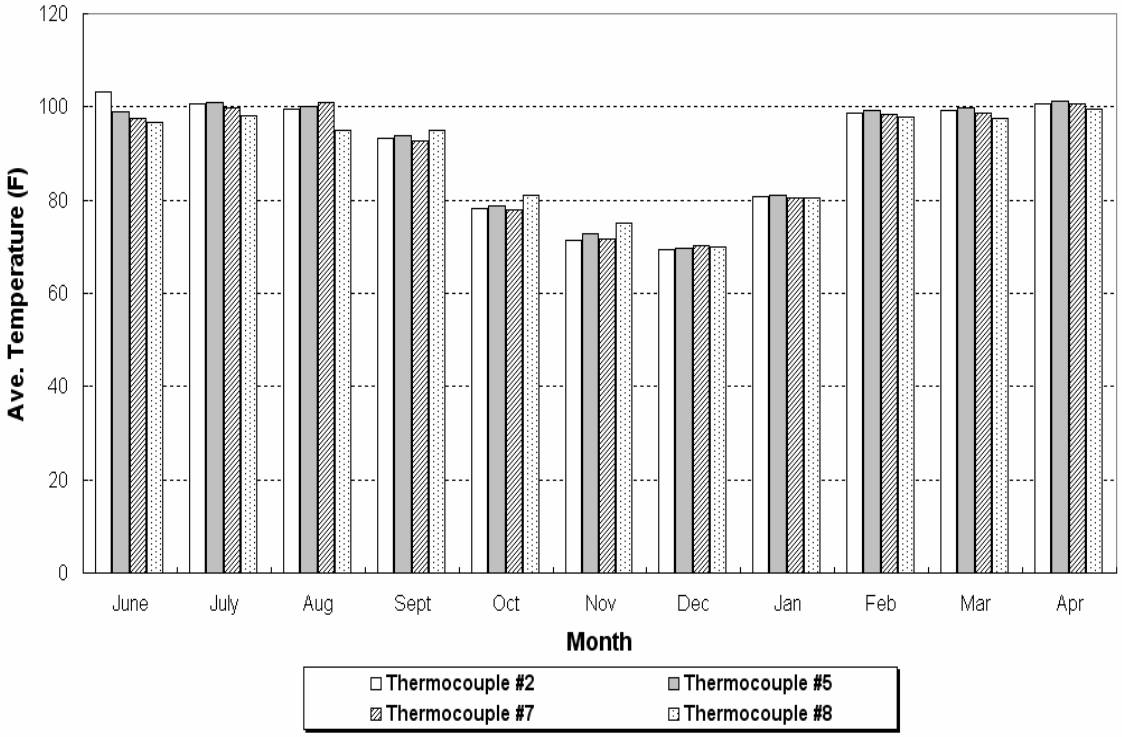

Figure 2.16. Variation of Temperature

The variation of each sensor was very similar during the test. The year can be divided into based on the above plot. Table 2.3 presents the average temperature with respect to each season. The analysis of performance prediction accounts for this seasonal variation.

Table 2.3. Average Temperature (°F) for Seasons

	Season 1	Season 2	Season 3
Thermocouple #2	89.61	75.10	99.10
Thermocouple #5	90.38	75.38	98.51
Thermocouple #7	89.52	75.37	97.79
Thermocouple #8	90.23	75.21	96.24

The variation of moisture was also investigated as illustrated through Figures 2.17 and 2.19. The change of moisture content of materials is attributed to the precipitation. It assumes that all of the rain that falls on the pavement is available for infiltration through the pavement surface directly into the base course (Lytton et al., 1990). It was observed that the moisture content within the flexible base layer varied with time while that of remains such as salvage, lime stabilized and subgrade did not show a pronounced change. In case of sensors embedded in lime stabilized and subgrade layers, measurement was not readable during the project due to the sensor problem. It may be attributed to the unstable electronical connection between sensor and data logger or damage by water intrusion since an unusually high moisture content was measured in the subgrade layer. Consequently, it is difficult to divide the year into seasonal variations based on moisture content measurement. Therefore, the seasonal change in the pavement

section will be considered only with respect to the temperature variation tabulated in Table 2.3.

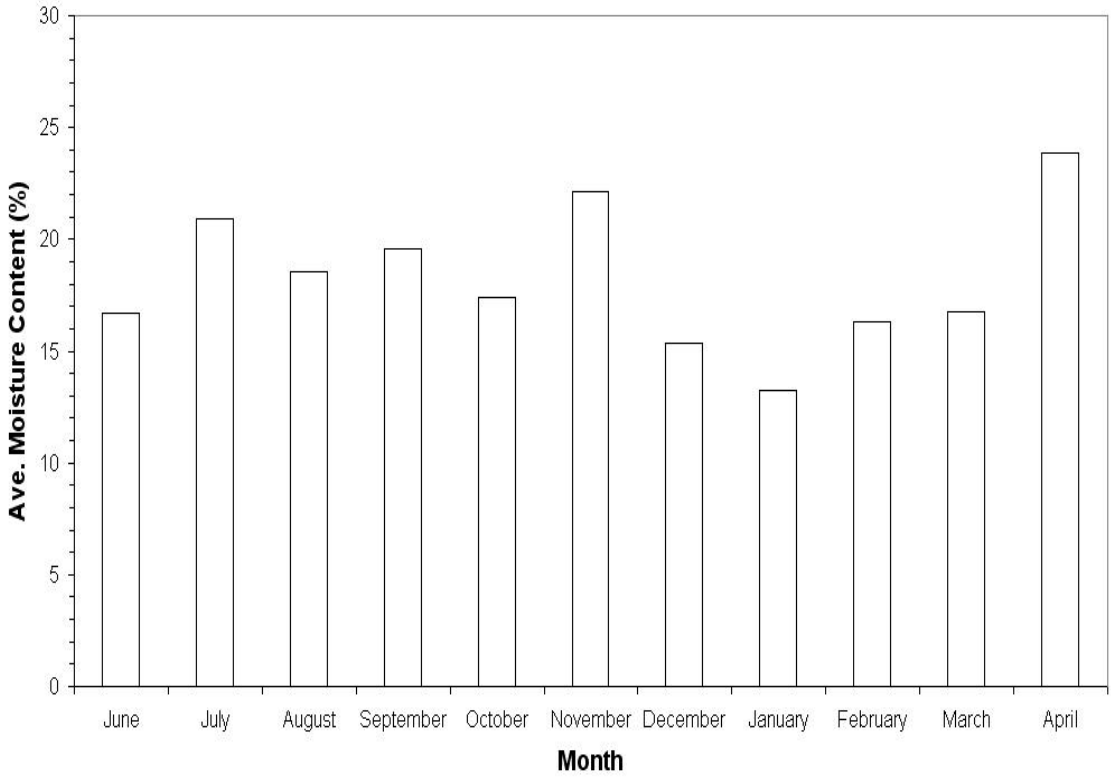

Figure 2.17. Variation of Moisture Content of Flexible Base

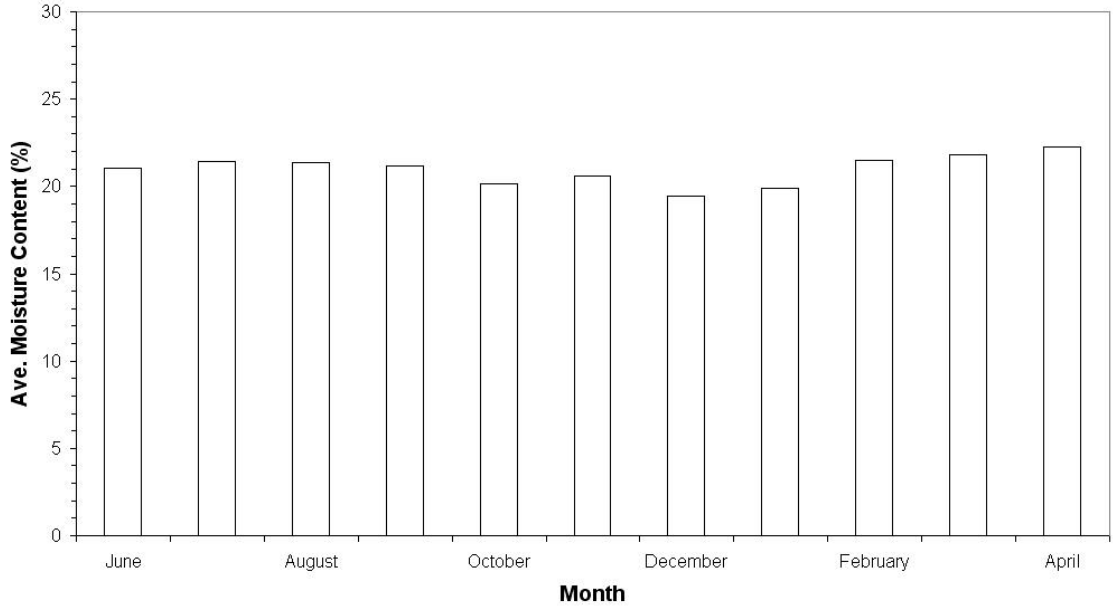

Figure 2.18. Variation of Moisture Content of Salvage Base

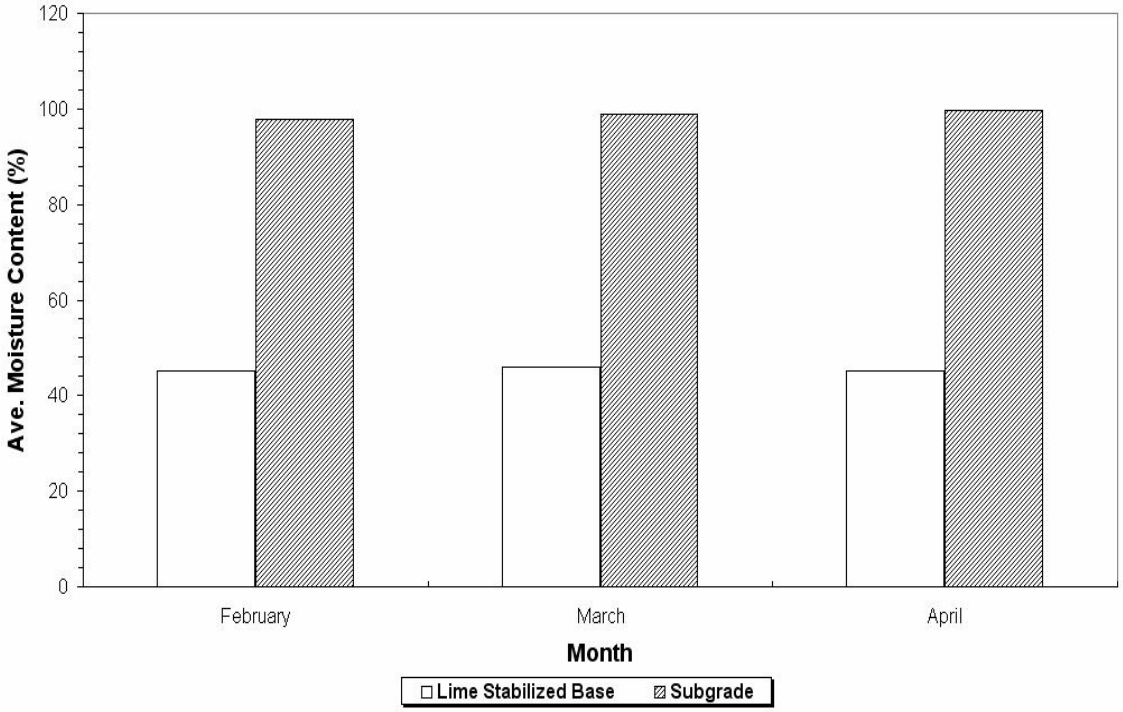

Figure 2.19. Variation of Moisture Content of Lime Treated subbase and Subgrade

CHAPTER III

CHARACTERIZATION OF MATERIALS

Laboratory tests were performed to determine material properties related to cross anisotropy and stress dependency. The nonlinear resilient and strength parameters can usually be determined from resilient modulus and triaxial tests, respectively. Test materials were taken at the field test section located along the SH4/48 test section at Brownsville, Texas. There are two lanes in this test section with the direction of travel from the port to the downtown area. The inside lane is designated K7 and the outside lane is for K6. A total of 56 FWD test stations for K6 and 50 FWD test stations for k7. Among the stations, K6-4 and K7-3 stations were selected for pavement assessment test sections because they are located closest to the WIM station. Three different types of base materials and subgrade soil were taken from the shoulder area beside the K6-4 station. In addition, the intact soil located at least 1 m below subgrade was sampled using a steel Shelby tube to minimize disturbance. Shelby tube soil samples were taken at several stations determined by soil classification determined from the County Soil Survey map on this area (1977) and Unified soil classification system. Table 3.1 shows the classified intact soil. For base materials, the following tests were conducted:

- Sieve analysis to determine size distribution
- Compaction test to determine optimum moisture content
- Cross-anisotropy test
- Permanent deformation test

Table 3.1. Soil Classification for Intact Soil

Soil Class	Soil Sample Corresponding to Station
Inorganic Clays (High plasticity) – CH	K7-11
Inorganic Clays (High plasticity) – CH	K6-23, K6-29, K7-12, K7-15, K7-20
Inorganic Clays (High plasticity) - CH	K6-11, K6-45, K7-9
Inorganic Clays (High plasticity) – CH	K6-50, K6-53, K7-40, K7-46
Inorganic Clays (Low to Medium plasticity) - CL	K6-1, K6-4, K7-3
Inorganic Clays (High plasticity) – CH	K6-35, K6-42, K7-31, K7-37

3.1. PARTICLE SIZE ANALYSIS

The particle size analysis of base materials was conducted in accordance with TEX –110-E method. This analysis provides information on how to achieve maximum compaction with the sampled aggregate. Three base materials types, flexible base, salvage base and lime treated base materials were prepared for the laboratory test. In the case of flexible and salvage base material, because the maximum aggregate size for mixing was assumed to be 19.05 mm, the grain size distribution below 19.05 mm was considered. Table 3.2 shows the results of the particle size analysis for base materials. Whether a coarse aggregate is well graded can be determined by plotting the grain size distribution curve and computing the coefficient of uniformity C_u and the coefficient of curvature C_c. These coefficients are defined as follows:

$$C_u = \frac{D_{60}}{D_{10}} \tag{3.1a}$$

$$C_c = \frac{D_{30}^2}{D_{10} \times D_{60}} \quad (3.1b)$$

Where D_{60} = grain diameter larger than 60% by weight,

D_{30} = grain diameter larger than 30% by weight

D_{10} = grain diameter larger than 10% by weight.

According to the Unified Soil Classification system (USCS), criteria for a well graded distribution in coarse aggregate are the coefficient of uniformity larger than 6 and the coefficient of curvature between 1 and 3. The values for tested materials were 45, 12 and 5 for flexible, salvage and lime treated base in that order. Although the value of lime stabilized base did not satisfy the uniformity criteria, since it appeared to be close to the criteria, tested materials are considered well graded. The particle size distributions curve for these base materials was shown in Figure 3.1.

Table 3.2. Sieve Analysis of Base Materials (Based on Percent Passing)

Sieve size (mm)	Flexible Base	Salvage Base	Lime Subbase
19.05	100	100	100
9.525	81.58	90.50	100
4.750	60.45	79.42	100
2.000	45.34	63.40	85.72
0.420	31.42	48.77	41.53
0.149	26.26	15.42	8.23
0.106	19.77	8.10	3.12

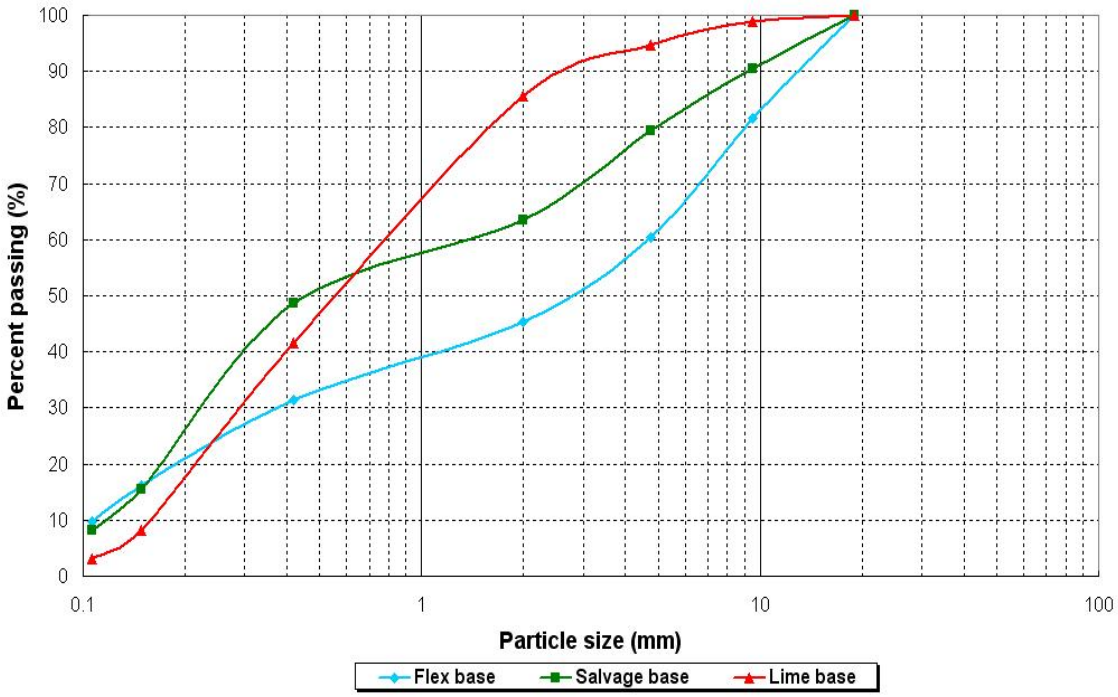

Figure 3.1. Particle Size Distribution for Base Materials

For intact soil maintained in a Shelby tube, the laser scattering particle size distribution analyzer was used instead to obtain size distribution and Atterberg limit test was conducted to get soil index properties as well. The results of intact soils are presented in Appendix B.

3.2. MOISTURE – DENSITY CHARACTERISTICS

Compaction is the densification of soils by the application of mechanical energy. The compaction is a function of four variables: (1) dry density, (2) water content, (3) compactive effort, and (4) soil type (gradation, presence of minerals, etc.). Samples were compacted in preparation for the cross anisotropy and permanent deformation tests. The

main objective of compaction in this research is to prepare a sample in a condition very similar to that of field. Field dry density and moisture content was measured using a nuclear density gage. In addition, TxDOT tested samples to obtain moisture content. To compare with this, the compaction test was performed in the laboratory of Texas Transportation Institute (TTI) based on the method denoted as Tex-113-E. A mold of diameter 101.6 mm (4 in.) and height 203.2 mm (8 in.) was used in all cases with a compactive effort of 22 blows per layer. Table 3.3 presents the results. The moisture content obtained from the laboratory is the optimum moisture content. A relatively large discrepancy was detected in the lime treated base material. However, because it was difficult to compact the sample with the same field density and with the moisture content measured by TxDOT, optimum moisture content obtained from laboratory was used instead.

Table 3.3. Moisture Content and Dry Density Obtained from Field and Laboratory

	$M.C._{Field}$ (%)	$Dry\ Density_{field}$ (kg/m^3)	$M.C._{TTI}$ (%)	$Dry\ Density_{lab}$ (kg/m^3)
Flexible Base	17.4	1671	16.8	1662
Salvage Base	15.4	1643	15.2	1683
Lime Subbase	15.5	1623	24.8	1394
Subgrade	28.9	1309	23.5	1506

3.3. STRESS DEPENDENT RESILIENT PROPERTY

One of the objectives of this study is to develop the best constitutive model, to predict the pavement response due to traffic loading with a high accuracy. There has been a recent emphasis on the use of mechanistic-empirical approaches to the design and analysis pavement structures. For this purpose, many computer programs based on linear-nonlinear elasticity have been developed to model field conditions. Resilient response of unbound granular materials is usually characterized by resilient modulus and Poisson's ratio or by shear and bulk modulus. For repeated load triaxial tests with constant confining stress, the resilient modulus and Poisson's ratio are defined. Several models have been suggested to explain the relationship between the resilient property and stress or strain and several of these are reviewed below.

Hicks et al. (1971) developed the so-called K-θ model in which the resilient modulus is expressed in the form of

$$M_R = K_1 \theta^{K_2} \tag{3.2}$$

The model has been widely used in pavement engineering to introduce a stress-dependent resilient modulus with constant Poisson's ratio. However the deviatoric stress effect is not considered. There is a limitation to apply this model to pavement structures where the shear stress is relatively large.

Uzan (1985) modified equation 3.2 to take into account the effect of deviatoric stress. The modified model is

$$M_R = K_1 P_a \left(\frac{\theta}{P_a} \right)^{K_2} \left(\frac{\tau_{oct}}{P_a} \right)^{K_3} \tag{3.3}$$

where,

M_R = resilient modulus,

Pa = atmosphere pressure (100 kPa),

θ = first stress invariant (bulk stress),

τ_{oct} = octahedral shear stress, and

K_i = material constants from laboratory tests.

In this model, a fixed Poisson's ratio problem still remains. However, Uzan (1992) updated the model using a relationship between the resilient modulus expression given by equation 3.3 and the thermodynamic constraints to derive an expression that relates the stress state and the rate of change of the Poisson's ratio with a changing stress state, to the Poisson's ratio. The derived equation with respect to the stress dependent Poisson's ratio is as follows:

$$\nu_j^i = \frac{\left[\left(\frac{2}{3k}\right)\times \nu_{j-1}^i + \left(\frac{1}{l\times I_1}\right)\times \nu_j^{i-1} - \frac{k_3^{'}}{3J_2} + \frac{k_2}{I_1^2}\right]}{\left[\frac{2}{3k} + \frac{1}{l\times I_1} - 2\frac{k_3^{'}}{3J_2} - \frac{k_2}{I_1^2}\right]} \qquad (3.4)$$

where,

I_1 = normalized first stress invariant,

J_2 = normalized second invariant of the deviatoric stress tensor,

l,k = step sizes for increasing I_1 and J_2, respectively,

i,j = counter for I_1 and J_2 respectively,

$k_3^{'}$ = $k_3/2$

Choosing a step size from increasing I_1 and J_2 and then increasing I_1 and J_2 from a fixed boundary condition for which the Poisson's ratio is known solves equation 3.4. In this

study, this procedure was incorporated into a finite element program which was developed to consider stress dependent modulus and Poisson's ratio. The nonlinear properties (K_1~K_3) were obtained from a modified triaxial test by multiple regression analysis in a process that will be described in the next section.

3.4. CROSS-ANISOTROPY PROPERTY

3.4.1. Application of Cross-Anisotropy in Granular Materials

Apart from modeling stress dependent moduli, the cross-anisotropic formulation has been applied to improve analysis accuracy. The applicability of the cross-anisotropy model to pavement engineering originates from soil mechanics. The relevance of this subject is that most natural soils, as well as rocks, in their response to stress exhibit some degree of anisotropy. In general, while an isotropic elastic material is characterized by only two independent elastic constants (e.g., Young's modulus, E, and Poisson's ratio, ν), five parameters are needed to describe the stress-strain relationships in a cross-anisotropic material: Young's modulus, E_v, in the vertical direction; E_h, in the horizontal direction ($E_h = nE_v$); Poisson's ratio, ν_{vh}, for the effect of vertical strain on horizontal strain; ν_{hh}, for the effect of horizontal strain on complementary horizontal strain; and shear modulus, G, for distortion in any vertical plane, $G = mE_v$ (Leknitskii, 1963 and Gazetas, 1982). A theoretical solution was presented on the effect of soil cross-anisotropy on surface displacement and stress distributions in a homogeneous thick soil deposit subjected to axisymmetric parabolic vertical surface loading (Gazetas 1982). The behavior of a granular medium depends at any point on the arrangement of particles,

which is usually determined by aggregate characteristics, construction methods, and loading conditions. Tutumluer et al. (1997) stated that an apparent anisotropy is induced due to random aggregate placement and compaction loading. The granular layer, therefore, becomes much stiffer in the vertical direction than in the horizontal direction even before the wheel load on the pavement imposes further anisotropic loading. The main reason to apply cross-anisotropy to granular materials in pavement engineering is that an unexpected tensile stress in granular materials that is generated from linear isotropic analysis could be eliminated. Because tensile forces cannot be transferred from particle to particle, when such forces act in the horizontal direction, the behavior of the granular material is significantly affected by a directional dependency of material stiffness that can be accommodated by using the anisotropic approach.

Several researchers have investigated tensile stress generation within unbound granular materials. Duncan et al. (1968) and Hicks (1970) found the possibility of the existence of tensile stress in a granular layer as a function of the modulus ratio of the AC to the base and also the base to the subgrade. Zienkiewicz et al. (1968) proposed an iterative tension correction procedure called the “stress transfer method” to offer a solution to the problem of rock and unbound aggregate not being able to produce the tension predicted by the finite element method. “No tension” could be achieved by applying compressive forces equal in magnitude but opposite in direction to the horizontal tensile stresses predicted in granular base materials.

Raad and Figueroa (1980) reported on an analysis for granular materials that is based on Mohr-Coulomb theory. The principle of Mohr-Coulomb theory that was

incorporated into a finite element program was to limit the horizontal tensile stresses predicted in the granular layer by linear or nonlinear elastic stresses under the Mohr-Coulomb envelope indicating compressive zone.

Selig (1987) used tank model to describe the existence of horizontal tensile stress in the tensile zone. General elastic layer theory gives a tensile incremental horizontal stress at the bottom of a two-layered system in which the upper layer has a greater stiffness than the lower layer. If the sufficient compressive horizontal stress to compensate it, failure will occur in this zone. Through laboratory testing using a tank model, it was found that large horizontal compressive stress could develop in granular material by compaction or repeated wheel loading.

Tutumluer (1995) developed the GT-PAVE finite element program that can handle nonlinear cross-anisotropy. With this effort, the horizontal tensile stress was reduced up to 75 percent. It was also observed that a horizontal resilient modulus that was 15 percent of the vertical resilient modulus was necessary to correctly predict the horizontal and vertical measured strain in the unbound granular base.

Adu-Osei (2000) performed laboratory tests to obtain cross-anisotropy properties of unbound granular materials with various moisture contents and density. A finite element program was modified to incorporate nonlinear cross-anisotropy material behavior and stress dependent Poisson’s ratio. Different pavement sections were analyzed with the finite element program. Nonlinear cross-anisotropy modeling was observed to predict self-confinement within granular layers.

3.4.2. Test for Cross-Anisotropy Property

Comprehensive laboratory tests have been conducted to characterize cross-anisotropy properties for cohesive and cohesionless soils. Ward et al. (1959) performed a series of undrained triaxial tests on undisturbed London clay samples. It was found that heavily over-consolidated clay showed a strong anisotropic character by having a value of n ranging from 1.35-2.37. Kirkpatric et al. (1972) conducted experimental tests to simulate the natural process of sedimentation of normal or slightly over-consolidated clays. From this study, n values for normally or slightly over-consolidated kaolinite and illitic clays were determined ranging from 0.9-1.35. Bellotti et al. (1996) carried out comprehensive tests in a large calibration chamber with dry Ticino silica sand. The seismic body wave propagation was modeled by five independent constants of the cross-anisotropy. Test results suggested that the anisotropic consolidation stress ratio K is responsible for anisotropy of the small strain stiffness of Ticino sand. Typical n and m values ranged from 0.8 to 1.8 and 0.35 to 0.60 respectively. A total of 50 triaxial test results on granular materials with different saturation and density levels were analyzed by Tutumluer (1995) to establish the typical variations of stress ratio values n and m. It was shown that a value of n is between 0.03 and 0.21 for dry to partially saturated aggregates having low to high densities. The range of the m value was distributed from 0.18 to 0.35 for most of the dry to partially saturated aggregate types.

Adu-Osei (2000) developed a test protocol by taking three stress state regimes; compression, extension, and shear test. The developed testing protocol permits the

application of a variety of both confining and deviatoric stress combinations. From this test, five cross-anisotropy properties are obtained using the expressions below:

$$M_R^V = \Delta\sigma_V^C / \Delta\varepsilon_V^C \tag{3.5}$$

$$M_R^H = \Delta\sigma_H^S / \Delta\varepsilon_H^S \tag{3.6}$$

$$G_{HV} = 3\Delta\sigma_V^S / 4(\Delta\varepsilon_V^S - \Delta\varepsilon_H^S) \tag{3.7}$$

$$\nu_{VH} = \left[\Delta\sigma_V^S / M_R^V - \Delta\varepsilon_V^S\right]\left[M_R^H / 2\Delta\sigma_H^S\right] \tag{3.8}$$

$$\nu_{HH} = 1 - \left\{\left[\Delta\varepsilon_H^S + \nu_{VH}\Delta\sigma_V^S / M_R^H\right]\left[M_R^H / \Delta\sigma_H^S\right]\right\} \tag{3.9}$$

where,

$\Delta\sigma_V^C$ = Change in Axial Stress for Triaxial Compression,

$\Delta\sigma_H^S$ = Change in Radial Stress for Triaxial Shear,

$\Delta\sigma_V^S$ = Change in Axial Stress for Triaxial Shear,

$\Delta\varepsilon_V^C$ = Axial Resilient Strain for Triaxial Compression,

$\Delta\varepsilon_H^S$ = Radial Resilient Strain for Triaxial Shear, and

$\Delta\varepsilon_V^S$ = Axial Resilient Strain for Triaxial Shear.

In this research, the modified triaxial test was performed based on the procedure developed by Adu-Osei (2000). The testing machine used was Universal Testing Machine (UTM). The repeated dynamic axial stress and static radial stress was imposed on the molded sample. The extension test was excluded because the five cross-anisotropic properties could be determined from compression and shear test regime and

it was difficult to handle stress states in the extension stress regime. The test procedure is summarized below:

1. Put a membrane on a molded sample and attach two vertical and radial LVDTs with a 90° angle at the middle of height as shown in Figure 3.2a.
2. A molded sample (101.6-mm diameter by 203.2-mm height) is loaded to a static stress state with axial and confining stress respectively during one minute. After a 30 second rest period, the axial stress is given a small dynamic stress increment while the confining stress is kept constant. The dynamic increment loading has a cycle which consists of 0.1 seconds loading followed by 0.9 seconds rest period and 100 repetitions to reach a stable stage. This is the compression test scheme. After a 30 second rest period, stress state returns to the original static stress state.
3. Again, the same level of static stress is applied during one minute. After the rest period, the dynamic increment axial stress is applied with the same frequency, while the confining stress is reduced to make the first stress invariant zero. This is the shear test scheme. After the shear test, the stress state returns to the original static stress state.
4. These steps are repeated for the seven different stress states. At each stress state, the resilient axial and radial strains are measured by LVDTs.
5. Replicate three samples for each material.

Like a standard resilient test, the test was conducted at different stress states. It allows us to investigate stress dependency and to obtain the parameters (K_1~K_3) used in the Uzan model. The seven stress states were determined from unconfined and confined

tests for different materials. Figures 3.3 to 3.6 show Mohr's circles to present stress states within failure envelope.

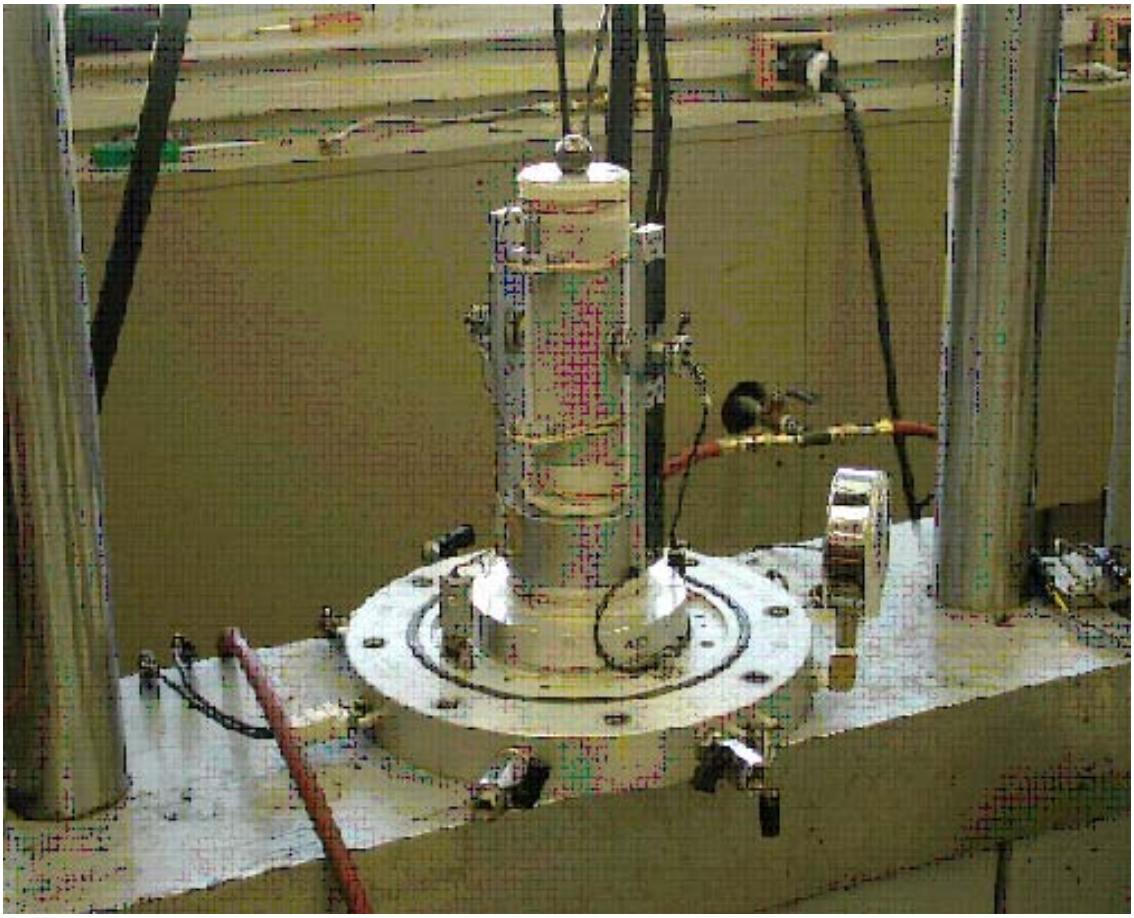

Figure 3.2a. Molded Sample before Load Application

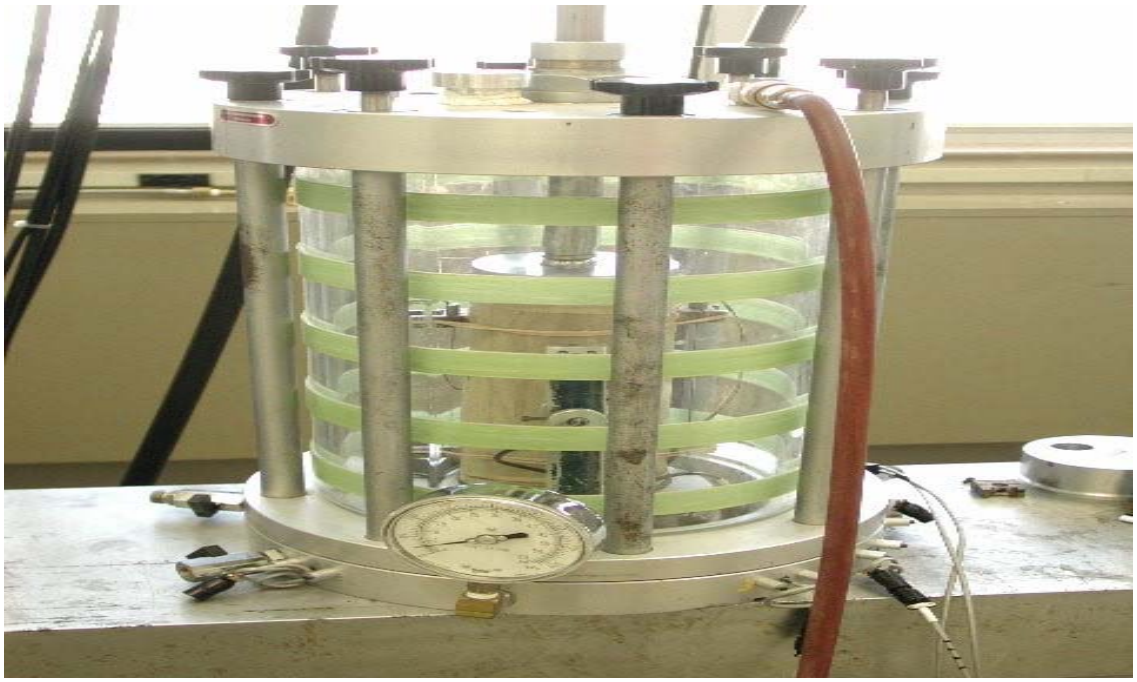

Figure 3.2b. Molded Sample during Load Application

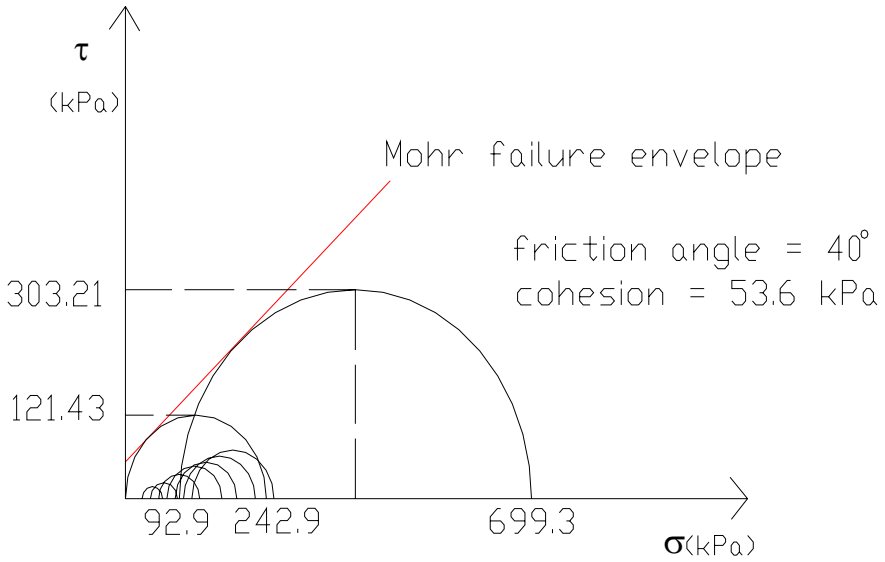

Figure 3.3. Stress States for Flexible Base

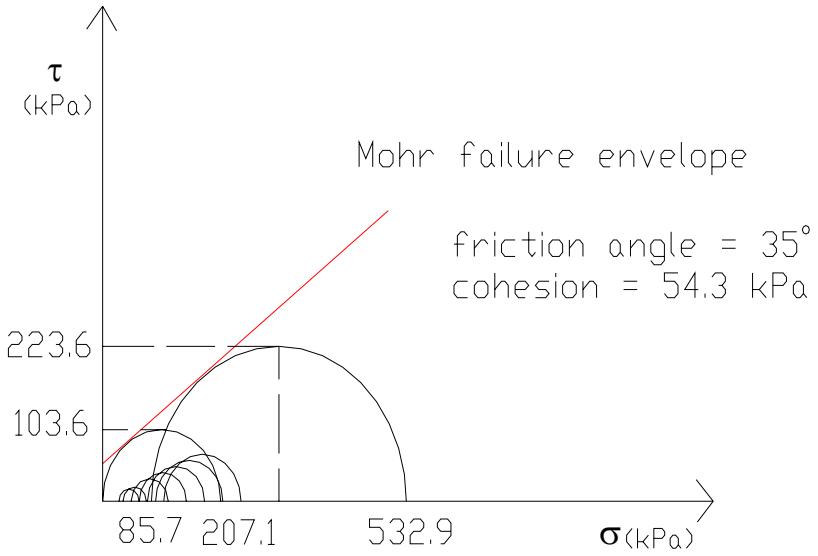

Figure 3.4. Stress States for Salvage Base

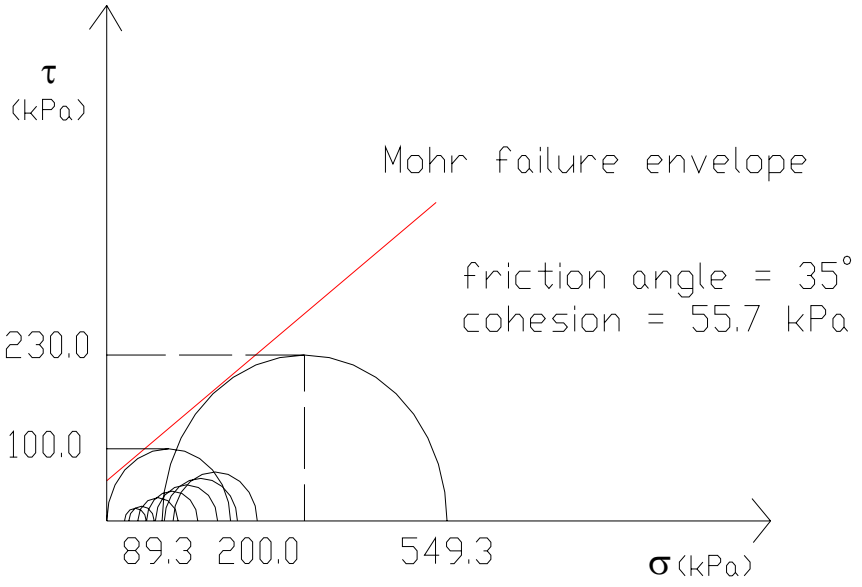

Figure 3.5. Stress States for Lime Treated Subbase

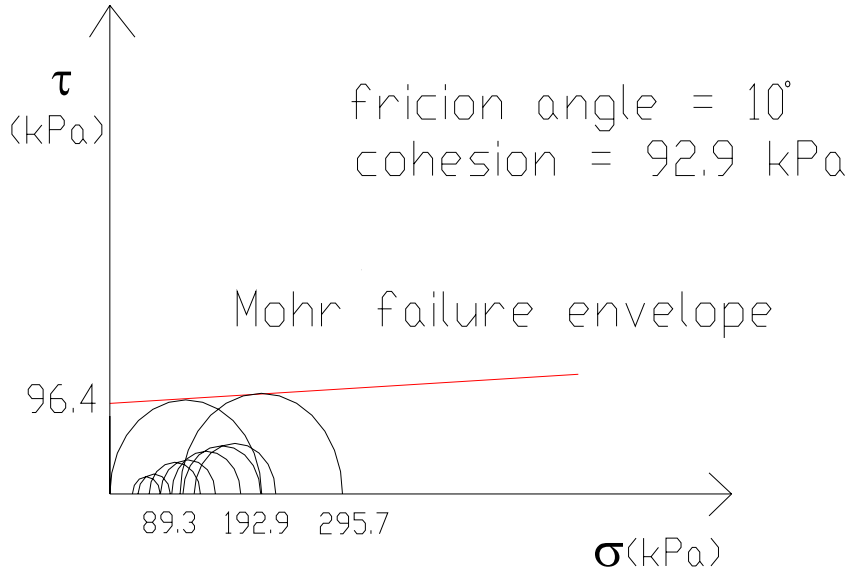

Figure 3.6. Stress States for Subgrade

The three cross-anisotropy properties are defined from obtained five parameters as following:

$$n = M_R^H / M_R^V \quad (3.10)$$

$$m = G_{HV} / M_R^V \quad (3.11)$$

$$p = \nu_{HH} / \nu_{VH} \quad (3.12)$$

There is a need to determine the representative value for each material to use it as an input to the developed finite element program that will be described in chapter V. Based on the finding by Tutumluer (1997), the Uzan model was expanded to calculate stress-dependent horizontal and shear modulus given in equation 3.13 and 3.14.

$$M_R^H = K_4 P_a \left(\frac{\theta}{P_a}\right)^{K_5} \left(\frac{\tau_{oct}}{P_a}\right)^{K_6} \tag{3.13}$$

$$G_{VH} = K_7 P_a \left(\frac{\theta}{P_a}\right)^{K_8} \left(\frac{\tau_{oct}}{P_a}\right)^{K_9} \tag{3.14}$$

According to the definition given above, the value of n and m can be expressed as following.

$$n = M_R^H / M_R^V = \frac{K_4}{K_1} \left(\frac{\theta}{P_a}\right)^{K_5 - K_2} \left(\frac{\tau_{oct}}{P_a}\right)^{K_6 - K_3} \tag{3.15}$$

$$m = G_{VH} / M_R^V = \frac{K_7}{K_1} \left(\frac{\theta}{P_a}\right)^{K_8 - K_2} \left(\frac{\tau_{oct}}{P_a}\right)^{K_9 - K_3} \tag{3.16}$$

The n and m values were determined by a constant term ($K_4/K1_1$ or K_7/K_1) based on comment by Tutumluer (1997) that because the difference of bulk stress exponents (K_5-K_2 or K_8-K_2) and that of the deviatoric stress exponents (K_6-K_3 or K_9-K_3) are similar in magnitude but opposite in sign, where the K_1, K_2, and K_3 parameters are defined in equation (3.3). Tables 3.4 - 3.7 show the laboratory test results. Three cross-anisotropy properties are calculated at each stress state using above equation. The modulus and Poisson's ratio presented in these tables are averaged with values obtained from three replications. For intact soils, several representative samples that were selected based on soil map as tabulated in Table 3.1 were tested to get properties. Since these samples were maintained in a Shelby tube in their in-situ condition, there was no necessity of remolding. The test results are presented in Appendix B. It was generally observed that the constant terms (K_4/K_1 or K_7/K_1) in the ratio models are almost identical to the

average stiffness ratio obtained from each stress state as shown in Table 3.8. Overall, this finding pointed out when deviatoric and bulk stresses take similar values under the applied wheel load, the constant ratio terms play a prevalent role in determining the stiffness ratios. The parameters obtained in the test series are tabulated in Table 3.8. The K_1~K_9 parameters were determined by multiple regression analysis. Hence, for practical purposes, when the exponents of the stress terms in the models are close to each other, the constant terms are good approximations for the horizontal and shear stiffness ratios under the wheel load (Tutumluer and Thompson, 1997). The value of p representing the ratio between two Poisson's ratios was determined using average value of all stress states because it varied in such a small range and the ratios were highly dependent on the ratio of stresses between the confining and deviatroic stress, which are almost fixed from 1.5 to 2 in this test.

Table 3.4. Cross-Anisotropy Property of Flexible Base

Stress state	Axial Stress (kPa)	Radial Stress (kPa)	M_R^V (MPa)	M_R^H (MPa)	ν_{VH}	ν_{HH}	G_{HV} (MPa)	n	m	p
1	57.14	28.57	170.06	53.45	0.27	0.44	30.84	0.31	0.18	1.60
2	83.57	42.86	173.74	63.67	0.09	0.14	41.94	0.37	0.24	1.53
3	115.00	57.14	199.88	71.57	0.17	0.23	44.41	0.36	0.22	1.38
4	146.43	71.43	243.70	90.30	0.15	0.19	50.53	0.37	0.21	1.28
5	172.14	85.71	281.37	114.14	0.14	0.17	59.47	0.41	0.21	1.23
6	198.57	100.00	324.16	134.02	0.21	0.33	73.90	0.41	0.23	1.55
7	230.00	114.29	435.83	158.07	0.05	0.10	108.77	0.36	0.25	1.97

Table 3.5. Cross-Anisotropy Property of Salvage Base

Stress state	Axial Stress (kPa)	Radial Stress (kPa)	M_R^V (MPa)	M_R^H (MPa)	ν_{VH}	ν_{HH}	G_{HV} (MPa)	n	m	p
1	57.14	28.57	163.59	68.64	0.28	0.44	25.41	0.42	0.16	1.60
2	70.71	35.71	187.34	71.42	0.21	0.31	30.13	0.38	0.16	1.49
3	102.14	50.00	242.57	81.67	0.10	0.20	48.35	0.34	0.20	1.97
4	127.86	64.29	257.89	98.53	0.28	0.55	72.71	0.38	0.28	1.97
5	159.29	78.57	271.73	113.13	0.24	0.46	84.69	0.42	0.31	1.97
6	185.71	92.86	292.69	132.32	0.19	0.39	88.28	0.45	0.30	2.03
7	217.14	107.14	315.93	139.29	0.14	0.28	108.70	0.44	0.34	1.97

Table 3.6. Cross-Anisotropy Property of Lime Treated Subbase

Stress state	Axial Stress (kPa)	Radial Stress (kPa)	M_R^V (MPa)	M_R^H (MPa)	ν_{VH}	ν_{HH}	G_{HV} (MPa)	n	m	p
1	57.14	28.57	58.34	37.50	0.50	0.88	29.24	0.64	0.50	1.77
2	70.71	35.71	92.49	58.97	0.35	0.60	43.32	0.64	0.47	1.69
3	102.14	50.00	138.42	81.28	0.07	0.12	51.37	0.59	0.37	1.82
4	127.86	64.29	148.55	98.09	0.16	0.22	54.16	0.66	0.36	1.36
5	159.29	78.57	159.22	109.11	0.26	0.41	72.10	0.69	0.45	1.58
6	185.71	92.86	182.15	128.10	0.20	0.30	73.73	0.70	0.40	1.52
7	217.14	107.14	189.87	134.08	0.25	0.39	83.79	0.71	0.44	1.56

Table 3.7. Cross-Anisotropy Property of Subgrade

Stress state	Axial Stress (kPa)	Radial Stress (kPa)	M_R^V (MPa)	M_R^H (MPa)	ν_{VH}	ν_{HH}	G_{HV} (MPa)	n	m	p
1	57.14	28.57	37.77	36.89	0.57	1.11	21.46	0.98	0.57	1.97
2	70.71	35.71	55.11	59.75	0.44	0.87	32.12	1.08	0.58	1.97
3	102.14	50.00	72.42	81.98	0.53	1.04	45.10	1.13	0.62	1.97
4	115.00	57.14	84.62	72.62	0.37	0.73	55.18	0.86	0.65	1.97
5	146.43	71.43	90.08	73.35	0.42	0.83	57.90	0.81	0.64	1.97
6	172.86	85.71	110.51	97.58	0.46	0.93	72.24	0.88	0.65	2.03
7	191.43	100.00	128.97	89.43	0.42	0.85	86.70	0.69	0.67	2.03

Table 3.8. Nonlinear Cross-Anisotropy Properties

	Flexible Base	Salvage Base	Stab. Lime Base	Subgrade
K_1	1147.69	1295.13	708.26	505
K_2	0.7	0.55	0.6	0.2
K_3	-0.1	-0.1	-0.1	-0.4
R^2	0.88	0.97	0.86	0.93
K_4	437.62	462.67	477.31	455.57
K_5	0.6	0.7	0.6	-0.3
K_6	0.0	-0.1	-0.1	0.1
R^2	0.87	0.97	0.85	0.87
K_7	208.27	349.54	243.93	296.51
K_8	0.9	0.7	0.8	0.1
K_9	-0.2	-0.1	-0.2	-0.32
R^2	0.85	0.89	0.92	0.82
$K_5 - K_2$	-0.1	0.15	0.0	-0.5
$K_6 – K_3$	0.1	0.0	0.0	0.5
$K_8 - K_2$	0.2	0.15	0.2	-0.1
$K_9 – K_3$	-0.1	0.0	-0.1	0.08
n	0.38	0.36	0.67	0.90
m	0.18	0.27	0.34	0.59
p_{ave}	1.51	1.86	1.61	1.99
n_{ave}	0.37	0.40	0.66	0.92
m_{ave}	0.22	0.25	0.43	0.63

3.5. PERMANENT DEFORMATION TEST

Repeated load triaxial tests were carried out to study the permanent deformation characteristics of materials, which were molded with the same moisture content, density and sample size used in the cross-anisotropy test. Each sample was tested at two stress levels with a

static confining stress and deviatoric stress axially cycled for 20,000 times. A haversine pulse-load was applied for 0.1 seconds with a 0.9 second rest at a frequency of 1 cycle per second. Initially, specimens were subjected to 200 cycles of preconditioning with vertical loads that were 10 % of the deviatoric stress. The accumulated vertical deformations were recorded throughout the test. The stress levels applied to the base are higher than those for the subgrade in consideration of the reduction in predicted stresses under loading with depth into the pavement (Park 2000). In addition, the full deformation data converting the loading and unloading portions of a given cycle were recorded for the 199^{th} , 200^{th} , and 201^{st} load cycles to determine the resilient strain at the 200^{th} repetition. In addition, several intact soil samples were tested without molding samples. These samples were tested as they were sampled and were only trimmed to make the sample size 76.2 mm in diameter with a height of 152.4 mm. Table 3.9 shows the stress levels used in test. The applied stress level on the subgrade was level 1. Unfortunately, the test was not performed on the Salvage Base under the level 2 condition due to lack of sample. Figures 3.7 through 3.12 show the accumulated plastic strains versus number of load cycles.

Table 3.9. Level of Test Loads for Materials

	Material	Flexible Base	Salvage Base	Lime Treated Base	Subgrade
Level 1	Confining (kPa)	57.1	57.1	28.6	28.6
	Deviatoric (kPa)	57.1	57.1	28.6	28.6
Level 2	Confining (kPa)	57.1	N/A	28.6	28.6
	Deviatoric (kPa)	114.3	N/A	57.1	57.1

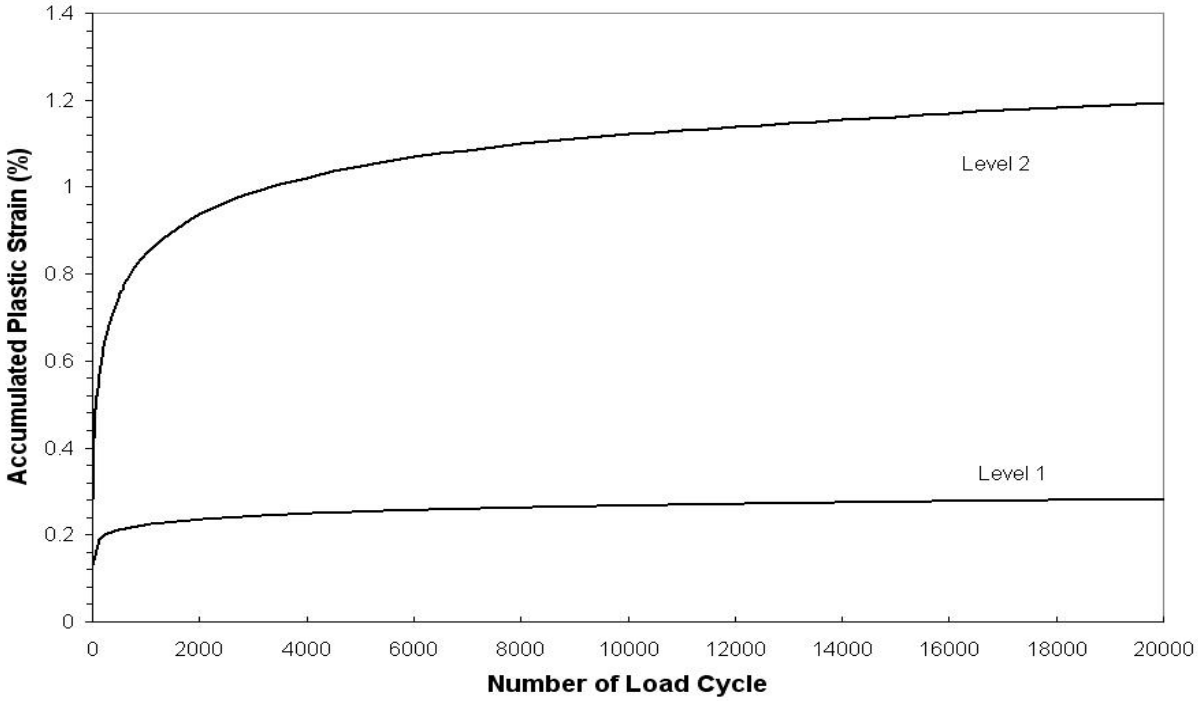

Figure 3.7. Plastic Strain versus Number of Load Cycles of Flexible Base

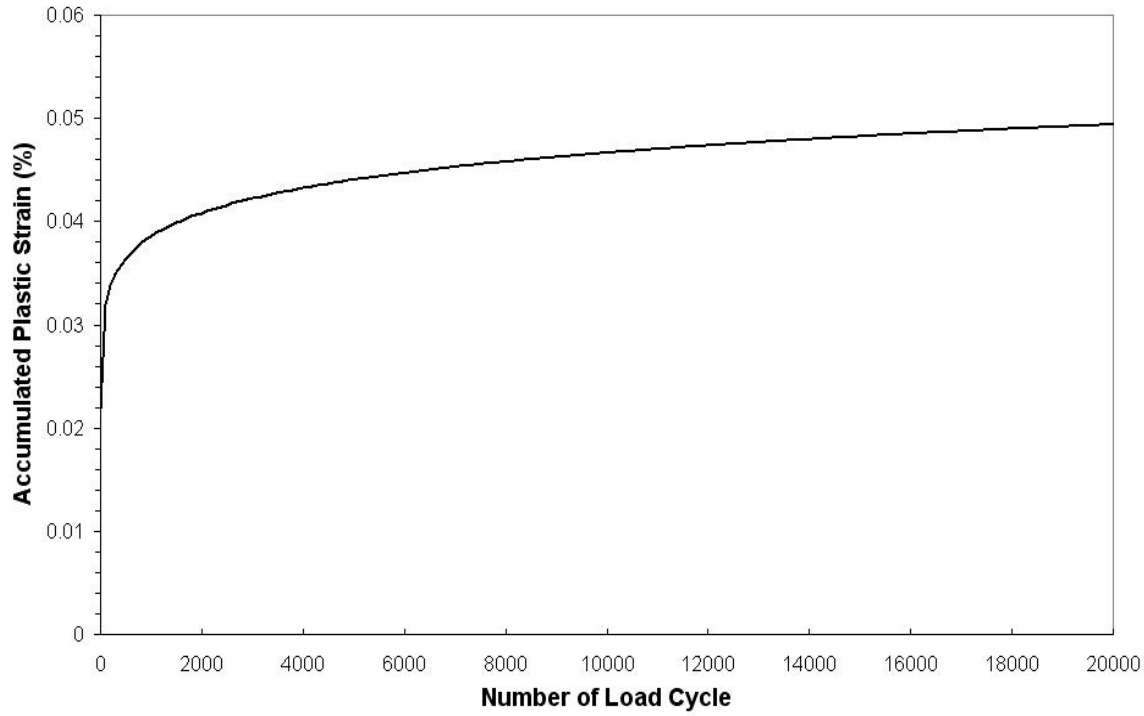

Figure 3.8. Plastic Strain versus Number of Load Cycles of Salvage Base

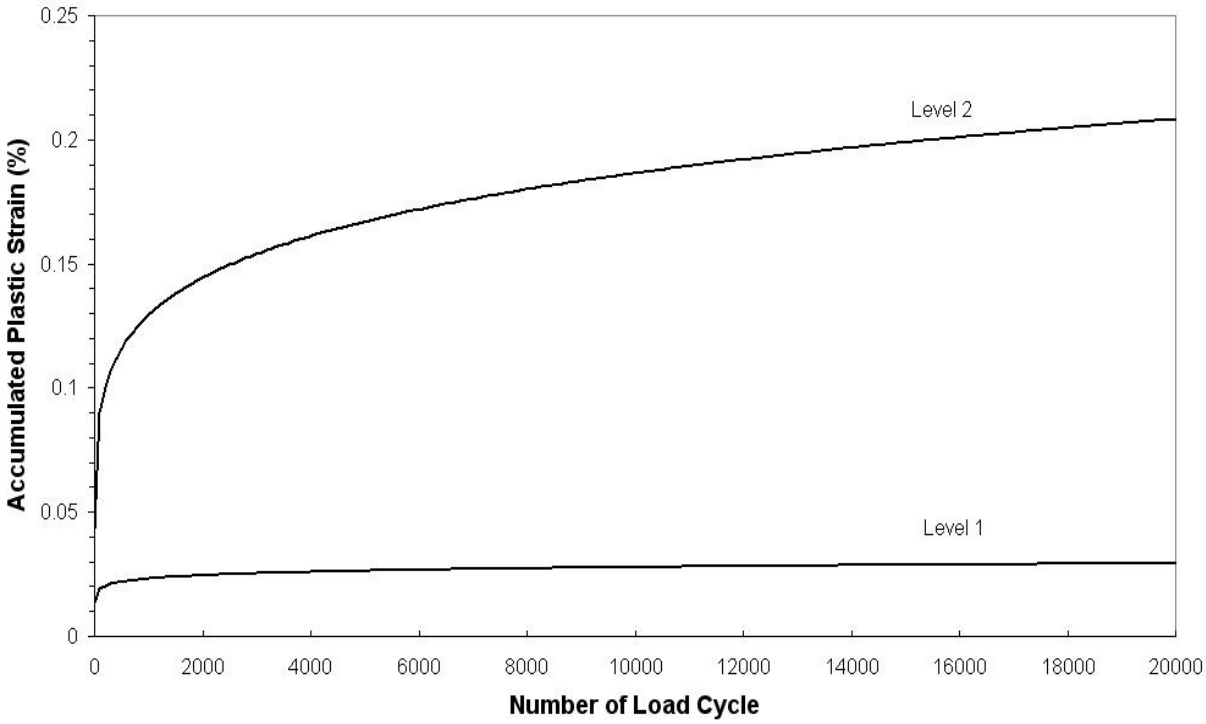

Figure 3.9. Plastic Strain versus Number of Load Cycles of Lime Treated Subbase

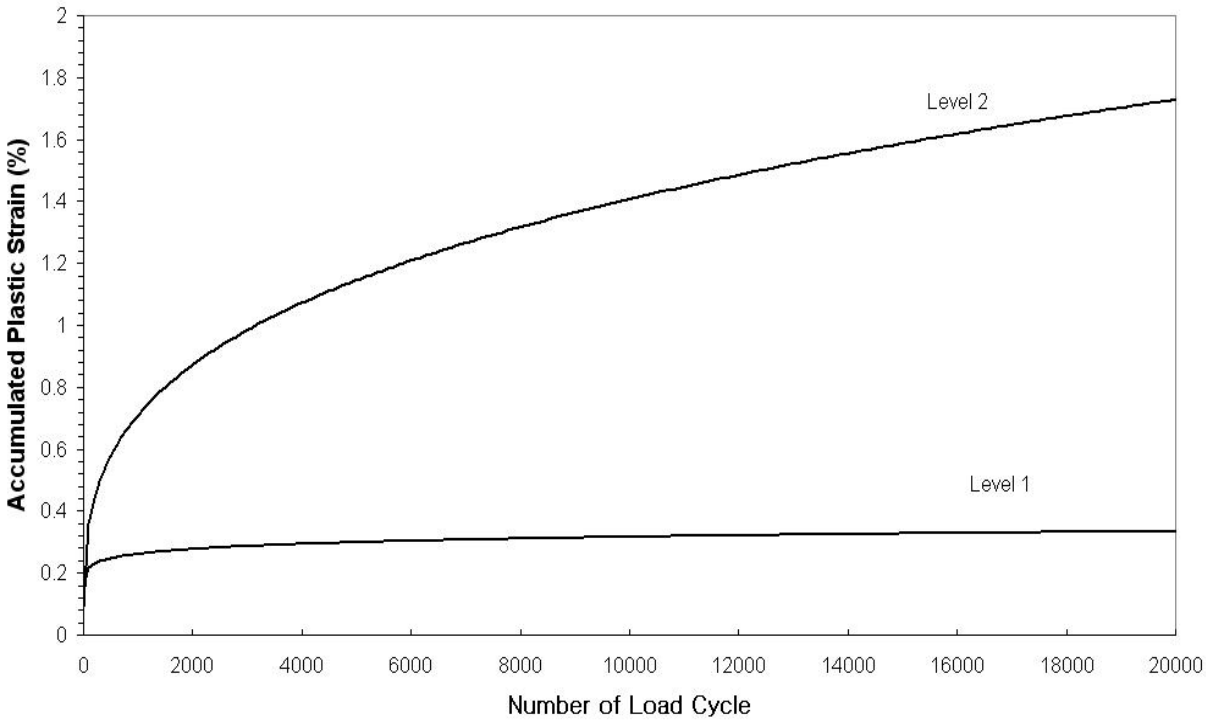

Figure 3.10. Plastic Strain versus Number of Load Cycles of Subgrade

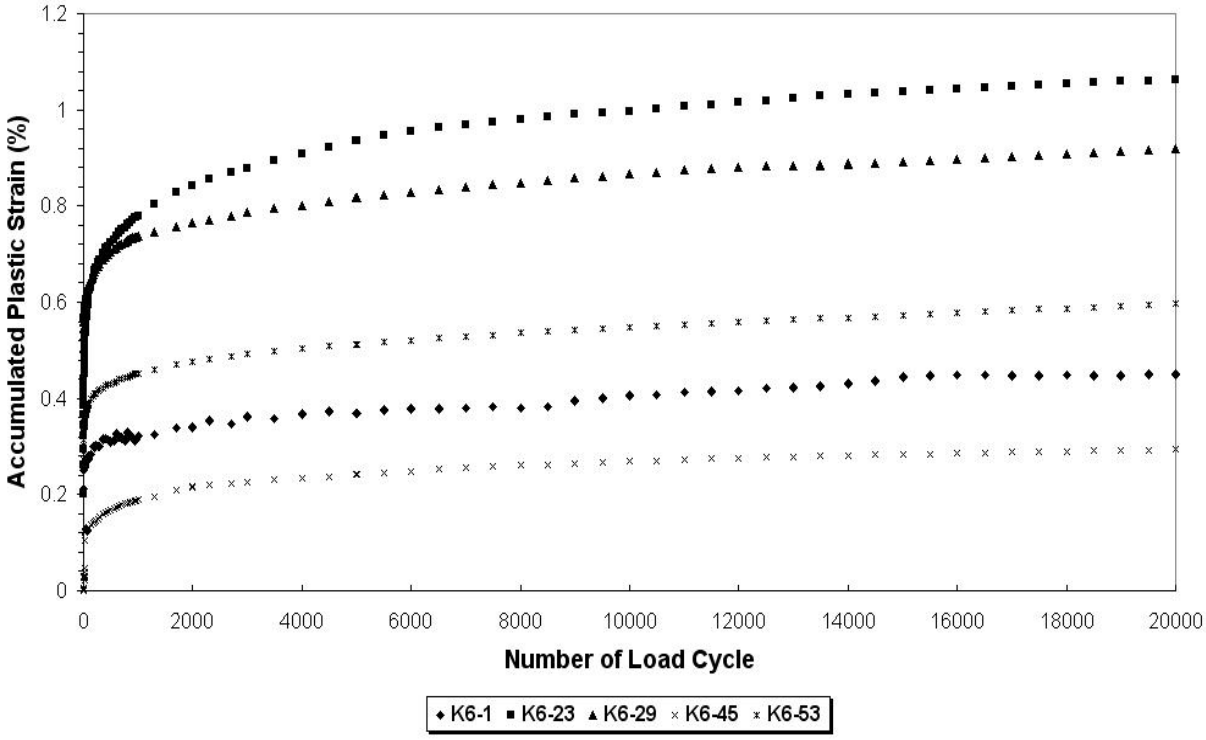

Figure 3.11. Plastic Strain versus Number of Load Cycles of K6 Intact Soils

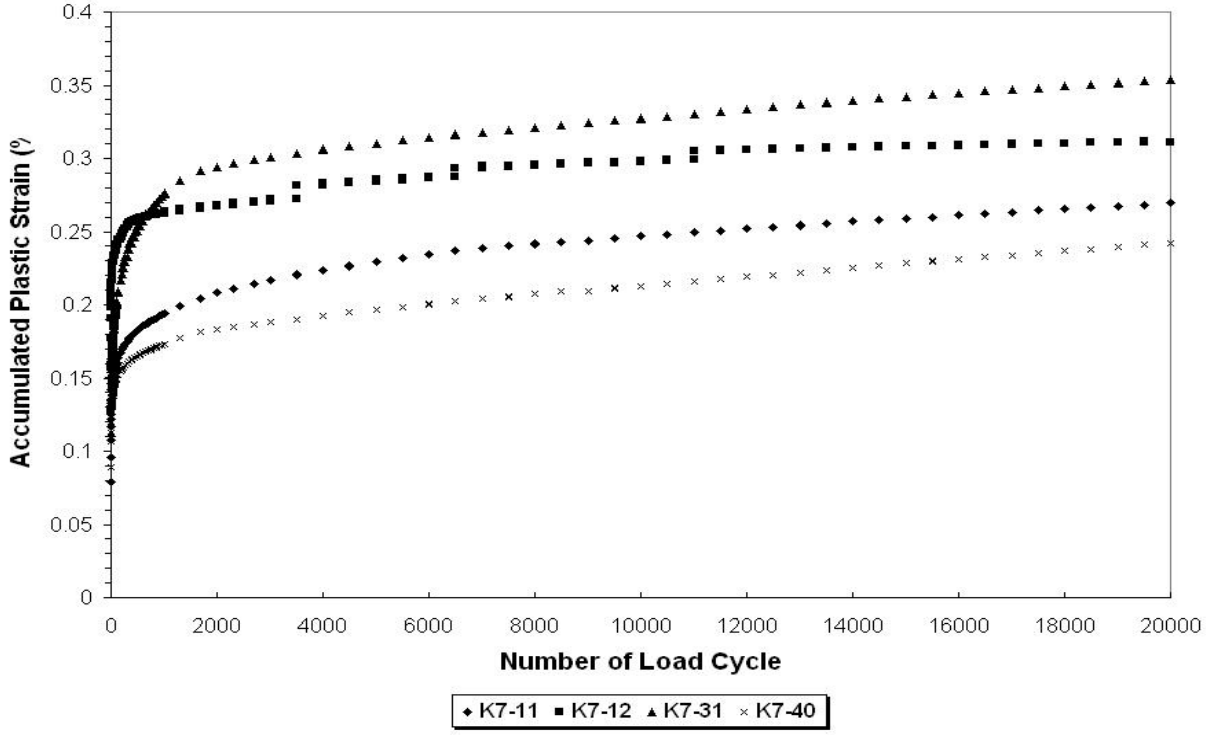

Figure 3.12. Plastic Strain versus Number of Load Cycles of K7 Intact Soils

As shown in the figures, the plastic strain develops rapidly during the initial stage but the rate of increase of plastic strain is diminished as the load cycles continue. The higher deviatoric stress generates the larger plastic strain. It implies that heavy traffic such as OTT can produce larger plastic strain within layers resulting in severe rut depth development. Flexible base and subgrade materials exhibit a relatively higher plastic strain than the other materials. Because the portion of two layers as are depicted in Figure 4.5 prevails in the tested pavement structure, it is expected that most of the rutting occurs within these two layers. In case of intact soils, the behavior of accumulated plastic strain under repeated load was different station by station. However the amount of accumulated plastic strain of the K6 soils is larger than that of the K7 soils. It could be associated with different damage potential between the two lanes since most of the OTT moves in the K6 lane.

Permanent deformation parameters were determined for the materials by fitting the repeated load triaxial test data with the VESYS model (Kenis 1978) and the Three Parameter model (Tseng and Lytton 1989). Three parameters were obtained using the SPSS statistical program (2001), which uses the least-squares method to estimate parameters in a nonlinear model. The model parameters are presented in Tables 3.10 and 3.11.

VESYS Model $$\varepsilon_P(N) = \mu N^{-\alpha} \tag{3.17}$$

Three-parameter Model $$\varepsilon_P(N) = \varepsilon_0 \exp -\left(\frac{\rho}{N}\right)^{\beta} \tag{3.18}$$

The parameters obtained are used as input in the finite element program developed in this study to predict performance. In the VESYS model, the smaller α value implies a larger rutting potential. The μ value indicates how fast rutting depth increase. The parameters obtained under

stress level 2 show a larger rut potential. In the Three-parameter model, the parameter, ρ, is the scale factor on accumulated permanent strain. A large number indicates a large number of load repetitions to reach a given level of permanent strain. The exponent, β, allows the curve to take on a variety of shapes. The most influential factor to rut depth in Three-parameter model is $\varepsilon_0/\varepsilon_r$. The higher value gives a larger rut depth. The three parameters under stress level 2 tend to exhibit larger rut depth than with the VESYS modle.

Table 3.10. Permanent Deformation Parameters for Stress Levels 1 and 2

Model Parameter	Flexible Base		Salvage Base		Lime Treated Subbase		Subgrade	
	Level 1	Level 2	Level 1	Level 2	Level 1	Level 2	Level 1	Level 2
μ	0.08	0.36	0.05	N/A	0.05	0.10	0.08	0.11
α	0.81	0.79	0.93	N/A	0.93	0.84	0.85	0.75
$\varepsilon_0/\varepsilon_r$	11.3	26.62	1.89	N/A	2.10	3.32	10.35	9.10
ρ	5143	269.34	1730	N/A	1800.21	85.27	7102	577.75
β	0.19	0.20	0.09	N/A	0.23	0.19	0.13	0.21

Table 3.11. Permanent Deformation Parameters for Intact Soils

	μ	α	$\varepsilon_0/\varepsilon_r$	ρ	β
K6-1	0.05	0.83	7.4	15	0.102
K6-23	0.06	0.88	181	184	0.128
K6-29	0.05	0.84	197	558	0.064
K6-45	0.07	0.86	56	1192	0.137
K6-53	0.05	0.93	121	478	0.074
K7-11	0.06	0.91	48.7	237	0.100
K7-12	0.04	0.95	73	1000	0.050
K7-31	0.06	0.89	70.6	689	0.102
K7-40	0.05	0.92	46.2	387	0.081

CHAPTER IV

COMPARISON AND VERIFICATION OF RESPONSE MODELS

4.1. FINITE ELEMENT MODEL

The finite element program NCPA (Nonlinear Cross-anisotropy Pavement Analysis) was developed to analyze flexible pavement more practically by modifying some drawbacks that previous programs contained. The finite element program used in this study is a modified version of the superheavy load analysis program (SLAP) developed by Jooste and Fernando (1995). The modification made in NCPA is summarized below.

NCPA uses an 8-node quadratic serendipity element and 9 Gauss points for calculations. This allows the user to obtain stress, strain and displacement values in more detail at different coordinates. For the boundary conditions, the sides of the finite element mesh were restrained in the horizontal direction, while the bottom of the mesh was restrained in both the vertical and horizontal directions to represent the fixed layer. In the finite element program, it is found that the accuracy of the analysis results is highly dependent on the mesh generation and element types. For this purpose, the ‘GRID’ program is used to generate a mesh automatically. The load is applied in an incremental fashion. For each load increment and each element, the stress dependent moduli and Poisson’s ratio, which are described in chapter III, are calculated iteratively until convergence is achieved. Convergence depends on the percentage difference between the new and previous values. In the program, a 15% difference in the calculated moduli from the current and previous iteration is accepted. In addition to this, the NCPA program can be analyzed under cross-anisotropic condition. Recent researches (Tutumluer, 1995; Adu-Osei, 2000) suggest that directional or anisotropic modeling can reduce and even reverse horizontal tensile stresses predicted in unbound granular layers with isotropic elastic properties. Since the

main objective of this study is to predict the pavement performance on SH4/48, the subroutine containing a procedure to evaluate pavement performance in terms of rut depth, fatigue cracking and service index was incorporated into the program.

4.1.1. FEM Formulation on Two-Dimensional Axisymmetric Solid

Virtual Work

The virtual work principle is defined (Weaver and Johnston, 1984):

"If a general structure in equilibrium is subjected to a system of small virtual displacements within a comparable state of deformation, the virtual work of external actions is equal to the virtual strain energy of internal stresses".

If a body is subjected to a set of body forces b then by the virtual work principle it can be written (Owen and Hinton, 1980):

$$\int_{\Omega}\left[\delta\varepsilon\right]^{T}\sigma d\Omega-\int_{\Omega}\left[\delta u\right]^{T}bd\Omega-\int_{\Gamma t}\left[\delta u\right]^{T}td\Gamma=0 \qquad (4.1)$$

where,

σ = the vector of stresses,

t = the vector of boundary tractions,

δu = the vector of virtual displacements,

$\delta\varepsilon$ = the vector of associated virtual strains,

Ω = the domain of interest, and

Γ_t = the part of boundary on which boundary tractions are prescribed.

Governing Equation

In a finite element representation, the displacements and strains and their virtual counterparts may be expressed by the relationships (Owen and Hinton, 1980)

$$u = \sum_{i=1}^{n} N_i d_i \qquad \delta u = \sum_{i=1}^{n} N_i \delta d_i \tag{4.2}$$

$$\varepsilon = \sum_{i=1}^{n} B_i d_i \qquad \delta \varepsilon = \sum_{i=1}^{n} B_i \delta d_i \tag{4.3}$$

where

d_i = the vector of nodal variables,

δd_i = the vector of virtual nodal variables,

N_i = the matrix of global shape functions, and

B_i = the global strain-displacement matrix.

Substituting Equation (4.2) and (4.3) into Equation (4.1) yields:

$$\sum_{i=1}^{n} [\delta d_i]^T \left\{ \int_\Omega [B_i]^T \sigma d\Omega - \int_\Omega [N_i]^T b d\Omega - \int_{\Gamma t} [N_i]^T t d\Gamma \right\} = 0 \tag{4.4}$$

since there exists an arbitrary set of virtual displacements, Equation (4.4) can be re-written as below:

$$\int_\Omega [B_i]^T \sigma d\Omega - \int_\Omega [N_i]^T b d\Omega - \int_{\Gamma t} [N_i]^T t d\Gamma = 0 \tag{4.5}$$

The stress-strain relationship at each element in finite element forms:

$$\sigma = D\varepsilon = D\left(\sum_{j=1}^{r} B_j d_j \right) \tag{4.6}$$

where D is the stress-strain matrix of elastic properties. The element stiffness matrix composed of the B and D matrix is given as

$$\sum_{j=1}^{n} K_{ij} d_j = \int_{\Omega} [B_i]^T D \left(\sum_{j=1}^{n} B_j d_j \right) d\Omega \tag{4.7}$$

Axisymmetric Solids

An axisymmetric solid is defined as a three-dimensional body that is developed by rotation of a planar section about an axis and which is subjected to loads and boundary conditions that are symmetrical about this axis, then the behavior is independent of the circumferential coordinate θ. The following components are used in the formulation of finite element model.

The displacements may be expressed as

$$u = \{u, v\} \tag{4.8}$$

where u and v are the displacements in the r and z directions respectively.

The nonzero strains are given as

$$\varepsilon = \{\varepsilon_r, \varepsilon_\theta, \varepsilon_z, \gamma_{rz}\} \tag{4.9}$$

where

ε_r = $\frac{\partial u}{\partial r}$; normal strain in the r direction,

ε_θ = $\frac{u}{r}$; normal strain in the θ direction,

ε_z = $\frac{\partial v}{\partial z}$; normal strain in the z direction, and

γ_{rz} = $\frac{\partial u}{\partial z} + \frac{\partial v}{\partial r}$; shear strain on the r-z plane.

For linear isotropic materials in an axisymmetric condition, the strain-displacement matrix is given as

$$B = \begin{bmatrix} \frac{\partial N_i}{\partial r} & 0 \\ \frac{N_i}{r} & 0 \\ 0 & \frac{\partial N_i}{\partial z} \\ \frac{\partial N_i}{\partial z} & \frac{\partial N_i}{\partial r} \end{bmatrix} \tag{4.10}$$

For linear isotropic materials in an axisymmetric condition, the stress-strain matrix is given as

$$D = \frac{E}{(1+\nu)(1-2\nu)} \begin{bmatrix} 1-\nu & \nu & 0 & 0 \\ \nu & 1-\nu & \nu & 0 \\ 0 & \nu & 1-\nu & 0 \\ 0 & 0 & 0 & \frac{1-2\nu}{2} \end{bmatrix} \tag{4.11}$$

An elemental volume is given by

$$d\Omega = 2\pi r dr dz \tag{4.12}$$

4.1.2. Cross-Anisotropy Under Axisymmetric Condition

While the isotropic model uses the same resilient properties in all directions, a cross-anisotropic material has different resilient material properties in the horizontal and vertical directions. Zienkiewicz and Taylor (1989) suggested the general axisymmetric elasticity strain-stress relations for an anisotropic stratified layered system in terms of the in plane and normal to the strata resilient moduli and Poisson's ratio. The constitutive axisymmetric anisotropic stress-strain relation matrix D takes the form:

$$D = \frac{M_R^V}{\alpha\beta} \begin{bmatrix} n(1-n\nu_{vh}^{\ 2}) & n(\nu_{hh}+n\nu_{vh}^{\ 2}) & n\nu_{vh}\alpha & 0 \\ n(\nu_{hh}+n\nu_{vh}^{\ 2}) & n(1-n\nu_{vh}^{\ 2}) & n\nu_{vh}\alpha & 0 \\ n\nu_{vh}\alpha & n\nu_{vh}\alpha & (1-\nu_{hh}^{\ 2}) & 0 \\ 0 & 0 & 0 & m\alpha\beta \end{bmatrix} \tag{4.13}$$

where

α = $(1+\nu_{hh})$

β = $(1-\nu_{hh}-2n\nu_{vh}^2)$

n = M_R^H / M_R^V

m = G_{HV} / M_R^V

The stress-strain matrix was incorporated into the developed program NCPA. The n and m values are used as input and the ratio of Poisson's ratio are considered by the input, p. Since the Poisson's ratio for horizontal strain due to vertical strain, ν_{VH}, is input initially, the Poisson's ratio for horizontal strain due to horizontal strain, ν_{HH}, is automatically calculated by the p value at every step. This procedure is accompanied with the calculation of stress dependent modulus and Poisson's ratio when the analysis is performed under the nonlinear cross-anisotropy (NA) model.

4.2. VERIFICATION OF CROSS-ANISOTROPY MODEL

In this section, the verification of the cross-anisotropy model was conducted by comparing its calculated results with a theoretical solution and commercial program (CIRCLY, 1999). As aforementioned, it was shown that the method to analyze the unbound granular base material as a nonlinear anisotropic method was the most effective in the reduction of tensile horizontal stress. Therefore it is important to check how the developed NCPA program works adequately in terms of the NA model for the following analysis. The comparison was performed by calculating vertical stress and horizontal stress.

Gazetas (1982) studied the effect of soil cross-anisotropy on surface displacements and stress distributions in a homogeneous thick soil deposits (halfspace) subjected to axisymmetric

parabolic vertical surface loading. The five independent material constants, E_H, E_V, ν_{VH}, ν_{HH} and G_{VH} cannot have entirely arbitrary values; they are restricted by strain energy considerations (Lekhnitskii, 1963):

$$E_{V,}E_{H,}G_{VH} \geq 0, \quad -1 \leq \nu_{HH} \leq 1-2n\nu_{VH}^2 \tag{4.14}$$

The derived expression for vertical stress and radial stress with depth under the center of loading is given by (Gazetas, 1982):

$$\sigma_z = \frac{p_0}{s_1 - s_2}\left[\frac{s_1}{(\lambda_1 + \sqrt{1+\lambda_1^2}\,)^2} - \frac{s_2}{(\lambda_2 + \sqrt{1+\lambda_2^2}\,)^2}\right] \tag{4.15}$$

$$\sigma_r = \frac{p_0}{(s_1 - s_2)\sqrt{g}}\left\{\frac{s_1\left[1-(1-\nu_{hh})\frac{q_2}{2}\right]}{\left(\lambda_1 + \sqrt{1+\lambda_1^2}\right)^2} - \frac{s_2\left[1-(1-\nu_{hh})\frac{q_1}{2}\right]}{\left(\lambda_2 + \sqrt{1+\lambda_2^2}\right)^2}\right\} \tag{4.16}$$

where

$$s_1, s_2 = \left\{\frac{a+c \pm \left[(a+c)^2 - 4g\right]^{1/2}}{2g}\right\}^{\frac{1}{2}},$$

$$c = a - \frac{1}{m\left(n\nu_{vh}^2 - 1\right)},$$

$$a = \frac{\nu_{vh}\left(1+\nu_{hh}\right)}{n\nu_{vh}^2 - 1},$$

$$g = \frac{1-\nu_{hh}^2}{n\left(1-n\nu_{vh}^2\right)}, \text{ and}$$

$$\lambda = \frac{z}{R}; \quad \lambda_i = \lambda s_i; \quad q_i = 1 - a s_i^2; \quad i = 1,2\,.$$

Since there is a difficulty in considering a two-layer structure composed of asphalt concrete and base material in a theoretical solution, the analyzed section was set to one layer composed of granular material with a thickness 508 mm. The calculation of stress dependent modulus and

Poisson's ratio could not be used in a theoretical solution due to its complexity thus the linear anisotropy model (LA) was used in the NCPA analysis. Vertical and horizontal stress was calculated by using a spreadsheet. Table 4.1 shows the input data used in this analysis.

Table 4.1. Input Used in Theoretical Solution

Input Parameter	Value
ν_{vh}	0.2
ν_{hh}	0.3
n	0.5
m	0.3
P_0	607 kPa

The distribution of vertical stress through granular materials obtained from the two solutions matched well even if there is an acceptable error as shown in Figure 4.1. The theoretical solutions showed slightly lower vertical stress up to 200 mm. It is more interesting to investigate the variation of radial stress within granular material. Both solutions showed a comparable trend as depicted in Figure 4.2. The cross-anisotropy model reduced tensile radial stress usually predicted by the linear isotropic approach even if the tensile stress was generated below 200 mm in the theoretical solution and near the bottom of the layer in the NCPA analysis. It remains a possibility to improve accuracy in the estimation of the radial stress when the stress dependent resilient property is applied. The reason why the theoretical solution gives more tensile radial stress can be explained by the characteristic of the formulated equations. For example, s_1 and s_2 are supposed to be satisfied under the condition that $(a+c)^2$ should be larger than 4g. This condition was very sensitive to the variation in both n and m. Therefore it is

considered that the boundary condition should be suggested in order to apply this equation to field conditions effectively.

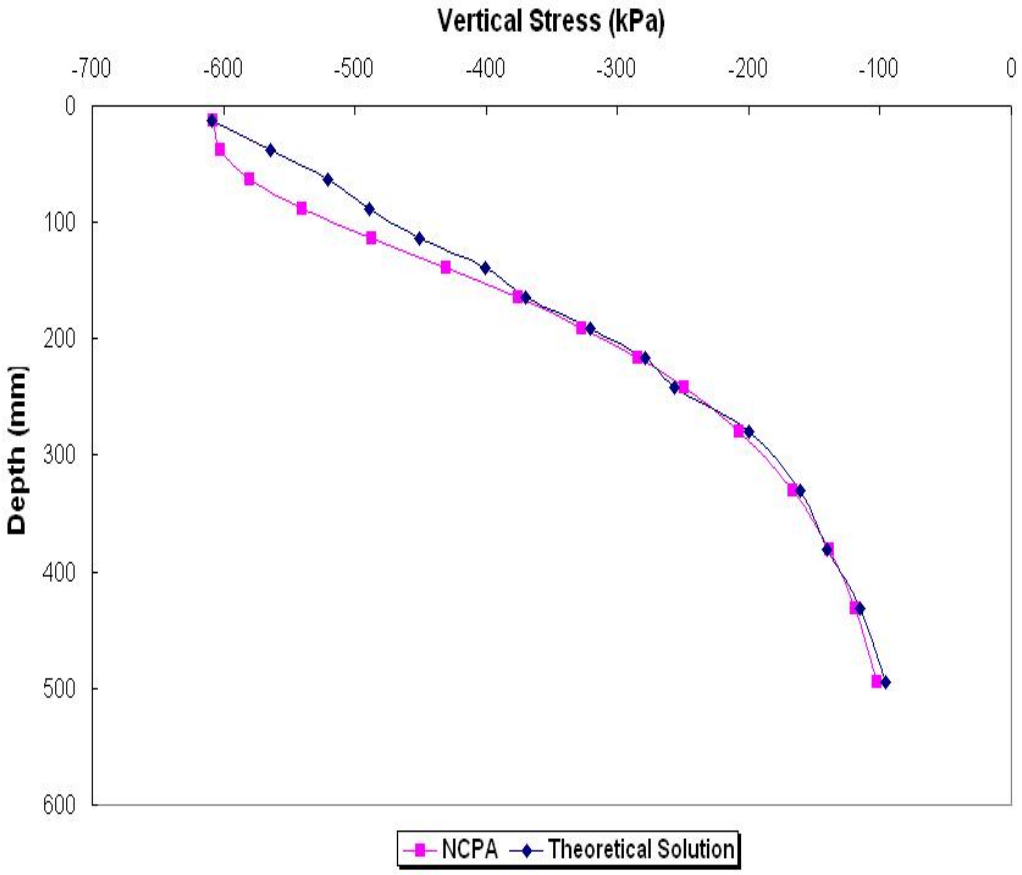

Figure 4.1. Comparison of Vertical Stress Computed by the Theoretical Solution and NCPA

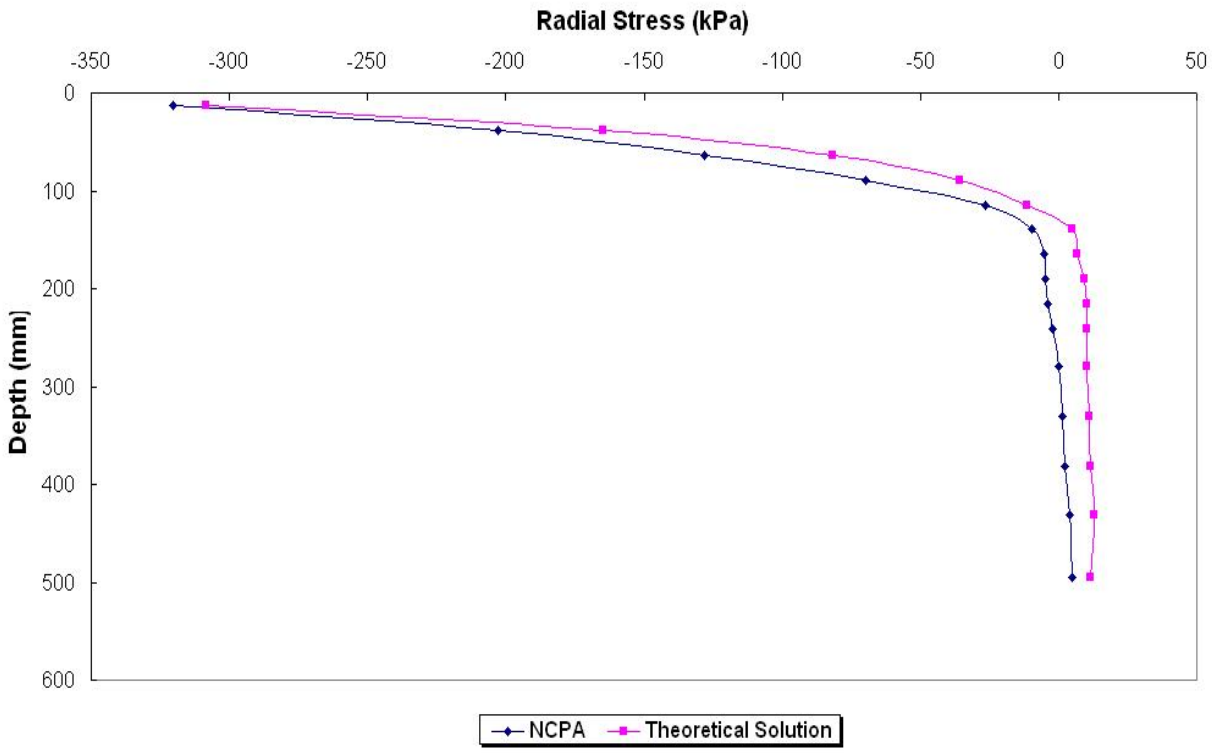

Figure 4.2. Comparison of Radial Stress Computed by the Theoretical Solution and NCPA

Porter et al. (1999) characterized granular layers as cross-anisotropic in the CIRCLY computer program. CIRCLY is an integral part of the Austroads Pavement Design Guide (Austroads, 1992) that uses the following simplifications to model the subgrade and unbound materials:

- n =0.5
- vertical and horizontal Poisson's ratio are the same
- $G_{VH} = \frac{M_R^V}{1+\nu}$

For the comparison of CIRCLY and NCPA, a two-layer structure composed of a 127 mm layer of asphalt concrete material and a 406.4 mm layer of granular base material was used. Since CIRCLY cannot evaluate the stress dependent resilient moduli, the LA model was adopted in both programs. According to the simplification described in the above, the asphalt concrete layer

was modeled by the linear isotropy and linear anisotropy model was used to characterize base material with a value of n equal to 0.5 and 1 of p because the same vertical and horizontal Poisson's ratio was assumed. As shown in Figure 4.3 and 4.4, the variation of vertical and radial stresses through the AC and base layers as calculated by two programs matched well. Gravity stresses due to overburden load and residual compaction stresses were not included in the finite element analysis because more emphasis was placed on the constitutive model. Most of the radial stresses in the granular materials fall within the compressive zone due to the cross anisotropy application. It is worth mentioning that this finding not only agrees with previous research observations (Tutumluer, 1995; Adu-Osei, 2000) but also confirms the capability of the program developed to use in this study.

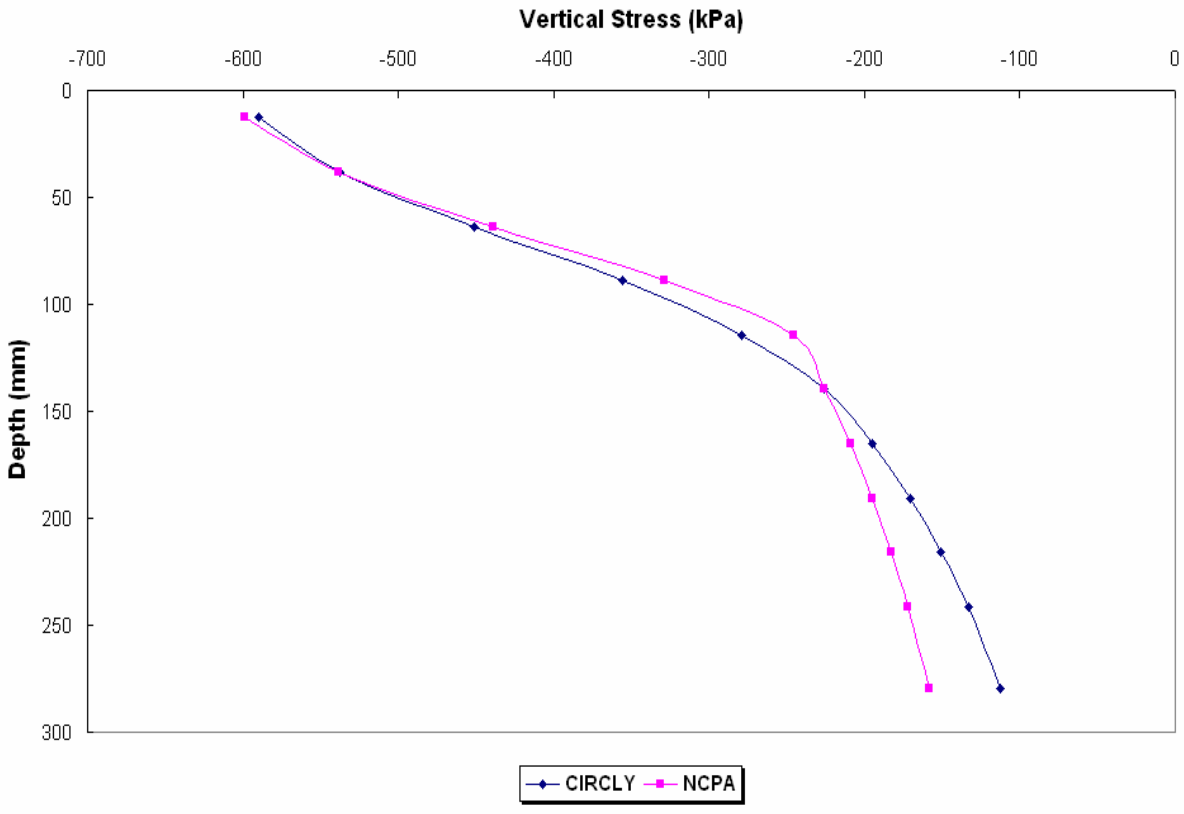

Figure 4.3. Comparison of Vertical Stress by CIRCLY and NCPA

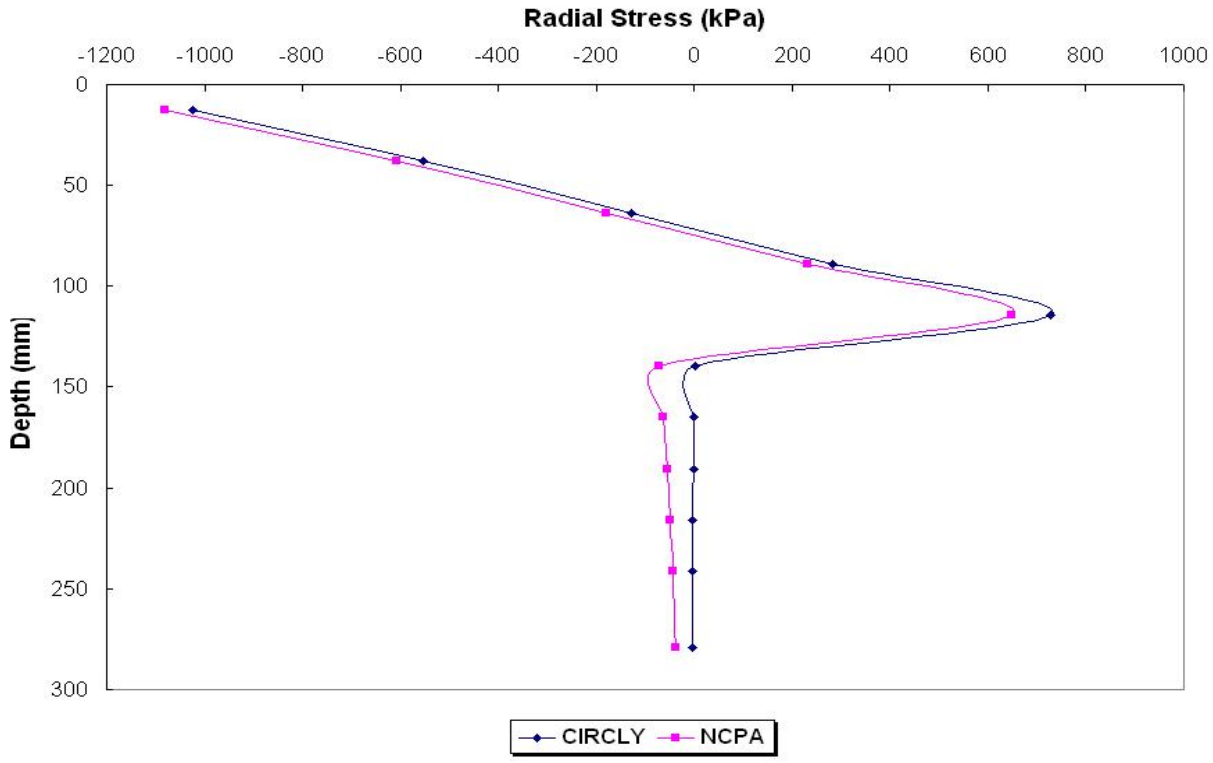

Figure 4.4. Comparison of Radial Stress by CIRCLY and NCPA

4.3. MODEL COMPARISON WITH FIELD MEASUREMENT

Along the SH 4/48 test section, the FWD test was performed to obtain the backcalculated layer moduli. For flexible pavements, the FWD measurements that are taken at load levels comparable with the wheel loads expected to account for nonlinear load response are analyzed using backcalcuation of pavement properties (Lytton, 1989). The backcalculation procedure was performed running the MODULUS program.

The MDD was installed at two locations that were closest to the WIM station as shown in Figure 4.5. The MDD is an assembly of linear variable differential transducers (LVDTs) installed inside a cylindrical vertical cavity within the pavement to measure vertical displacements at selected depths under moving wheel loads. Both recoverable and permanent displacement can be measured with the MDD (Jooste and Fernando, 1994). The salvage base

material layer was around 127 mm thick between the flexible base and lime treated subbase layer. However, the salvage base layer was not considered separately in the analysis because it is impossible to backcalculate the modulus for five layers in the MODULUS program. Perhaps similarity in material characteristic with flexible base explains why the flexible base layer contains the salvage base material in the analysis. The three layer system which is composed of the AC, a base layer which includes the flexible base, salvage base, and lime treated material, and the subgrade layer showed the least error in estimation of backcalculated modulus as reported (Ramos et al., 2003). Despite this, the LVDTs were placed in between four different layers that have a unlike material characteristic among them. The four layers in the structure were composed of asphalt concrete, flexible base including salvage base, lime stabilized base and subgrade was used in this analysis. After installing the MDD, grid lines were drawn around the cap of the MDD to check the distance from a passing truck tire relative to the sensor. All traffic which passed over the MDD was recorded using a VCR so as to investigate the damage effect due to overweight truck loading. The permitted overweight trucks were labeled with numbers issued by researchers to determine more accurate truck information. Table 4.2 shows the backcalculated moduli based on FWD tests and a number of permitted trucks monitored with the MDD test. Because the layer backcalculated moduli of the K7 lane are higher than those of K6, it could be concluded that the extent of damage in the K6 lane is more significant than K7 lane. Although more trucks were monitored during the test, information on several trucks such as axle weight or MDD measurement was missing, and these are omitted for this analysis.

In verifying the pavement analysis, four constitutive models were considered: Linear isotropic (LI), nonlinear isotropic (NI), linear cross-anisotropic (LA), and nonlinear cross-anisotropic (NA). For the linear analysis, K_2 and K_3 are set to zero. The isotropic materials are

characterized by n and p equal to 1. A value of 1/m is equal to 2(1+ν). In the nonlinear analysis, K_2 and K_3 values obtained from laboratory tests were used and the K_1 value was backcalculated using equation (3.3) and known backcalculated resilient modulus. Model verification was conducted by comparing the MDD measurements with predicted displacements using the four different constitutive models. The principal reason for using the MDD measurements was to establish a model for predicting pavement response. By comparing the measured displacements with the predicted displacements from theory, a verification of the pavement model could be made before an evaluation of stresses and strains for damage assessment was undertaken (Jooste and Fernando, 1994). First the displacement measured by the MDD due to FWD loading was compared with the predicted displacements. The weight is dropped onto a 300 mm (11.8 in.) diameter loading plate resting on a 5.6 mm (0.22 in.) thick rubber buffer. The offset distance between the center of the load plate and the MDD sensor was recorded to improve the accuracy of modeling.

Table 4.2. Backcalculated Modulus and Monitored Number of Traffic.

Date	K6 lane					K7 lane				
	E_{AC} (MPa)	E_{flex} (MPa)	E_{lime} (MPa)	E_{sub} (MPa)	No. of Truck	E_{AC} (MPa)	E_{flex} (MPa)	E_{lime} (MPa)	E_{sub} (MPa)	No. of Truck
08/02	2634	331	131	97	69	2795	1331	325	176	56
10/02	3661	234	131	97	51	4326	1996	458	125	21
12/02	4295	290	214	165	40	5550	1032	499	103	17
02/03	3282	221	138	76	19	4440	2068	469	152	40

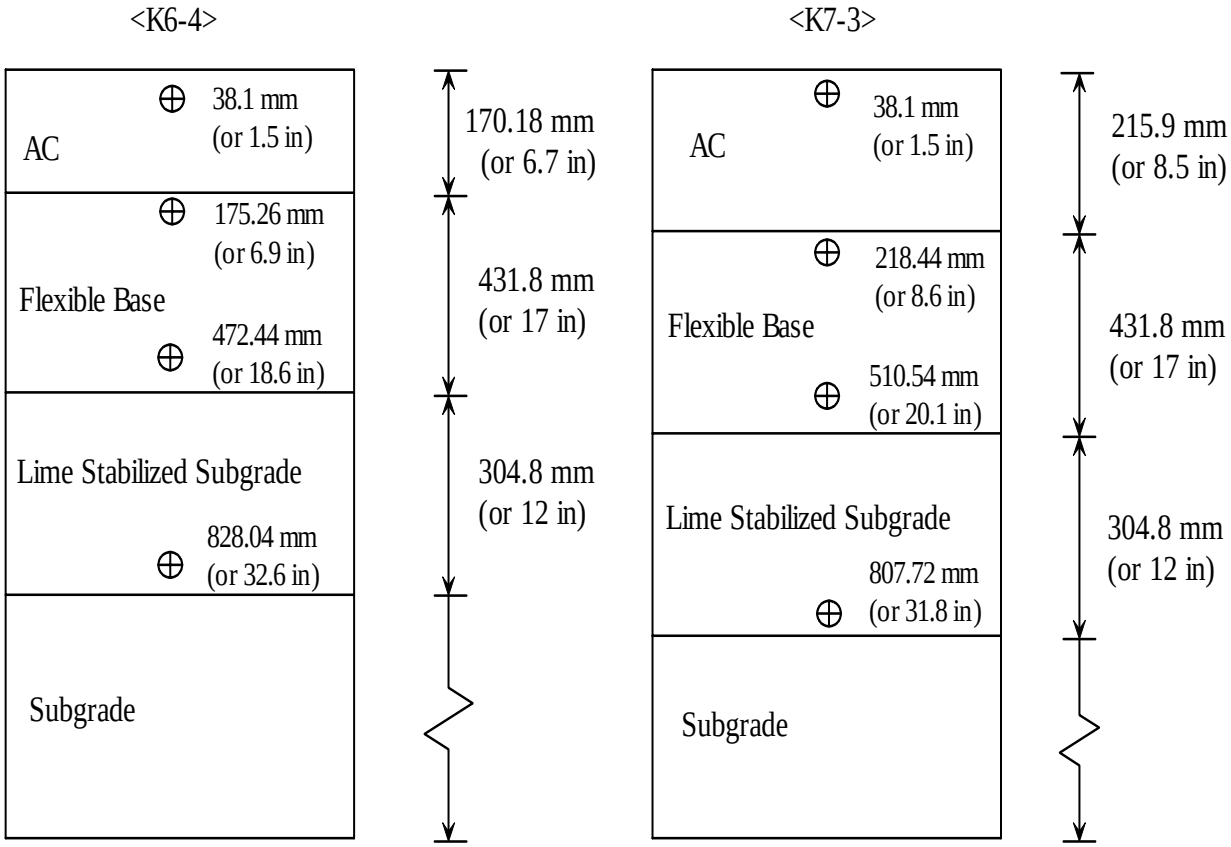

Figure 4.5. Layout of MDD Installation

In the second stage of the analysis, MDD displacement due to permitted OTT monitored during test period was compared with prediction. Firstly, two trucks per month from each of the two lanes were selected making a total of 8 trucks were chosen. Secondly, to confirm the model verification, forty trucks in the K6 lane were selected from August and December of 2002. Because two months cover a typically high and low temperature, the verification is more general. The selected truck data includes a test temperature, traffic time, axle weight, and offset distance. An example of the MDD measurements of selected trucks is shown in Figure 4.6a and 4.6b. From the view of the MDD response, peak displacements are generally indicated under the passing trailer axle. It should be noted that larger displacements are generated during August due to the effect of temperature on layer material properties. The unbound aggregate base layers

composed of two different material types and subgrade were treated by four constitutive models, while the AC layer was modeled as a linear isotropic material. The stress dependent and cross anisotropy parameters used in this analysis are tabulated in Table 4.3 and are based on laboratory test results.

Table 4.3. Stress Dependent and Cross-Anisotropy Parameters

	August / 02				December / 02			
	AC	Flexible Base	Stab.Lime Subgrade	Subgrade	AC	Flexible Base	Stab.Lime Subgrade	Subgrade
K_1	24120	2836	1347	830	39290	2617	2164	1386
K_2	0.1	0.7	0.6	0.2	0.1	0.7	0.6	0.2
K_3	0.0	-0.1	-0.1	-0.4	0.0	-0.1	-0.1	-0.4
n	1.0	0.38	0.67	0.90	1.0	0.38	0.67	0.90
m	0.38	0.18	0.34	0.59	0.38	0.18	0.34	0.59
p	1.0	1.7	1.9	2.0	1.0	1.7	1.9	2.0

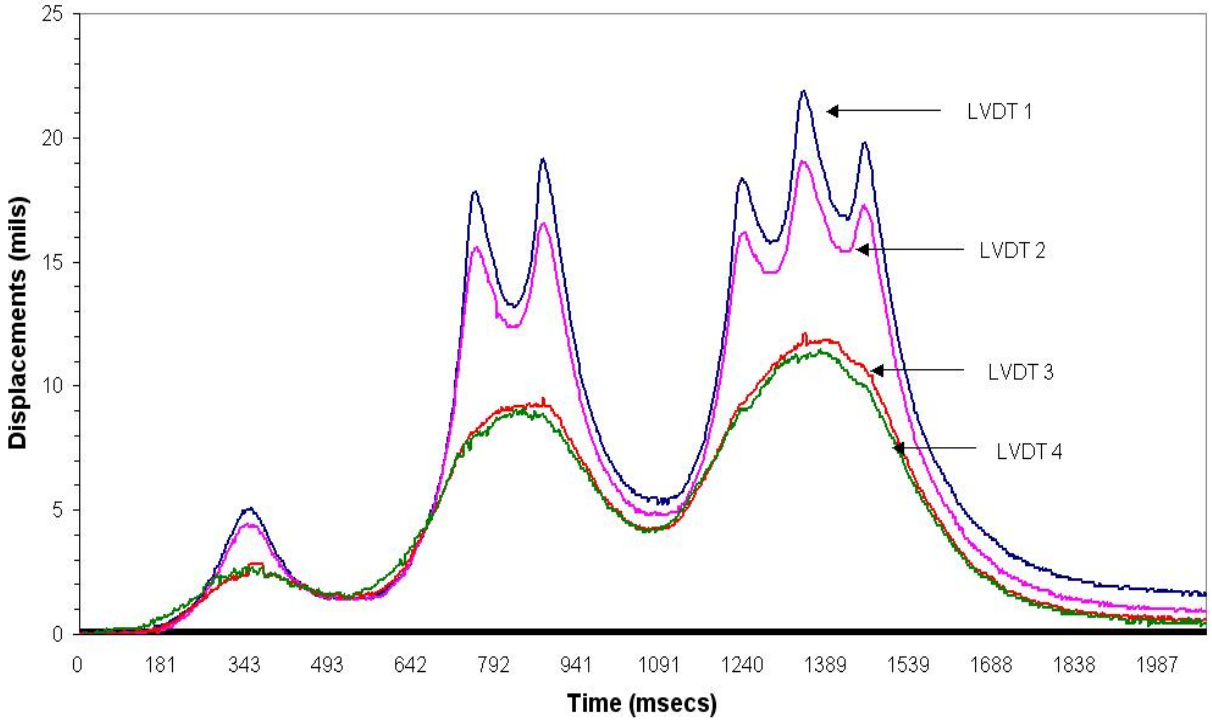

Figure 4.6a. MDD Response of OTT in August

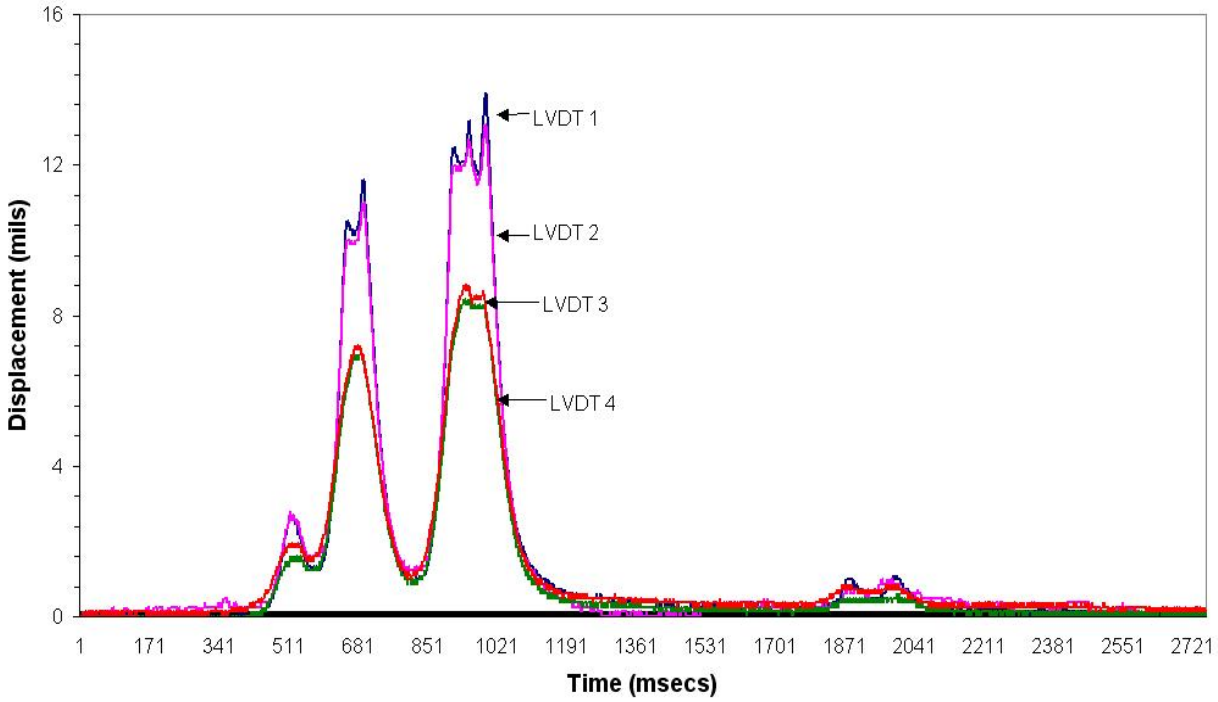

Figure 4.6b. MDD Response of OTT in December

Figure 4.7 shows the absolute difference between the measured displacement and the predicted displacement due to FWD loading. The difference between the measured displacement and the predicted displacement due to selected 8 OTTs is illustrated from Figures 4.8 to 4.15. The difference between measured and predicted value is expressed as a percent of the predicted displacement as given in equation 4.17.

$$Abs.Difference\% = \frac{\left|\delta_{measured} - \delta_{predicted}\right|}{\delta_{predicted}} \times 100 \tag{4.17}$$

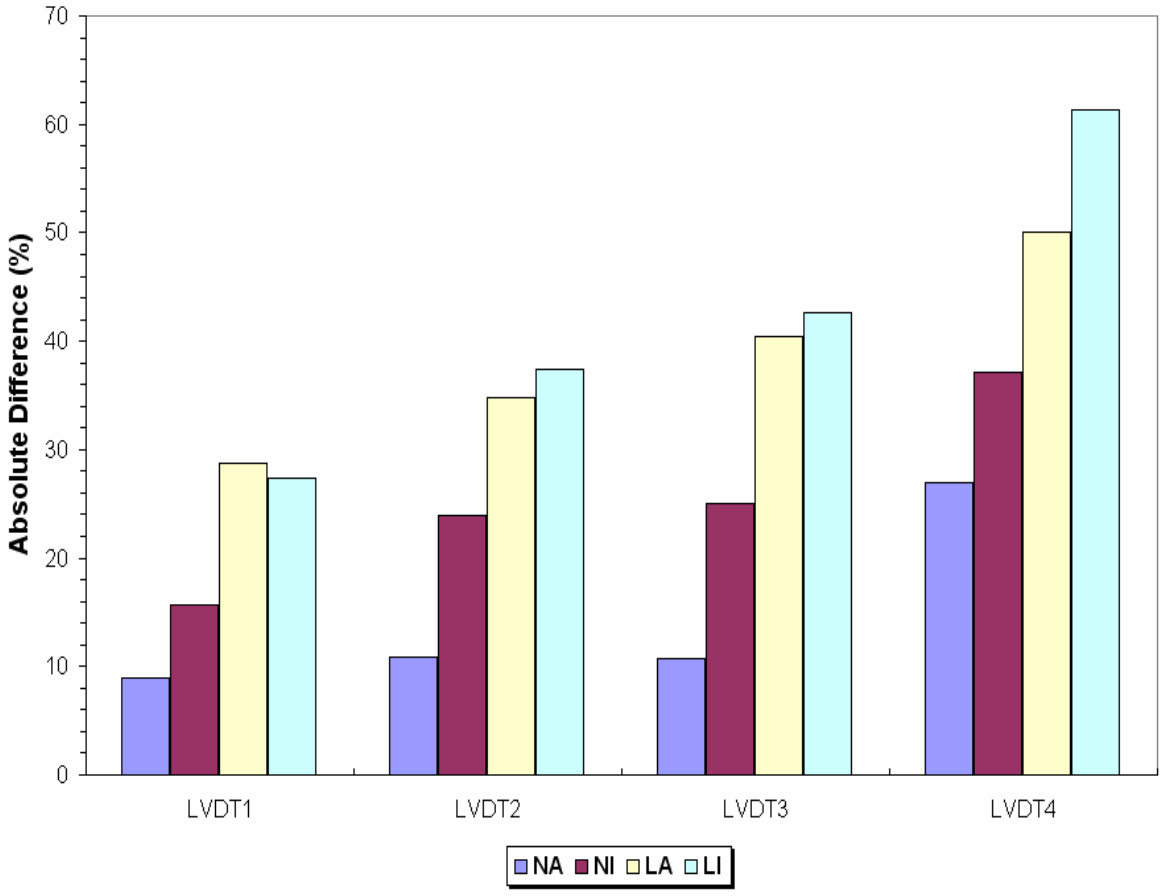

Figure 4.7. Comparison of Displacements due to FWD Loading

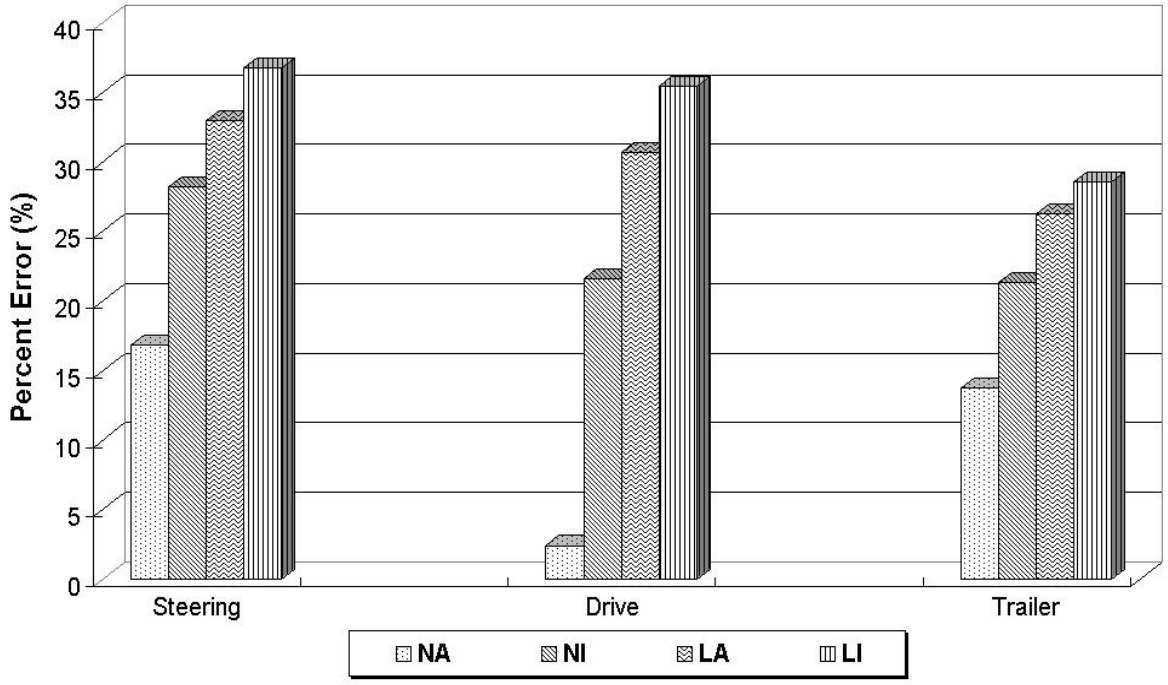

Figure 4.8. Comparison of Displacements due to No. 215 OTT (K7 Lane, August 2002)

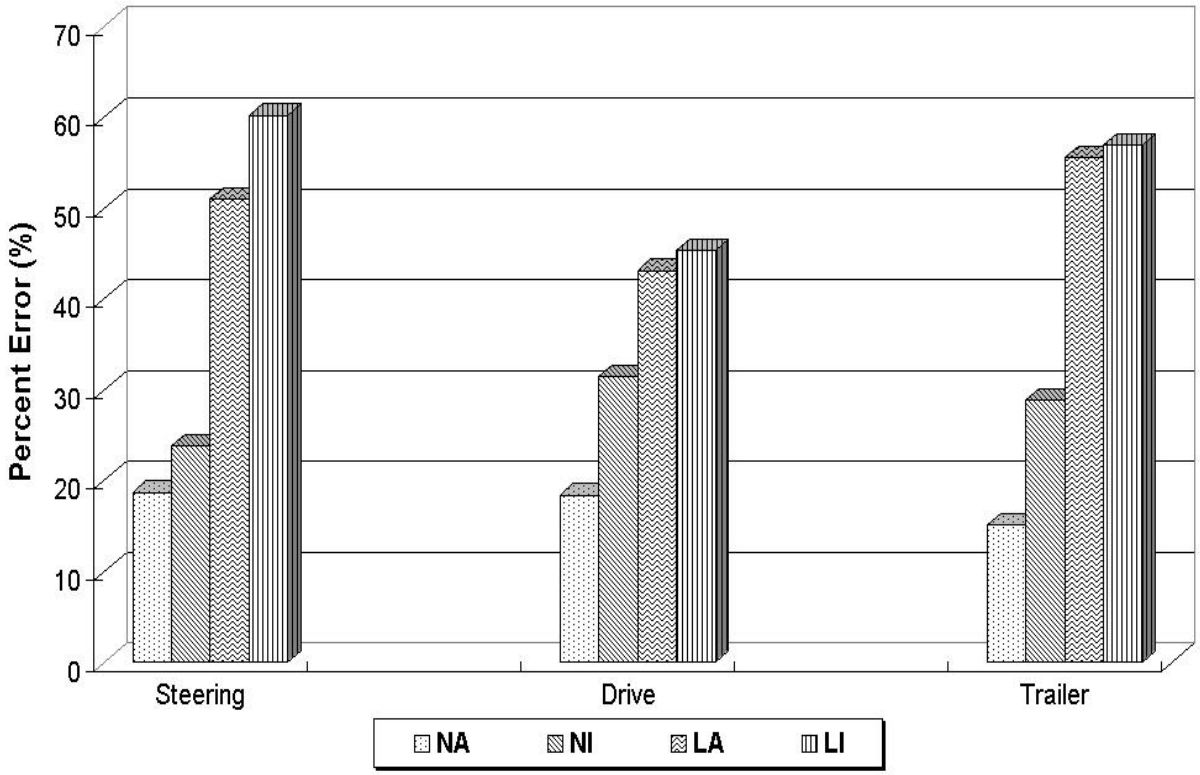

Figure 4.9. Comparison of Displacements due to No. 342 OTT (K6 Lane, August 2002)

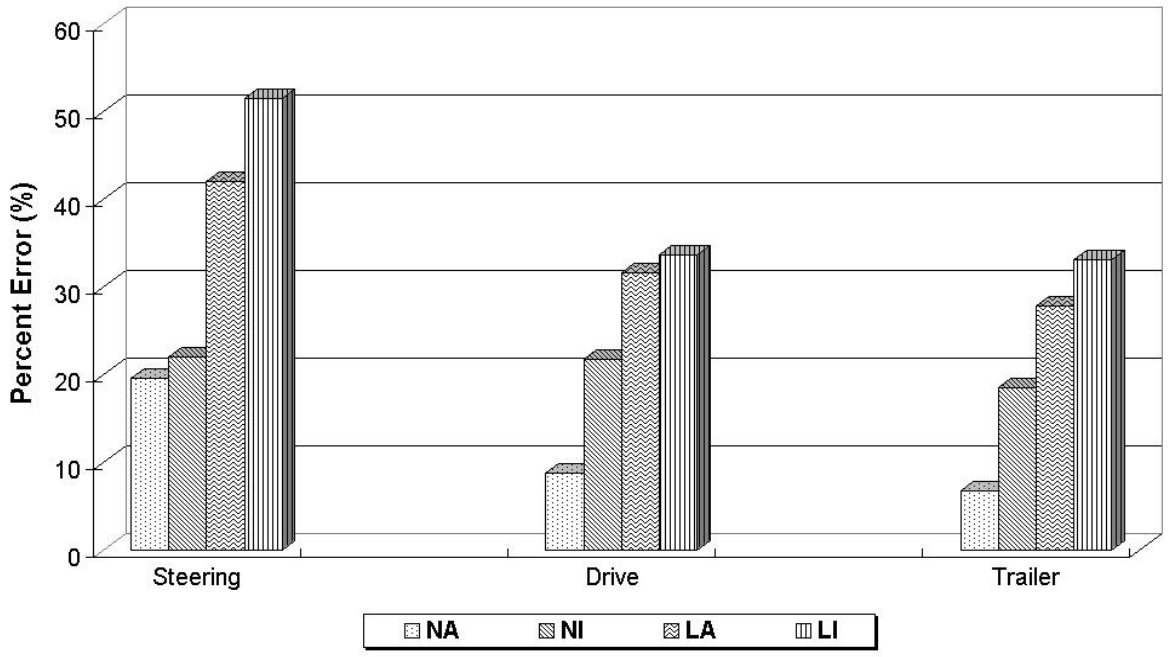

Figure 4.10. Comparison of Displacements due to No. 403 OTT (K7 Lane, October 2002)

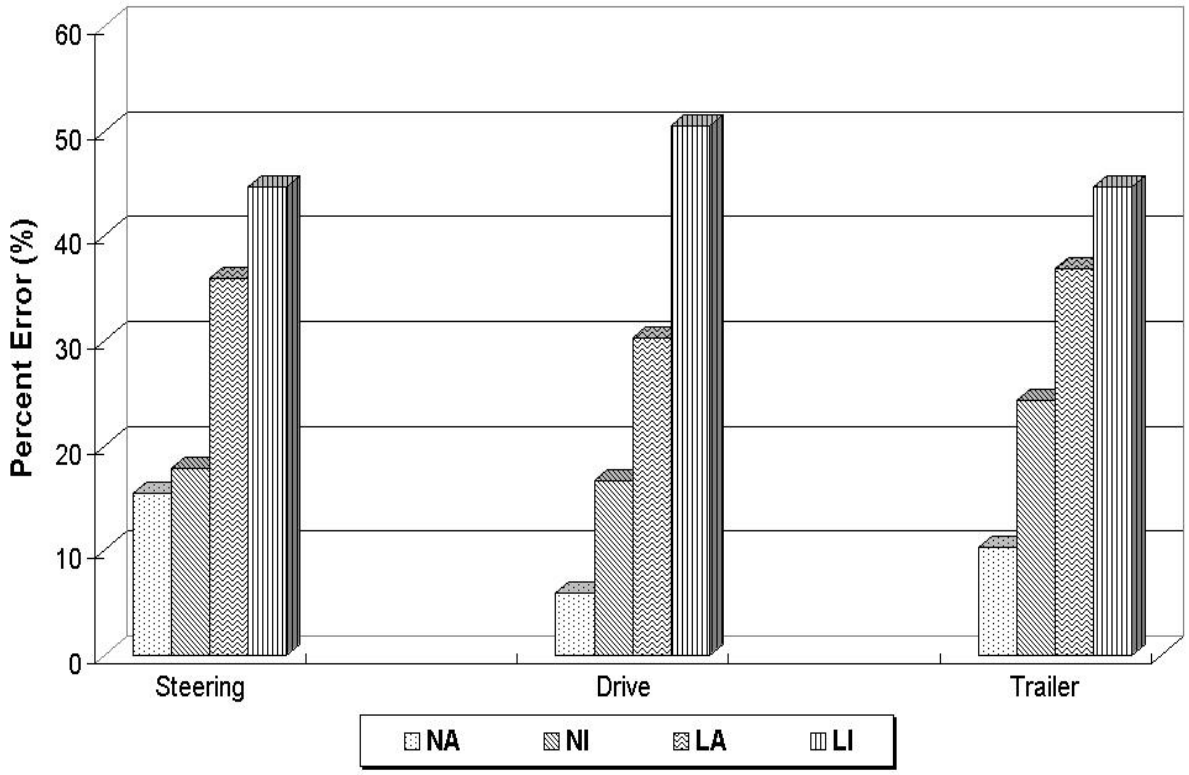

Figure 4.11. Comparison of Displacements due to No. 418 OTT (K6 Lane, October 2002)

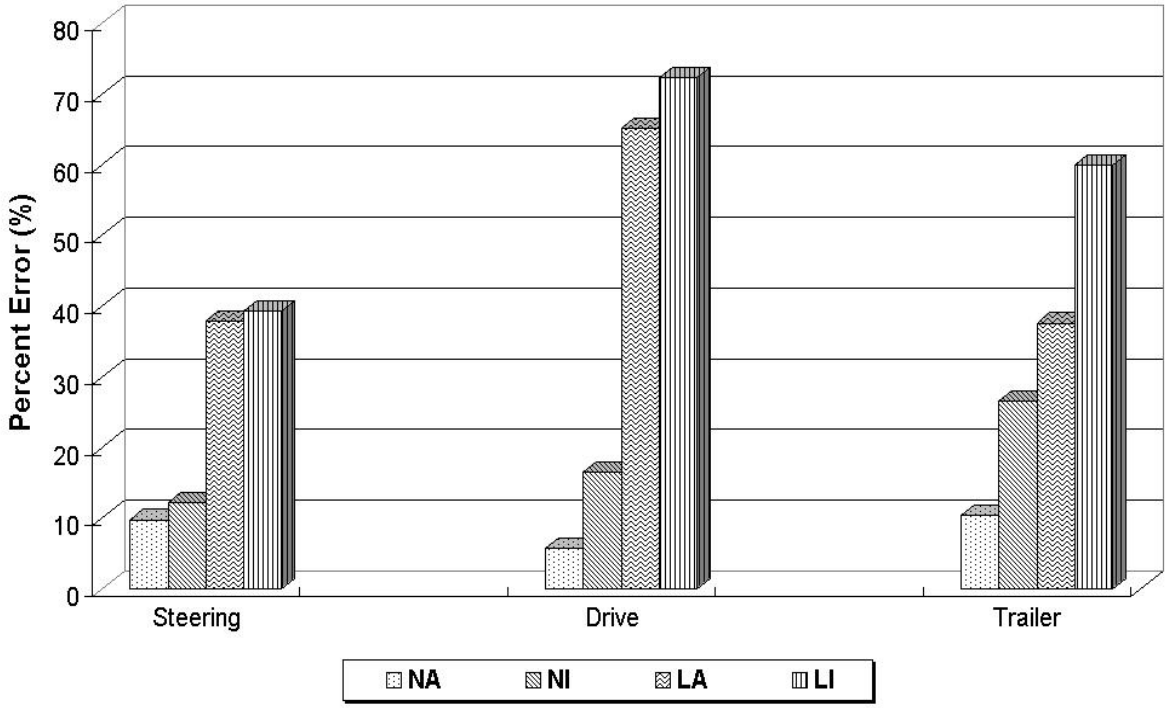

Figure 4.12. Comparison of Displacements due to No. 486 OTT (K7 Lane, December 2002)

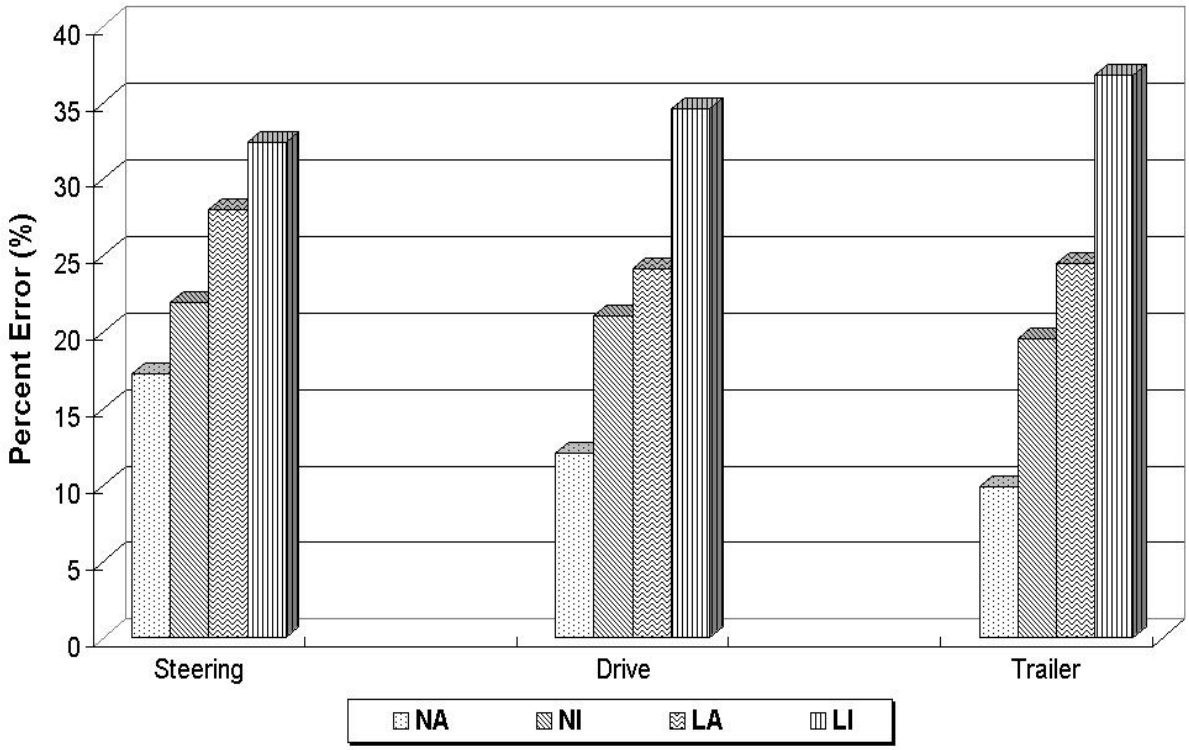

Figure 4.13. Comparison of Displacements due to No. 553 OTT (K6 Lane, December 2002)

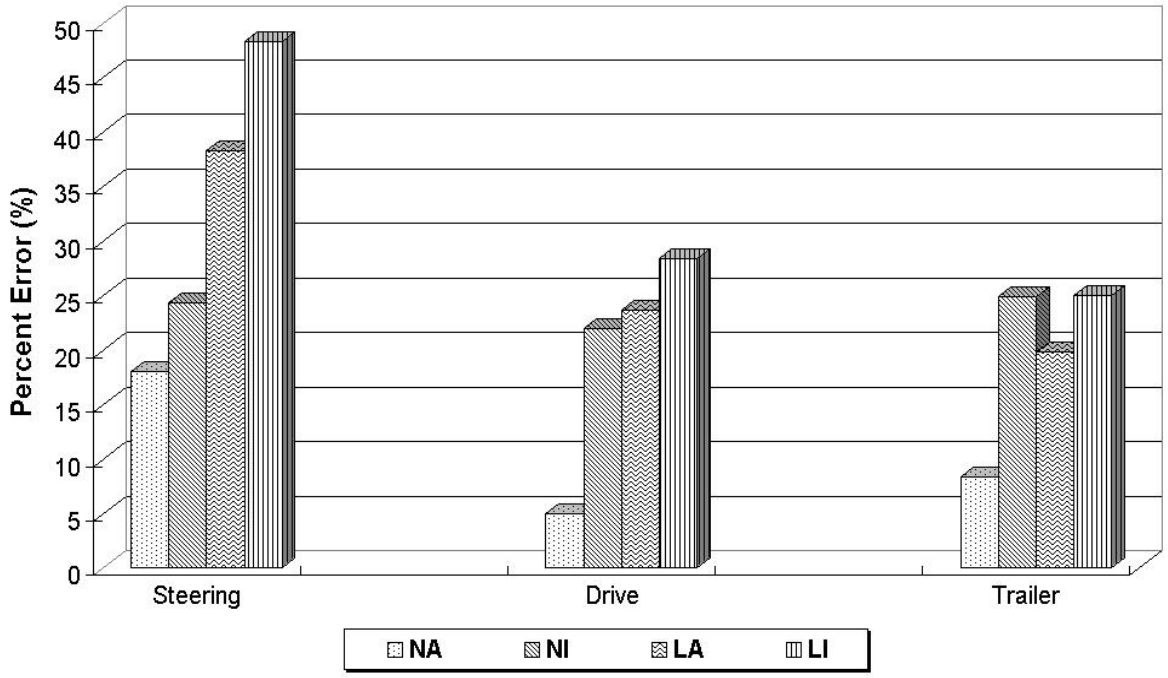

Figure 4.14. Comparison of Displacements due to No. 609 OTT (K7 Lane, February 2003)

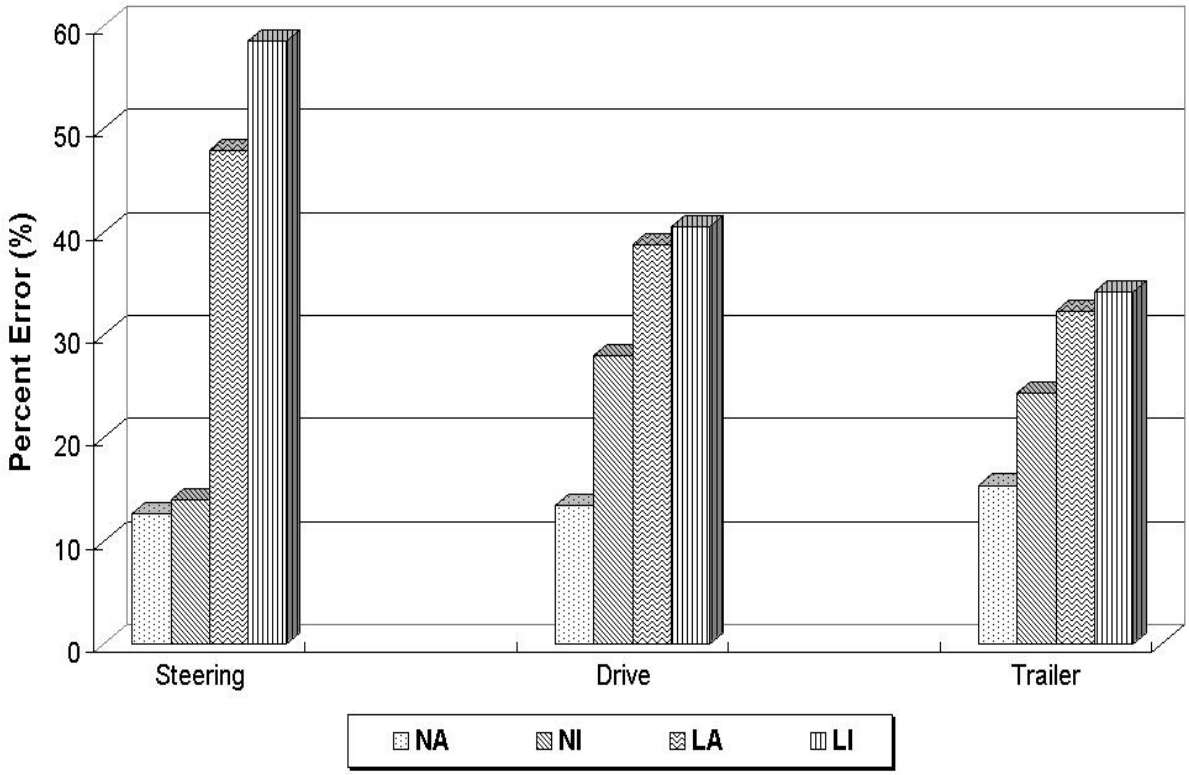

Figure 4.15. Comparison of Displacements due to No. 638 OTT (K6 Lane, February 2003)

Overall, the predicted displacement using the NA model showed the least absolute difference range thus it implies that the NA model models pavement response in the most appropriate manner. The tested model is ranked based on above analysis; (1)NA, (2)NI, (3)LA, and (4) LI. In Figure 4.7, a relatively high error range was detected in the comparison of the last sensor (LVDT4) This discrepancy may be caused due to water intrusion into the sensor resulting from a shallow water table or a poor electronic wire connection. The NI model can be selected as a model to simulate pavement response when there is no available data with respect to cross anisotropy because it reduces error significantly from that obtained from LA and LI prediction.

To confirm the above analysis, more trucks were selected and analyzed. In this task, model accuracy was indicated by taking the average difference given in equation (4.18) that gives information on data bias. Since the peak displacement usually occurs under the passing trailer axle, the focus was placed on the peak displacement for selected 40 trucks. From this indicator, it is also feasible to investigate whether the calculated displacement is overestimated or vice versa.

$$Ave.Difference\,(\%) = \sum_{i=1}^{4}\left(\frac{\delta_{FEMi} - \delta_{MDDi}}{\delta_{MDDi}}\right)\times 100 \tag{4.18}$$

It was shown that the NA model gives the least bias among the four models shown in Figures 4.16a and 4.17b. The closer the average difference is to zero, the lesser is the bias in the calculated displacements relative to the measured one. A negative average difference indicates that the NCPA tends to underestimate the measured displacements. The results in this section confirm that the NA model can predict the pavement response under OTT loads effectively and the LI and LA models are not appropriate for modeling the behavior of unbound granular materials.

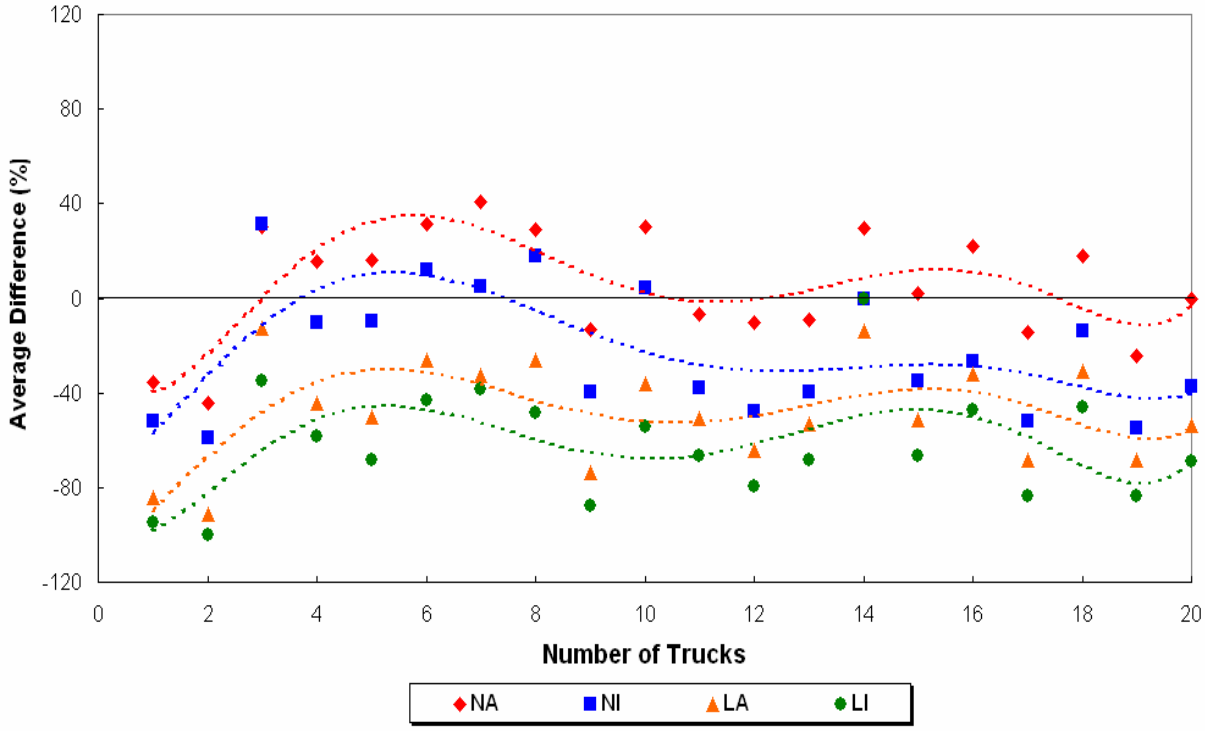

Figure 4.16a. Model Verification Using OTT Collected in August 2002.

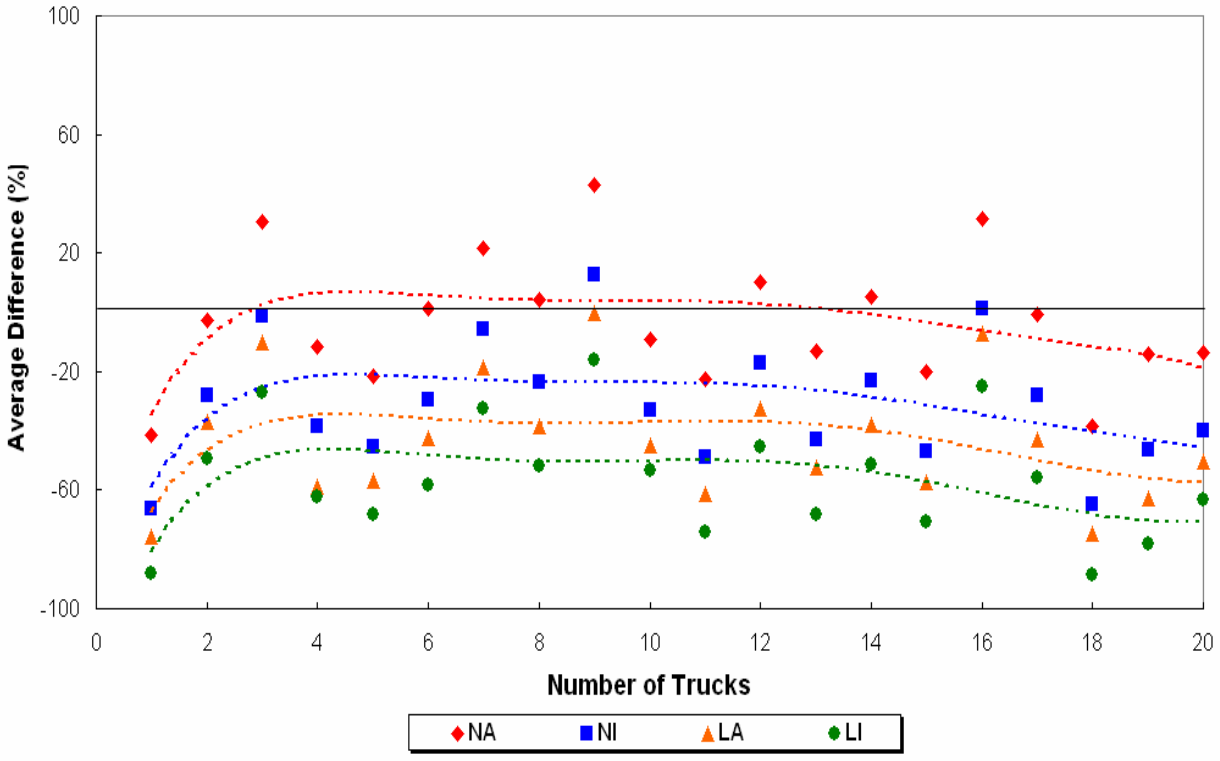

Figure 4.16 (b). Model Verification Using OTT Collected in December 2002.

4.4. SENSITIVITY ANALYSIS

The pavement response model based on the nonlinear-cross anisotropy model has estimated displacements close to the field measurement using the MDD. Although the model itself is complex, the combination of stress dependence and cross-anisotropy model can simulate the behavior of granular base and subgrade material with a high accuracy, which has a dilation and compaction effect due to the moving traffic load. In this section, a sensitivity analysis is presented which investigates the factors that have a significant influence in the MDD displacement and the development of permanent deformation and fatigue cracking. For this purpose, the K6-4 station section as shown in Figure 4.17 was analyzed with the four layers that have standard material properties. A 38.5 KN single wheel load with a radius of 127 mm. was used in the finite element analysis to model the pavement response. Figure 4.18 shows the MDD sensor location and three positions to calculate strains with respect to the performance prediction. The extent of the sensitivity was identified by reducing the parameters by 30% for each layer. For example, the sensitivity of the K_1 variation in the flexible base layer to the displacement was obtained by reducing K_1 by 30 % in the flexible base while keeping all other parameters unchanged.

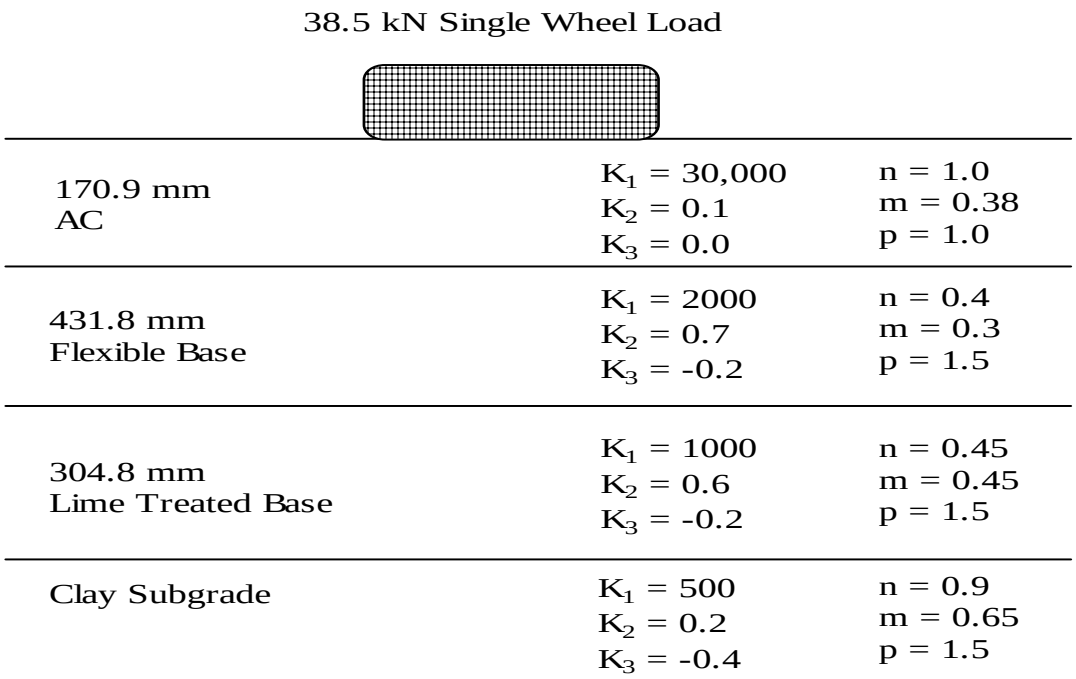

Figure 4.17. Pavement Structure with Standard Material Property

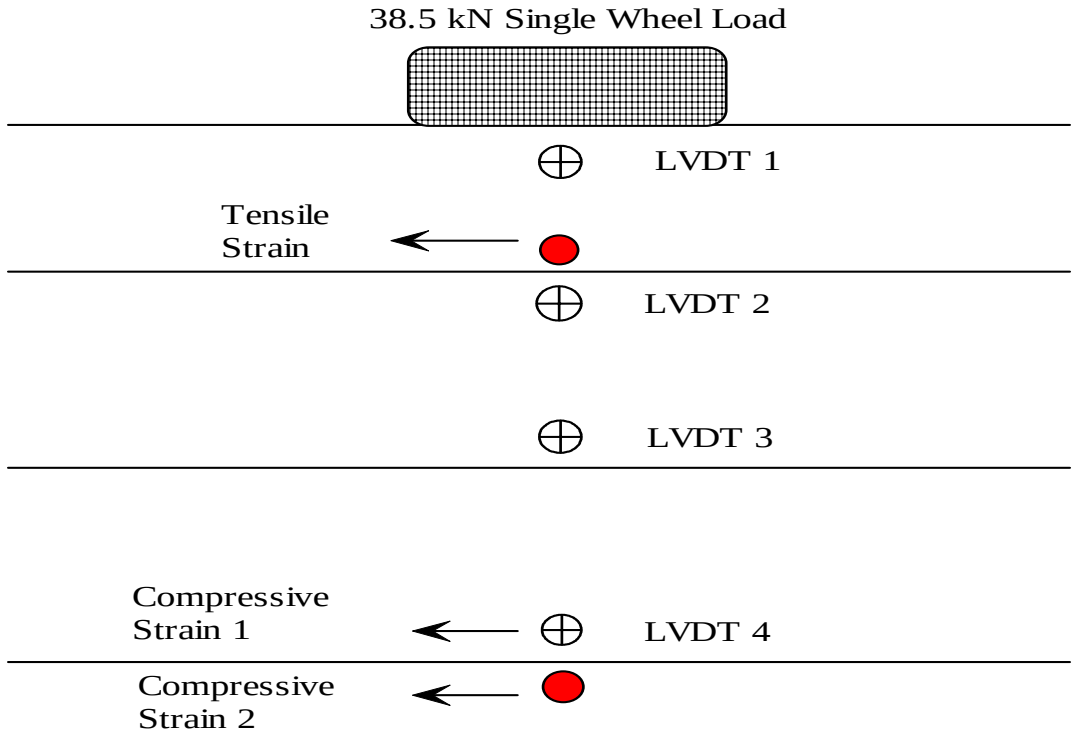

Figure 4.18. Sensitivity Evaluation Points

4.4.1. Sensitivity Analysis of Stress-Dependent Property

The coefficients, K_1, K_2, and K_3 were determined from resilient modulus tests. Those coefficients used in this analysis were assumed on the basis of the laboratory test and backcalculation modulus using FWD data. Table 4.4 presents the change of parameters for this analysis. Since K_3 is negative through all materials, the 30 % reduction of the parameter was conducted in terms of absolute value.

Table 4.4. Variation of Resilient Parameters in Sensitivity Analysis

Layer	K_1	-30% K_1	K_2	-30% K_2	K_3	-30% K_3
Flex Base	2000	1400	0.7	0.49	-0.2	-0.14
Lime Base	1000	700	0.6	0.42	-0.2	-0.14
Subgrade	500	350	0.2	0.14	-0.4	-0.28

First, the sensitivity to the displacements was studied. Figure 4.19 to 4.21 show the results of the analysis. In these plots, an absolute change in displacement due to a corresponding change in the parameters is estimated. As shown in the figures, the predicted displacements are most sensitive to the parameter, K_1. It should be noted that K_3 was more dominant than K_2 in the subgrade because the softening term which is the ratio of octahedral stress to the atmosphere pressure is more critical factor because of the K_3 value of powered by -0.4 than hardening the term with the K_2 value. Additional sensitivity analysis was conducted to determine how the displacement varied due to the increase or decrease of parameters. For this analysis, the parameters in subgrade were changed ± 30 % because the previous analysis showed that the change of parameters in the subgrade results in more significant influence on the displacement variation. Figures 4.22 to 4.24 illustrate the results of the analysis. It is shown that the increase

K_1 in equation (3.3) resulting in higher resilient modulus leads to a decrease of displacements. In the case of K_2 and K_3, their impacts on displacements are highly dependent on the quantity of the normalized terms composed of the bulk and octahedral shear stress divided by atmospheric pressure. If the term is less than one, an increase of the parameters leads to a decrease of the modulus and vice versa. In this analysis, since both normalized terms were less than one, as K_2 and K_3 increase up to 30 percent, a positive change in displacement was detected due to the decrease of modulus. Secondly, the sensitivity of the strains was investigated and is presented in Figures 4.25 to 4.27. Stress dependent parameters in the flexible base layer were changed ± 30 percent to check variation of strains. Because the flexible base layer is located below the AC layer, the change in the parameters in the layer has a large influence on the strain at the bottom of the AC. As expected, the decrease in K_1 resulted in an increase of the strain. The same trend in the variation K_2 and K_3 results in a lower modulus and a slightly higher strain.

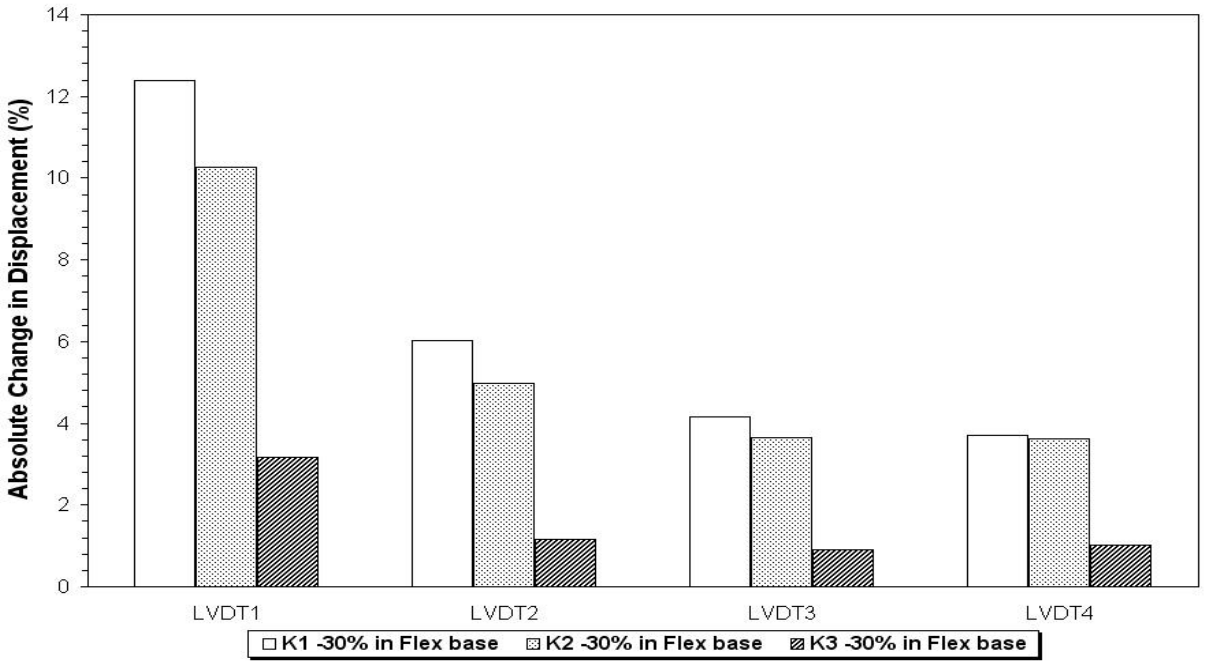

Figure 4.19. Sensitivity of the Displacement to Changes in Parameters in Flexible Base

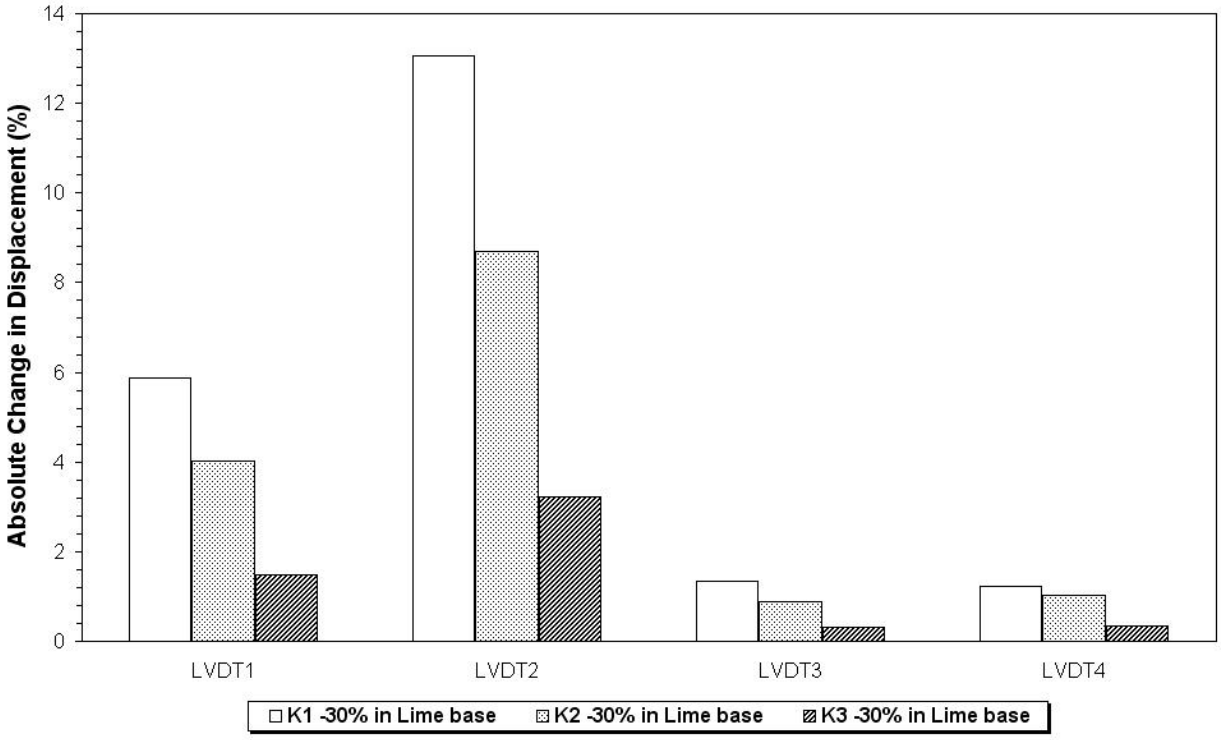

Figure 4.20. Sensitivity of the Displacement to Changes in Parameters in Lime Treated Subbase

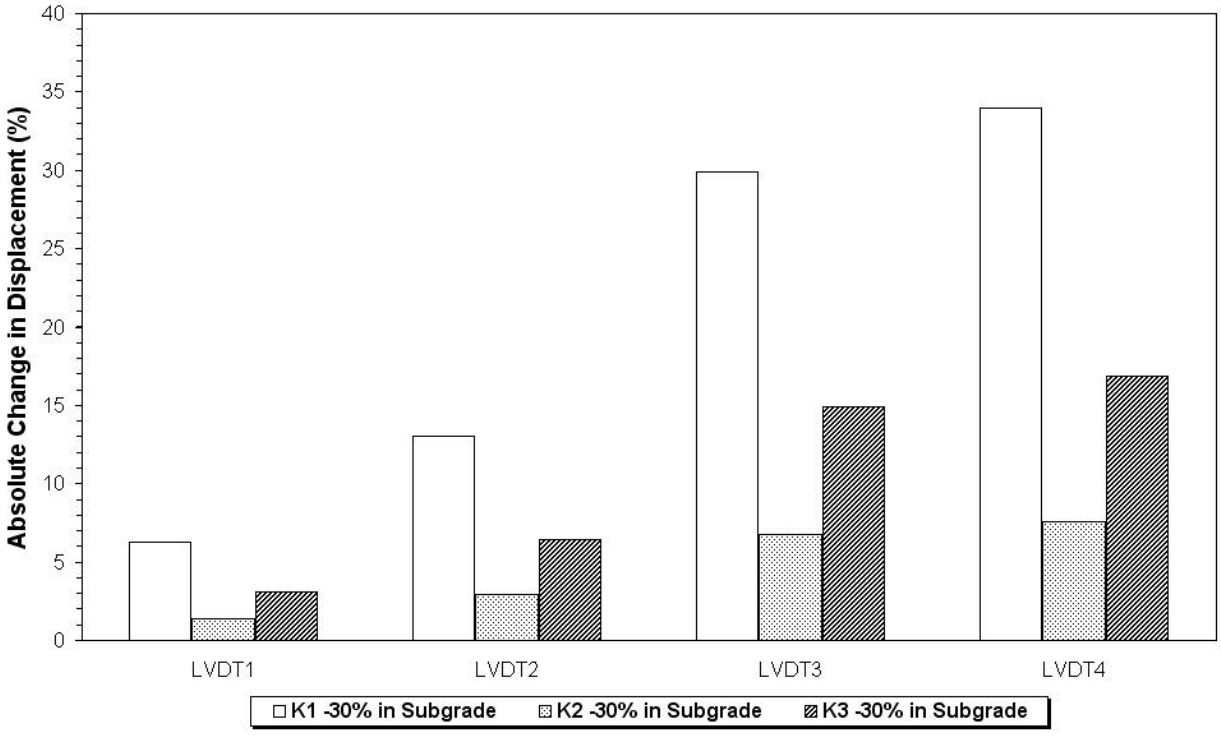

Figure 4.21. Sensitivity of the Displacement to Changes in Parameters in the Subgrade

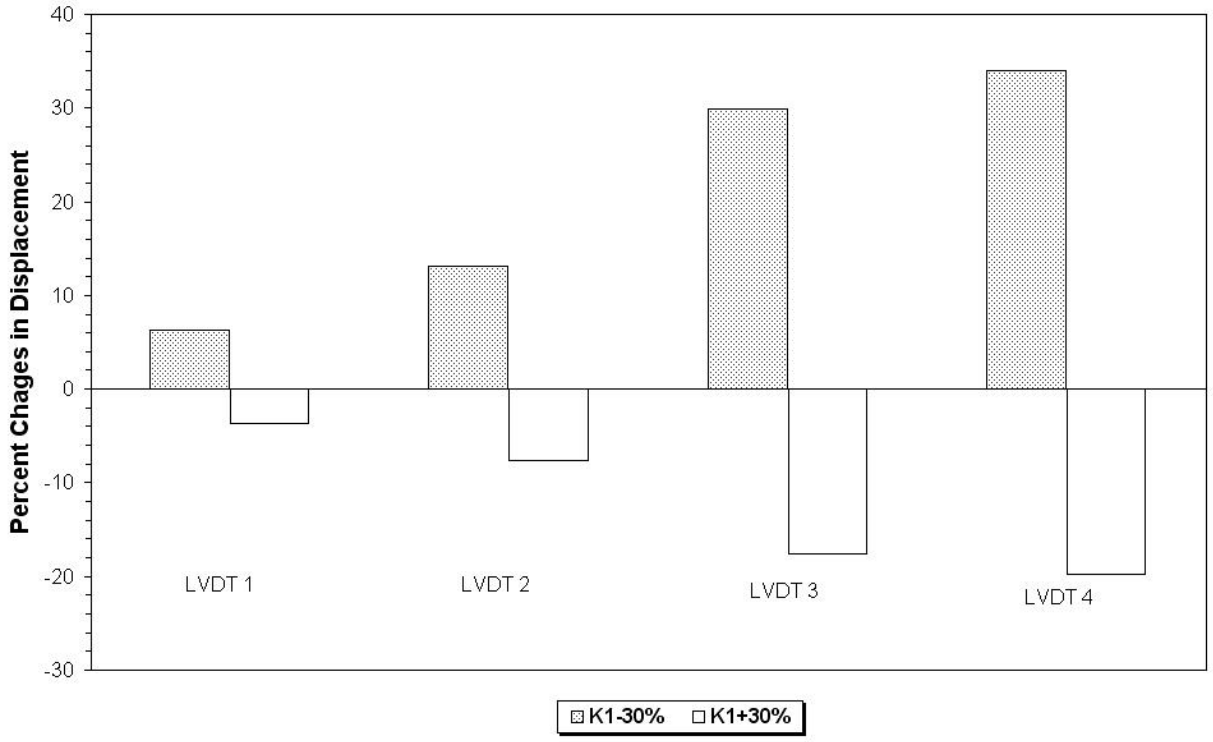

Figure 4.22. Sensitivity of the Displacement to Changes K_1 in the Subgrade

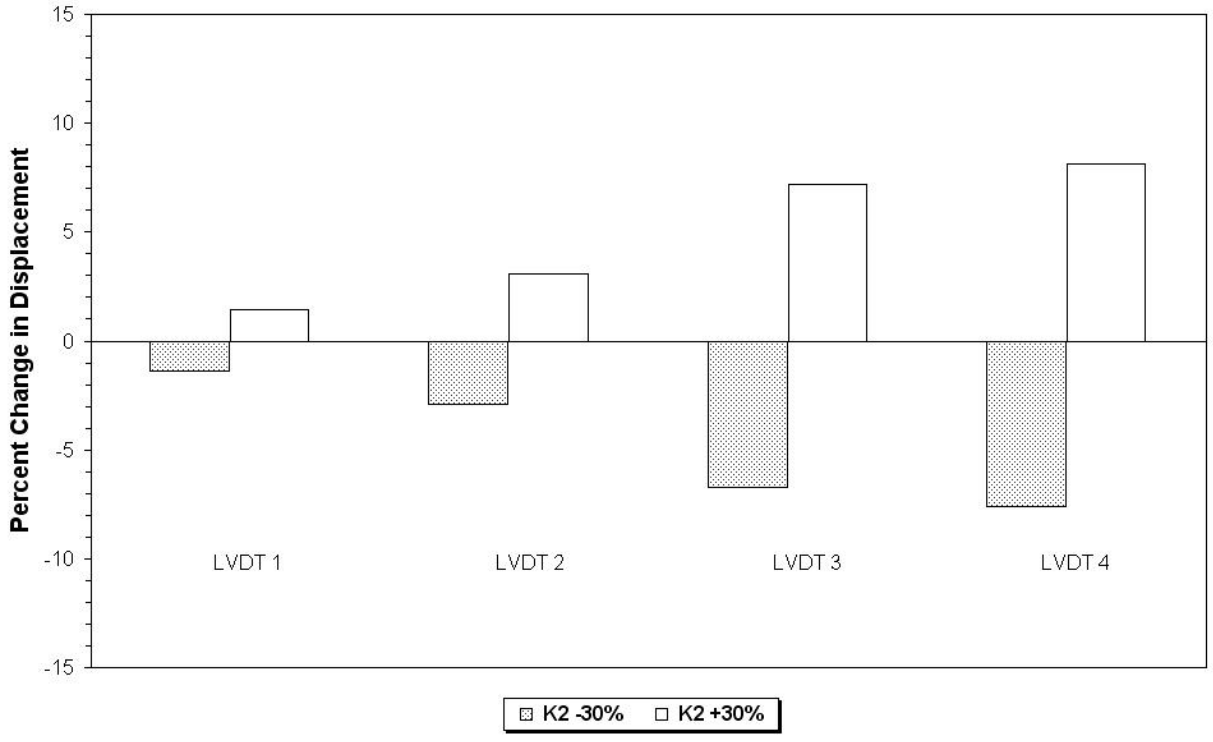

Figure 4.23. Sensitivity of the Displacement to Changes K_2 in the Subgrade

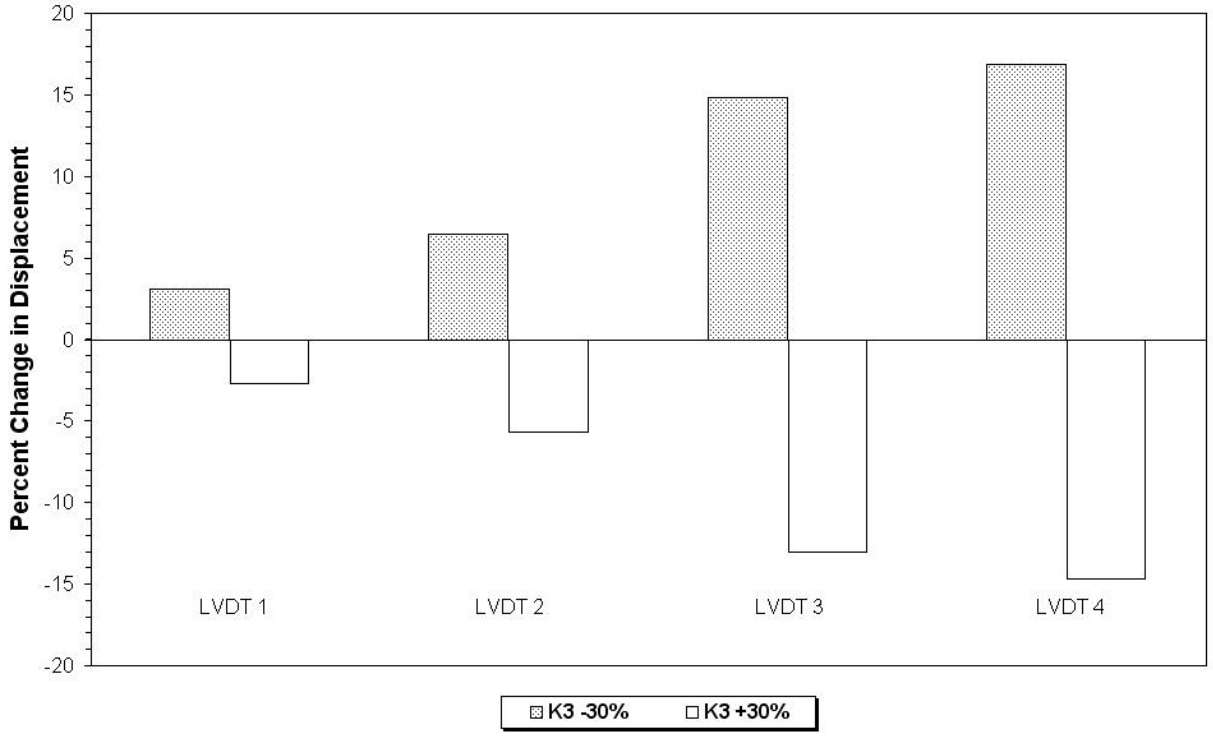

Figure 4.24. Sensitivity of the Displacement to Changes K_3 in the Subgrade

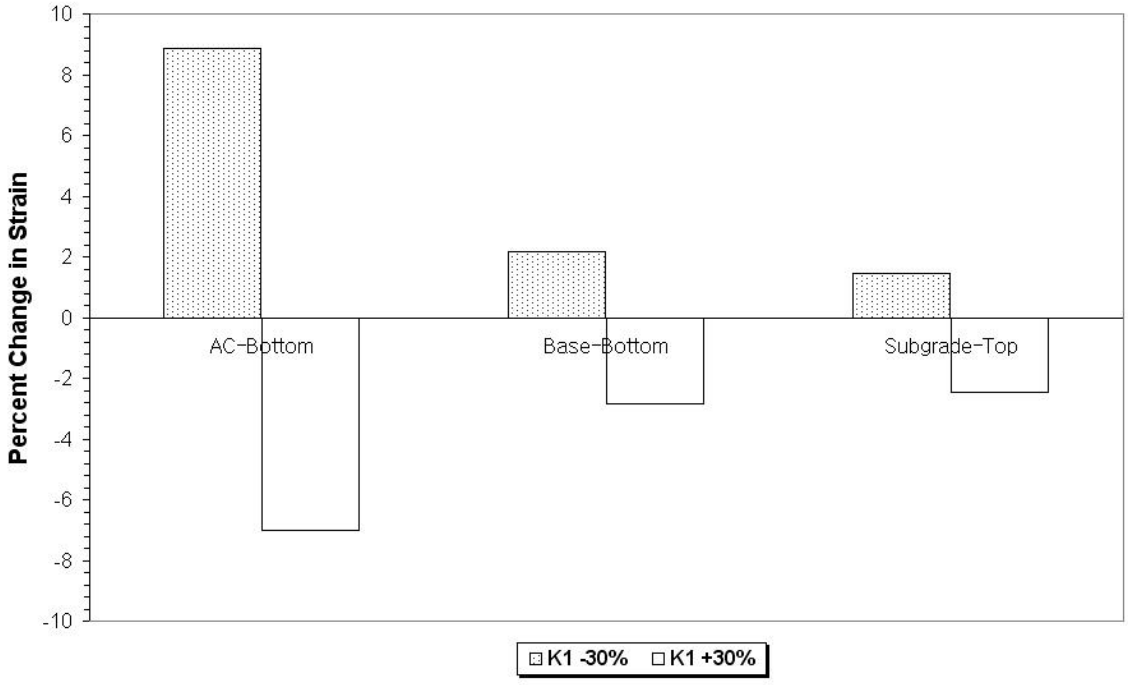

Figure 4.25. Sensitivity of the Strain to Changes K_1 in Flexible Base

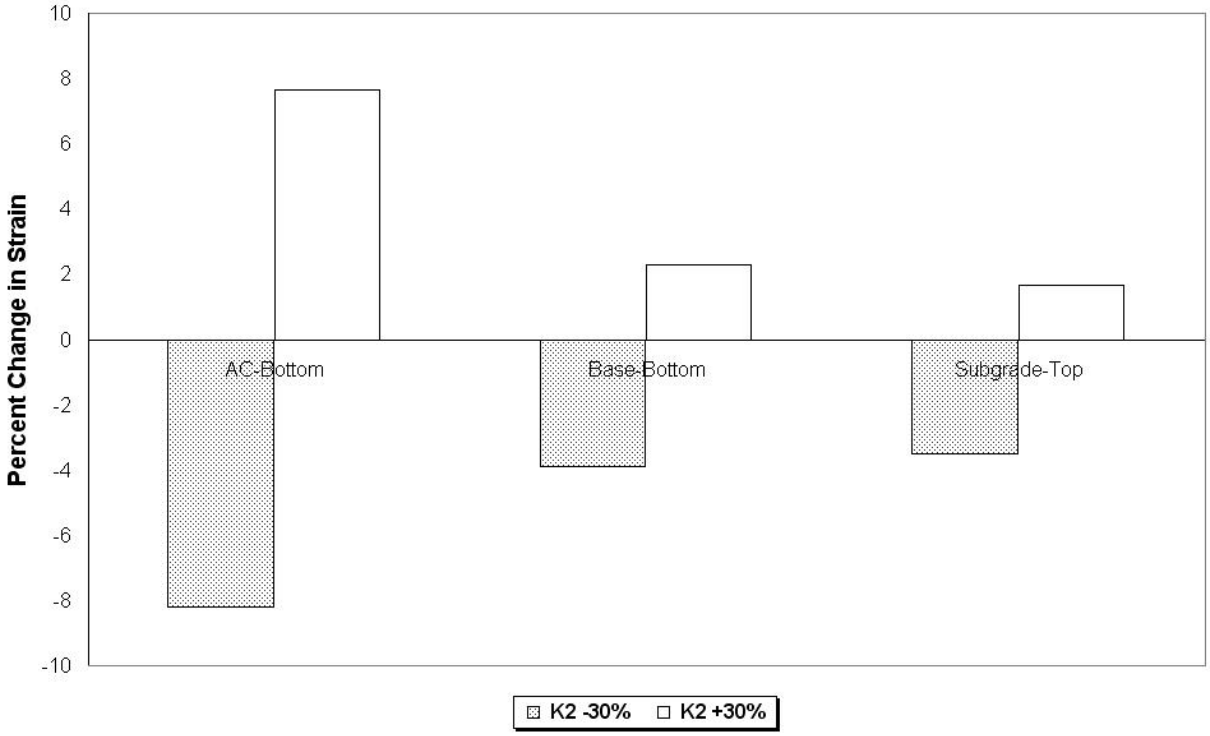

Figure 4.26. Sensitivity of the Strain to Changes K_2 in Flexible Base

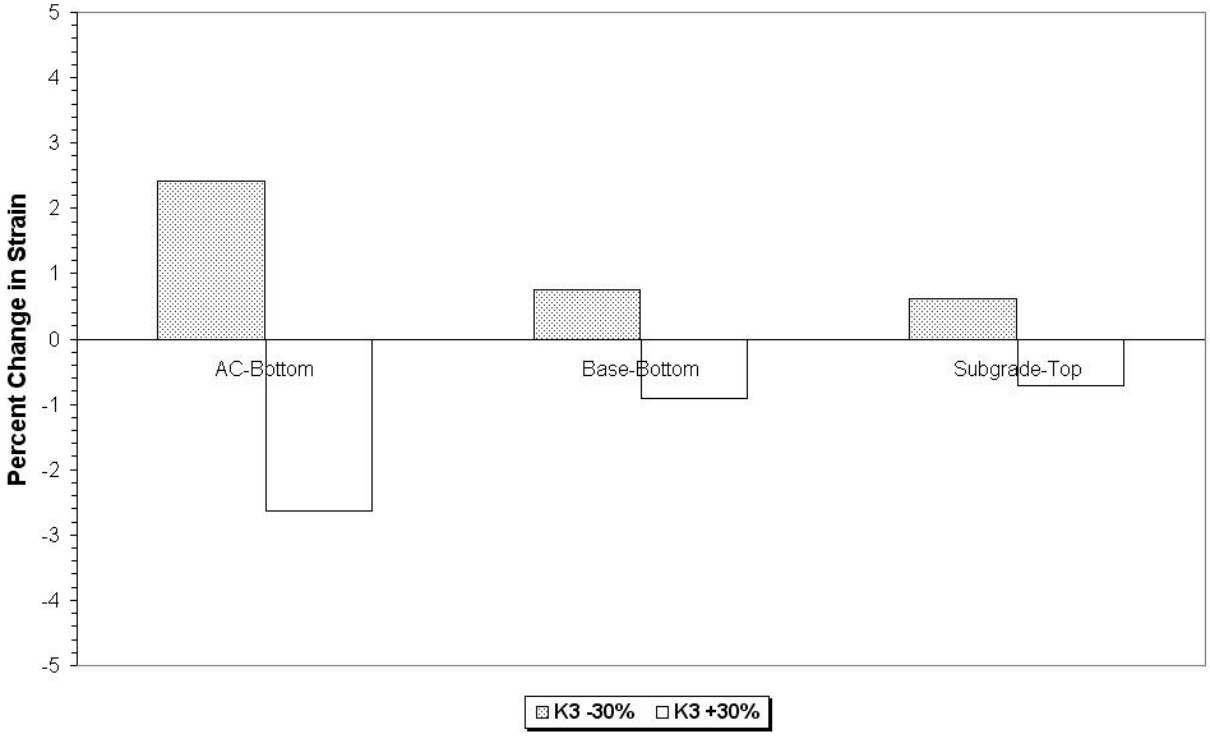

Figure 4.27. Sensitivity of the Strain to Changes K_3 in Flexible Base

4.4.2. Sensitivity Analysis of Cross-Anisotropy Properties

The behavior unbound granular or subgrade material depends on the arrangement particles that is related to the moisture content, density and load condition. It has been reported that the anisotropy characteristic of granular base in flexible pavements eliminates the tensile radial stress drastically, which is calculated using the linear isotropic approach. In this study, the impact of three parameters (n, m, p) obtained by the ratio of modulus and Poisson's ratio in different directions on the variation of displacement and strain is presented. It is valuable to investigate the sensitivity to the displacements because the pavement response significantly depends upon the resilient material property imposed in different directions. Table 4.5 presents the change of parameters for this analysis.

Table 4.5. Variation of Cross-Anisotropy Parameters in the Sensitivity Analysis

Layer	n	-30% n	m	-30% m	p	-30% p
Flex Base	0.4	0.28	0.30	0.21	1.5	1.05
Lime Base	0.45	0.315	0.45	0.315	1.5	1.05
Subgrade	0.90	0.630	0.65	0.455	2.0	1.40

Figures 4.28 to 4.30 reveal an appreciable sensitivity of all displacements to variations in both n and m. This means that the pavement response depends highly on the ratio of modulus. The displacements predicted at three LVDT positions except the first sensor are distributed through the granular base and subgrade. If the pavement response is analyzed with a linear isotropic approach, a constant modulus value in each layer is not appropriate for describing the complex behavior of those materials. It should be noted that the cross-anisotropy properties can affect the response of pavement independently without a change in its stress dependent properties. Since the cross anisotropy model was applied to predict displacements, which are

most similar to the field measurement, it is essential to check the variation in displacements due to the magnitude of the parameters. For this analysis, the three parameters in the subgrade were varied ± 30 percent. Figures 4.31 to 4.33 illustrate results of the analysis. As three ratios increase to 30 percent, displacements decrease to some extent. The trend was more pronounced in the n variation. Figures 4.34 to 4.36 present the sensitivity of critical strains to the variation of three parameters. Both n and m influence the magnitude of strains. It can be inferred that cross-anisotropic soils, characterized by large n values, experience a higher confinement along the vertical axis and improves the load spreading capacity of the medium. Most of overconsolidated clay shows some extent of cross anisotropy with a typical range of n value from 1 to 3 (Barden, 1963). Such clays will possess a greater load spreading capacity than normally consolidated clay. This trend can be seen by observing the variation of the modulus as presented in Figure 4.37 to 4.42. Each block in the figures represents an element in the finite element mesh. Each block contains three numbers: the initial case, the -30 percent case and the +30 percent case in that order. The resilient modulus was calculated in each stress state. On the whole, the base layers such as the flexible and lime treated subbase have a higher modulus at the top of the layer. The modulus of the layer then decreases as the confining stresses decrease and the octahedral shear stress increases towards the bottom of the layer. It should be noted that the reduction of n value causes a decrease of both vertical and horizontal modulus. It confirms that a smoother layer due to the reduced modulus generates much higher deformation.

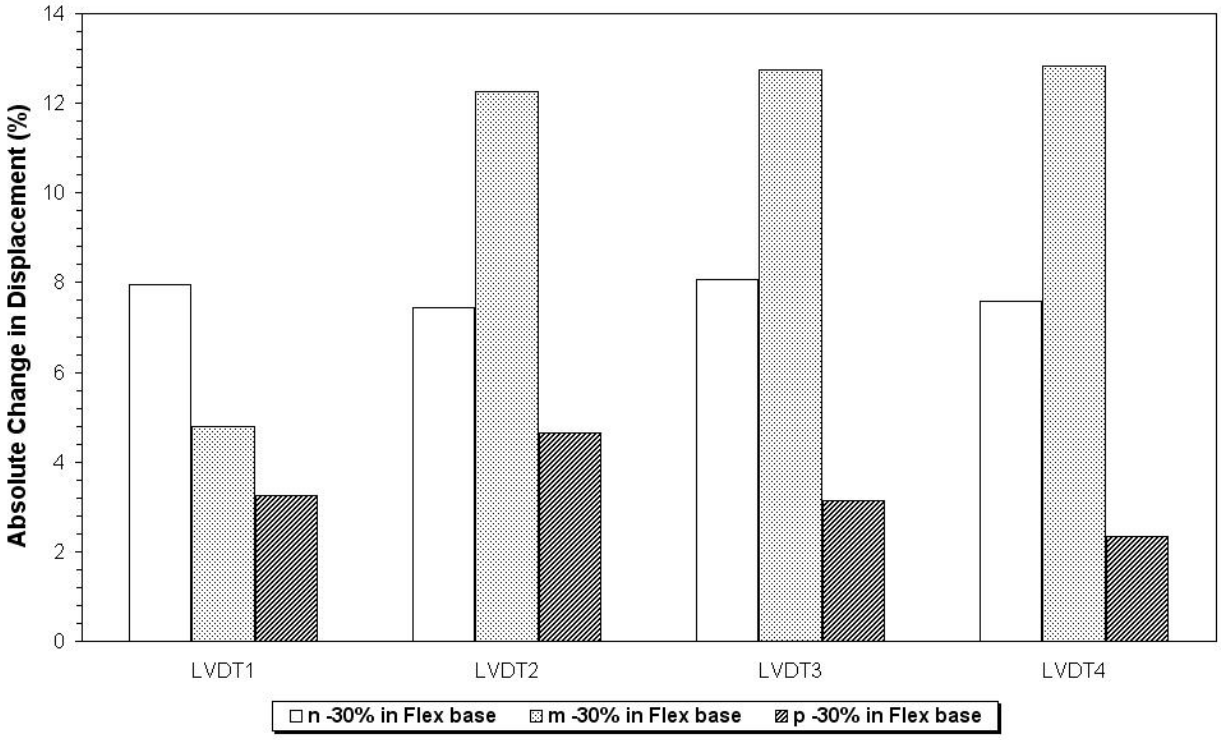

Figure 4.28. Sensitivity of the Displacement to Changes in Parameters in Flexible Base

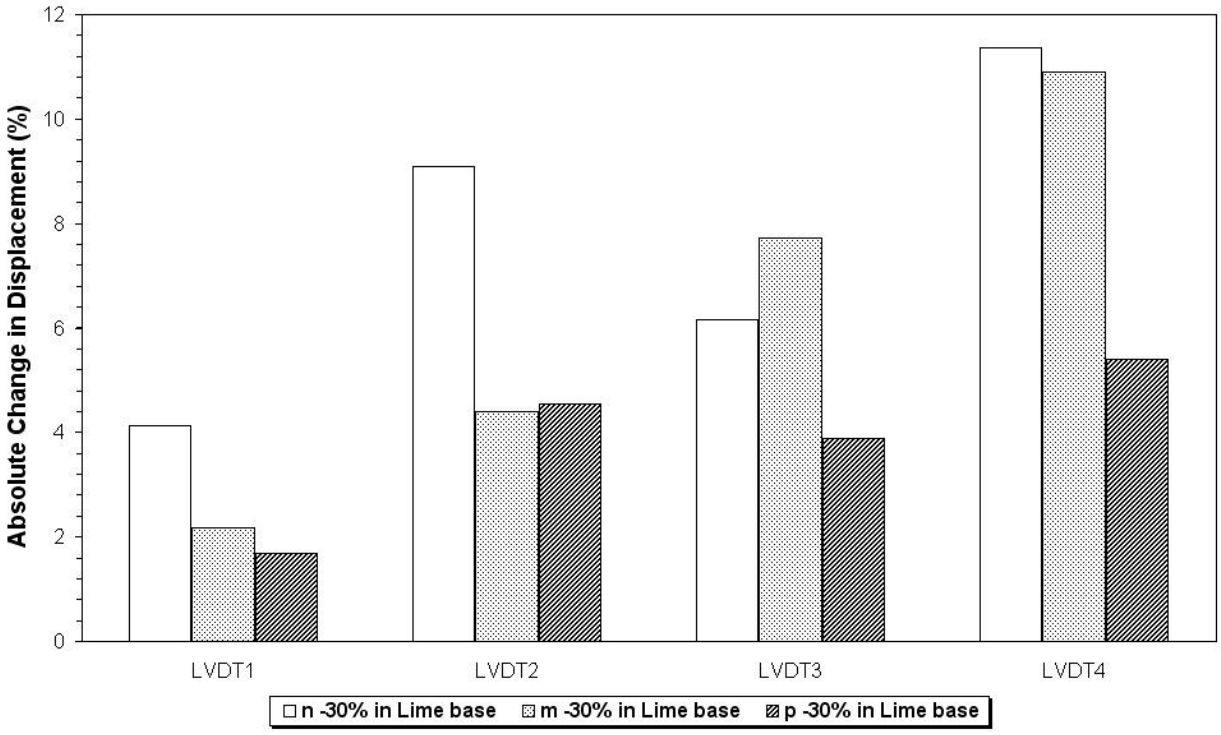

Figure 4.29. Sensitivity of the Displacement to Changes in Parameters in Lime Treated Subbase

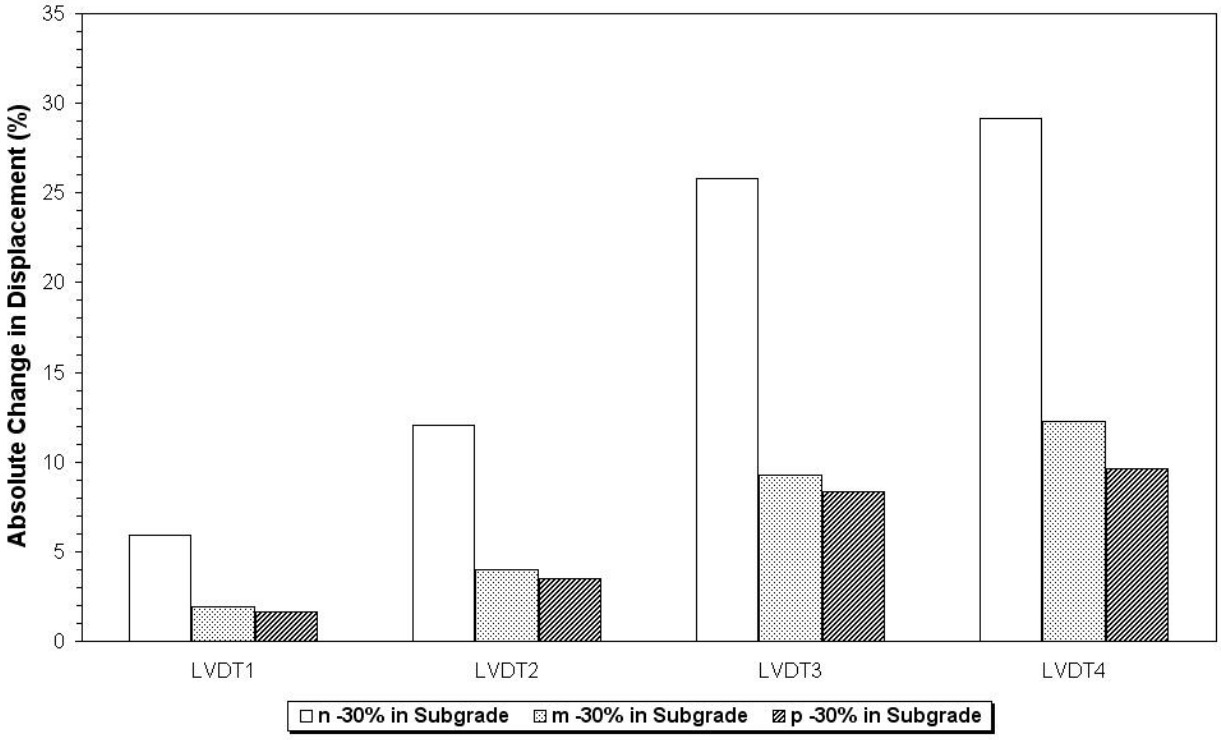

Figure 4.30. Sensitivity of the Displacement to Changes in Parameters in Subgrade

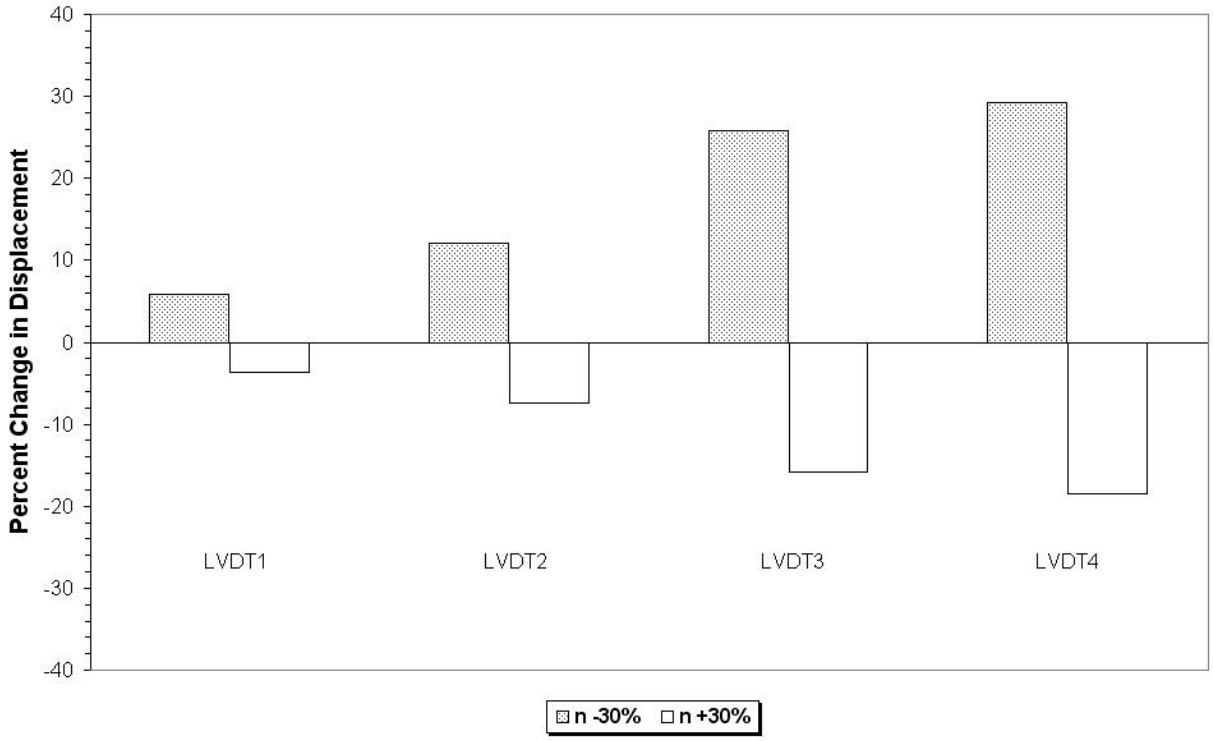

Figure 4.31. Sensitivity of the Displacements to Changes in the n Value in Subgrade

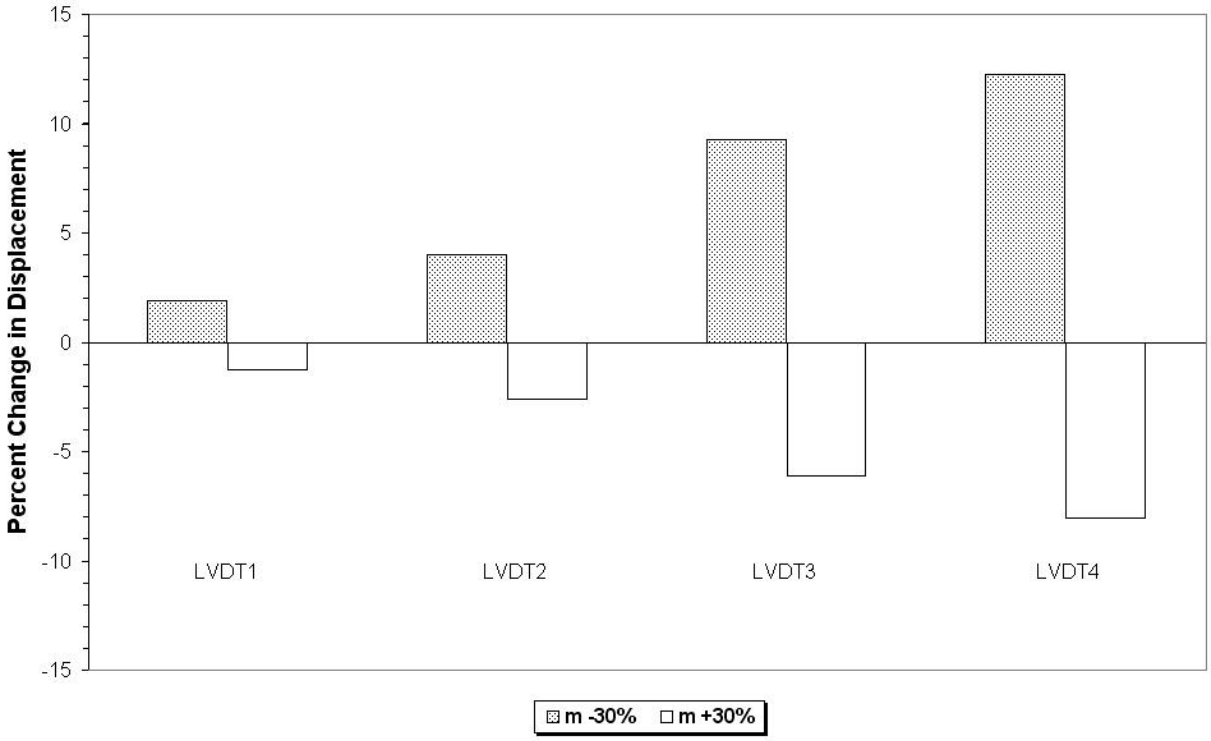

Figure 4.32. Sensitivity of the Displacements to Changes in the m Value in Subgrade

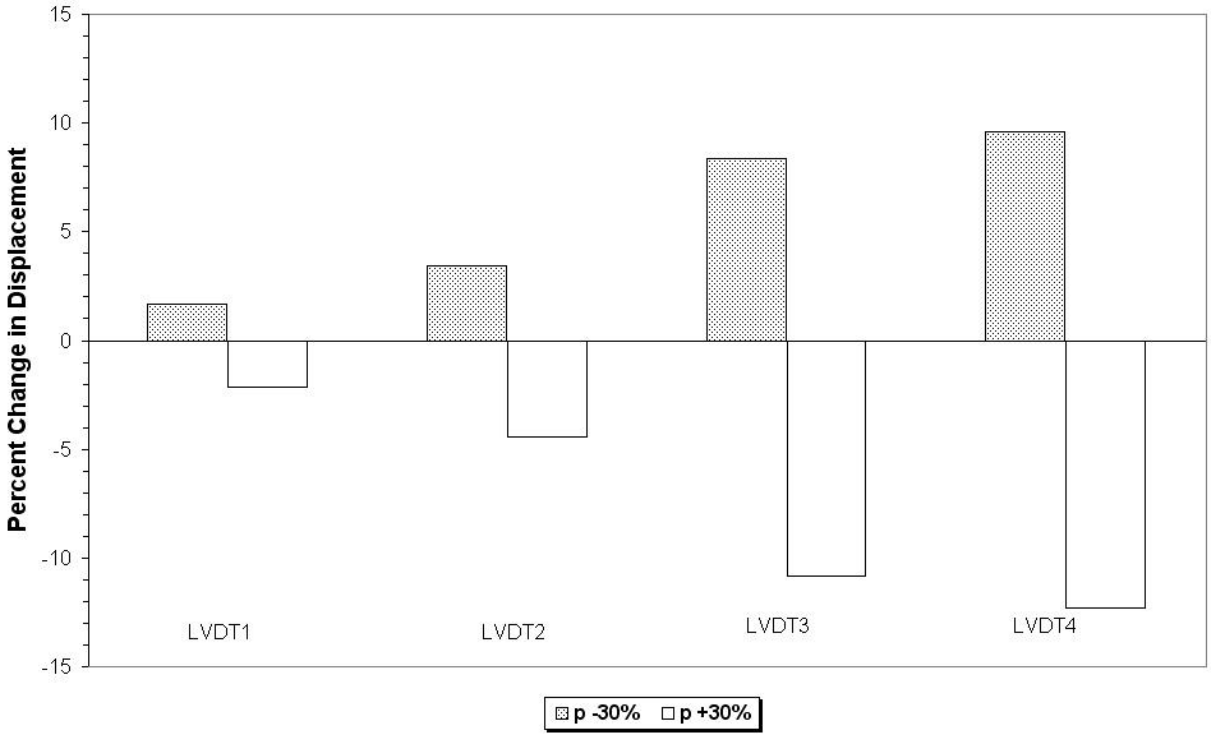

Figure 4.33. Sensitivity of the Displacements to Changes in the p Value in the Subgrade

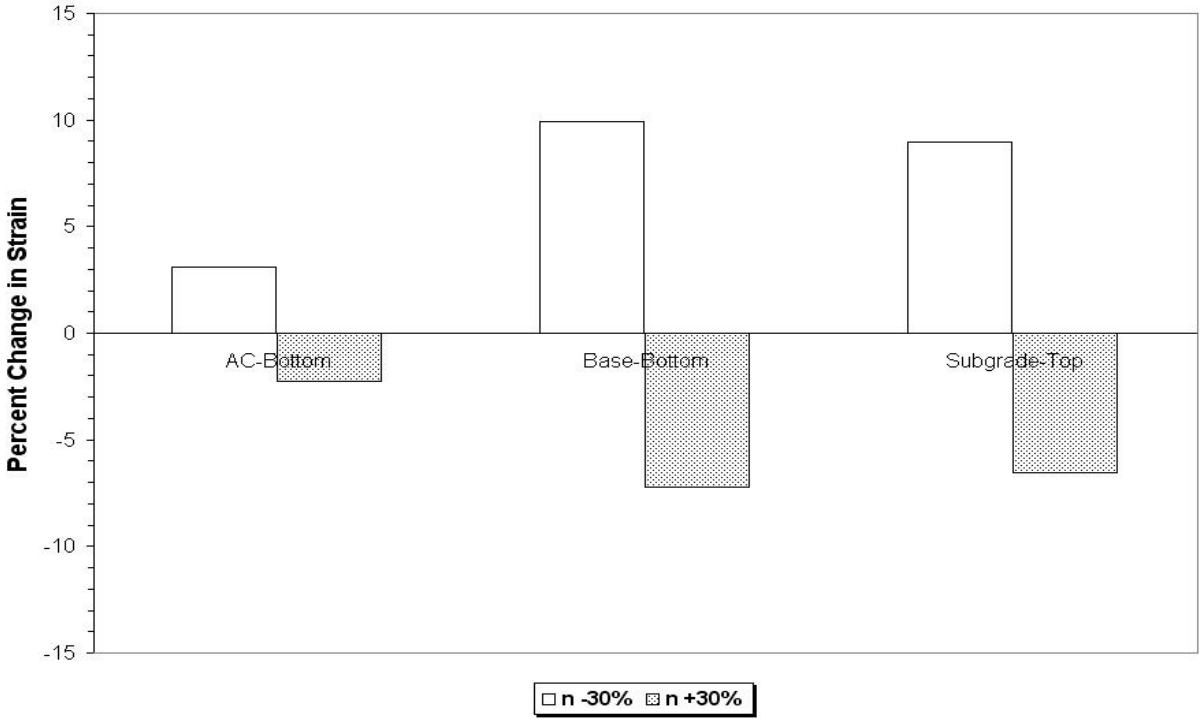

Figure 4.34. Sensitivity of the Strains to Changes in the n Value in Subgrade

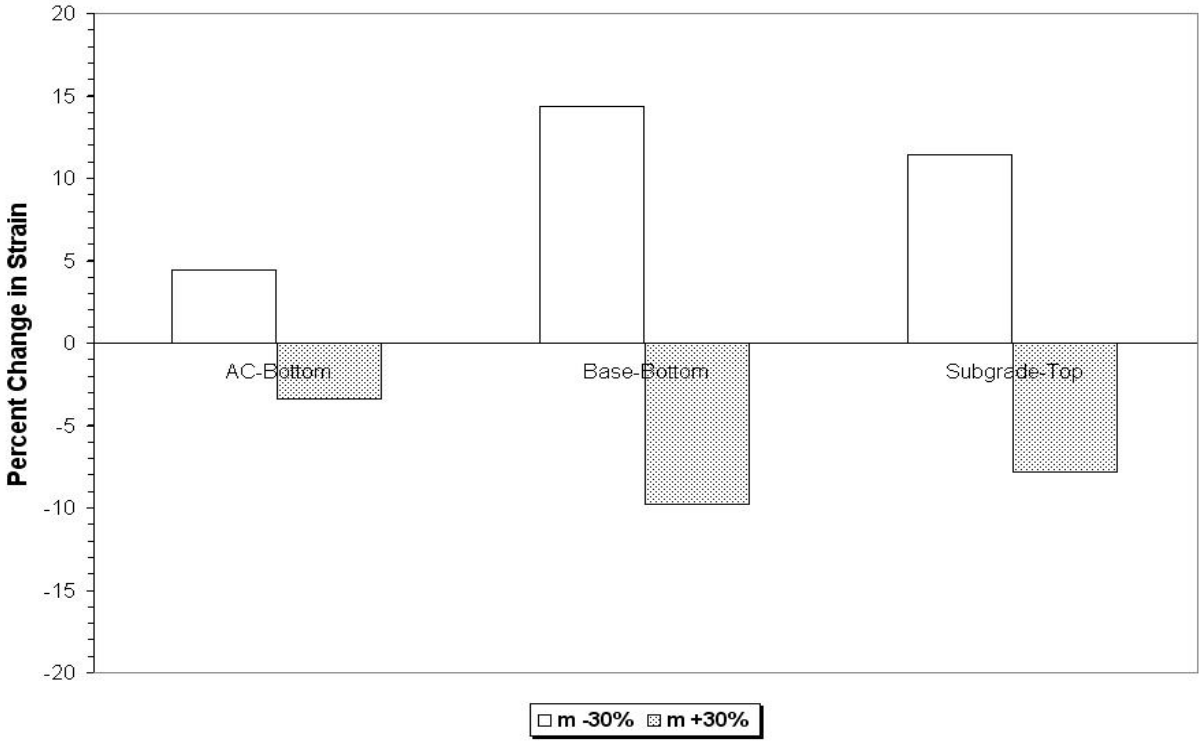

Figure 4.35. Sensitivity of the Strains to Changes in the m Value in Subgrade

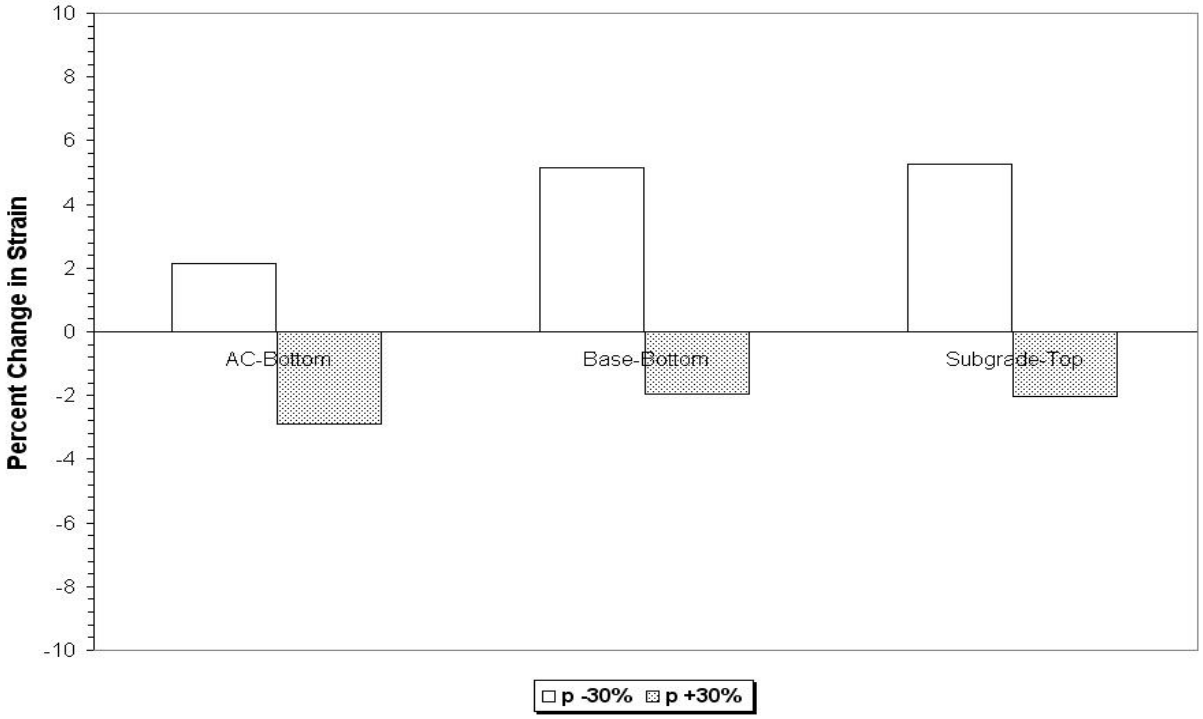

Figure 4.36. Sensitivity of the Strains to Changes in the p Value in Subgrade

Asphalt concrete layer			
162	214	265	387
154	206	251	363
162	215	267	388
136	171	232	322
130	163	195	299
137	176	233	324
114	140	170	256
109	133	161	238
115	142	172	257
109	115	140	208
109	109	132	194
109	116	142	209
109	109	109	159
109	109	109	148
109	109	111	160

Figure 4.37. Resilient Vertical Modulus (MPa) Variation within Flexible Base due to the Change of the n Value in Subgrade

Asphalt concrete layer			
81	107	133	193
77	103	125	182
81	108	133	194
68	86	116	161
65	81	98	150
69	88	117	162
57	70	85	128
55	66	81	119
58	71	86	128
55	57	70	104
55	55	66	97
55	58	71	104
55	55	55	79
55	55	55	74
55	55	55	80

Figure 4.38. Resilient Radial Modulus (MPa) Variation within Flexible Base due to the Change of the n Value in Subgrade

Asphalt concrete layer Flex base layer			
53	53	56	66
53	53	53	62
53	53	56	66
53	53	53	60
53	53	53	57
53	53	53	60
53	53	53	55
53	53	53	53
53	53	53	56
53	53	53	53
53	53	53	53
53	53	53	53

Figure 4.39. Resilient Vertical Modulus (MPa) Variation within Lime Treated Subbase due to the Change of the n Value in Subgrade

Asphalt concrete layer Flex base layer			
24	24	25	30
24	24	24	28
24	24	25	30
24	24	24	27
24	24	24	26
24	24	24	27
24	24	24	25
24	24	24	24
24	24	24	25
24	24	24	24
24	24	24	24
24	24	24	24

Figure 4.40. Resilient Radial Modulus (MPa) Variation within Lime Treated Subbase due to the Change of the n Value in the Subgrade

Asphalt concrete layer Flex base layer Lime base layer			
69	69	69	69
67	67	67	67
71	71	71	71
69	69	69	69
67	67	67	67
71	71	71	71
69	69	69	69
67	67	67	67
71	71	71	71
69	69	69	69
67	67	67	67
71	71	71	71

Figure 4.41. Resilient Vertical Modulus (MPa) Variation within Subgrade due to the Change of the n Value in Subgrade

Asphalt concrete layer Flex base layer Lime base layer			
63	63	63	63
43	43	43	43
85	85	85	85
63	63	63	63
43	43	43	43
85	85	85	85
63	63	63	63
43	43	43	43
85	85	85	85
63	63	63	63
43	43	43	43
85	85	85	85

Figure 4.42. Resilient Radial Modulus (MPa) Variation within the Subgrade due to the Change of the n value in Subgrade

CHAPTER V

EVALUATION OF DAMAGE POTENTIAL

5.1. GENERAL

The evaluation of damage due to OTT loads using MDD measurement was performed in accordance with the objectives of this study. The principal reason for using MDD measurements was to assist in establishing a model for predicting pavement response. By comparing the measured displacements with the predicted displacements from theory, a verification of the pavement model could be made before an evaluation of stresses and strains for damage assessment was undertaken. The MDD is an assembly of linear variable differential transducers (LVDTs) installed inside a cylindrical vertical cavity within the pavement to measure vertical displacements at selected depths under moving wheel loads. Both recoverable and permanent displacement can be measured with the MDD (Jooste and Fernando, 1995).

For this purpose, trucks monitored with MDD displacement in both K6 and K7 lane and in different months were examined to evaluate the damage potential on the considered route. In addition, legal trucks loaded within the axle limit described in Table 1.1 were taken into account to determine the extent of the additional damage due to OTT loads by comparing the damage between two types of traffic.

5.2. EVALUATION OF DAMAGE POTENTIAL USING MDD

To compare the damage potential due to OTT and legal truck loads, several pairs of trucks monitored at almost an identical time were selected because it removes a discrepancy in pavement response due to the difference of environmental conditions. An example of MDD measurement is shown in Figures 5.1 and 5.2. As shown in the figures, it is expected that the

larger displacement occurs under the OTT loads (Figure 5.2) if the trucks hit the sensor accurately. Now that most of the monitored trucks have three axle groups such as steering, drive, and trailer, an evident trace separation (i.e. three parts of the measurement group) is detected. Displacement per each axle group was determined by taking a maximum value.

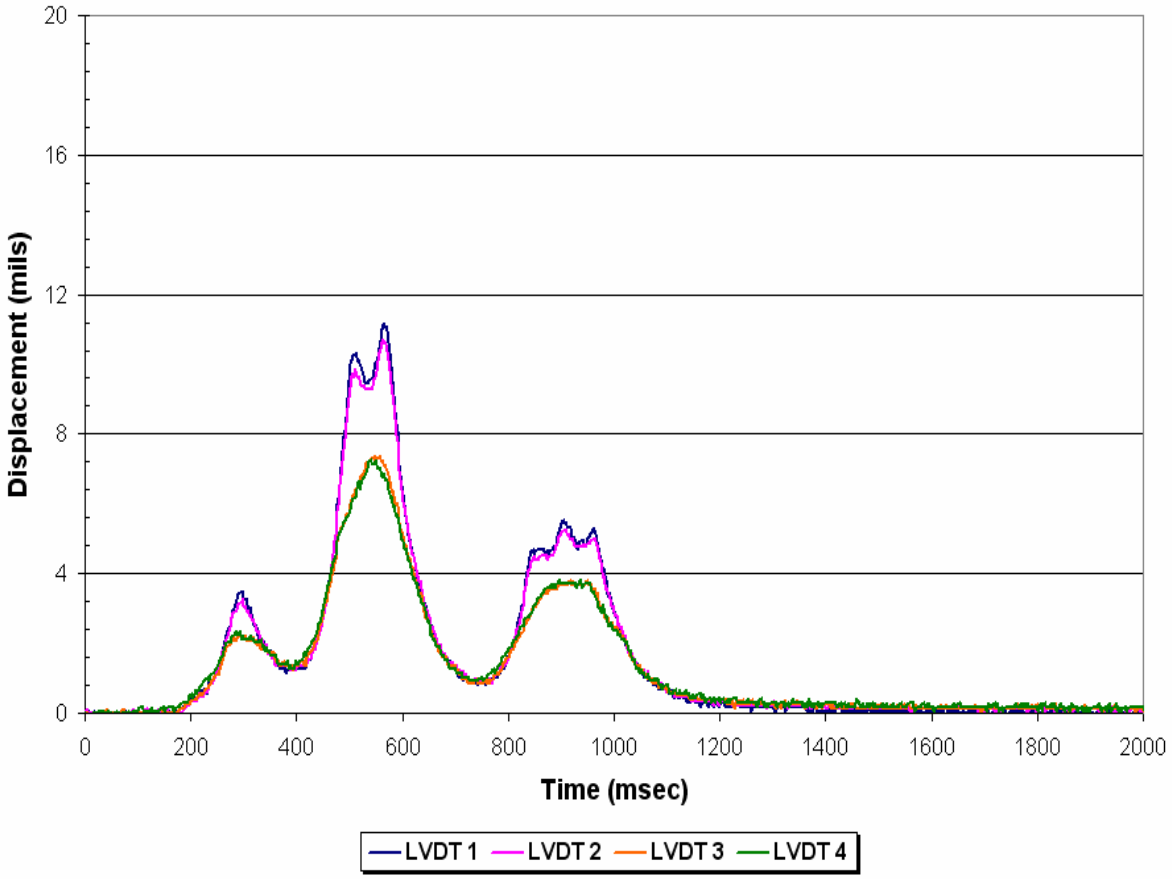

Figure 5.1. MDD Response under Legal Truck

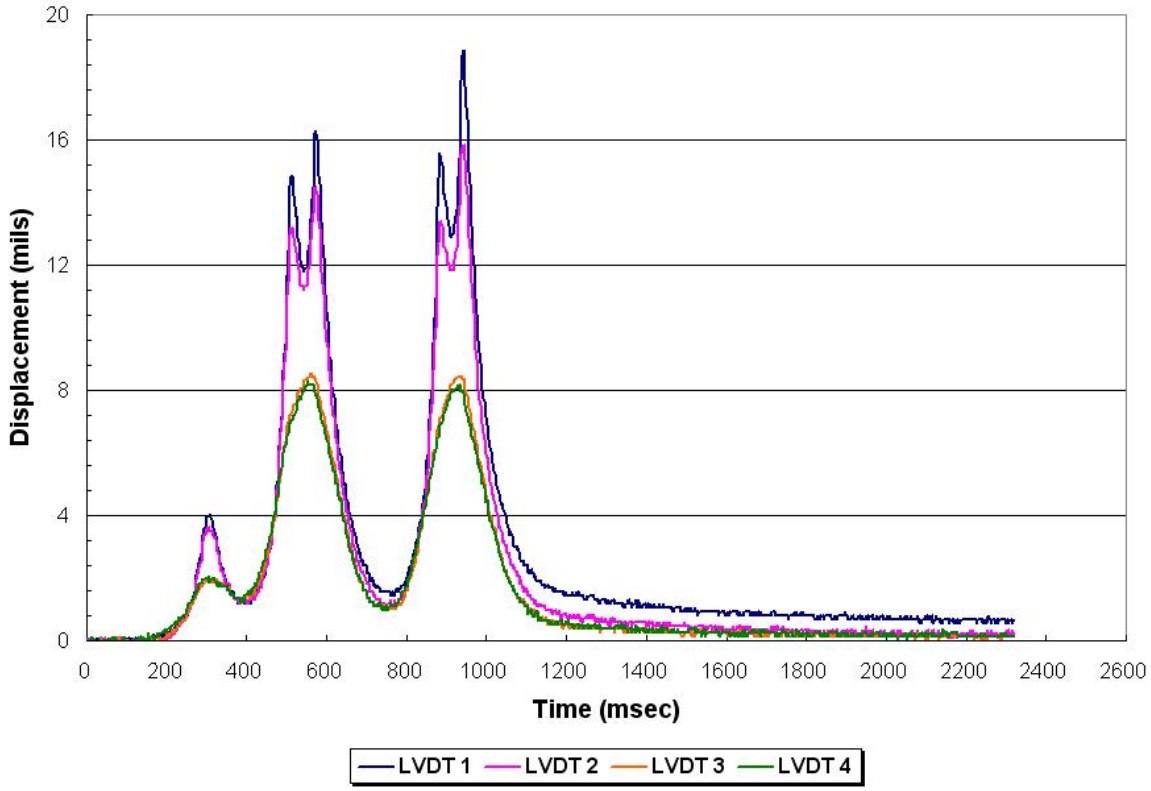

Figure 5.2. MDD Response under Permitted Overweight Truck

MDD measurements can be used to predict service life in terms of rut depth. Usually, the last two sensor readings are taken to calculate the compressive strain at the top of the subgrade. However it was difficult to use two measurements to estimate the subgrade strain because the installed position could not represent an average strain within the subgrade layer. Also, the difference between the two readings from the third and fourth sensors was too small to estimate the strain which resulted in an unreasonable estimate of the minimal damage potential. Therefore researchers tried to take an alternative to solve this problem. As presented chapter IV, a computer program NCPA using finite element method (FEM) was developed in this study. The objective of this task is to develop a tool that can model pavement response with as high accuracy as possible. For this purpose, the MDD measurements were compared with the

displacements calculated by the program. Throughout the work, modeling of granular material and subgrade with a nonlinear stress-dependent, cross-anisotropy approach was considered as the best one. Based on these results, the NCPA program was run with combinations of input that cover the variations of resilient modulus, axle weight, and offset distance during the test period for both the K6 and K7 lanes, respectively. After running the program, the correlated equation was developed by static analysis using the SPSS statistical analysis package. Table 5.1 shows the result. The independent variables used for statistical analysis consisted of modulus, axle weight, offset distance and predicted displacements. To get equations, the presence of multicollinearity was investigated in terms of variance inflation factors (VIF) denoted in the last column in table. This factor measures how much the variances of the estimated regression coefficients are inflated as compared to when the predictor variables are not linearly related. A maximum VIF value in excess of 10 is frequently taken as an indication of multicollinearity. All variables were normalized by dividing a maximum value to have the same unit with that of strain. It was observed that the compressive strain at the top of the subgrade could be evaluated in terms of predicted displacement for both lanes. The reason why the selected independent variable for the K6 and K7 lanes different is because the two structures are different for both the K6 and K7 lanes. The different composition of layer thicknesses had an influence on the determination of the independent variable to be correlated with strain. The developed equations were applied to calculate the subgrade strain using field measurement. To compare the damage potential due to OTT and legal truck loads, firstly the strain for each axle assembly was calculated. And then the Asphalt Institute (AI) equation was used to determine the service life for a given pavement and loading condition with respect to rutting.

$$(N_f)^r = 1.365 \times 10^{-9} \left(\frac{1}{\varepsilon_z} \right)^{-4.477} \quad (5.1)$$

where,

ε_z = predicted vertical compressive strain at the top of the subgrade,

$(N_f)^r$ = number of allowable load applications based on a limiting rut depth criterion of 12.5 mm.

Table 5.1. Equations for Predicting Vertical Strain at the Top of Subgrade

	Equation	N	R-square	Variance Influence Factor (VIF)
$\varepsilon_{c \text{ at K6}}$	Log (ε_c) = 1.059*D_2 + 1.707	144	0.967	1.0
$\varepsilon_{c \text{ at K7}}$	Log (ε_c) = 0.981*D_3 + 1.604	144	0.930	1.0

(Note : D_2 and D_3 is normalized MDD displacement at the second and third LVDTs.)

A new term is used as an indicator called unit service life consumed equal to a reciprocal number of allowable load repetition. Because three components of subgrade strain are calculated from three axle assemblies, the unit service life consumed ($1/N_f$) by each truck is expressed by equation (5.2).

$$\frac{1}{(N_f)_{steering}} + \frac{1}{(N_f)_{drive}} + \frac{1}{(N_f)_{trailer}} = \frac{1}{(N_f)_{truck}} \quad (5.2)$$

As mentioned before, an analysis to evaluate damage potential of OTT and legal truck loads was performed for selected pairs of truck data as presented in Table 5.2. The damage ratio denoted in the last column represents the ratio of unit service life consumed by the two types of traffic. In the table, a label composed of a unique number was assigned to OTTs.

Additionally, an attempt was made to estimate the damage potential with respect to fatigue cracking. The equation showing correlation between the asphalt tensile strain and the MDD displacement was established by running the NCPA tabulated in Table 5.3. The tensile strain at the bottom of the AC layer was substituted into the AI equation as follows.

$$(N_f)^c = 7.9488 \times 10^{-2} \left(\frac{1}{\varepsilon_{ac}} \right)^{3.29} \left(\frac{1}{E_{ac}} \right)^{0.854} \quad (5.3)$$

where,

ε_{ac} = predicted tensile strain at the bottom of the asphalt surface layer, and

E_{ac} = asphalt concrete modulus.

Table 5.2. Prediction of Damage Effects of Overweight vs. Legal Trucks by Rutting in K6 & K7 Lanes

Date	Time	Truck ID	Axle Weights (kips)			$1/N_f$	Damage Ratio
			Steering	Drive	Trailer		
10/02	12:18:43	T26	10.2	38.1	56.0	2.89E-07	1.71
10/02	12:21:47	414	12.1	44.9	55.6	4.93E-07	
10/02	12:46:07	T27	13.9	37.2	58.7	6.87E-08	1.83
10/02	12:49:43	415	12.7	41.2	56.1	1.26E-07	
10/02	16:29:17	T32	15.0	38.0	38.3	1.50E-07	3.05
10/02	16:33:57	441	12.1	44.2	52.0	4.58E-07	
10/02	18:30:55	T35	12.5	31.7	26.9	1.49E-08	12.62
10/02	18:17:12	470	10.0	44.1	39.6	1.88E-07	
10/02	18:32:57	T37	11.6	31.8	20.3	2.30E-07	2.12
10/02	18:33:48	472	12.5	40.0	43.7	4.88E-07	
10/02	18:42:18	T41	10.6	25.0	24.0	3.85E-08	7.35
10/02	18:41:16	474	11.7	41.4	57.5	2.83E-07	
12/02	12:03:25	T14	11.4	33.3	31.4	2.11E-07	9.43
12/02	12:05:35	509	9.5	42.1	43.4	1.99E-06	
12/02	12:03:25	T30	10.6	25.0	24.0	2.10E-07	11.3
12/02	12:05:35	512	9.6	39.1	34.1	2.38E-06	
12/02	12:03:25	T41	10.6	35.0	44.0	5.02E-07	1.72
12/02	12:05:35	520	12.9	45.2	56.4	8.63E-07	
K6 Lane				**Average Ratio : 5.7**			
12/02	15:04:52	T2	8.6	37.9	43.7	7.44E-08	3.98
12/02	15:00:25	484	11.3	41.8	55.6	2.96E-07	
12/02	15:14:16	T3	10.7	32.2	38.4	7.10E-08	1.77
12/02	15:09:24	485	10.8	42.4	44.8	1.26E-07	
12/02	15:25:55	T4	9.8	32.4	31.7	3.03E-08	3.99
12/02	15:28:52	486	12.5	41.3	43.7	1.21E-07	
12/02	15:50:23	T5	9.5	32.4	31.7	2.34E-09	2.27
12/02	15:50:13	493	8.7	43.2	42.0	5.31E-09	
12/02	16:09:20	T9	9.8	35.1	39.6	1.41E-07	1.09
12/02	16:03:28	497	9.0	37.7	44.5	1.54E-07	
K7 Lane				Average Ratio : 2.6			

Table 5.3. Equations for Predicting Horizontal Strain at the Bottom of the AC Layer

	Equation	N	R-square	Variance Influence Factor (VIF)
ε_{ac} at K6	$\text{Log}(\varepsilon_{ac}) = 0.646*D_1 + 1.856$	144	0.958	1.0
ε_{ac} at K7	$\text{Log}(\varepsilon_{ac}) = 0.763*D_1 + 1.548$	144	0.964	1.0

(Note : D_1 is the normalized MDD displacement at first LVDT.)

Table 5.4 shows the damage ratio between the OTT and legal truck loads due to fatigue cracking. It was observed that damage by both rutting and fatigue cracking was much more severe under the OTT loads. The estimated damage ratio from the above analysis is restricted to the K6-4 and K7-3 stations because of the location of the MDD installation. Therefore the fact provides evidence of additional damage by OTT loads and calls for a specific design to sustain that traffic in order to prevent an accelerated damage potential. It should also be noted that the damage potential was more pronounced in the K6 lane. As a part of this study, the temperature correction of backcalculated AC moduli was attempted to check if there exists a potential of damage due to temperature (Ramos, 2003). Figure 5.3 illustrates the evidence of damage in the pavement by the reduction of the corrected AC modulus. It is observed that the K6 lane becomes deteriorated due to a larger number of OTT than in the K7 lane, where a relatively small amount of OTT moves by showing a steeper reduction of modulus. In addition, the magnitude of the damage ratio was larger with respect to rutting. When viewed in developing rutting, because rutting stems from the permanent deformation in all of the pavement layers or the subgrade, usually caused by the consolidation or lateral movement of the materials due to traffic loads, it is considered that the layer structure of the K6 lane becomes weaker due to repeated traffic loads than does that of the K7 lane.

Table 5.4. Prediction of Damage Effects of Overweight vs. Legal Truck Weight by Fatigue Cracking in K6 & K7 Lanes

Date	Time	Truck ID	Axle Weights (kips)			$1/N_f$	Damage Ratio
			Steering	Drive	Trailer		
10/02	12:18:43	T26	10.2	38.1	56.0	1.60E-06	1.62
10/02	12:21:47	414	12.1	44.9	55.6	2.59E-06	
10/02	12:46:07	T27	13.9	37.2	58.7	1.06E-06	2.65
10/02	12:49:43	415	12.7	41.2	56.1	2.81E-06	
10/02	16:29:17	T32	15.0	38.0	38.3	1.52E-06	1.58
10/02	16:33:57	441	12.1	44.2	52.0	2.40E-06	
10/02	18:30:55	T35	12.5	31.7	26.9	3.54E-07	3.98
10/02	18:17:12	470	10.0	44.1	39.6	1.41E-06	
10/02	18:32:57	T37	11.6	31.8	20.3	1.88E-06	3.15
10/02	18:33:48	472	12.5	40.0	43.7	5.93E-06	
10/02	18:42:18	T41	10.6	25.0	24.0	7.88E-07	3.12
10/02	18:41:16	474	11.7	41.4	57.5	2.46E-06	
12/02	12:03:25	T14	11.4	33.3	31.4	2.39E-06	2.15
12/02	12:05:35	509	9.5	42.1	43.4	5.15E-06	
12/02	12:03:25	T30	10.6	25.0	24.0	2.36E-06	3.46
12/02	12:05:35	512	9.6	39.1	34.1	8.15E-06	
12/02	12:03:25	T41	10.6	35.0	44.0	3.64E-06	2.60
12/02	12:05:35	520	12.9	45.2	56.4	9.45E-06	
K6 Lane				**Average Ratio : 2.7**			
12/02	15:04:52	T2	8.6	37.9	43.7	6.04E-07	1.13
12/02	15:00:25	484	11.3	41.8	55.6	6.82E-07	
12/02	15:14:16	T3	10.7	32.2	38.4	4.66E-07	2.15
12/02	15:09:24	485	10.8	42.4	44.8	1.00E-06	
12/02	15:25:55	T4	9.8	32.4	31.7	2.83E-07	1.97
12/02	15:28:52	486	12.5	41.3	43.7	5.57E-07	
12/02	15:50:23	T5	9.5	32.4	31.7	7.01E-07	3.15
12/02	15:50:13	493	8.7	43.2	42.0	2.21E-06	
12/02	16:09:20	T9	9.8	35.1	39.6	1.35E-06	3.41
12/02	16:03:28	497	9.0	37.7	44.5	4.61E-06	
K7 Lane				**Average Ratio : 2.4**			

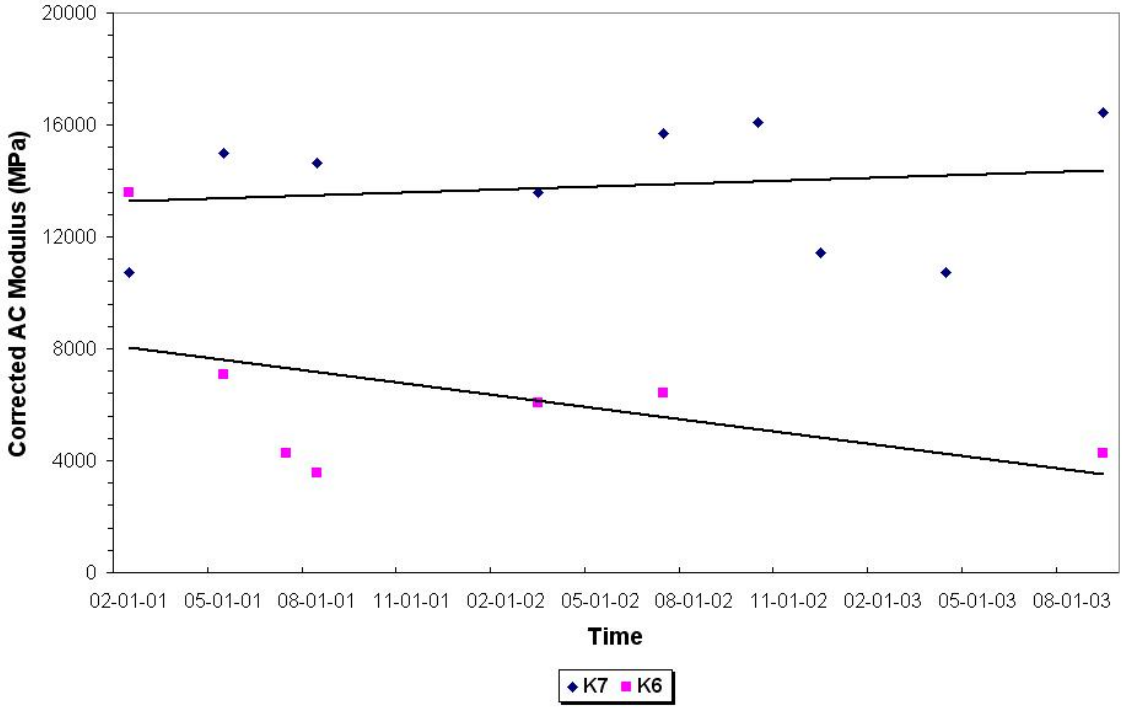

Figure 5.3. Evidence of Damage of Pavement Group 1A of SH4/48 (after Ramos, 2003)

5.3. PAVEMENT PERFORMANCE MEASUREMENT

Prediction of pavement performance from pavement response is the core of the analytical-empirical method of pavement design. Pavement performance may be composed by different measures of the functional condition (ride quality, safety) and structural condition. The test section SH4/48 was divided into several sections based on FWD and GPR test results in order to faciliate a better interpretation of the pavement condition (Ramos ,2003).

They are:

Group 1A : From FM 511 to FM 802

Lane K6 : FWD Stations from K6-1 to K6-8

Lane K7 : FWD Stations from K7-1 to K7-8

Group 1 : From FM 8021 to Coffee Port Rd.

Lane K6 : FWD Stations from K6-9 to K6-15

Lane K7 : FWD Stations from K7-9 to K7-15

Group 2 : From Coffee Port Rd. to Dunlap St.

Lane K6 : FWD Stations from K6-16 to K6-18

Lane K7 : FWD Stations from K7-16 to K7-17

Group 3 : From Dunlap St. to Central Ave.

Lane K6 : FWD Stations from K6-19 to K6-23

Lane K7 : FWD Stations from K7-18 to K7-21

Group 4 : From Central Ave. to Austin Rd.

Lane K6 : FWD Stations from K6-24 to K6-26

Lane K7 : FWD Stations from K7-22 to K7-23

Group 5 : From Austin Rd. to Fruitdale Rd.

Lane K6 : FWD Stations from K6-27 to K6-36

Lane K7 : FWD Stations from K7-24 to K7-33

Group 6 : From Fruitdale Rd. to Boca Chica Blvd.

Lane K6 : FWD Stations from K6-37 to K6-41

Lane K7 : FWD Stations from K7-34 to K7-37

Group 7 : From Boca Chica Blvd. to Cleveland St.

Lane K6 : FWD Stations from K6-42 to K6-56

Lane K7 : FWD Stations from K7-38 to K7-50

To detect the change of pavement condition in service, the rut bar was used to measure rutting, the profiler was used to obtain the roughness index, and visual surveys based on Pavement Management Information System (PMIS) of TxDOT were conducted.

5.3.1. Analysis of Rut Bar Data

Rut depth was measured using an ultra-sonic, 5-sensor rut bar by TxDOT. The rut bar is mounted on the front bumper of the profiler/rut bar van and is used to collect data. This device measures the distance from a reference point on the survey vehicle to the pavement surface at five points across the pavement width. These data are then used to average rut depth using the CALCURUT program. In this study, a kind of sorting program was written to evaluate the variation of rutting station by station. The rut bar data was analyzed with an interval 30.48 m from the beginning point at each FWD station. Rut depth data was taken in the K6 lane until May of 2003, even though the K6 lane was milled beyond the K6-9 station on December of 2002. Consequently, the data beyond that point was not considered. Additionally, since rut depth was measured in the visual survey, the two sets of data were combined and then calibrated to obtain a more reasonable result. The rut depth was plotted against time in Figures 5.4 to 5.11.

Plots show that larger rut depth developed in the K6 lane as compared to the K7 lane. These results support the higher damage ratio with respect to rutting due to OTT truck loads that was obtained in the K6 lane from the previous analysis. The group 1A pavement section shows the most rapid rut depth development in K6 lane.

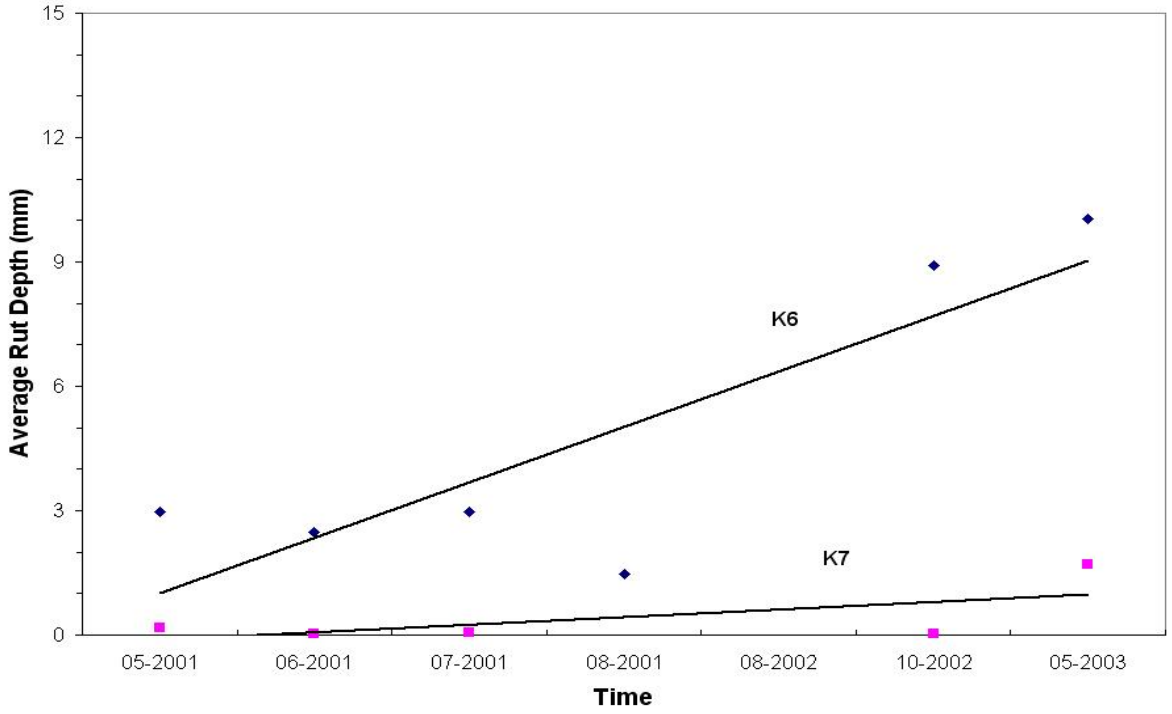

Figure 5.4. Average Rut Depth Variation in Group 1A

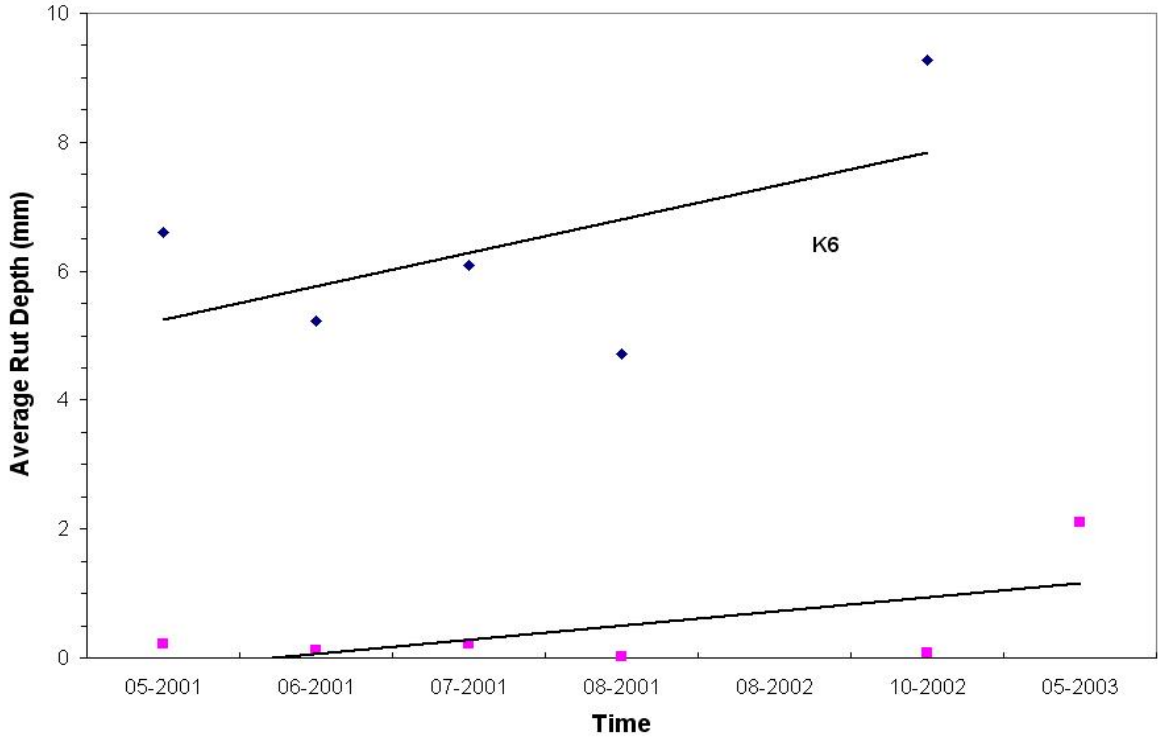

Figure 5.5. Average Rut Depth Variation in Group 1

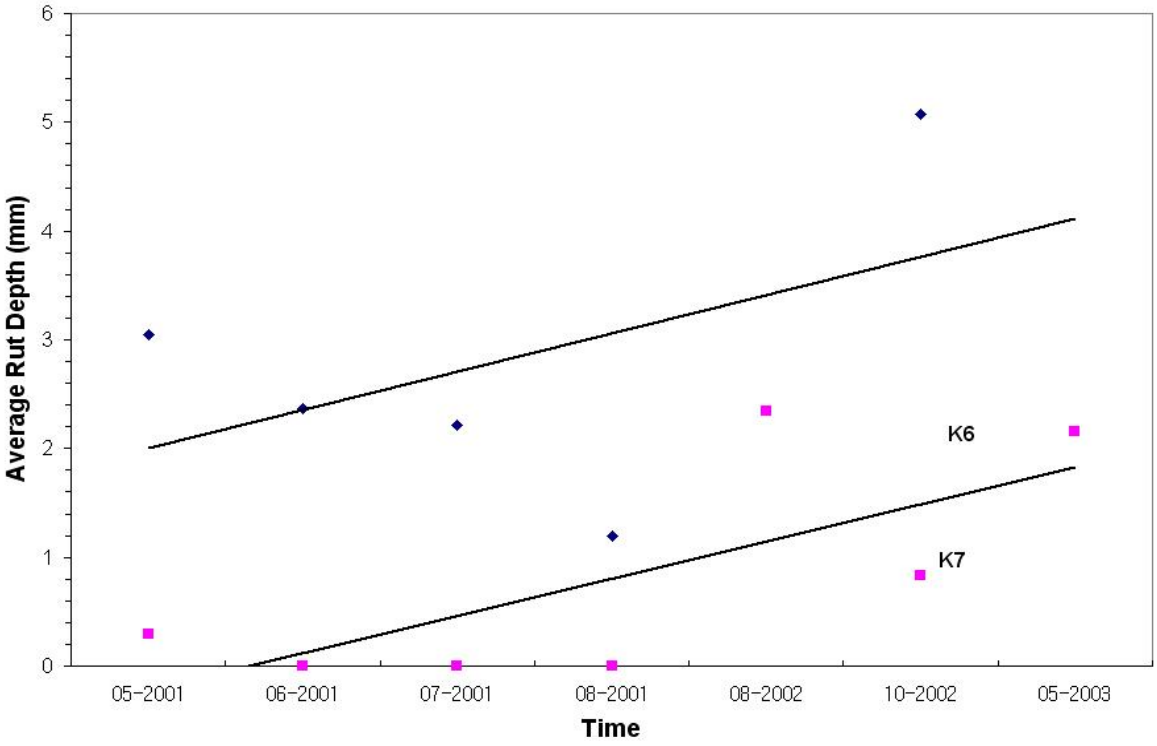

Figure 5.6. Average Rut Depth Variation in Group 2

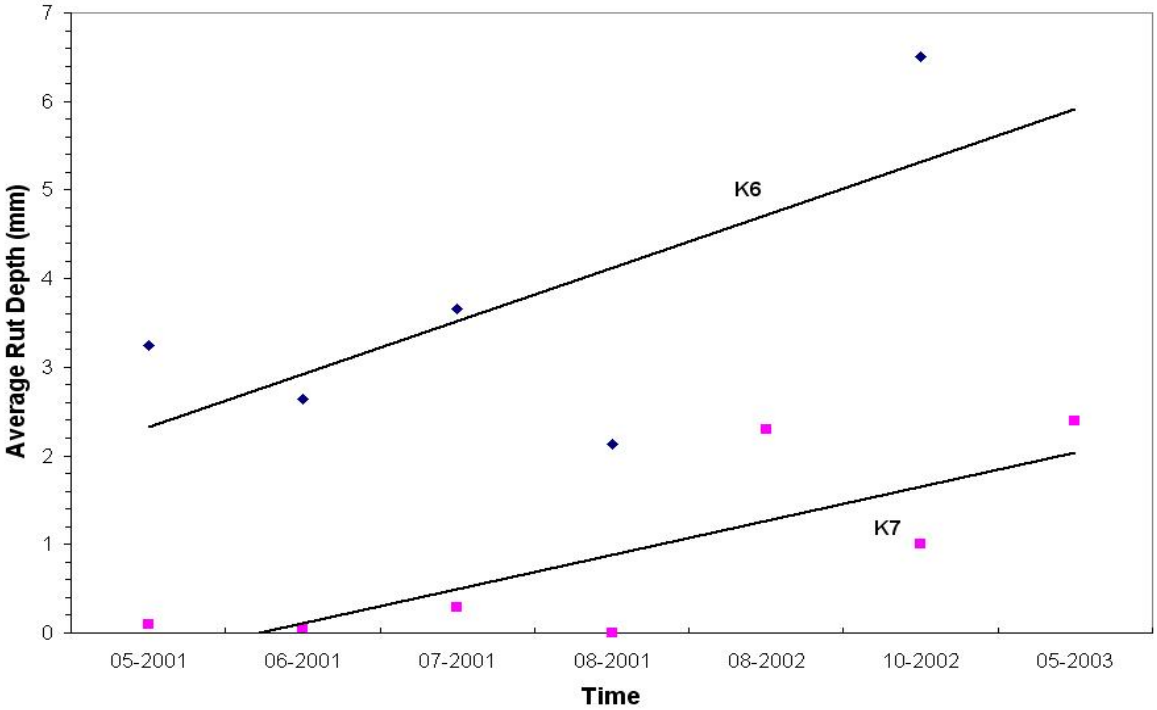

Figure 5.7. Average Rut Depth Variation in Group 3

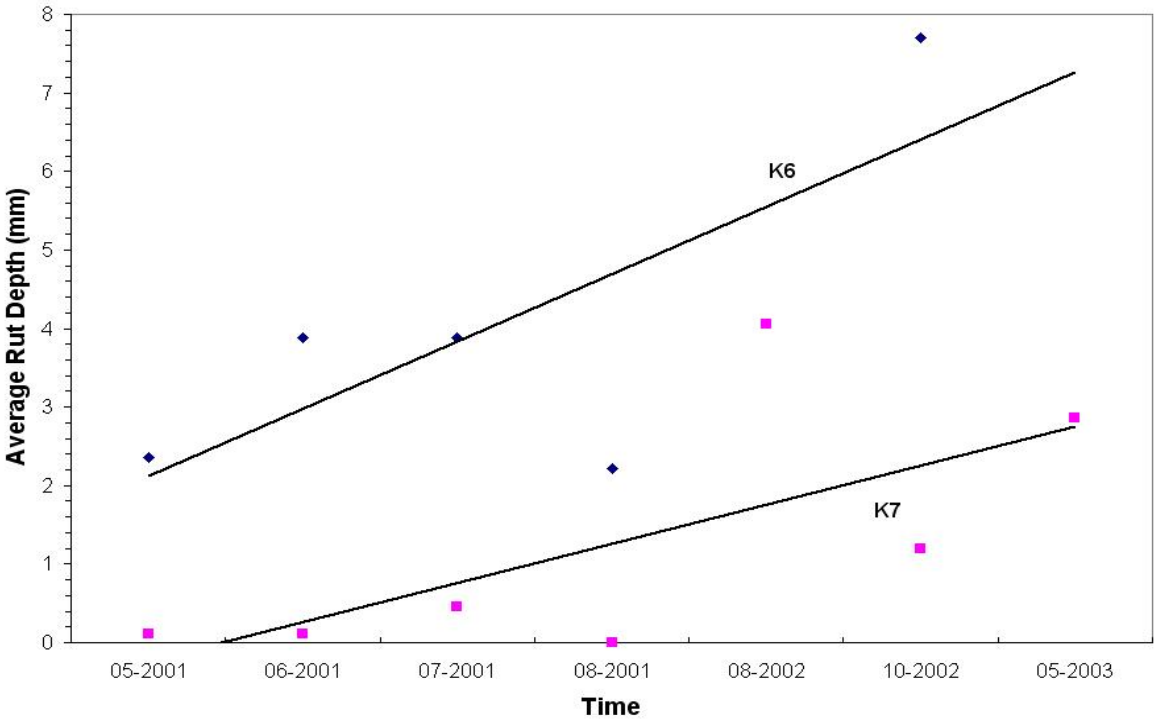

Figure 5.8. Average Rut Depth Variation in Group 4

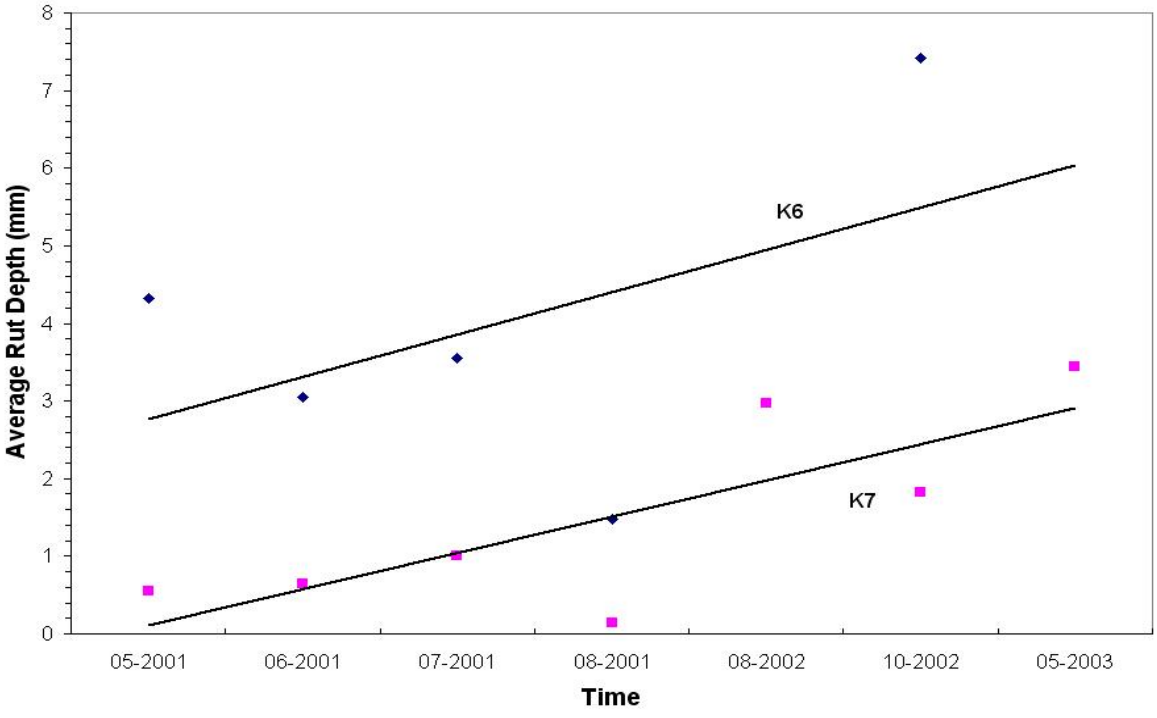

Figure 5.9. Average Rut Depth Variation in Group 5

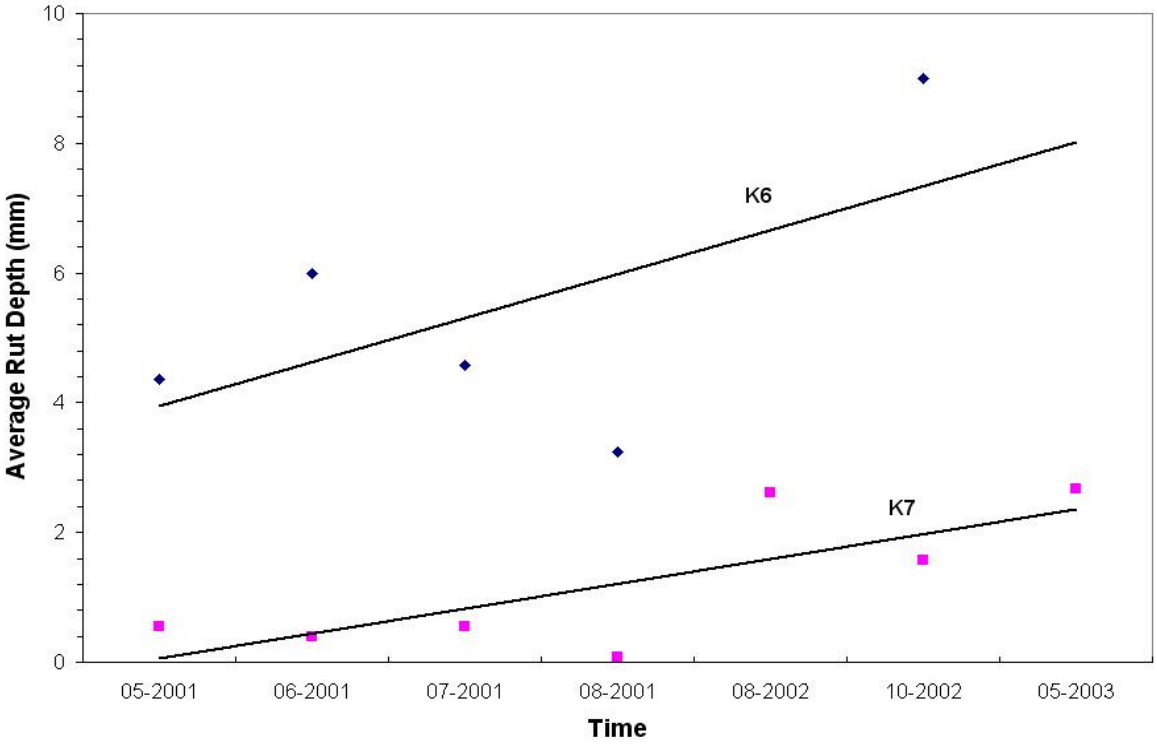

Figure 5.10. Average Rut Depth Variation in Group 6

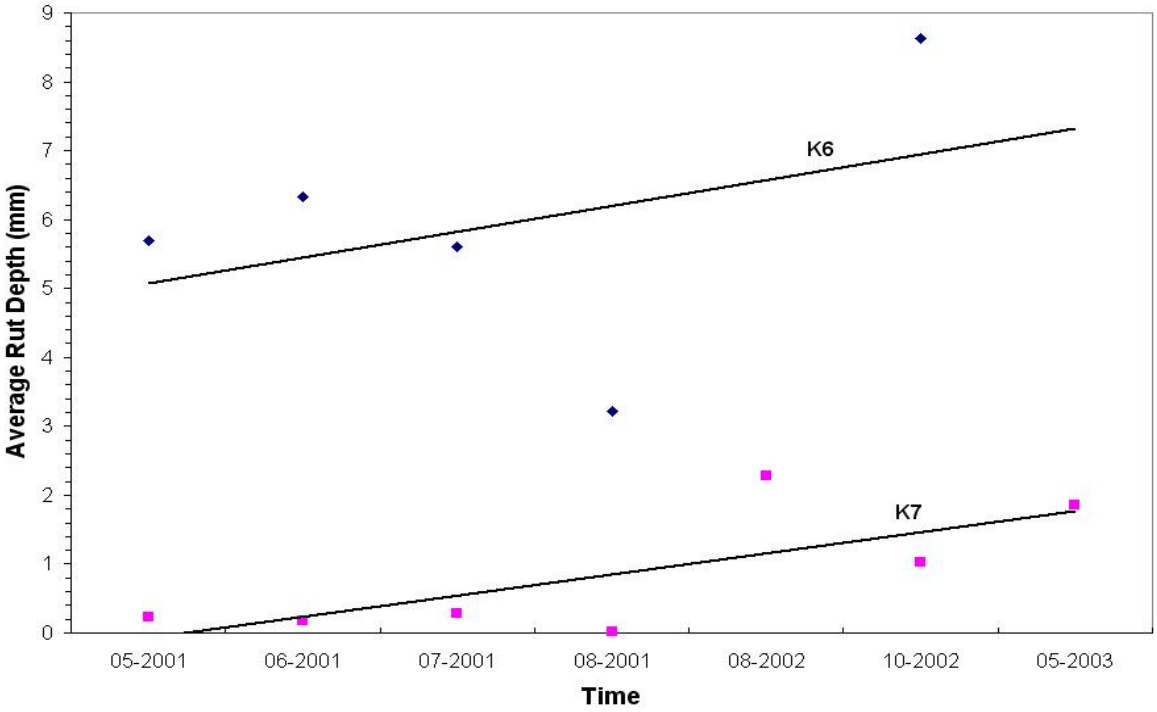

Figure 5.11. Average Rut Depth Variation in Group 7

5.3.2. Analysis of Roughness Data

The International Roughness Index (IRI) is a mathematically defined summary statistic of the longitudinal profile in the wheel-path of a traveled road surface. The index is an average rectified slope statistic computed from the absolute profile elevations. The IRI describes a scale of roughness which is zero for a true planar surface, increasing to about 5.6 (m/km) for moderately rough paved roads, 11.9 (m/km) for extremely rough paved roads with potholing and patching, and up to about 19.8 (m/km) for extremely rough unpaved roads as shown in Figure 5.12. The units of IRI are actually dimensionless, because it is a slope statistic, but it has been scaled by a factor of 1000, so that it represents m/km, mm/m or inches/mile. From the test method Texas-1001-S, the test wheelpath on smooth section shall have an IRI not exceeding 1.2 in/mile while the corresponding wheelpath on the medium-smooth section shall have an IRI within the range of 1.5 to 2.0 m/km.

The IRI and average rut depth was evaluated by using data which had been collected from April of 2001 to May of 2003 on the SH 48 test section. Data was analyzed using 'IRICALC' program to calculate roughness index from both wheel-paths. As processed in the analysis of rut bar data, an average IRI for eight groups of FWD station was evaluated to investigate the variation of ride quality along the tested pavement as shown in Figure 5.13 to 5.20. It was considered that the higher average IRI ranging from 1.3 to 2.5 m/km was obtained in the K6 lane through all sections resulting in lower ride quality. The results appear to be reasonable because the higher rut depth was measured in the K6 lane in the previous work. Based on the IRI scale depicted in Figure 5.12, the pavement condition exhibits an intermediate stage between new pavement and older pavement.

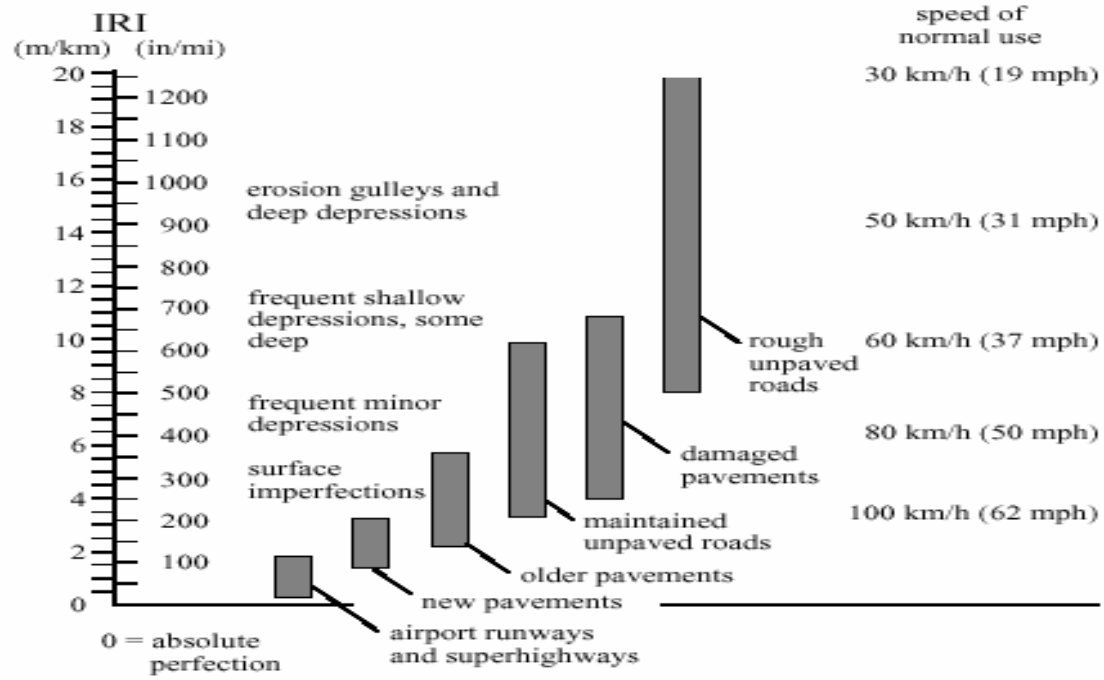

Figure 5.12 The International Roughness Index (IRI) Scale of Road Roughness (After Sayers et al., 1986)

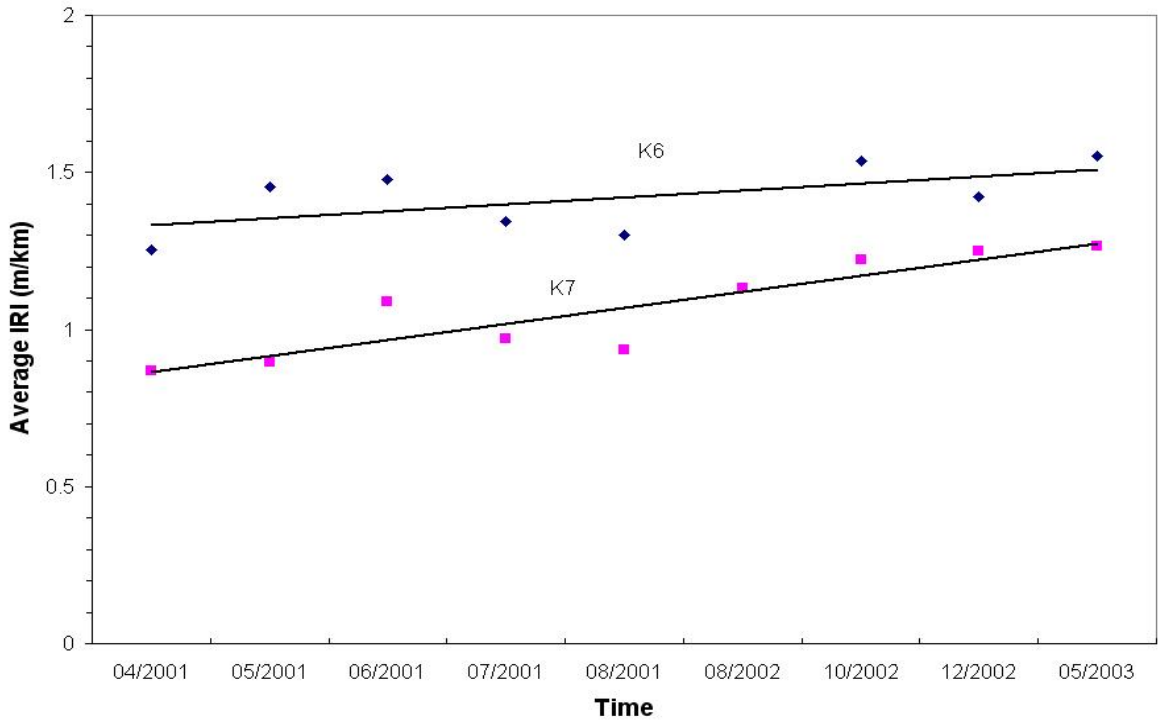

Figure 5.13. Average IRI Variation in Group 1A

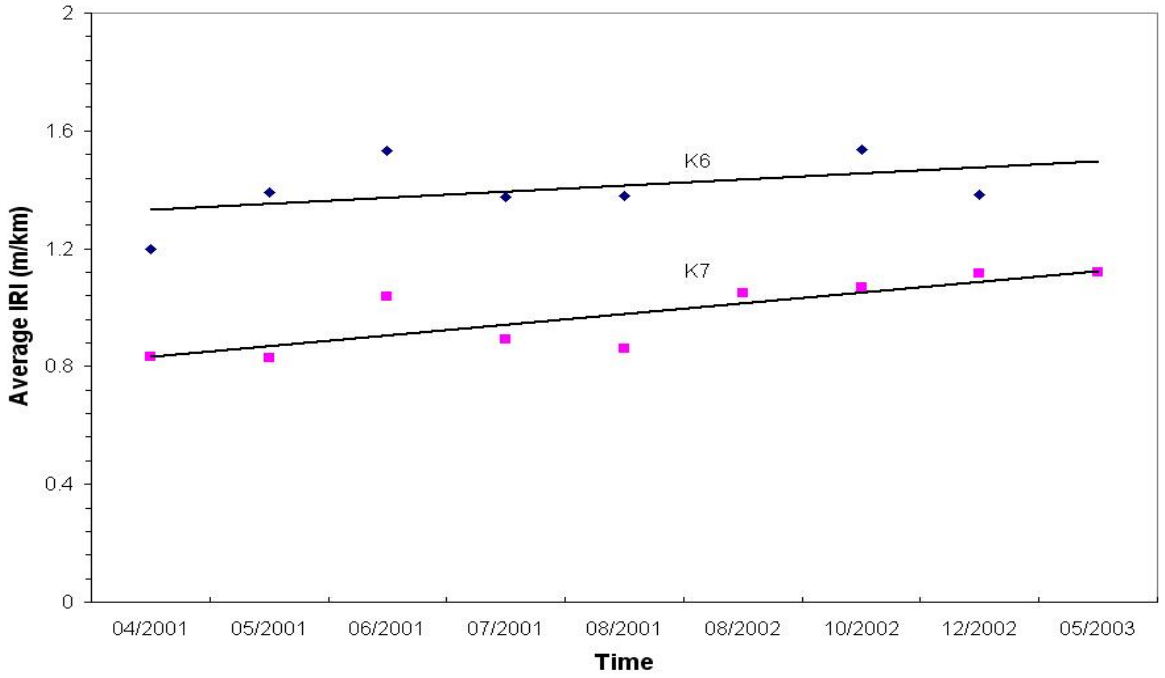

Figure 5.14. Average IRI Variation in Group 1

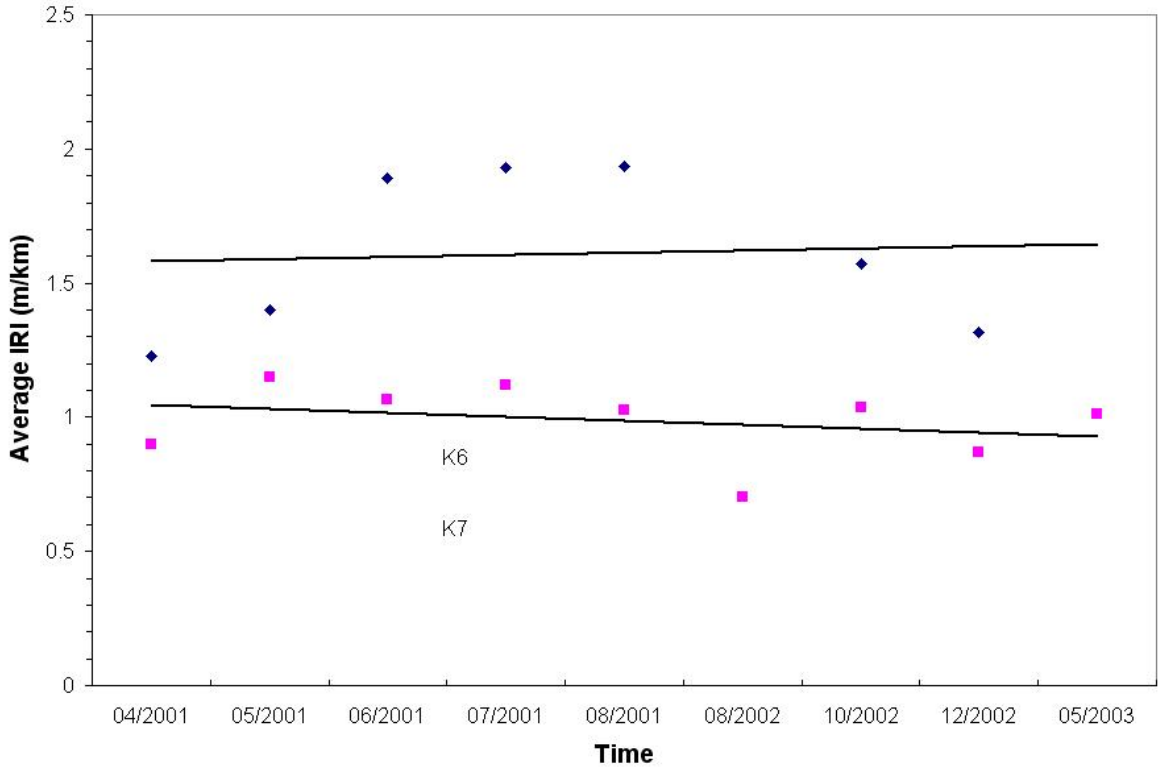

Figure 5.15. Average IRI Variation in Group 2

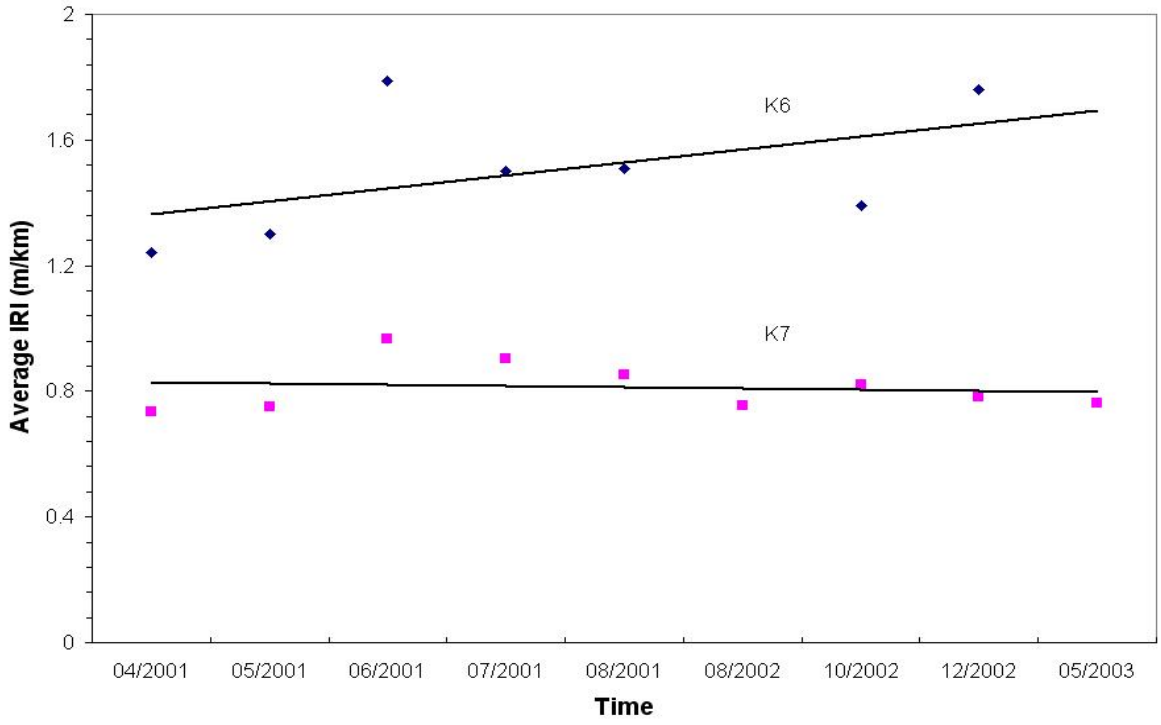

Figure 5.16. Average IRI Variation in Group 3

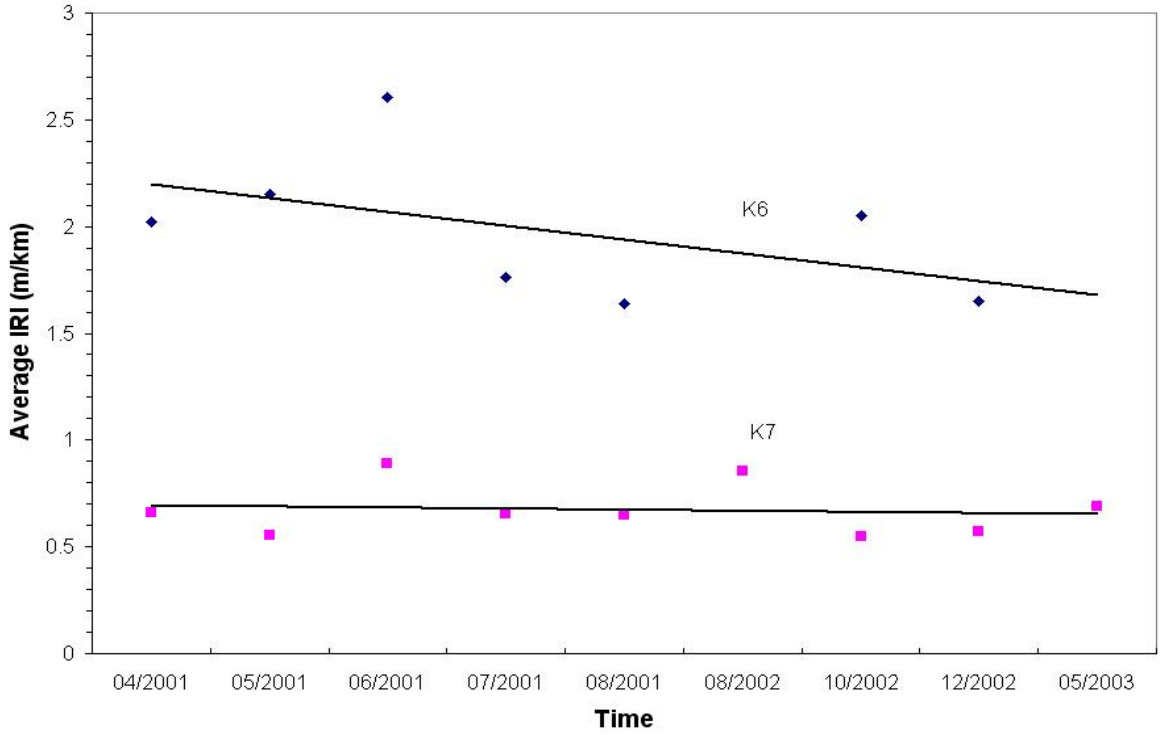

Figure 5.17. Average IRI Variation in Group 4

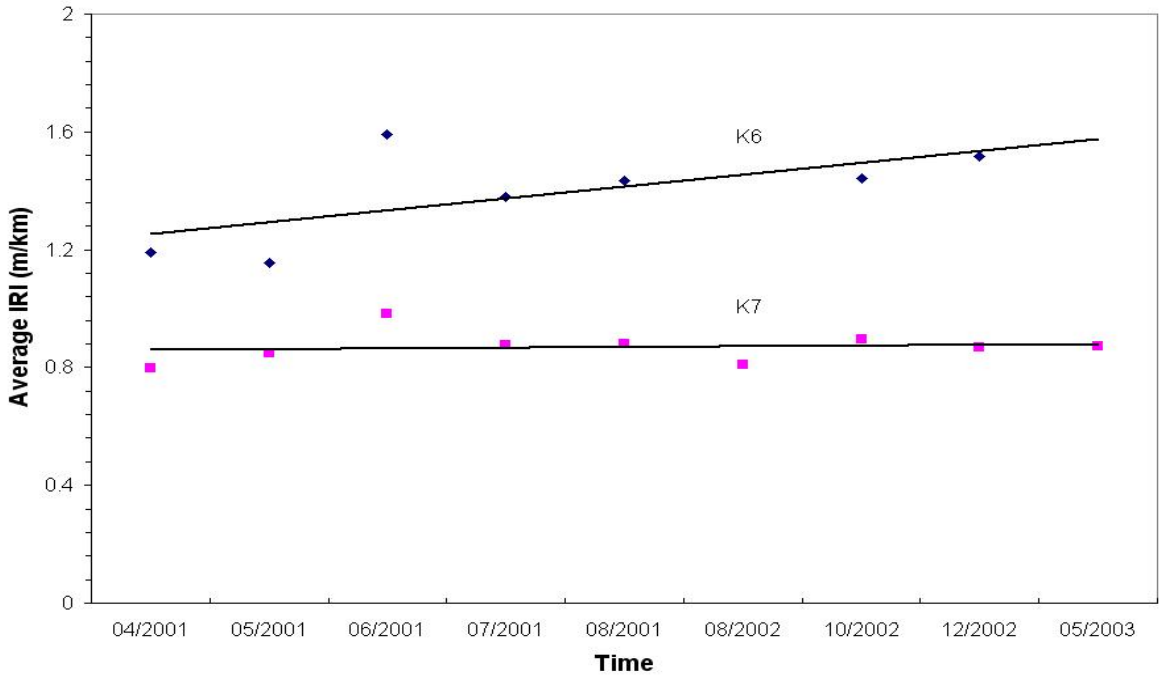

Figure 5.18. Average IRI Variation in Group 5

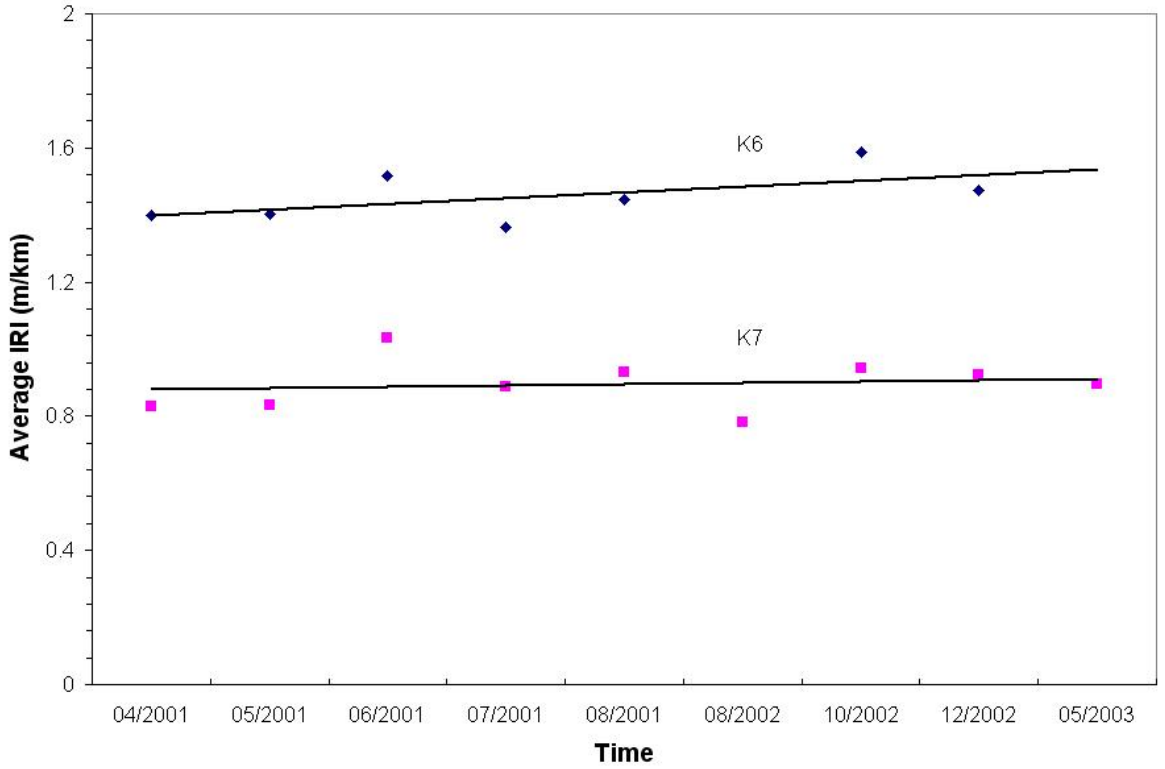

Figure 5.19. Average IRI Variation in Group 6

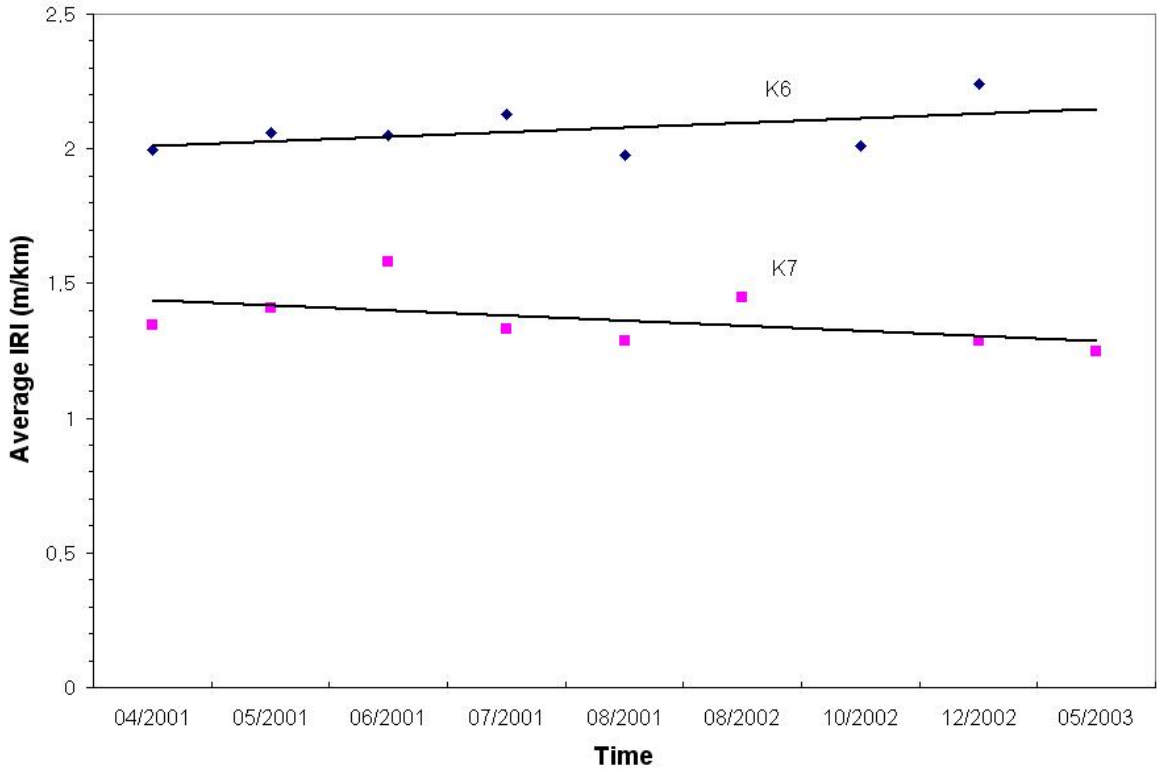

Figure 5.20. Average IRI Variation in Group 7

5.3.3. Analysis of Cracking Data

The extent of cracking due to repeated traffic loads on SH4/48 was examined by visual survey during the project. The types of cracking considered were alligator cracking, longitudinal cracking, and transverse cracking. The rating value of alligator cracking measures the percentage of the rated lane's total wheelpath area that is covered by this distress. Longitudinal cracking consists of cracks or breaks which run approximately parallel to the pavement centerline. This is measured in terms of linear feet per station (i.e. average feet of cracking in each 100 ft of surface). Transverse cracking consists of cracks or breaks which travel at right angles to the pavement centerline. It is measured in terms of number per station (i.e. average number of cracks in each 100 ft of surface). This study focused on the longitudinal cracking since it was the most pronounced in test pavement. Thus, plots representing the variation of longitudinal crack type

and pavement score which is estimated combining visual survey data based on the PMIS method are presented in appendix C. As expected, longitudinal cracks were predominant within the K6 lane. It was interesting to detect that the magnitude of longitudinal cracking in the K7 lane in group 7 was slightly larger than that of other groups which covers the downtown area from Boca Chica Blvd. to Cleveland St. It is compatible with a relatively lower backcalculated AC modulus in this section. When it comes to the pavement score, most of the K7 lane show an apparent sound condition indicated by a 100 score while the quality of the K6 pavement falls gradually.

5.4. PERFORMANCE PREDICTION OF NCPA

The developed program NCPA contains a tool that can evaluate pavement performance with respect to most of the common distresses in flexible pavement while accounting for seasonal variations. This task was completed by integrating the procedure to estimate performance used in FLEXPASS (Tseng, 1988) into NCPA. If the pavement has no standard thickness and materials, the evaluation of rutting based on the subgrade strain does not appear to be reasonable as adopted in AI equation. Alternatively, summing up the permanent deformation in each layer and sum up to determine the rut depth can be more reasonable because the rutting is caused by the accumulation of permanent deformation over all layers. In the developed program, the layer strain approach was used to calculate overall rutting by taking into account the permanent deformation property. The deformations, like stress and strain, are evaluated by an increment of loading and an iterative solution for each load increment. Three components of stress and strain are calculated at nine points in every element. For the calculation of rut depth, vertical strains at the center of each element equal to the fifth Gaussian point are summed up by multiplying the layer thickness by the plastic strain determined from the permanent deformation

properties for each layer. The two sets of permanent deformation properties considered were the VESYS and 3-parameter models. The following equations explain how to calculate rut depth with the two different models:

VESYS Model

$$\delta_a(N) = \sum_{i=1}^{n} \left[\frac{\mu_i N^{1-\alpha_I}}{1-\alpha_i} \int_{d_{i-1}}^{d} \varepsilon_c(Z)dz \right] \tag{5.4}$$

3-Parameters Model

$$\delta_a(N) = \sum_{i=1}^{n} \left[\int_{0}^{N} \frac{\varepsilon_{0_I}}{\varepsilon_{r_i}} e^{-(\rho_i/N)^{\beta_I}} dN \int_{d_{i-1}}^{d} \varepsilon_c(Z)dz \right] \tag{5.5}$$

The permanent deformation properties can be input not only for each layer but also by different seasons. In addition, the traffic data based on the average equivalent single axle load (ESAL) during each season of the year within a given traffic period are required to evaluate rut depth during the service life.

Fatigue cracking, which is caused by fatigue damage, is the principal structural distress that occurs in asphalt pavements with base and subgrade. Factors which affect the development of fatigue cracking, are the number and magnitude of applied loads, pavement structure, the quality of foundation support, the consistency of the asphalt concrete, the asphalt content, the air voids and aggregate characteristics of the asphalt concrete mixture. The evaluation of fatigue cracking is based on fracture mechanics for both crack initiation and propagation. In this program, Lytton's model considering the stress intensity factor and crack geometry is used as follows:

$$N_f = \frac{d^{1-\frac{n}{2}}\left[1-\left(\frac{c_0}{d}\right)^{1-nq}\right]}{A(1-nq)(Er)^n}\left(\frac{1}{\varepsilon}\right)^n \quad (5.6)$$

where,

c_0 = initial crack length

d = depth of beam (i.e. Asphalt layer thickness)

q = 1.1798 (regression constant)

r = regression constant

A,n = Paris law fracture coefficient

E = Asphalt modulus

ε = tensile strain at the bottom of asphalt layer

From the above equation, phenomenological regression constants K_1 and K_2 are determined. It is reported that the fatigue damage property K_1 is dependent on the asphalt mixture and pavement properties such as the parameters of the Paris crack growth law, elastic stiffness, and thickness of the asphalt concrete layer, and that the fatigue damage property K_2 varies with the initial asphalt cement properties such as asphalt content, viscosity, penetration, and temperature (Tseng and Lytton, 1990).

$$K_1 = \frac{d^{1-\frac{n}{2}}\left[1-\left(\frac{c_0}{d}\right)^{1-nq}\right]}{A(1-nq)(Er)^n} \quad (5.7)$$

$$K_2 = n \quad (5.8)$$

where,

A = $7.0889 - 2.4755K_2 - 2.1163 \text{ Log } E_r$

Schapery (1973) derived a theoretical equation of crack growth to calculate A and n values. To verify Schapery's equation, experimental studies on asphaltic concrete mixes were performed by German and Lytton (1979) and the value of n is evaluated by the following relationship which is derived from theory:

$$n = \frac{2}{m} \tag{5.9}$$

where m is the slope of the tensile creep compliance curve obtained from laboratory creep tests.

In general, the fatigue life of pavement determined from laboratory tests underestimates field fatigue life. Tseng and Lytton (1990) pointed out that relaxation behavior between traffic applications of pavement and residual stresses at the bottom of the surface layer can cause much less fatigue damage compared to that of a laboratory test. In order to reduce this discrepancy, Lytton (1983) presented an analytical technique leading to a shift factor between laboratory and field fatigue life as shown in Figure 5.21. The shift factor consists of two components and given by :

$$SF = (SF_r)\ (SF_h) \tag{5.10}$$

Where

SF_r = Shift factor due to residual stresses.

SF_h = Shift factor due to healing during rest periods.

During a rest period, the residual stress is produced after the passage of traffic loading. With time, the effective residual strain is equal to residual stress divided by the initial elastic modulus, E_0. Therefore, the actual tensile strain at the bottom of the asphaltic concrete is given by :

$$\varepsilon_t - \varepsilon_r = \varepsilon_t(1 \pm p_0 t^{-m}) \quad (5.11)$$

where

p_o = the percent of total strain remaining in the pavement as residual strain immediately after the passage of the load,

m = the exponential relaxation rate.

From the geometry of the plot in Figure 5.21, the shift factor due to residual stress can be estimated by:

$$SF_r = \frac{N_{fc}}{N_{fa}} = \left(\frac{1}{1 \pm p_0 t^{-m}} \right)^{K_{2l}} \quad (5.12)$$

In here, N_{fa} is the number of cycles to failure for the total tensile strain and N_{fc} is the number of load cycles to failure for the tensile strain altered by the residual stress, and K_{2l} is the value of K_2 determined from the laboratory.

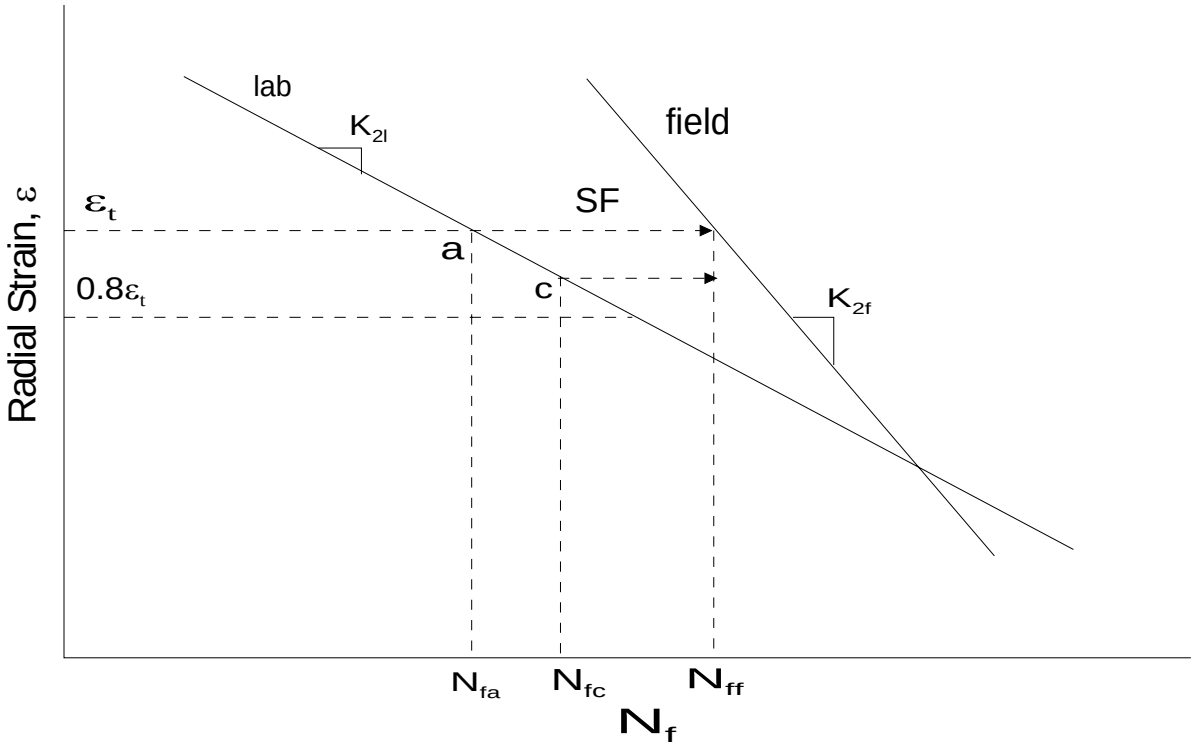

Figure 5.21. Schematic Illustration of Shift Factor (after Balbissi, 1983)

The development of the shift factor due to the healing effect used the data from the overlay tester. Balbissi (1983) reported that two empirical relations can be derived from the results of the overlay tester tests to evaluate the shift factor for Sulflex due to the effect of the rest period as follows.

$$\frac{\Delta u_i}{\Delta u_0} = \left(\frac{t_i}{t_0}\right)^h \tag{5.13}$$

and

$$\frac{N_i - N_0}{n_r} = \frac{\Delta N_i}{n_r} = m_0\left(\frac{\Delta u_i}{\Delta u_0}\right) \tag{5.14}$$

where

t_i = the time length of a load pulse with rest periods,

t_0 = the time length of a load pulse without rest periods,

N_f = number of cycles to failure with rest period, ti,

N_0 = number of cycles to failure without rest period,

N_i = number of rest periods of length, ti,

Δu_i = change of fracture energy with rest period, ti,

Δu_0 = change of fracture energy without rest period, and

m_0 and h = regression constants.

Thus, the shift factor due to healing can be expressed by combining equations (5.13) and (5.14):

$$SF_h = \frac{N_f}{N_0} = 1 + \frac{n_r m_0}{N_0}\left(\frac{t_i}{t_0}\right)^h \qquad (5.15)$$

Finally, fatigue cracking is indicated by the cracked area which developed based on a probabilistic approach using the following equation (Tseng, 1988).

$$\bar{c} = 1000 * [(1 - F(1)] \qquad (5.16)$$

where $\bar{c}$ is the expected cracked area (ft^2 / 1000 ft^2).

The probability F(1) that the variable D_j (damage index) reaches the value of one is computed.

5.4.1. Verification of Performance Prediction of NCPA

For this purpose, available permanent deformation data obtained from laboratory test results are used in the verification effort. Verification was carried out by running FLEXPASS to compare overall rutting. To simplify the geometric condition, a three layer pavement matrix

combination of 101.6 mm. (4 in.) thick hot mix asphalt layers on 304.8 mm (12 in.) thick base course resting on subgrade with thickness of 2540 mm (100 in) were used. Three layers were treated by linear isotropy because FLEXPASS cannot handle the anisotropy condition. Although layers can be modeled under nonlinear conditions through FLEXPASS based on the K-θ model, since a slight error would be expected according to its difference, decision was made to select the linear condition. A single wheel load of 30 kN with radii of 127 mm. was imposed on the surface assuming uniformly distributed circular tire pressure areas. One season with design life of 20 years and average daily traffic rate based on 18-kip Equivalent Single Axle Load (ESAL) equal to 90 were assumed in the analysis.

The permanent deformation property of asphalt concrete materials was obtained by Ramos (2003). Based on the data, the permanent deformation property that was used is tabulated in Table 5.5. Figure 5.22 and 5.23 illustrate the rut development evaluated from two programs.

Table 5.5. Permanent Deformation Property Used in Analysis

	3 Parameter model			VESYS model	
	$\varepsilon_0/\varepsilon_r$	ρ	β	μ	α
AC	3879	5.6 E+11	0.072	0.6	0.65
Base	26.62	269.34	0.2	0.36	0.79
Subgrade	9.10	577.75	0.21	0.11	0.75

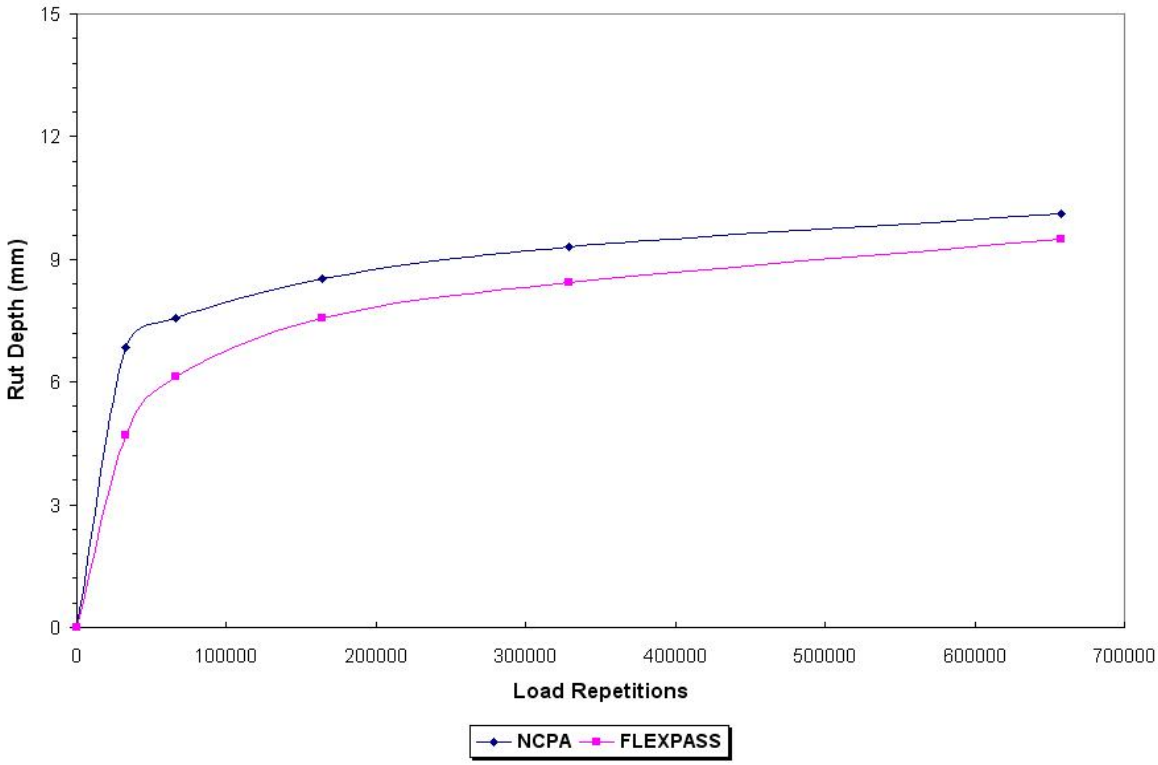

Figure 5.22. Comparison of Rut Depth Using 3 Parameter Model

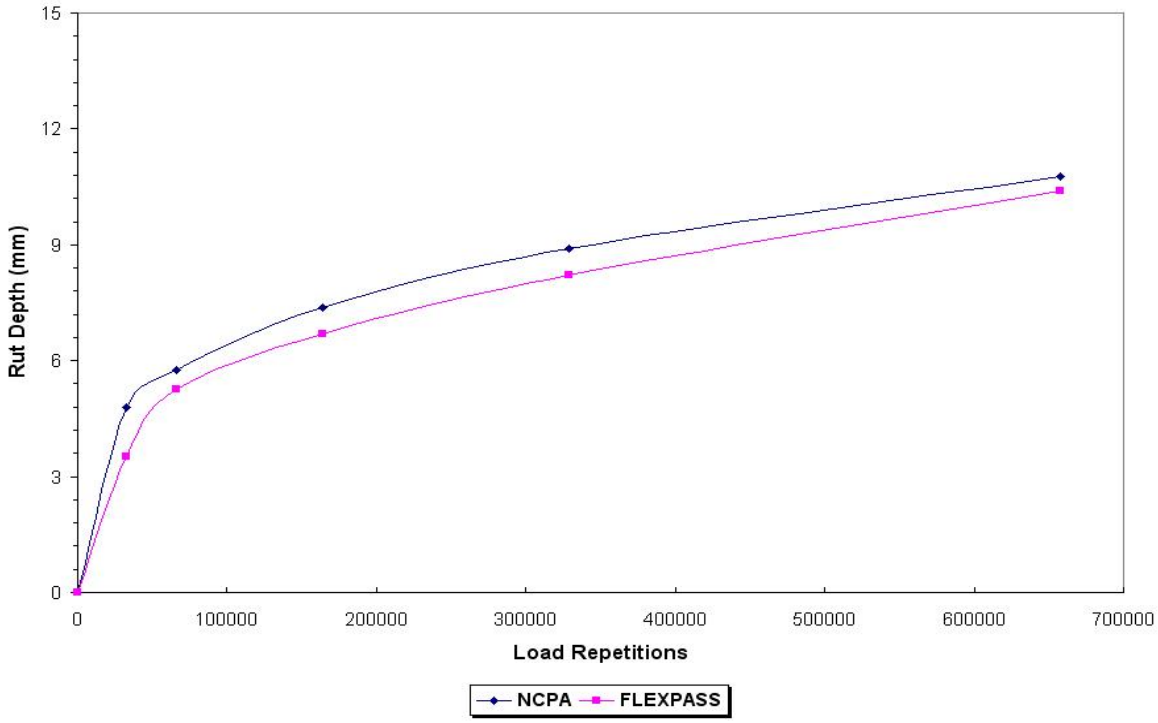

Figure 5.23. Comparison of Rut Depth Using VESYS Model

It is observed that rutting curves generated by the two programs fit well with each other. Overall, NCPA predicts a slightly higher rutting. The difference may be caused by element type because NCPA uses 8-node quadratic serendipity element while a 4-node rectangular element is used in FLEXPASS. The same finite element mesh was used in both analyses. A general conclusion has been made that the higher order element gives more accurate results if the convergence of the solution is satisfied (Roesset, 2002). When the curve shape is considered, the Three Parameters model is fits better than the VESYS model because it follows a typical trend of accumulated permanent deformation curve that ruts develop rapidly at the initial stage and reach an equilibrium stage due to the decrease of permanent deformation development rate.

When it comes to fatigue cracking, the data obtained from the creep compliance test as part of this study performed by Ramos (2003) was used to verify the capability of estimating fatigue crack in NCPA. Three parameters are obtained from a creep compliance test as given in equation (5.17).

$$D(t) = D_0 + D_1 t^m \qquad (5.17)$$

where

$D(t)$ = creep compliance at loading time t,

$D_0, D_1 \text{ and } m$ = coefficients of the power law model

The slope m of the log creep compliance verse log time curve is directly associated with the material damping as characterized by the phase angle (Ramos, 2003). One set of this data is presented in Table 5.6. To examine the fatigue cracking procedure in NCPA, the same structure and loading condition used in rutting calculations was adopted and input data relevant to crack

propagation and shift factors was assumed on the basis of laboratory test results mentioned in the paper (Tseng and Lytton, 1990). The value of m at 100 °F was used as input. Figure 5.24 illustrates the result.

Table 5.6. Creep Compliance Parameters of the K6-4 FWD Station (after Ramos, 2003)

No	Temp. (°F)	ID	D_0	D_1	m	SSE
1	70	C1	4.11E-05	3.47E-04	4.64E-01	2.22E-01
2	85	C2	4.89E-05	4.91E-04	4.90E-01	1.52E-01
3	100	C2	1.12E-04	1.66E-03	5.31E-01	5.61E-01
4	110	C4	3.06E-04	1.24E-03	5.62E-01	1.55E+00
5	130	C3	1.27E-04	2.72E-03	3.49E-01	7.72E-01

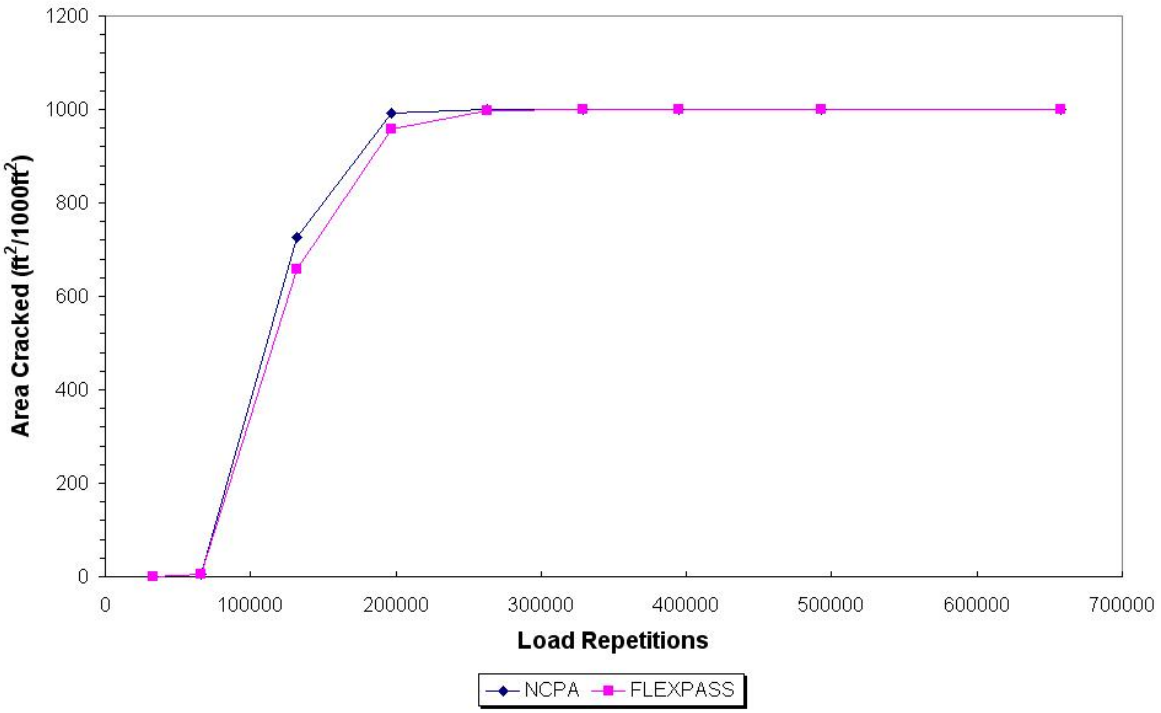

Figure 5.24. Comparison of Fatigue Cracking

It was found that two programs calculated compatible fatigue cracking with given input data in spite of a slight gap between values due to a larger tensile strain at the bottom of AC layer in NCPA. Since the prediction of fatigue cracking significantly depends on the value of m and several coefficients associated with the shift factor, careful determination of those coefficients should be made to obtain accurate results.

5.4.2. Comparison of Performance with NCPA and Filed Measurement

In this section, the algorithm developed is verified against field data. As noted previously, rutting and different types of cracking were measured during this study permitting a comparison of the field measurements with the predictions of NCPA. For the purpose of this, firstly, realistic traffic data based on ESAL needs to be prepared to enhance the accuracy of analysis. Ramos (2003) estimated ESAL to find evidence that pavements are damaged by an increasing number of load repetitions. To obtain ESALs in each lane, current traffic data and the historical Average Daily Traffic (ADT) from TxDOT traffic record were used. Equation (5.18) was used to compute the total number of 18-kip ESAL's for each year before Fiscal Year 2003.

$$\text{Total 18-kip ESAL}_n = (\text{Total 18-kip ESAL}_O) \times \left(\frac{(1+g)^n - 1}{g} \right) \qquad (5.18)$$

where

g : Growth rate = $\left(\frac{ADT_n}{ADT_o} \right)^{\frac{1}{n}} - 1$;

ADT_0 : Average daily traffic at the start of the design period;

ADT_n : Average daily traffic at the end of the design period;

n : Number of the years of the design period;

Total 18-kip $ESAL_n$: The total number of 18-kip ESALs up to the year of n;

Total 18-kip $ESAL_0$: The total number of 18-kip ESALs at the year of o;

The Table 5.7 shows the cumulative number of 18-kip ESALs by year, from 1993 up to 2003. The year 1993 was chosen since repaving of SH4/48 sections was performed during that year. The ESALs were estimated by the pavement groups described in 5.3. The traffic for group 2 to group 5 was combined because the ADT was identical for all of these groups. To compare rutting measurements with predictions of NCPA, it is necessary to estimate the ESALs differences between May of 2001 and May of 2003 for each group and lane respectively. The assumption was made that the extent of damage due to rutting at initial point i.e. May of 2001 is same for both field measurement and predictions to take into account the previous damage developed from 1993. The ESALs presented in Table 5.8 include the calculated ESALs from May of 2001 to May of 2003. Rut depths measured in field were matched corresponding to the estimated ESAL instead of the date of measurement so as to compare directly with the prediction.

Table 5.7. Cumulative 80 kN ESAL by Year and by Pavement Groups (after Ramos, 2003)

	Pavement Groups			
Year	1-1A	2-5	6	7
1993	2.3E+05	2.6E+05	2.6E+05	2.9E+05
1994	2.3E+05	2.6E+05	2.6E+05	2.9E+05
1995	4.8E+05	5.3E+05	5.2E+05	5.9E+05
1996	7.3E+05	8.0E+05	7.9E+05	8.9E+05
1997	9.8E+05	1.1E+06	1.1E+06	1.2E+06
1998	1.2E+06	1.4E+06	1.3E+06	1.5E+06
1999	1.5E+06	1.7E+06	1.6E+06	1.8E+06
2000	1.8E+06	1.9E+06	1.9E+06	2.1E+06
2001	2.1E+06	2.2E+06	2.2E+06	2.4E+06
2002	2.4E+06	2.5E+06	2.5E+06	2.7E+06
2003	2.7E+06	2.9E+06	2.8E+06	3.0E+06

Table 5.8. Cumulative 80 kN ESAL by Lanes and by Pavement Groups (after Ramos, 2003)

		Cumulative 80 kN ESALs				
Lane	Date	1A	1	2 to 5	6	7
K7	Feb 01	5.0E+05	5.0E+05	5.4E+05	5.3E+05	5.8E+05
	May 01	5.2E+05	5.2E+05	5.6E+05	5.5E+05	6.0E+05
	Aug 01	5.4E+05	5.4E+05	5.8E+05	5.7E+05	6.2E+05
	Mar 02	5.8E+05	5.8E+05	6.3E+05	6.2E+05	6.7E+05
	Jul 02	6.1E+05	6.1E+05	6.5E+05	6.5E+05	7.0E+05
	Oct 02	6.3E+05	6.3E+05	6.7E+05	6.7E+05	7.2E+05
	Dec 02	6.4E+05	6.4E+05	6.9E+05	6.8E+05	7.4E+05
	Apr 03	6.7E+05	6.7E+05	7.2E+05	7.1E+05	7.6E+05
	May 03	6.8E+05	6.8E+05	7.2E+05	7.2E+05	7.7E+05
K6	Feb 01	1.3E+06	1.3E+06	1.5E+06	1.4E+06	1.6E+06
	May 01	1.4E+06	1.4E+06	1.5E+06	1.5E+06	1.6E+06
	Jul 01	1.4E+06	1.4E+06	1.5E+06	1.5E+06	1.7E+06
	Aug 01	1.5E+06	1.5E+06	1.6E+06	1.5E+06	1.7E+06
	Mar 02	1.6E+06	1.6E+06	1.7E+06	1.7E+06	1.8E+06
	Jul 02	1.7E+06	1.7E+06	1.8E+06	1.7E+06	1.9E+06
	May 03	1.8E+06	1.8E+06	2.0E+06	1.9E+06	2.1E+06

Based on the results of analysis of weather station data presented in Chapter II, three seasons were considered. The comparison was focused on two stations i.e., K6-4 and K7-3 because base and subgrade samples were taken at these locations and it seems to be unreasonable if identical permanent deformation properties are assumed through all stations. Rutting was predicted using the 3-Parameter model. Used parameters for different seasons are tabulated in Table 5.9. The results are illustrated from Figure 5.25 to 5.26. Different models were used to match field measurement. Base and subgrade materials are modeled with the nonlinear isotropy condition denoted by NI and nonlinear anisotropy condition for NA. Lytton (2000) suggested that the asphalt concrete material needs to be modeled considering anisotropy due to voids which are produced by the shape of the aggregates and viscous characteristics. The extent of anisotropy in the asphalt concrete material was investigated using the relationship between static and dynamic backcalulated modulus (Ramos 2003). The extent of anisotropy in the asphalt concrete material is represented using the value of c in given equation (5.19).

$$E_{horizontal} = \frac{E_{vertical}}{c} \tag{5.19}$$

Backcalculated AC modulus from dynamic analysis using DBSID program (Fernando and Liu, 1999) is an isotropic modulus composed of two directional components of modulus:

$$E_{DBSID} = \sqrt{E_{vertical} \times E_{horizontal}} \tag{5.20}$$

The backcalculated AC static modulus from using the program MODULUS is compared with the dynamic (complex) modulus (E*) obtained from a laboratory test. The following expression can be applied between two values:

$$|E^*| = (1+a)E_{static} \tag{5.21}$$

In addition, the linear relationship between the backcalculated AC modulus obtained from the DBSID program and those obtained from the MODULUS program can be given by:

$$E_{static} = (1+b)E_{DBSID} \tag{5.22}$$

By combining above equations, c is expressed using the equation below.

$$c = (1+a)^2 \times (1+b)^2 \tag{5.23}$$

It was observed that the value of c was determined as 1.26 on the basis of backcalculated AC modulus obtained from both K6 and K7 lanes in SH4/48 (Ramos, 2003). Therefore the case where AC is modeled by the anisotropy condition using a value of n equal to 0.8 is included in the NCPA analysis. As shown in Fgures 5.25 and 5.26, larger rut depths were produced when layers are modeled using the anisotropy condition and the prediction based on that modeling

matched field measurement well. In the sensitivity analysis in Chapter IV, the reduced horizontal modulus due to the anisotropy characteristic leads to larger deformation in the vertical direction and results in a more critical performance prediction compared to that predicted using the isotropy condition. It is worth mentioning that modeling of AC accounting for directional modulus is promising because it predicts larger deformation and reasonable rut depth even though sometimes it slightly overestimates rutting due to the larger vertical strain within AC layer. In addition, perhaps rut bar misses the upward shoving at the edge of the rut which is common with anisotropic mixes. Therefore, the prediction under the anisotropic condition is larger than the actual measurements because of consideration of upward shoving (Lytton, 2004).

Table 5.9. Permanent Deformation Property of Materials Based on 3-Parameter Model

Layer	Parameter	Season 1 (37.8 °C)	Season 2 (23.9 °C)	Season 3 (32.2 °C)
AC	$\varepsilon_0 / \varepsilon_r$	3.879E+03	8.800E+02	1.079E+03
	ρ	5.693E+11	5.693E+11	5.693E+11
	β	0.072	0.072	0.072
Flexible Base	$\varepsilon_0 / \varepsilon_r$	1.622E+01	1.622E+01	1.622E+01
	ρ	2.693E+03	2.693E+03	2.693E+03
	β	0.200	0.200	0.200
Lime Treated Base	$\varepsilon_0 / \varepsilon_r$	3.320E+00	3.320E+00	3.320E+00
	ρ	8.527E+01	8.527E+01	8.527E+01
	β	0.190	0.190	0.190
Subgrade	$\varepsilon_0 / \varepsilon_r$	0.910E+01	0.910E+01	0.910E+01
	ρ	5.778E+01	5.778E+01	5.778E+01
	β	0.210	0.210	0.210

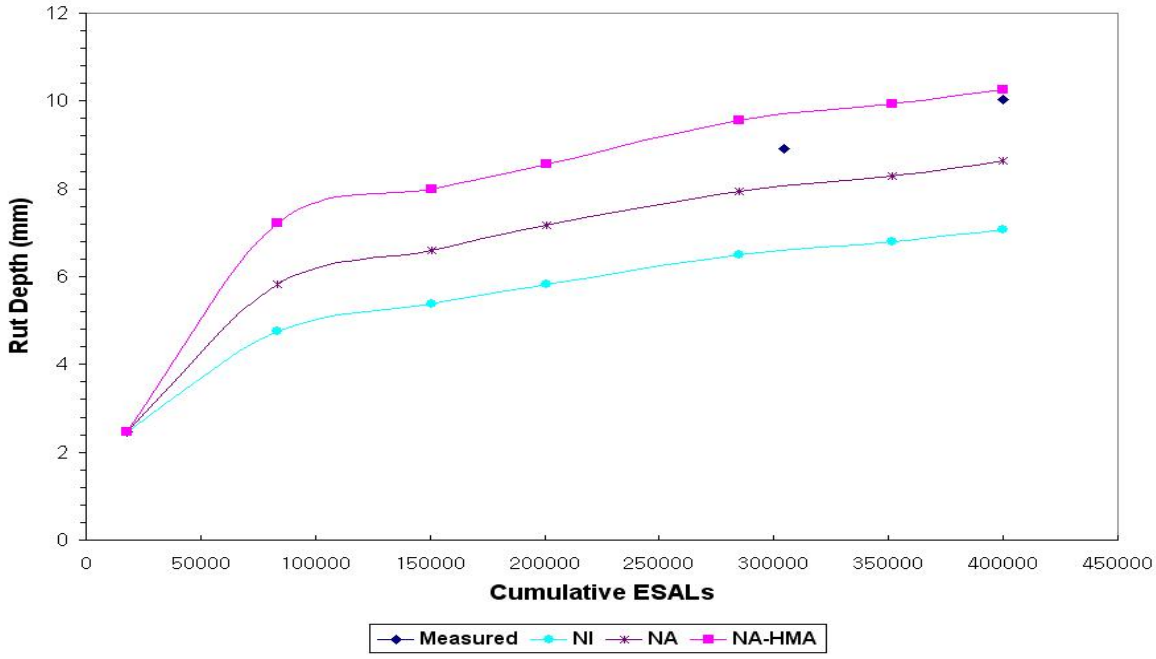

Figure 5.25. Comparison of Rut Depth from Measurement and Prediction at K6-4 Station

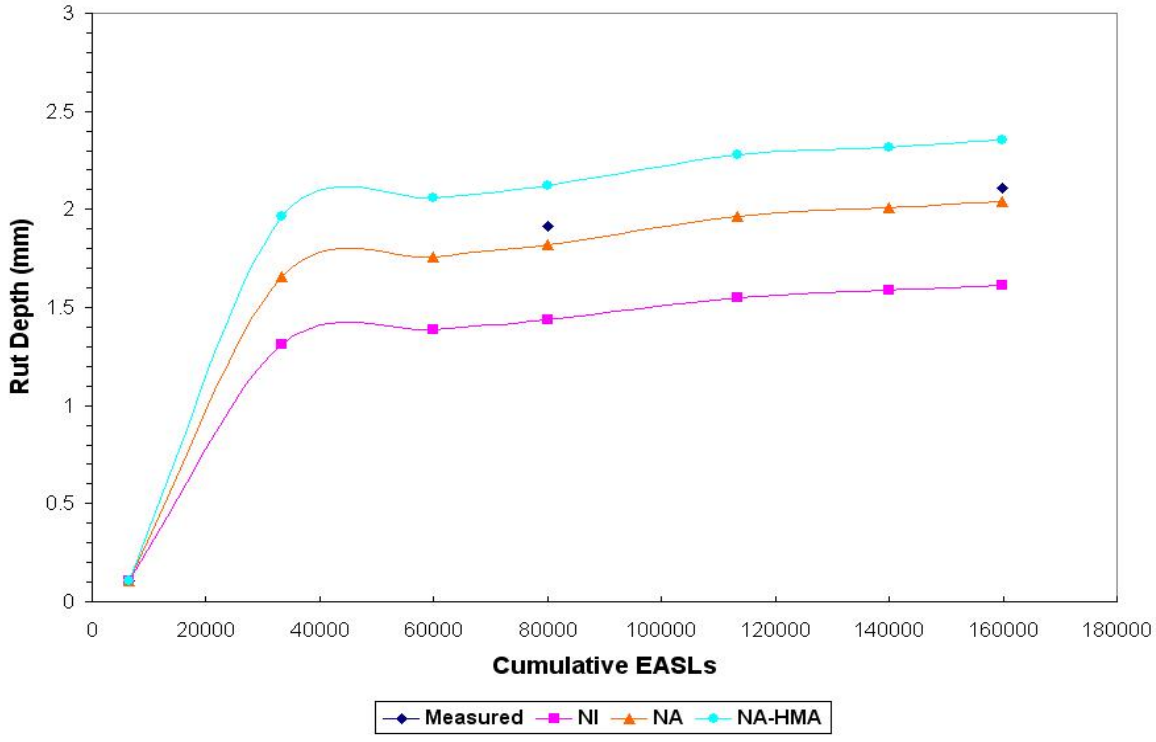

Figure 5.26. Comparison of Rut Depth by Measurement and Prediction at K7-3 Station

The different types of fatigue cracking such as alligator, transverse, and longitudinal cracking have been measured. Among them, the longitudinal cracking is compared with prediction of NCPA since the algorithm included in the program is limited to estimation of longitudinal cracking. Among factors influencing the amount of cracking, the m value was corrected with temperature to consider the seasonal effect. Ramos (2003) corrected the m values obtained from creep compliance tests and dynamic analysis with respect to the reference temperature 75 °F. From this task, the correction factor m_{ref}/m_{temp} was obtained and variations of corrected m values were plotted versus time for both the K6 and K7 lanes as shown in Figures 5.27 and 5.28. It was found that the m values increased with time in the K6 lane and are almost flat in K7. The increase of m value reflects deterioration. Input parameters to calculate fatigue cracking in NCPA are summarized in Table 5.10.

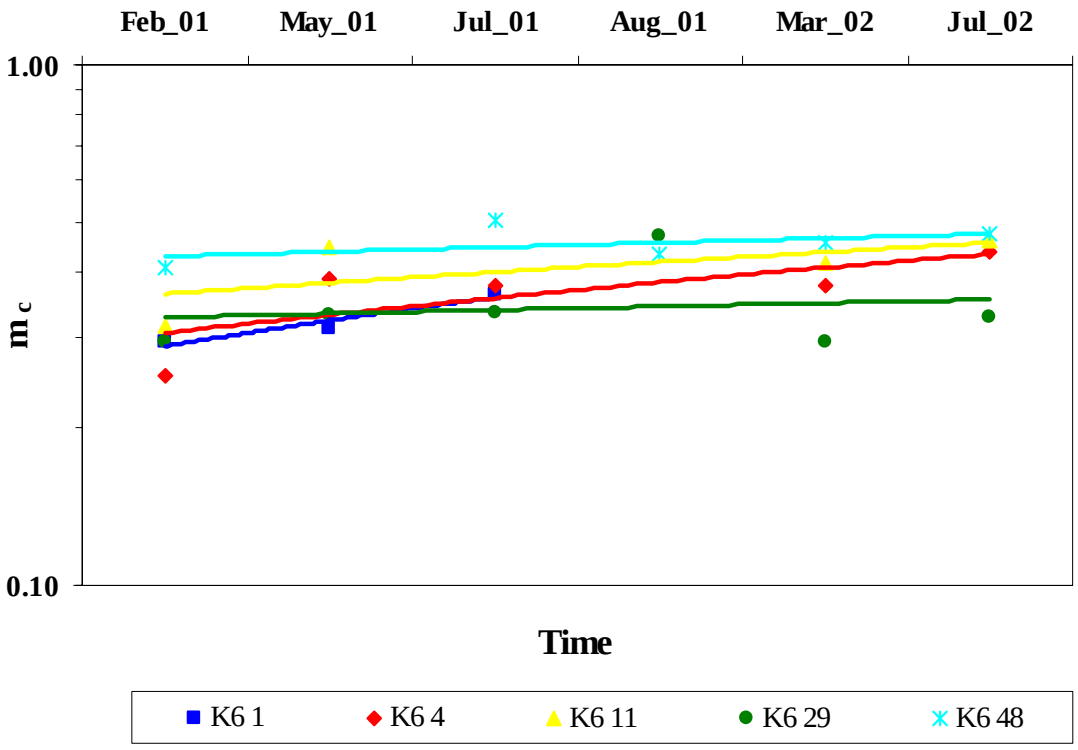

Figure 5.27. Variation of mc Values over Time at the K6 Lane (after Ramos, 2003)

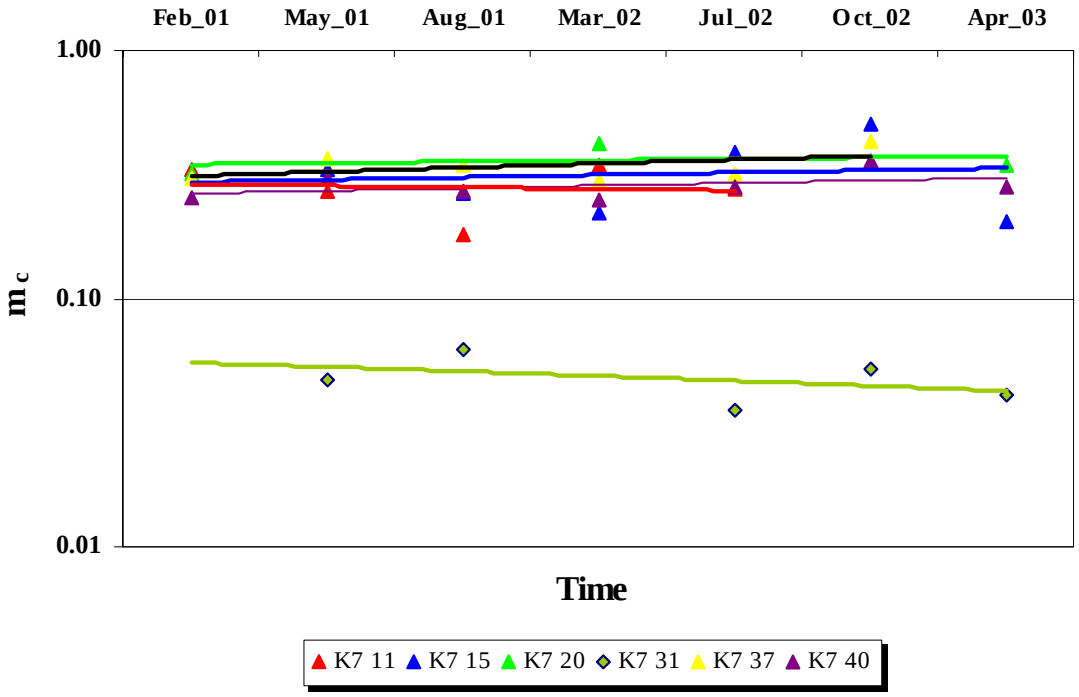

Figure 5.28. Variation of mc Values over Time at the K7 Lane (after Ramos, 2003)

Table 5.10. Used m Values and Parameters in Fatigue Cracking Evaluation

	Season 1	Season 2	Season 3
m	0.4	0.25	0.35
c_0 (mm)	1.4	1.4	1.4
m_0	0.20	0.20	0.20
h	0.427	0.427	0.427
AC tensile strength (kPa)	550	1229	757

The value of m was determined on the basis of variation shown in above plots. The denoted m value was assigned to the analysis of the K6-4 station and the constant m value, 0.3, was used in K7-3 station evaluation without respect to the change of season. Initial crack length,

c_0, was assumed and calibrated through several runs of the program to obtain reasonable predictions. Definitely, the larger c_0 value gives the shorter fatigue life. The variable, m_0, which are used in equation (5.15), was found to vary from 0.1 to 0.2 from an evaluation of the performance of a limited number of SHRP A-005 test sites (Tseng, 1988). From the same evaluation, the variable, h, was found to vary from 0.2 to 0.30. Laboratory data obtained by Balbissi (1983) from fracture tests done using the overlay tester showed the constant, h, to be as high as 0.427. Higher values of the healing factors indicate a higher shift in the fatigue life due to healing. In the analysis, 0.427 was selected because it gives the most comparable prediction. The asphalt tensile strength in different seasons was determined based on previous test results (Molenaar et al. 2000). The comparison of fatigue cracking was performed following the same approach intended in rutting evaluation. Figures 5.29 and 5.30 show the result.

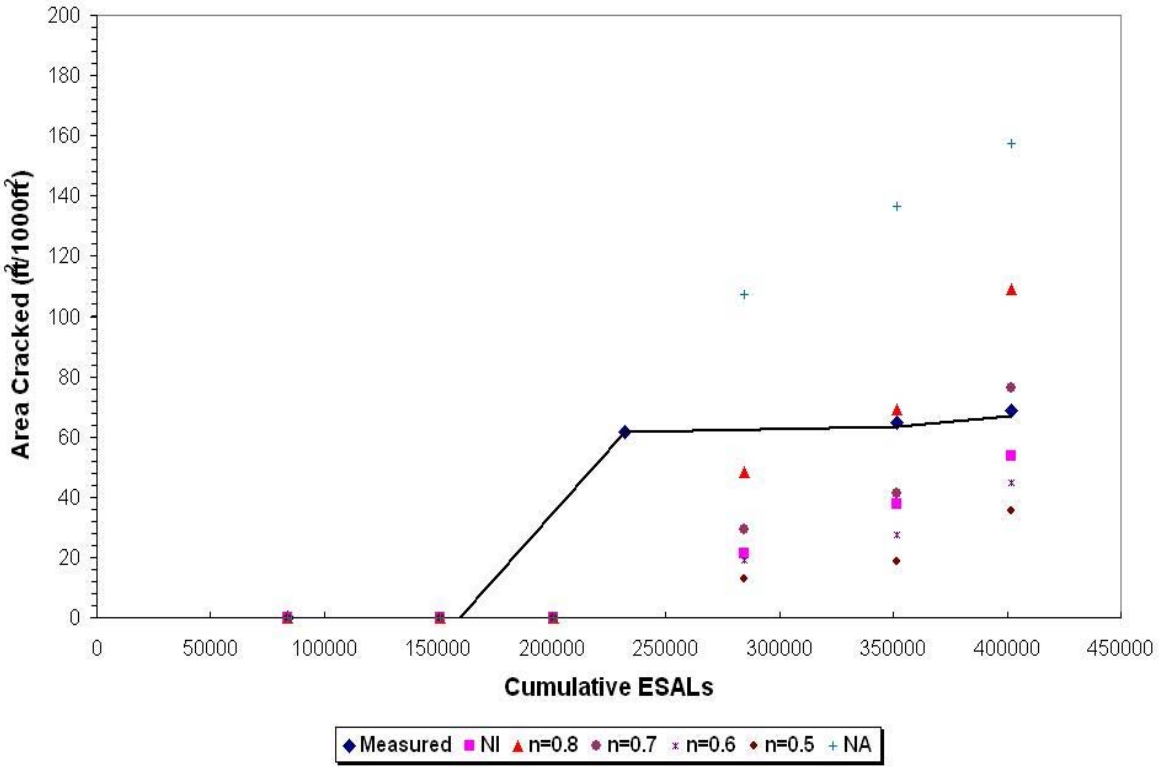

Figure 5.29. Comparison of Fatigue Cracking from Measurement and Prediction at K6-4

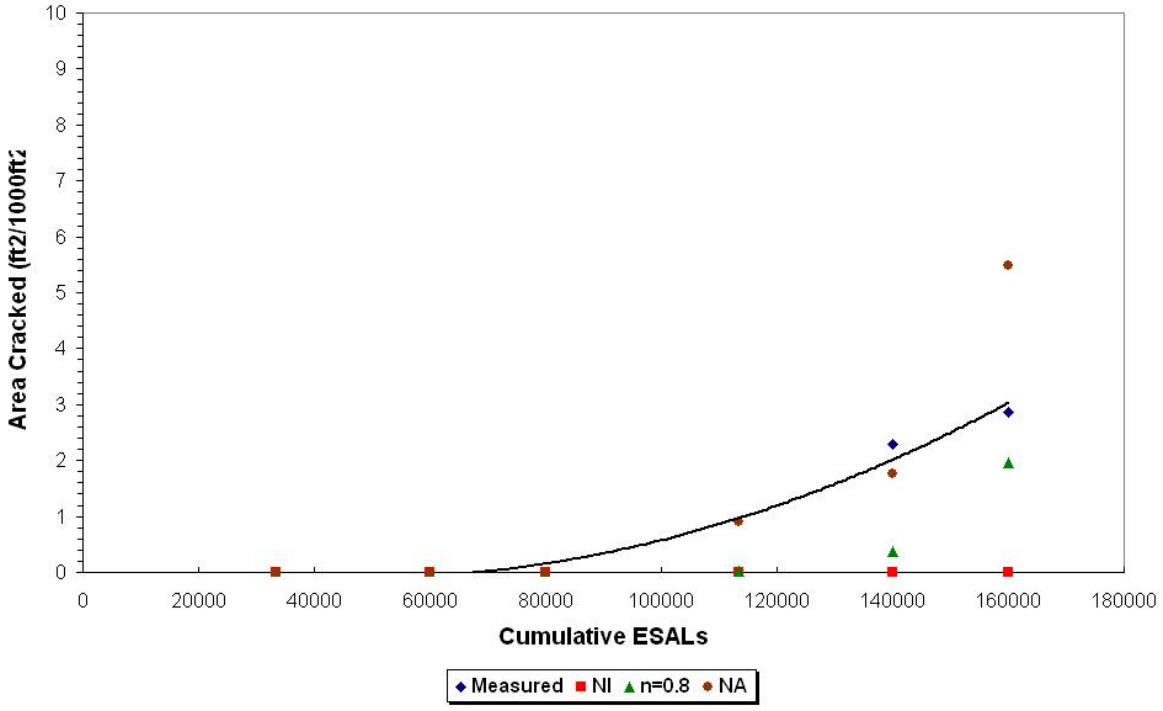

Figure 5.30. Comparison of Fatigue Cracking from Measurement and Prediction at K7-3

It was observed that the NI modeling has a tendency to underestimate fatigue life overall while the NA model gives a more or less prediction compared to measured value. In case of the K6-4 station, the NA model predicts a relatively larger area cracked than expected. Thus, to find an improved prediction, several runs were made forcing the AC layer to be modeled with cross-anisotropy. Firstly, the value of n was selected as 0.8 based on the previous analysis result. It reduced the discrepancy between the measured and predicted values because a small magnitude of tensile strains at the bottom of AC layer were generated as the level of anisotropy increased. It is interesting to note that the predicted cracked area is less than that of the NI prediction when the n value is less than 0.6. This suggests that the behavior of the AC layer can be significantly influenced by the variation of the n value thus it infers the necessity to model the AC layer taking into account the cross-anisotropy characteristic.

CHAPTER VI

DEVELOPMENT OF CHARTS TO EVALUATE SERVICE LIFE OF EXISTING PAVEMENT DUE TO OVERWEIGHT TRUCK LOADS

6.1. GENERAL

In this chapter, the procedure to establish charts to evaluate the service life of existing pavements due to OTT loading is presented which will enable engineers to assess the structural adequacy of a pavement under permitted OTTs. The OTT loads stem from the desire of truckers to maximize their productivity by carrying as much payload per trip as can be accommodated by their trucks. Therefore governments or local authorities are confronted with the dilemma of balancing the need to promote commerce and economic growth through increased trucking productivity with high quality highway maintenance program to meet the needs within economic constraints. However, this requirement stands in direct opposition to the relatively complex behavior of pavements. While the permit is issued based on the gross vehicle weight, the tire loads and the geometric arrangement of the tires comprising the axle transmit the gross load from a vehicle into the pavement. Recently, researchers developed a procedure to evaluate the pavement response under superheavy loads and the potential for pavement damage using the Mohr-Coulomb failure criterion (Jooste and Fernando, 1995). From charts established in this procedure, it is feasible to determine the maximum wheel load that can be sustained by a given pavement. The concept of this procedure leads to a load-zoning analysis. For this purpose, Fernando and Liu (1999) developed the Program for Load-Zoning Analysis (PLZA) to improve the quality of previous load-zoning analyses. The framework used in this procedure includes route characterization through nondestructive testing and laboratory tests, traffic characterization, pavement response and distress

prediction and the determination of load limits and time to resurfacing. Since it is crucial to maintain or rehabilitate a number of pavements in order not only to improve ride quality but also to save additional taxes, a main concern is to develop the charts for the assessment of service life to sustain the expected OTTs. The charts are expressed in terms of unit service life consumption obtained from using the existing pavement condition which was determined in this study.

6.2. CHART ESTABLISHMENT

6.2.1. Overweight Truck Route Analysis (OTRA) Program

The charts were developed through repetitive runs of the Overweight Truck Route Analysis (OTRA) program developed by Fernando and Liu (2003). In the OTRA program, the predicted pavement responses, namely the horizontal strain at the bottom of the asphalt layer and the vertical strain at the top of the subgrade, are used with the Asphalt Institute (1982) equations to determine the service life for a given pavement and loading condition with respect to the rutting and fatigue cracking using equations (5.1) and (5.3). In addition, Miner's rule (1945) of cumulative damage is used in predicting service life accounting for the effects of different axle loads and axle configurations using the given equation.

$$D_r = \sum_{i=1}^{m} \frac{n_i}{N_i} \tag{6.1}$$

where D_r is the damage ratio accumulated over the design period due to all load groups, m is the total load groups, n_i is the predicted number of repetitions for the i^{th} load group, and N_i is the number of repetitions to reach failure for the i^{th} load group.

The OTRA program can handle triple axles which is the most typical type of axle used in the OTT trailers. Due to the large spacing between axles, the critical tensile and

compressive strains under multiple axles are slightly different from those under a single axle. In the OTRA program, the critical strains are evaluated at different lateral positions: at the outside tire edge, at the center of the tire, inside tire edge, and midway between dual tires. The program is capable of analyzing pavement structure using both linear and non-linear elastic methods. Jooste and Fernando (1995) reported that the nonlinear characteristic becomes more pronounced in thin-surfaced pavements and believe that a nonlinear analysis will provide a more realistic prediction of the stresses induced under loading. For the non-linear elastic method, the resilient material property should be provided from laboratory testing of base and subgrade or from a previously developed database. In the OTRA program, the Uzan model (1985 and 1992) was adopted to calculate the stress dependent moduli. However, since the OTRA program is not able to simulate cross-anisotropy, basic charts are established based on nonlinear isotropic conditions using the OTRA and then additional charts are developed taking into the account cross-anisotropic characteristic by applying a shift factor between two constitutive models.

6.2.2. Determination of Standard Material Property

Three pavement layers were used in all of the analyses conducted in this study. The materials used in each layer have a wide range of moduli. The nomenclature used to distinguish between material types, therefore, is composed of rather loose terms such as stiff, weak, or stabilized. The thickness varied for the asphalt concrete layer (76.2 mm ~ 203.2 mm with increment of 25.4 mm) and base layer (152.4 mm ~ 508.0 mm with increment of 50.8 mm) respectively. The pavement structural combinations are designated as cases 1 through 4.

- Case 1 : Asphalt Concrete + Weak Base + Weak Subgrade,
- Case 2 : Asphalt Concrete + Weak Base + Stiff Subgrade,

- Case 3 : Asphalt Concrete + Stabilized Base + Weak Subgrade,
- Case 4 : Asphalt Concrete + Stabilized Base + Stiff Subgrade.

Table 6.1 summarizes the material parameters both for the nonlinear isotropic model i.e., $K_1 \sim K_3$ and for the cross anisotropic model i.e., n, m, and p for each material type on the basis of material properties used in previous research (Jooste 1995; Adu-Osei 2000) and the results of laboratory tests performed in this study. Because the moduli of each layer were not fixed but depended on the load magnitude, the range of moduli for each material was obtained. This range will enable users to determine which case is suitable for the pavement condition that is considered. A description of the selection of parameters follows.

Table 6.1. Material Parameters Used in Design Charts

Layer Description	Non-linear Material Constants			Anisotropy Constants			Range of Moduli (MPa)
	K_1	K_2	K_3	n	m	p	
Asphlat surface	10000 to 15000	0.1	0.0	0.8	0.38	1.3	1000 to 2500
Weak Base	1500	0.6	-0.2	0.10	0.18	1.5	82 to 271
Stiff Base	15000	0.1	0.0	0.50	0.35	1.2	1039 to 3150
Weak Subgrade	500	0.0	-0.4	0.90	0.45	1.5	50 to 75
Stiff Subgrade	900	0.0	-0.4	1.20	0.55	1.5	85 to 179

Asphalt Surface

As shown in Table 6.1, the asphalt stiffness varied from approximately 1000 to 2500 MPa, which falls in the range from low to normal modulus asphalt concrete. The range of asphalt moduli may exhibit conservative trends in the damage analysis but it might remove the potential of uncertainty to apply charts in practice. The asphalt concrete layer can be modeled as an isotropic or an anisotropic material. Based on a comment by Jooste and Fernando (1995), the non-linear constants for the asphalt concrete layer were chosen to represent only a slightly non-linear material.

Weak Base

The condition described as “weak base” was chosen to represent an unstabilized granuluar base with a moisture content wetter than optimum. This base may consist of crushed lime stone, iron ore gravel, shell or Caliche (Jooste and Fernando, 1995). The value of K_2 and K_3 is obtained from the laboratory test results. Based on the relationship between Texas Triaxial Class and modulus value, the “weak base” is considered to represent a material with an approximate Texas Triaxial class number of 3.5 to 4.0 and a California Bearing Ratio (CBR) of between 15 to 60 (Huang 1993; Van Til et al 1972). The cross-anisotropic properties for this material were chosen on the basis of laboratory test results and previous test results as described in chapter III.

Stiff Base

The base or subbase material is often stabilized with lime or cement to enhance its quality and to provide a good support. The stiffness and cohesion of stabilized materials can vary considerably, depending on the amount of stabilizer such as curing time, and material quality (Little, 1992 and 1994). The chosen moduli range for stabilized base implies the stabilized material has already been aged to some extent by traffic and the environmental

effect. The nonlinear parameter was based on the assumption reported by Jooste and Fernando (1995). The cross-anisotropic property was chosen to have a higher n and m value than that of weak base. From the sensitivity analysis conducted in chapter IV, higher n and m values makes a stiffer layer condition due to the improvement of load spreading capacity. In addition, it was observed that the n and m values of a high density granular material are distributed around 0.4 and 0.3, respectively from the test results reported by Adu-Osei (2000). Thus, since most of stabilized base material has higher density and strength than those of normal granular material, a value of n was assumed to be 0.7.

Weak Subgrade

This material was considered to be too soft to support the overlying structure. The nonlinear coefficients were chosen so that the modulus under typical stress conditions varied between 50 and 75 MPa. The weak subgrade condition can be used to represent a wet clay, a poorly compacted sand, or any other material with high plasticity and relatively high moisture content (Jooste and Fernando, 1995). The cross-anisotropic property was chosen based on laboratory test results and previous test results as described in chapter III.

Stiff Subgrade

The stiff subgrade represents a fairly stiff (modulus values varied from 85 to 179 MPa) and well compacted material. The stiff subgrade condition can also represent a lightly stabilized poor quality material. The cross-anisotropic property of the stiff subgrade was chosen with a slight higher value than that of weak subgrade in order to represent that characteristic of overconsolidated clay.

6.2.3. Separation of Cases

It is required to differentiate cases to enable users to recognize their pavement condition effectively. This classification can be accomplished in a number of ways. If FWD deflections or backcalculated layer moduli on candidate routes are available from previous tests, the engineer can use the existing data with the range in moduli values given in Table 6.1 to classify the pavements found along the routes. The availability of such data improves the accuracy of the analysis by reducing the uncertainty associated with the materials comprising the candidate routes. In the absence of such data or in cases where the historical information is suspect, the engineer should collect the data needed to make informed decisions. The representative option is to use the CBR and dynamic cone penetrometer (DCP) index. The CBR is a percentage ratio of penetration pressure at 0.1 inch penetration to that of a standard crushed rock. A typical CBR value for different soil types is summarized in Table 6.2.

Heukelom and Klomp (1962) presented the relationship between the resilient modulus and CBR as below.

$$M_R = 1500(CBR) \tag{6.2}$$

in which Mr is the resilient modulus in psi. The coefficient of 1500 may vary from 750 to 3000 with a factor 2. The correlation appears to be more reasonable for fine grained soils and fine sands with the CBR values less than 20 rather than for granular materials.

Higher CBR values indicate stronger materials that offer greater penetration resistance relative to the standard crushed rock. As a tool for evaluating road and airfield materials, the DCP has been widely used to determine the strength profile of flexible pavements by measuring the depth of penetration per blow. Several agencies and researchers have developed correlations between CBR and the DCP penetration rate (Livneh et al., 1995).

Webster et al. (1992) compared some of the published correlations. Based on this review, the following equation was recommended:

$$Log\,CBR = 2.46 - 1.12(Log\,DCP) \quad (6.3)$$

where DCP is the penetration rate in mm/blow and CBR is in percent. Usually, DCP testing involves coring through the top asphalt layers to expose the top of the granular base where the test is commenced. The DCP is driven through the pavement to some required depth or until refusal. During the test, the depth penetrated per blow is measured and the data are subsequently plotted as illustrated in Figure 6.1. By identifying where slope changes occur on the penetration curve, the layering within the pavement can be established, as illustrated in Figure 6.1. The penetration rate for each layer can then be determined and used in Eq. (6.2) to predict the CBR for the given layer or material.

Table 6.3 shows suggested guidelines for classifying a given pavement into one of the four groups considered in developing the charts. The guidelines are based on the DCP penetration rate for a given material and information taken from the literature on typical CBR ranges for various coarse- and fine-grained materials. Thus, if DCP data are available, the engineer can establish the pavement layering as illustrated in Figure 6.1. From this analysis, he/she can estimate the thickness and compute the penetration rate for each layer identified from the DCP data. The engineer can then use the penetration rates to classify a given pavement for using charts.

Table 6.2. Typical CBR Ranges of Soils (U.S. Army Engineer, 1960)

Major Divisio	Subdivisio n	Unified Soil Classification	CBR Range (%)	Value as Subgrade[1]	Value as Base[1]
Coarse-grained soils	Gravel and gravelly soils	GW	40 – 80	Excellent	Good
		GP	30 – 60	Good to excellent	Fair to good
		GM (LL < 25 and PI < 5)	40 – 60	Good to excellent	Fair to good
		GM (LL > 25 or PI > 5)	20 – 30	Good	Poor to not suitable
		GC	20 – 40	Good	Poor to not suitable
	Sand and sandy soils	SW	20 – 40	Good	Poor
		SP	10 – 40	Fair to good	Poor to not suitable
		SM (LL < 25 and PI < 5)	15 – 40	Fair to good	Poor
		SM (LL > 25 or PI > 5)	10 – 20	Fair	Not suitable
		SC	5 – 20	Poor to fair	Not suitable
Fine-grained soils	Silts and clays with liquid limit < 50	ML	≤ 15	Poor to fair	Not suitable
		CL	≤ 15	Poor to fair	Not suitable
		OL	≤ 5	Poor	Not suitable
	Silts and clays with liquid limit > 50	MH	≤ 10	Poor	Not suitable
		CH	≤ 15	Poor to fair	Not suitable
		OH	≤ 5	Poor to very poor	Not suitable

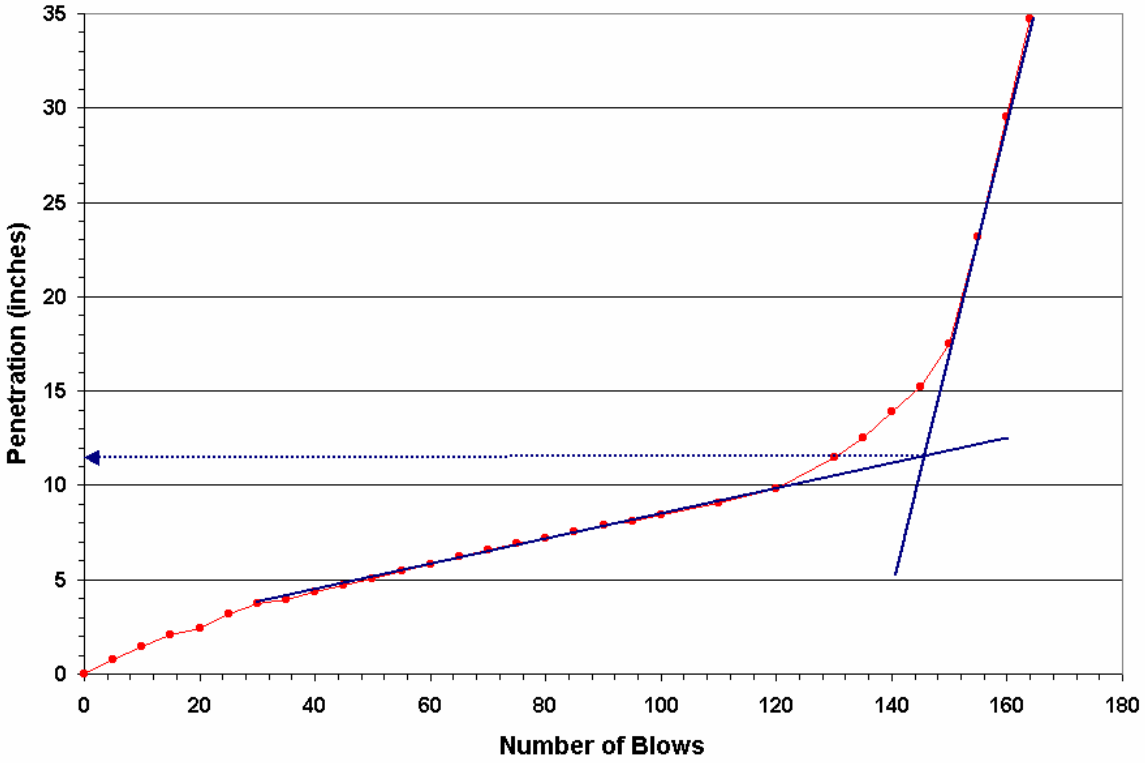

Figure 6.1. Establishing Pavement Layering Using DCP Data

Table 6.3. Classification of Pavement Materials Based on DCP Penetration Rate

Material	DCP Penetration Rate (mm/blow)
Weak base	≥ 3.048
Weak subgrade	≥ 13.97
Stabilized base	≤ 1.778
Stiff subgrade	≤ 8.382

6.2.4. Procedure to Develop Charts

The OTRA program was run to obtain the number of traffic repetitions to failure for both fatigue cracking and rutting criteria using prepared material properties for each case. The thickness of asphalt concrete and base layers varied and different axle configurations

from single to triple axle were considered. All kinds of traffic were included: legal trucks with 5 axles and permitted overweight trucks with 5 or 6 axles are considered as depicted in Figure 6.2. Because all tires except the steering axle are dual tires, the value of tire and axle spacing was selected to be 355.6 mm (14 in) and 1219.2 mm (48 in) respectively on the basis of information on configurations of monitored OTTs. In addition, various combinations of traffic were used to account for the influence on the damage potential. Firstly, the percentage of class 9 and 10 OTTs was determined to be 45 % and 55% respectively from the truck data collected during the study. For example, of 100 overweight trucks, 45 will be of class 9 and 55 will be of class 10 trucks. The following four combinations were selected to represent possible combinations of legal and overweight trucks as noted:

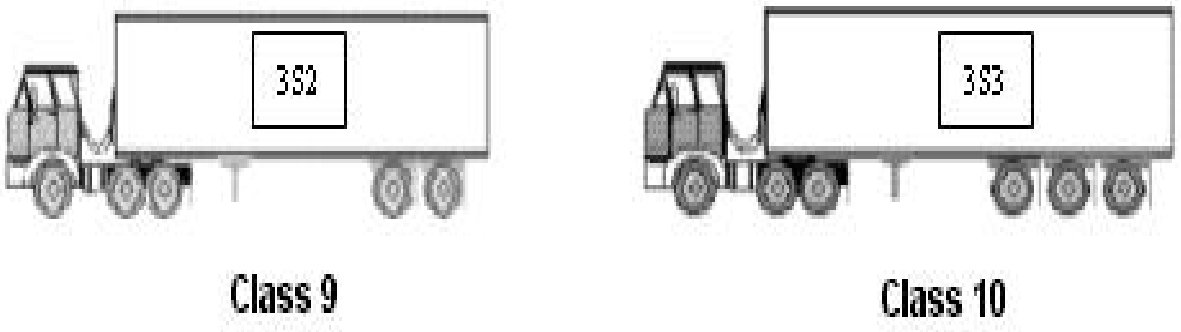

Figure 6.2. Permitted Overweight Truck Class and Configuration

- ♦Combination 1 (80/20) : 80% legal and 20% overweight trucks,
- ♦Combination 2 (70/30) : 70% legal and 30% overweight trucks,
- ♦Combination 3 (60/40) : 60% legal and 40% overweight trucks, and
- ♦Combination 4 (50/50) : 50% legal and 50% overweight trucks.

Secondly, the limits of axle weight were determined for each truck based on the static weight data. The 90-percentile axle weight from the distribution of weights was used to represent the axle weight corresponding to the type of trucks as tabulated in Table 6.4. It was noted that each truck is weighed at the port before permits are issued to verify that the axle and gross vehicle weights do not exceed the allowable limits for the overweight truck route shown in Table 1.1. The measured weights are then recorded on the permits. The data was used to determine the weight corresponding to the 90^{th} percentile of the weight distribution for each truck axle. For the legal or non-permitted trucks, it was assumed that the legal tandem axle weight limit of 151.2 kN (34 kips) for the drive and trailer axles.

The weights in Table 6.4 are assumed to be equally distributed among the tires comprising a given axle group. The lateral spacing of 355.6 mm (14 in) between the dual tires at each end of the drive and trailer axles. In addition, a spacing of 1219.2 mm (48 in) was assumed between the axles of the drive and trailer axle groups. Each wheel load was represented as a uniform contact pressure of 689.48 kPa (100 psi).

Table 6.4. Used Axle Weight Limit (kN) in Charts

Traffic	Steering Axle	Driving Axle	Trailer Axle
Legal	53.4	151.2	151.2
Class 9	53.4	200.2	204.6
Class 10	53.4	200.2	266.9

The charts were established in terms of unit service life consumed ($1/N_f$) denoted by a reciprocal of the number of traffic loads at failure (N_f) with respect to the rutting and the fatigue cracking. Each unit service life consumed value corresponds to thickness variations in asphalt and base layer so that it is feasible to select appropriate thickness levels and

determine the service life for different cases. For each case, 48 combinations (6 levels of thickness for asphalt × 8 levels of thickness for base) of structure were run to determine the maximum critical strains and N_f. One set of runs consists of 48 structures which are computed for three different types of trucks repeatedly i.e., legal, class 9 and class 10 OTTs. Because three axle assemblies such as steering, driving and trailer are considered for all trucks, the N_f is evaluated from each axle group. Therefore the unit service life consumed ($1/N_f$) for each truck is expressed by equation (6.4).

$$\frac{1}{(N_f)_{steering}} + \frac{1}{(N_f)_{drive}} + \frac{1}{(N_f)_{trailer}} = \frac{1}{(N_f)_{truck}} \tag{6.4}$$

Based on the above equation, a value of $1/ N_f$ due to a mixture of trucks per day and truck can be obtained using equation (6.4).

$$\left[\frac{1}{(N_f)_{steering}} + \frac{1}{(N_f)_{driving}} + \frac{1}{(N_f)_{trailer}}\right] \times (\%_{legal}) + \left[\frac{1}{(N_f)_{steering}} + \frac{1}{(N_f)_{driving}} + \frac{1}{(N_f)_{trailer}}\right] \times (\%_{over} \times \%_{class9}) + \left[\frac{1}{(N_f)_{steering}} + \frac{1}{(N_f)_{driving}} + \frac{1}{(N_f)_{trailer}}\right] \times (\%_{over} \times \%_{class10}) = \left(\frac{1}{N_f}\right)_{truck} \tag{6.5}$$

where

$\%_{legal}$ = the percentage of legal trucks in the mixture of traffic (i.e. 80, 70, 60 and 50 %),

$\%_{over}$ = the percentage of overweight trucks in the mixture of traffic (i.e. 20, 30, 40 and 50 %),

$\%_{class9}$ = the percentage of class9 trucks in the overweight trucks (i.e. 45%), and

$\%_{class10}$ = the percentage of class10 trucks in the overweight trucks (i.e. 55%).

The value obtained by equation (6.5) is multiplied by an expected number of traffic loads per year. The reciprocal of these numbers represents service life. Several possible

allowable numbers of traffic loads were determined from weigh-in-motion data that were collected during this study. Through this procedure, 8 curves composed of 4 different combinations of traffic and two distress types were established for each case based on the nonlinear isotropic condition. To check the sensitivity of different traffic combinations in the determination of thickness, both case 1 and case 4, which represent the most extreme pavement strength conditions, weak or strong, were tested. A specific base thickness 304.8 mm (12 in) and unit service life consumed were assumed. Figures 6.3 through 6.6 show the comparison of the selected thickness with different traffic combinations. As shown in these figures, it was concluded that selected thickness was not sensitive to the different traffic combinations, having no more than a 25.4 mm (1 in) variation. In terms of fatigue cracking, it was suggested that the combination of 50/50 be used to provide a conservative design approach. When it comes to rutting, because there is more spread in the curves compared to those of fatigue cracking, two traffic combinations can be used. If the percent of overweight trucks is 20 percent or lower, use the 80/20 combination. If there is more than 20 percent of overweight trucks, the 50/50 combination should be applied. The established charts are presented in Figures 6.7 to 6.20.

Figures 6.7 and 6.8 present the reduction of service life with the increase of traffic rate and unit service life consumed in the development of fatigue cracking and rutting respectively. Charts that show the variation of unit service life consumed with the different base and AC thicknesses were established with the specific traffic combinations as depicted from Figure 6.9 to 6.20. Note that a smaller range of base thickness was considered with the fatigue cracking since the change of unit service life consumed was not relatively sensitive to the variation of base thickness compared to a similar assessment of rutting. It infers that the variation of base thickness is a more critical factor in the development rutting than that of

fatigue cracking when the AC layer condition is identical. In addition, the extent of spreading of the curves was more pronounced when the base layer is stiff as in cases 3 and 4. It might be attributed to the fact that the weak base layer considered in cases 1 and 2 is not sufficient to sustain the traffic loading thus the resultant damage will be similar even if the base layer is thicker.

Charts which are related to rutting present a desired trend to apply in practice. As both the AC and the base are thicker, a lesser unit service life is consumed in all cases. A higher unit service life consumed was detected in the structure composed of weak support layers such as case 1 and case 2. Besides, the higher OTT proportion denoted by 50/50 produced a larger damage potential than the traffic combination of 80/20.

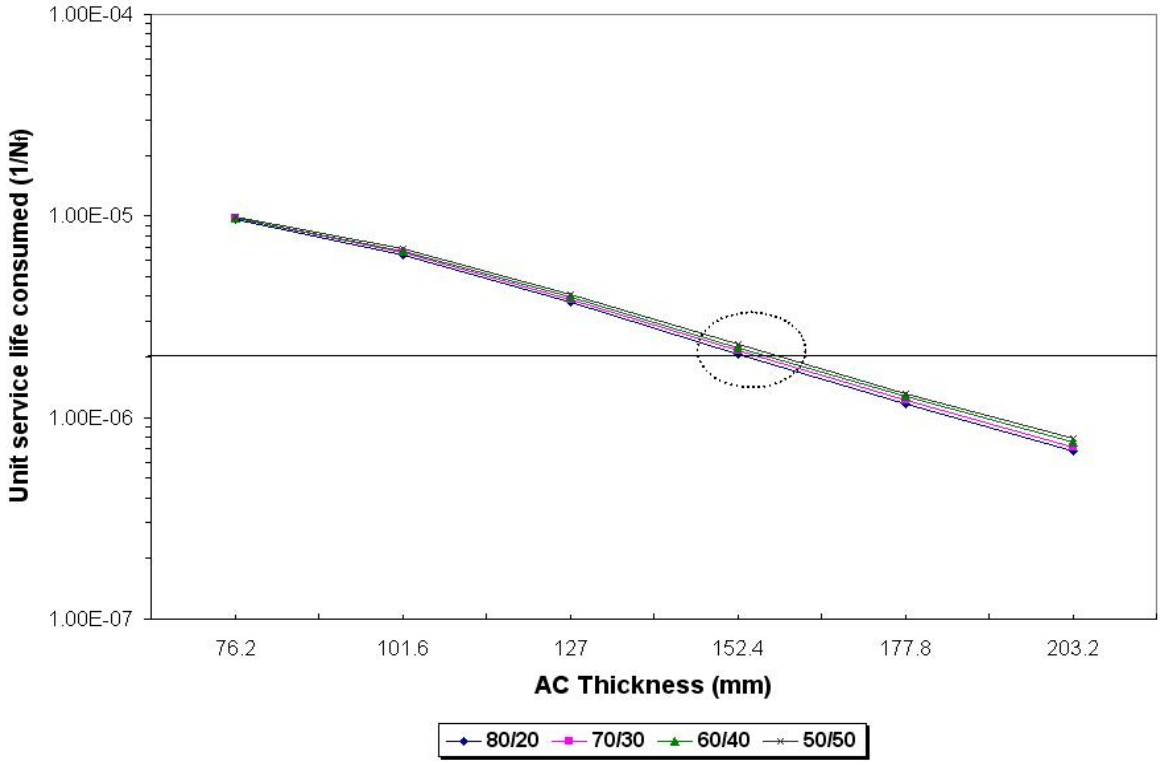

Figure 6.3. Comparison of AC Thickness in Fatigue Cracking Criteria for Case 1

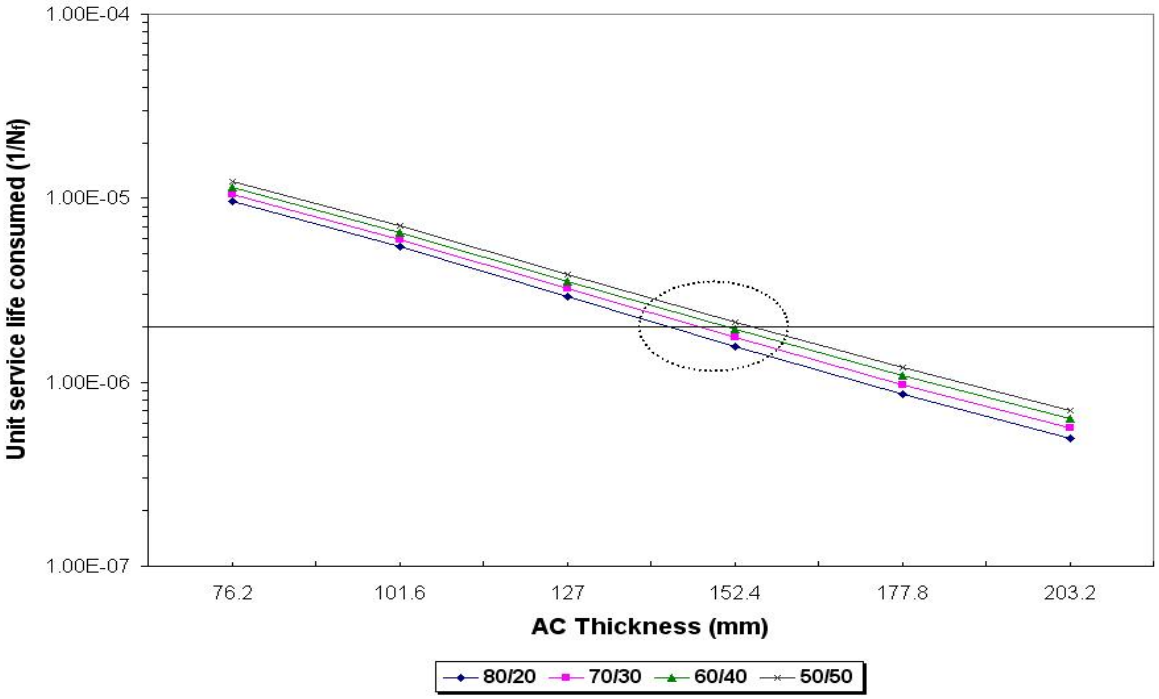

Figure 6.4. Comparison of AC Thickness in Rutting Criteria for Case 1

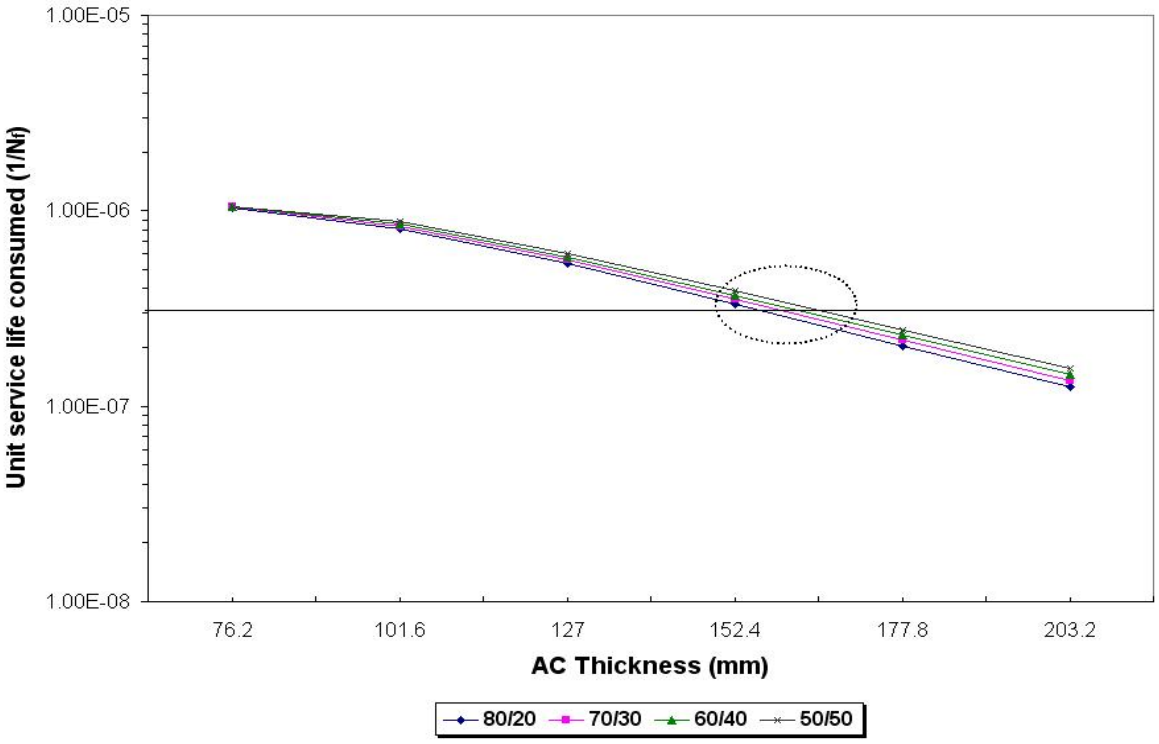

Figure 6.5. Comparison of AC Thickness in Fatigue Cracking Criteria for Case 4

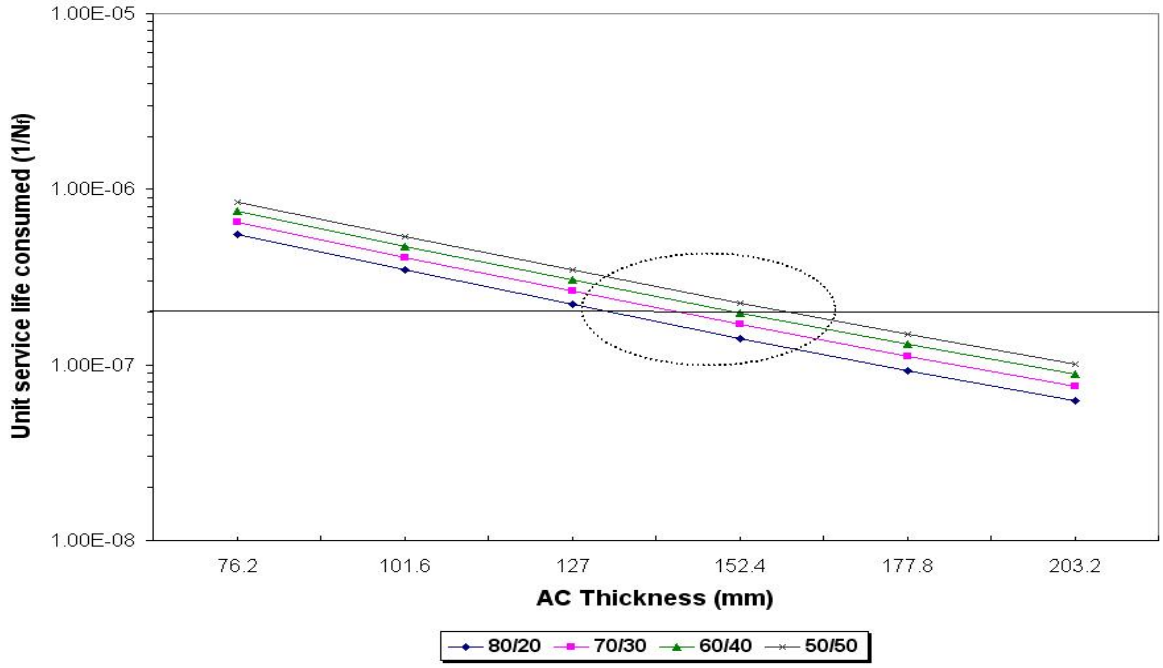

Figure 6.6. Comparison of AC Thickness in Rutting Criteria for Case 4

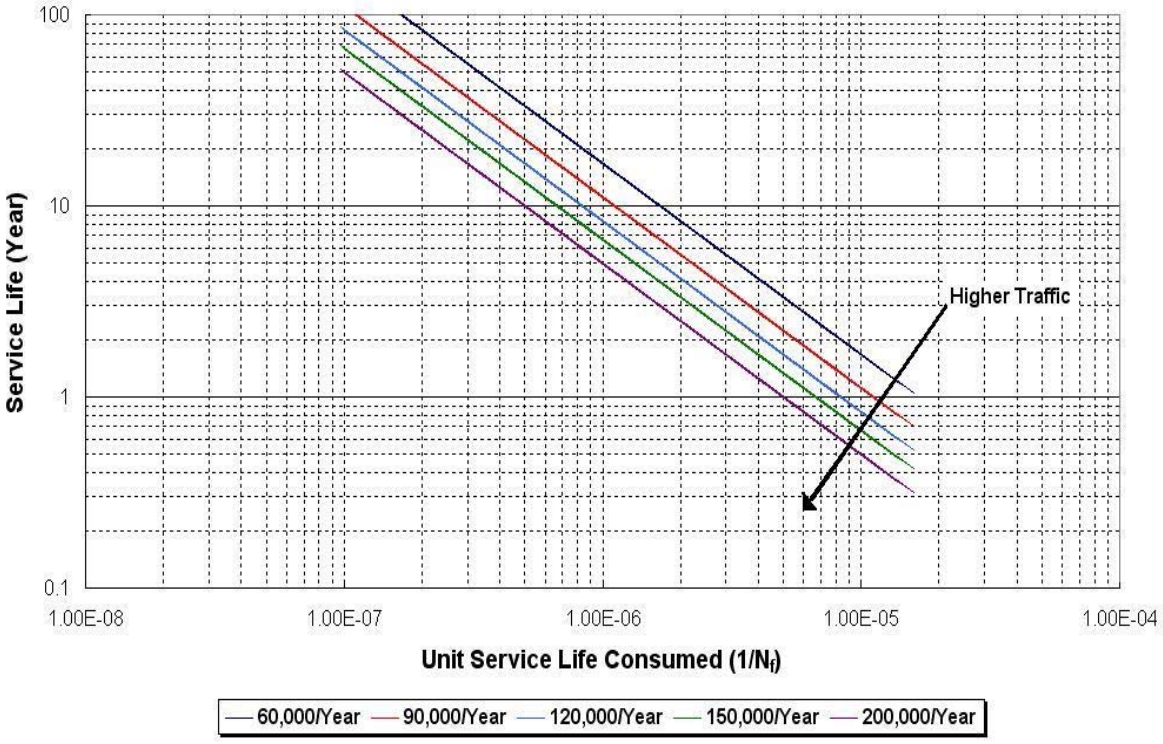

Figure 6.7. Variation of Service Life with $1/N_f$ and Traffic for Fatigue Cracking

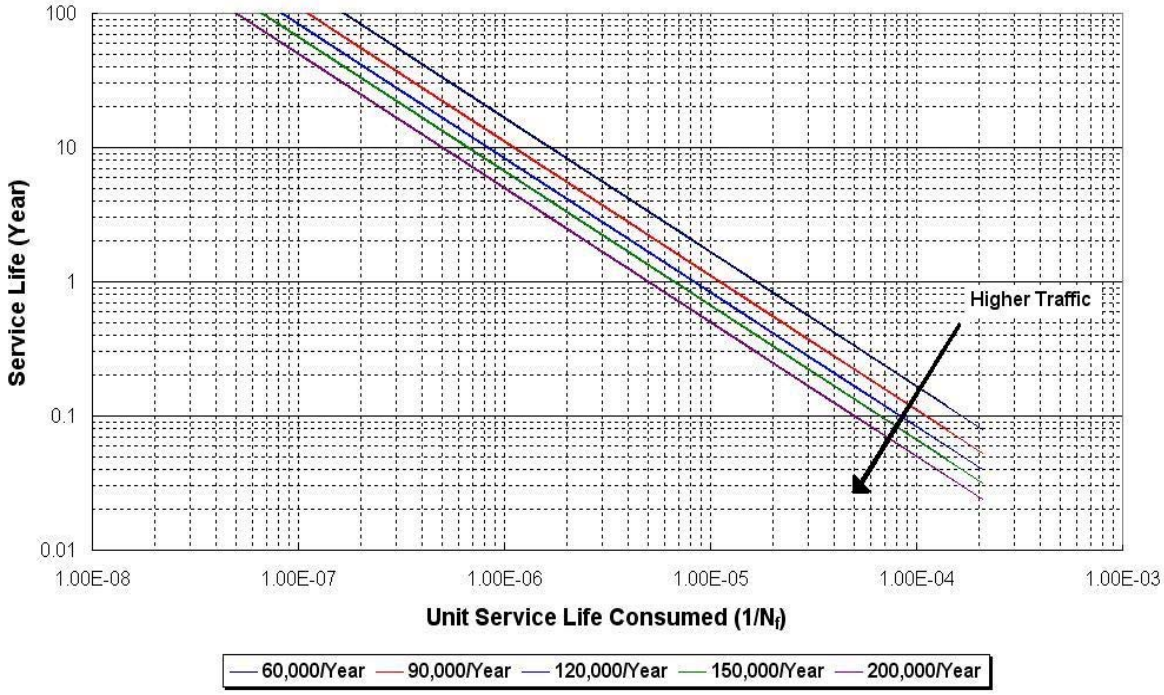

Figure 6.8. Variation of Service Life with $1/N_f$ and Traffic for Rutting

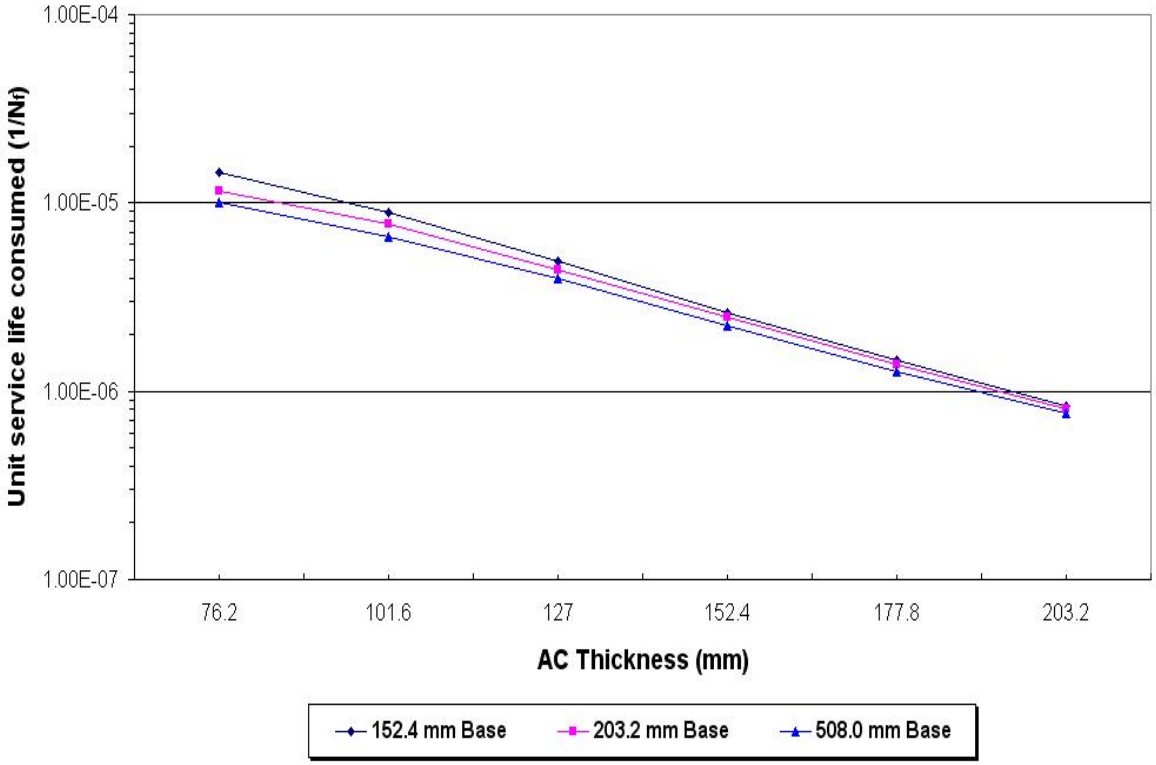

Figure 6.9. Variation of $1/N_f$ with AC and Base Thickness for Fatigue Cracking in Case 1

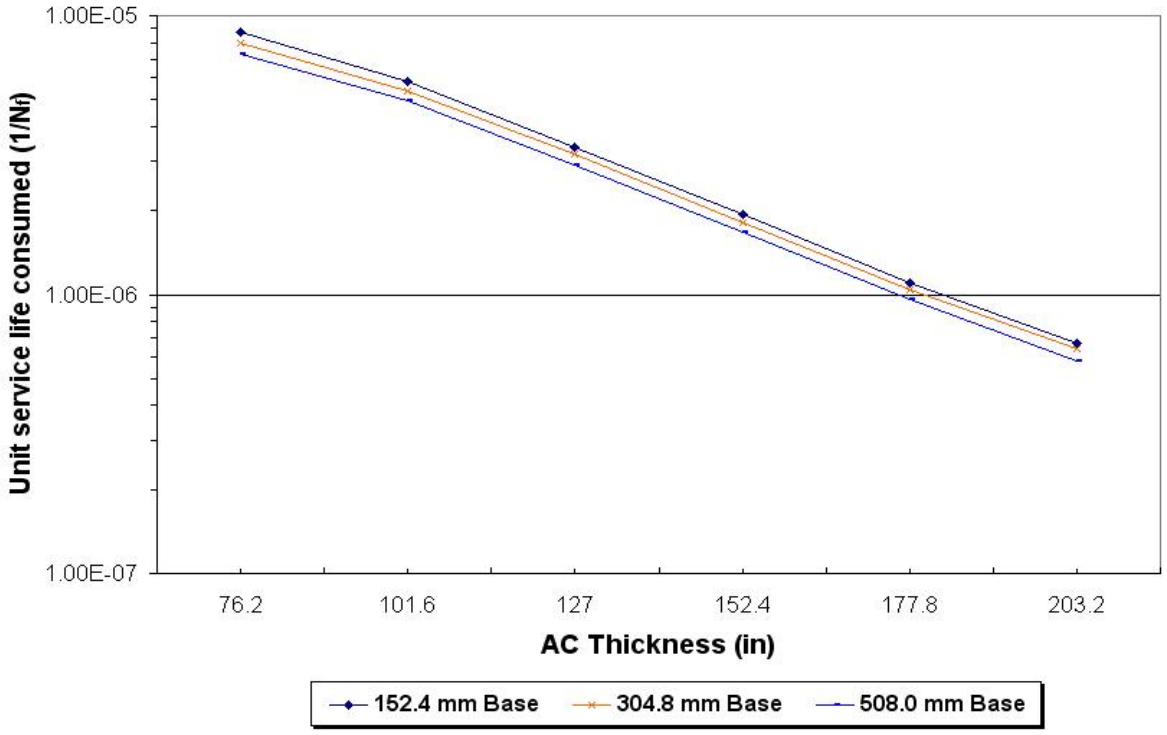

Figure 6.10. Variation of $1/N_f$ with AC and Base Thickness for Fatigue Cracking in Case 2

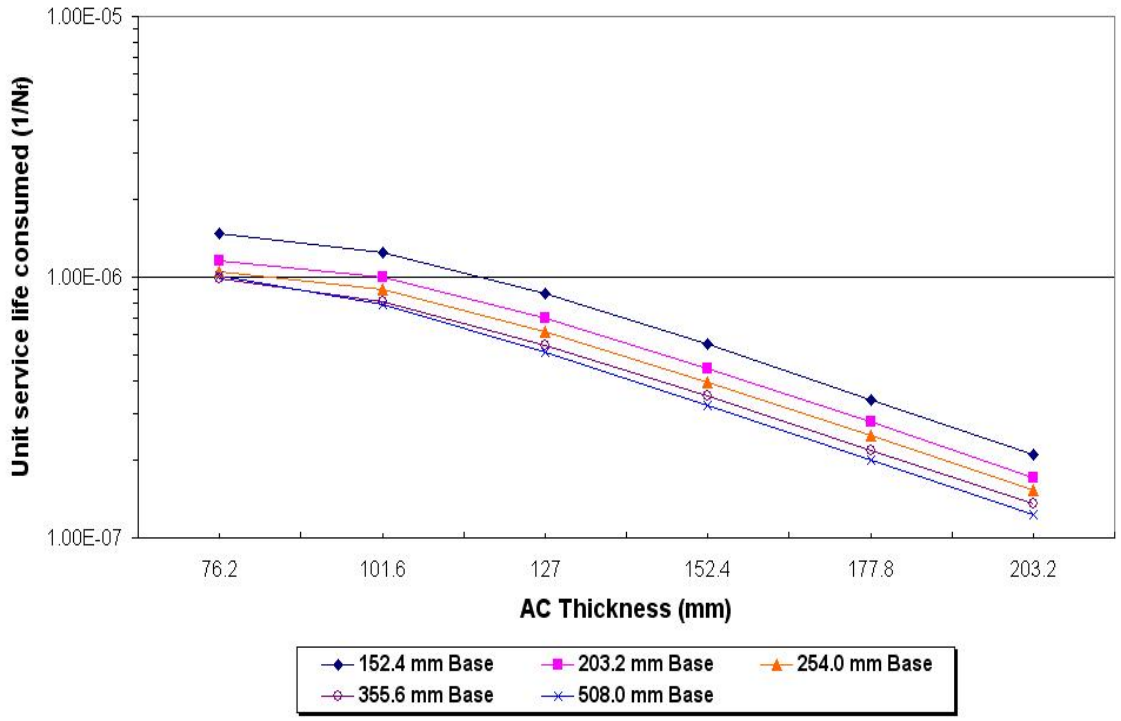

Figure 6.11. Variation of $1/N_f$ with AC and Base Thickness for Fatigue Cracking in Case 3

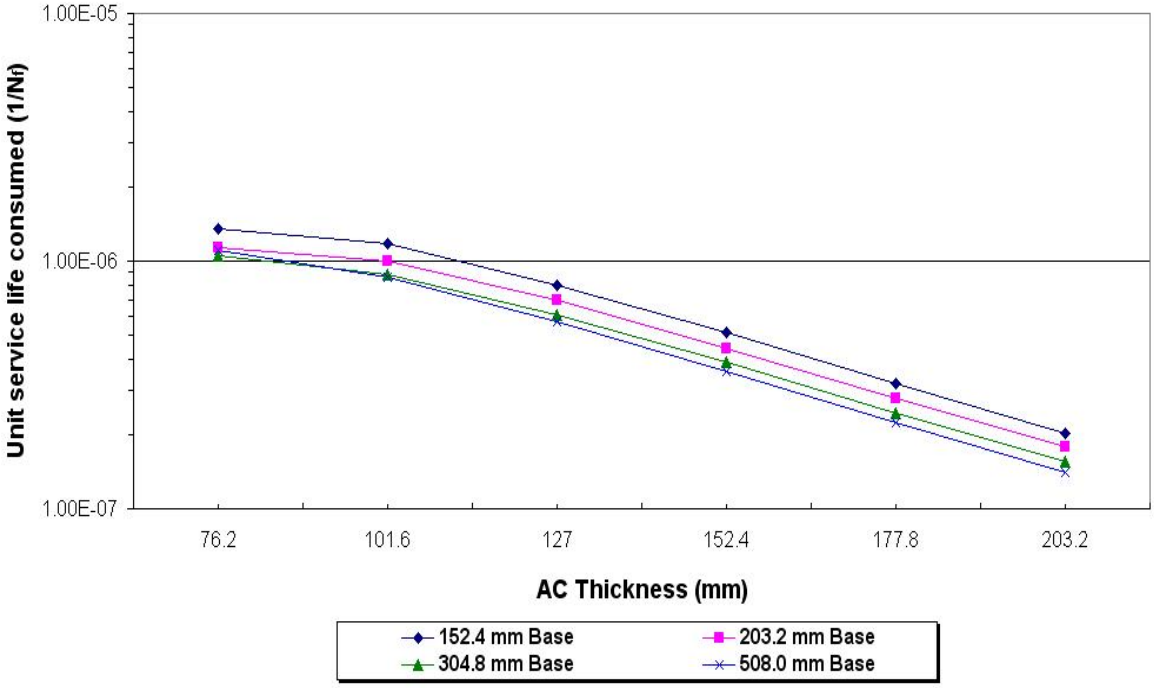

Figure 6.12. Variation of $1/N_f$ with AC and Base Thickness for Fatigue Cracking in Case 4

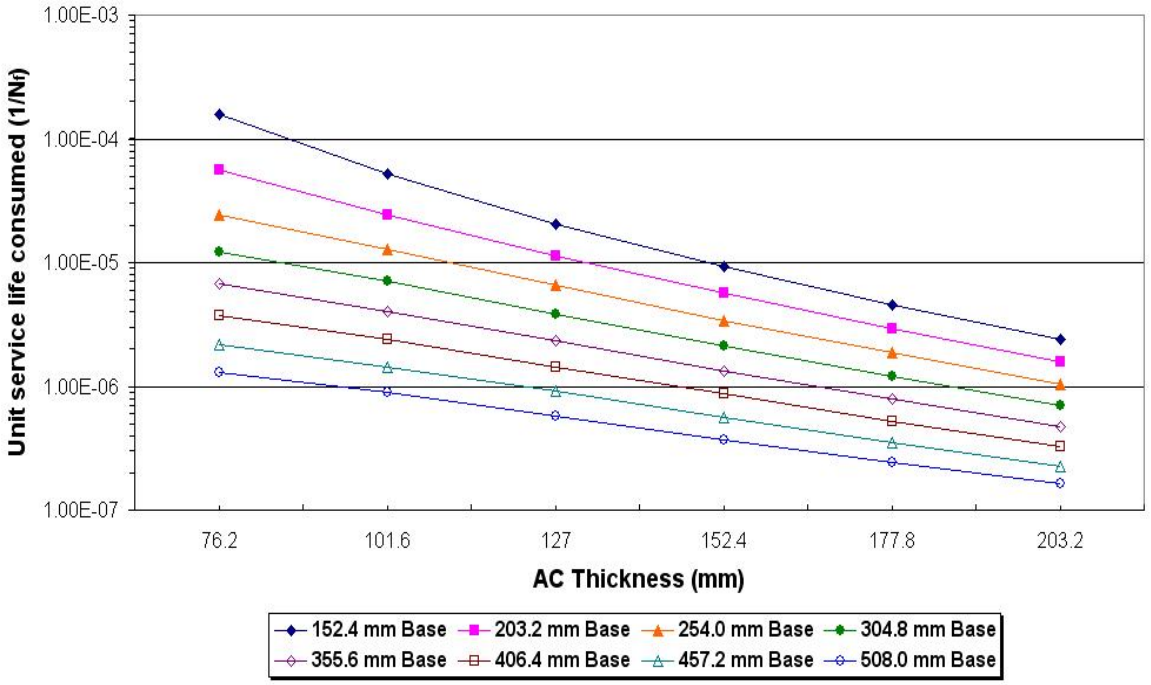

Figure 6.13. Variation of $1/N_f$ with AC and Base Thickness for Rutting in Case 1 (50/50)

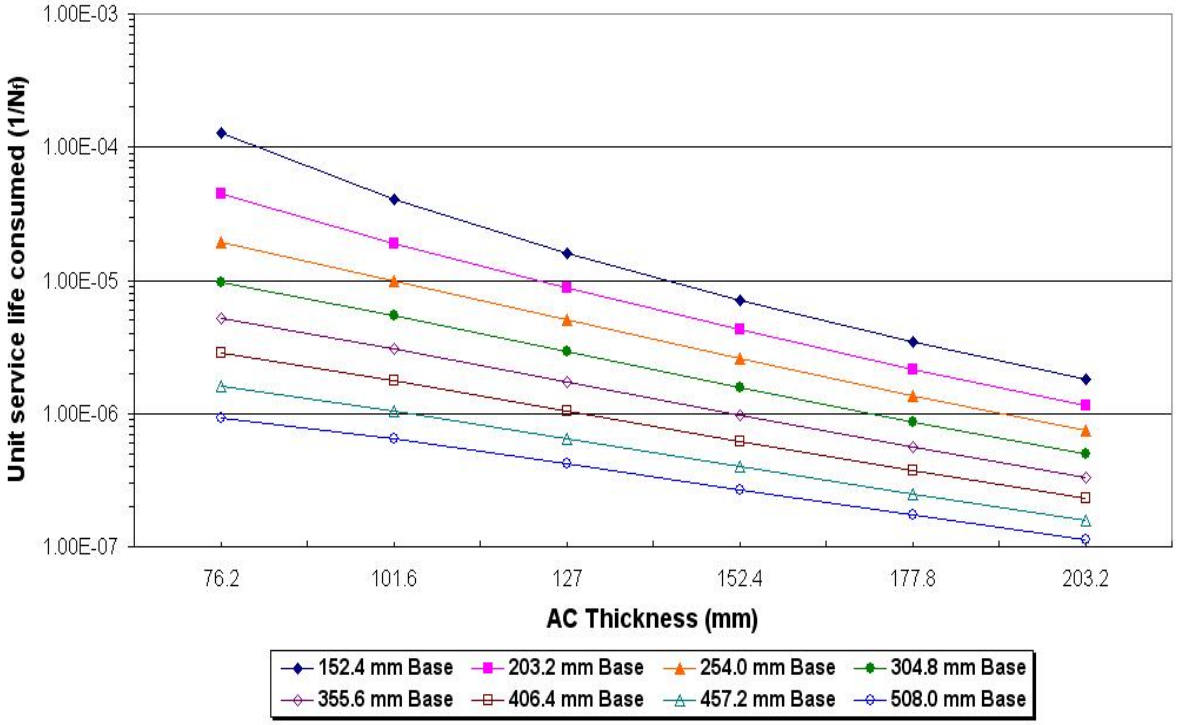

Figure 6.14. Variation of $1/N_f$ with AC and Base Thickness for Rutting in Case 1 (80/20)

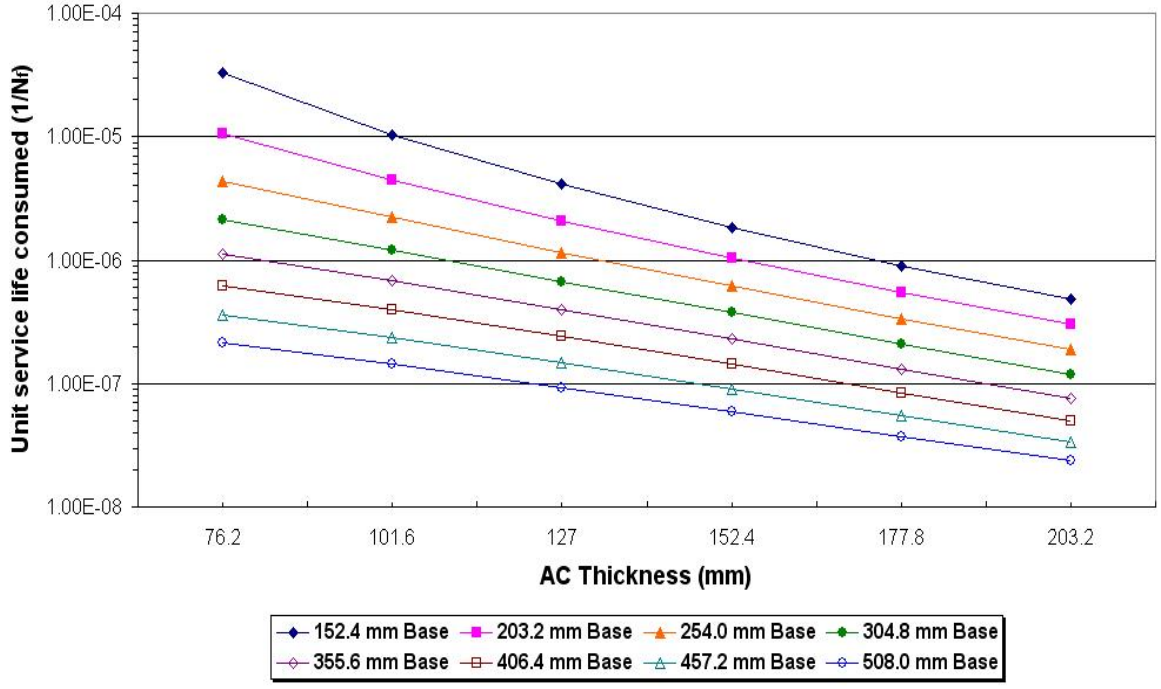

Figure 6.15. Variation of $1/N_f$ with AC and Base Thickness for Rutting in Case 2 (50/50)

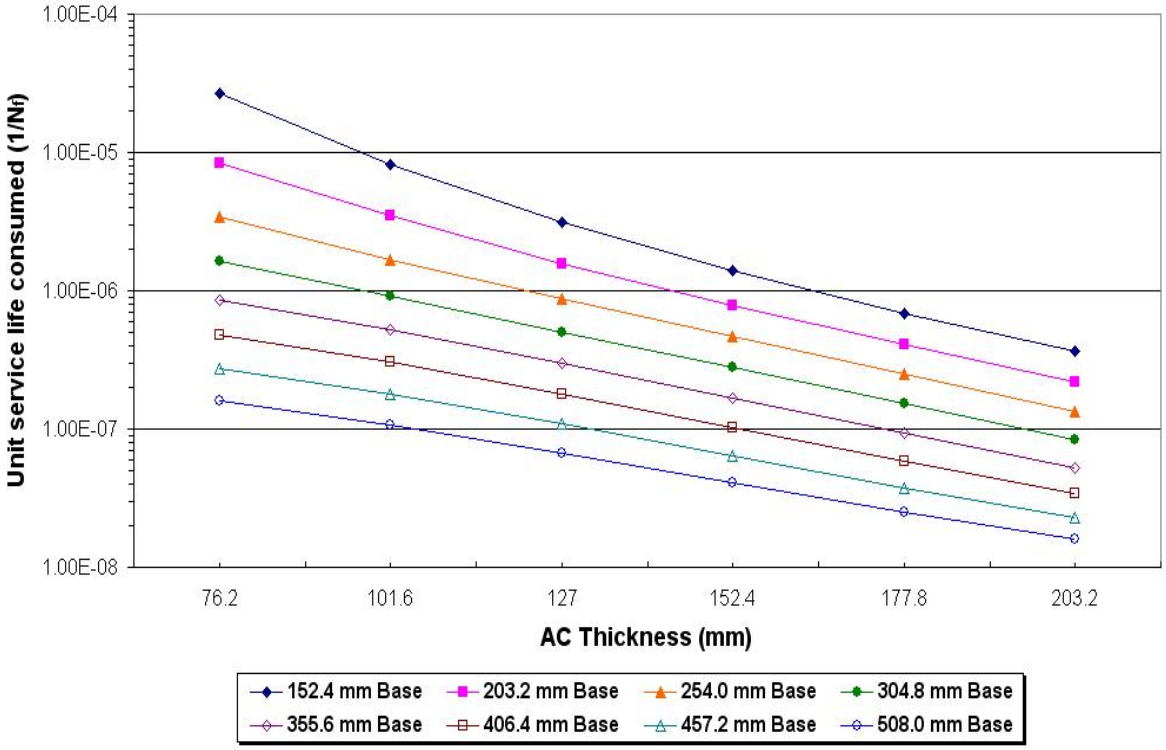

Figure 6.16. Variation of $1/N_f$ with AC and Base Thickness for Rutting in Case 2 (80/20)

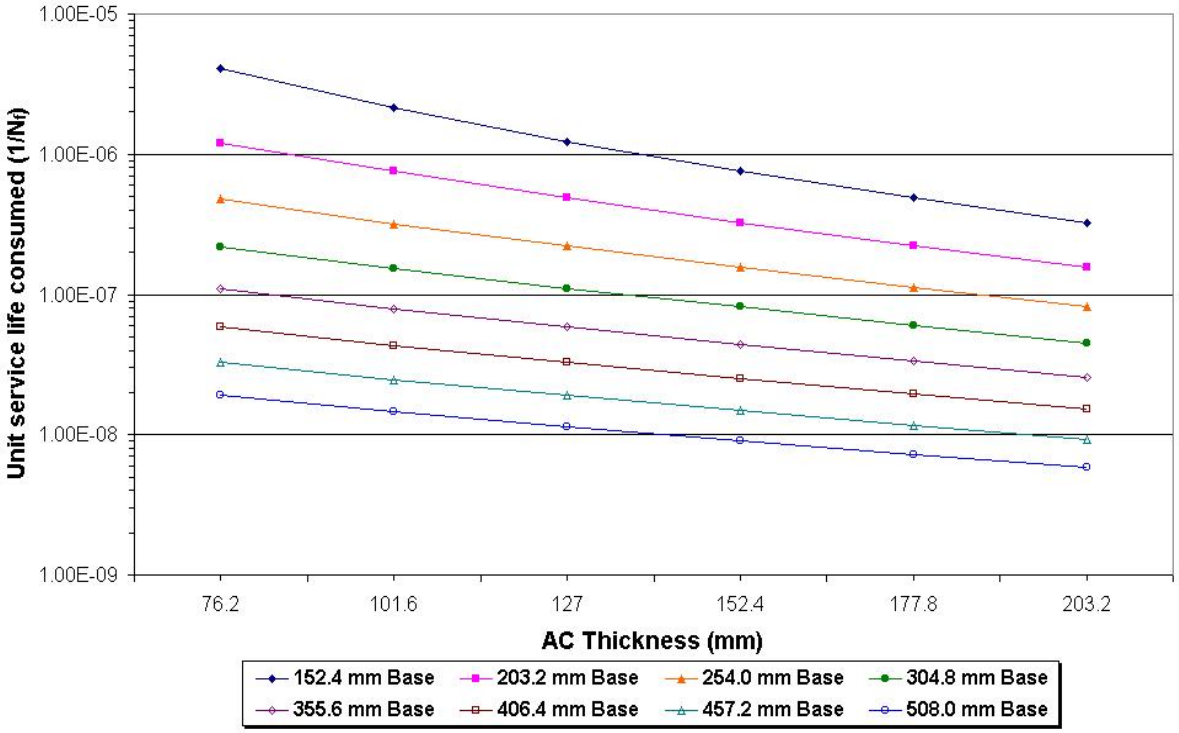

Figure 6.17. Variation of $1/N_f$ with AC and Base Thickness for Rutting in Case 3 (50/50)

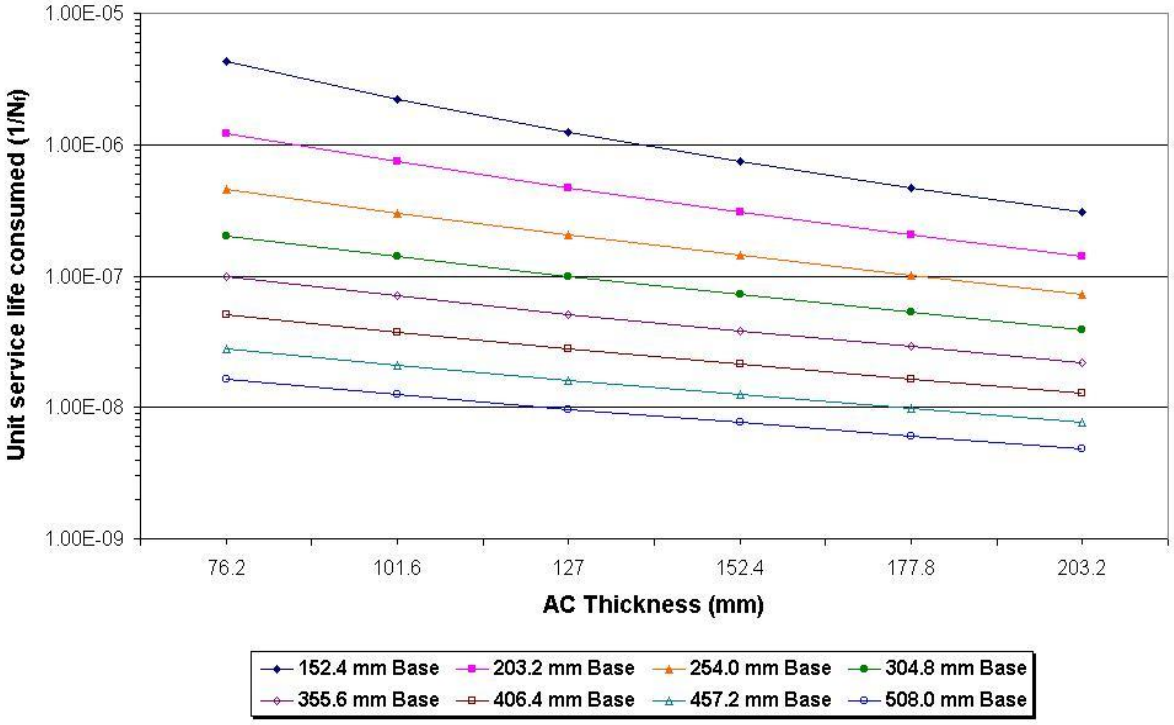

Figure 6.18. Variation of $1/N_f$ with AC and Base Thickness for Rutting in Case 3 (80/20)

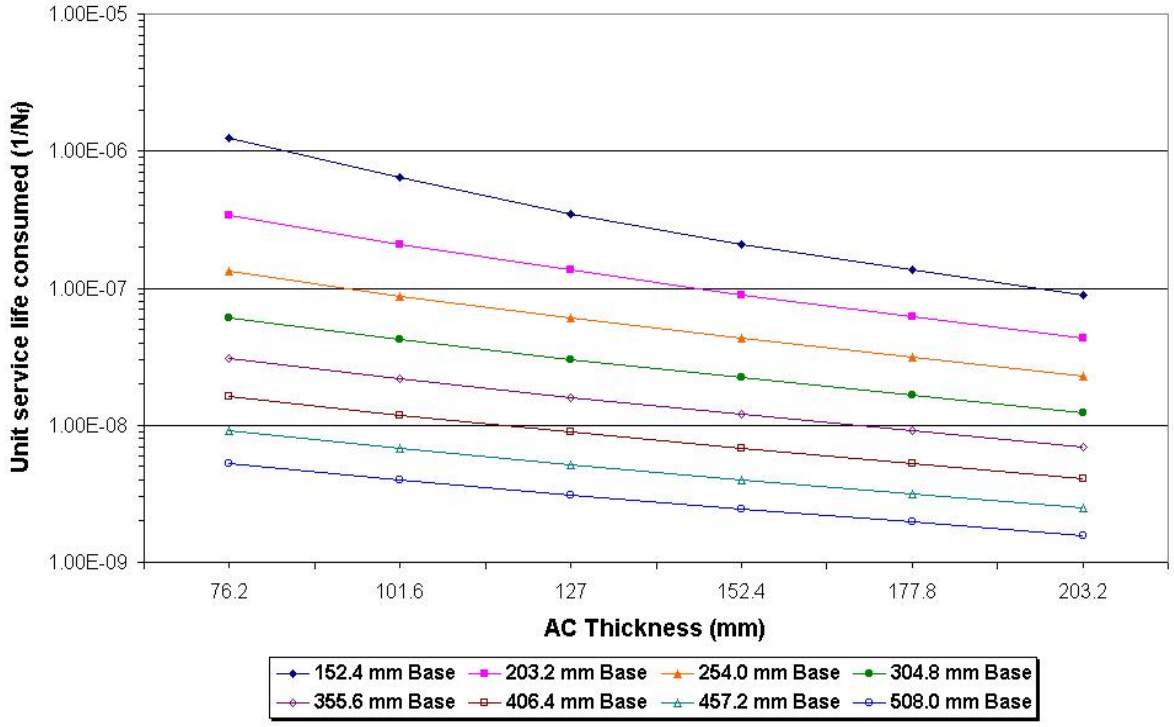

Figure 6.19. Variation of $1/N_f$ with AC and Base Thickness for Rutting in Case 4 (50/50)

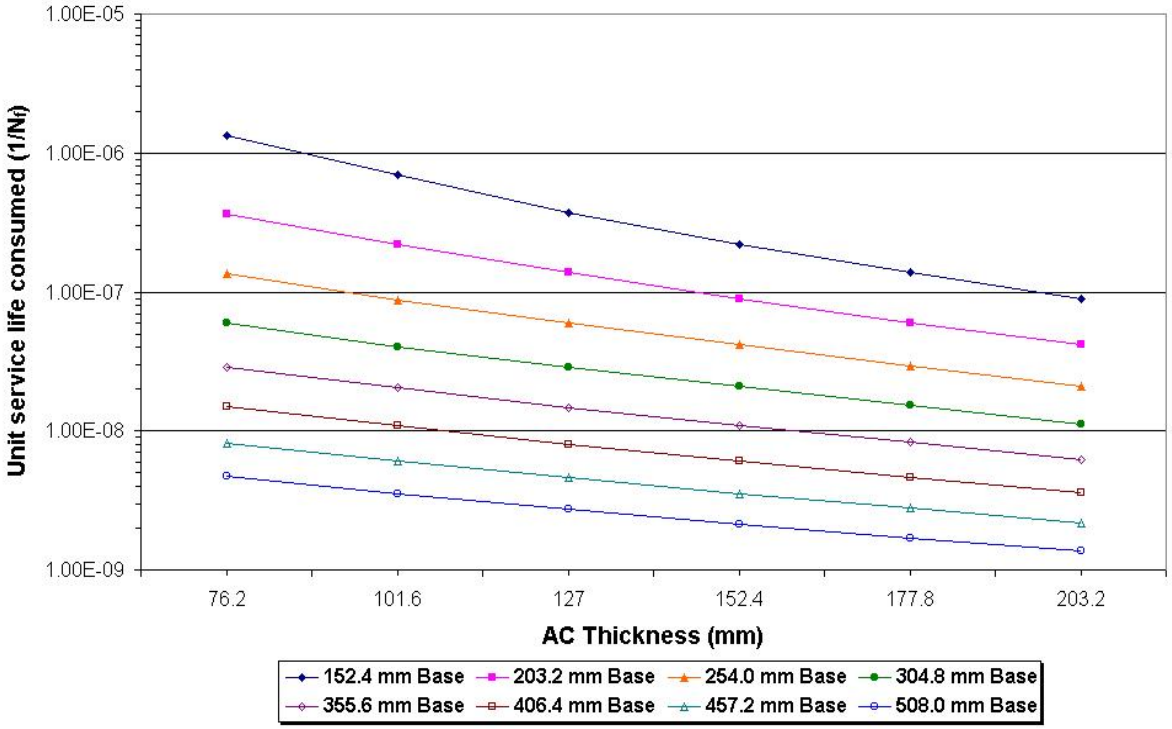

Figure 6.20. Variation of $1/N_f$ with AC and Base Thickness for Rutting in Case 4 (80/20)

6.3. APPLICATION OF CROSS-ANISOTROPY IN CHARTS

Charts established in the previous section are developed on the basis of the nonlinear isotropic (NI) condition because the NI model was also qualified as a tool to model pavement response through the model verification presented Chapter IV. First of all, it was difficult to integrate the cross-anisotropic model into the developed OTRA program due to its complexity. However, it needs to take into account the nonlinear cross-anisotropic (NA) characteristic of pavement materials in order to make the assessment of pavement response due to OTTs more reliable based on findings of this study. To achieve this, firstly, the task to investigate the change of the amount of critical strains obtained by the NA model compared to the NI model was conducted when the same pavement geometry condition and traffic loading was given. A number of runs were made by the NCPA program to obtain the critical strains under the LI, NI, NA, and NNA model in different pavement conditions

corresponding to the cases mentioned earlier. The thickness of the base and the AC varied in the same range used in the previous analysis. The NNA model represents all layers including the AC which are treated by the NA model. The determined the cross-anisotropic properties for different types of material tabulated in Table 6.1 that were used in this analysis. The calculated compressive stains at the top of the subgrade are plotted against the allowable number of load applications (N_f). Because the AI equation to evaluate the allowable number of applications was developed by calibrating to field data, it did not consider any effect of stress dependency or cross-anisotropy. So, it is identical to the LI condition. Therefore, each strain from the NI, NA, and NNA model is matched with the same allowable number of applications estimated by the LI model. From this, it is reasonable to find a specific shift factor among the strains. The results of these analyses are presented in Figures 6.20 to 6.23.

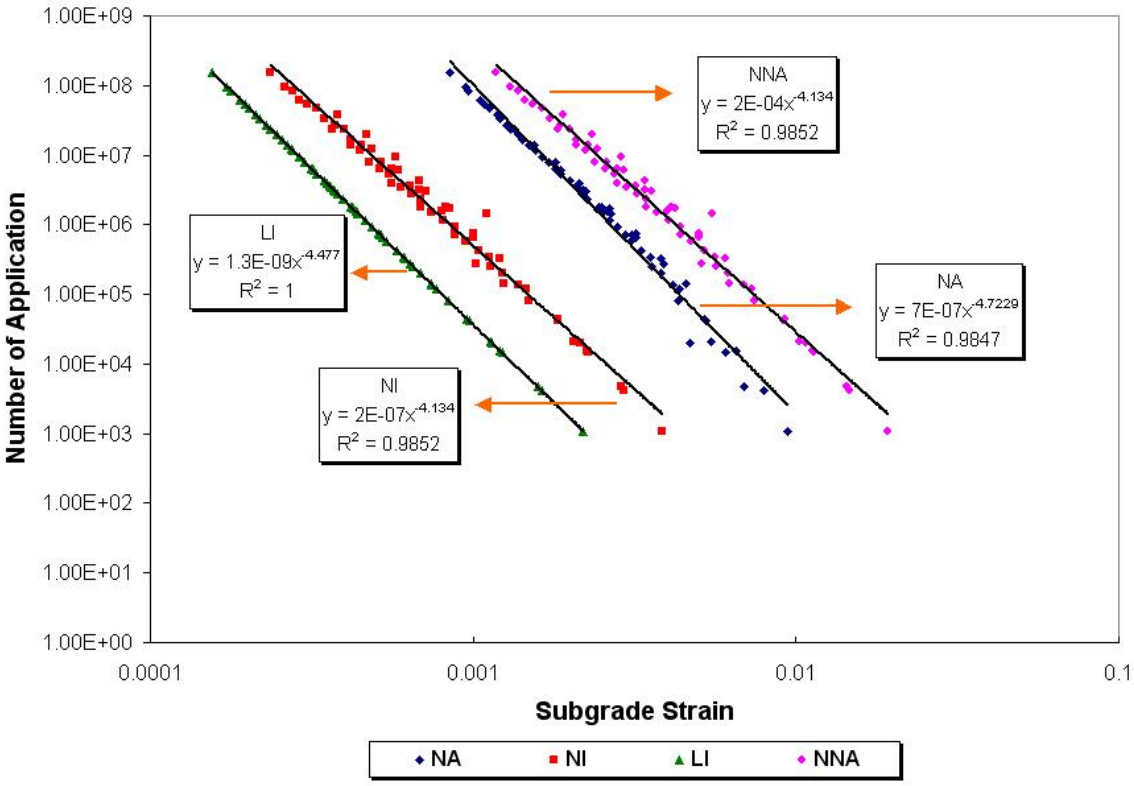

Figure 6.21. Shift of Critical Strain at the Top of the Subgrade in Case 1

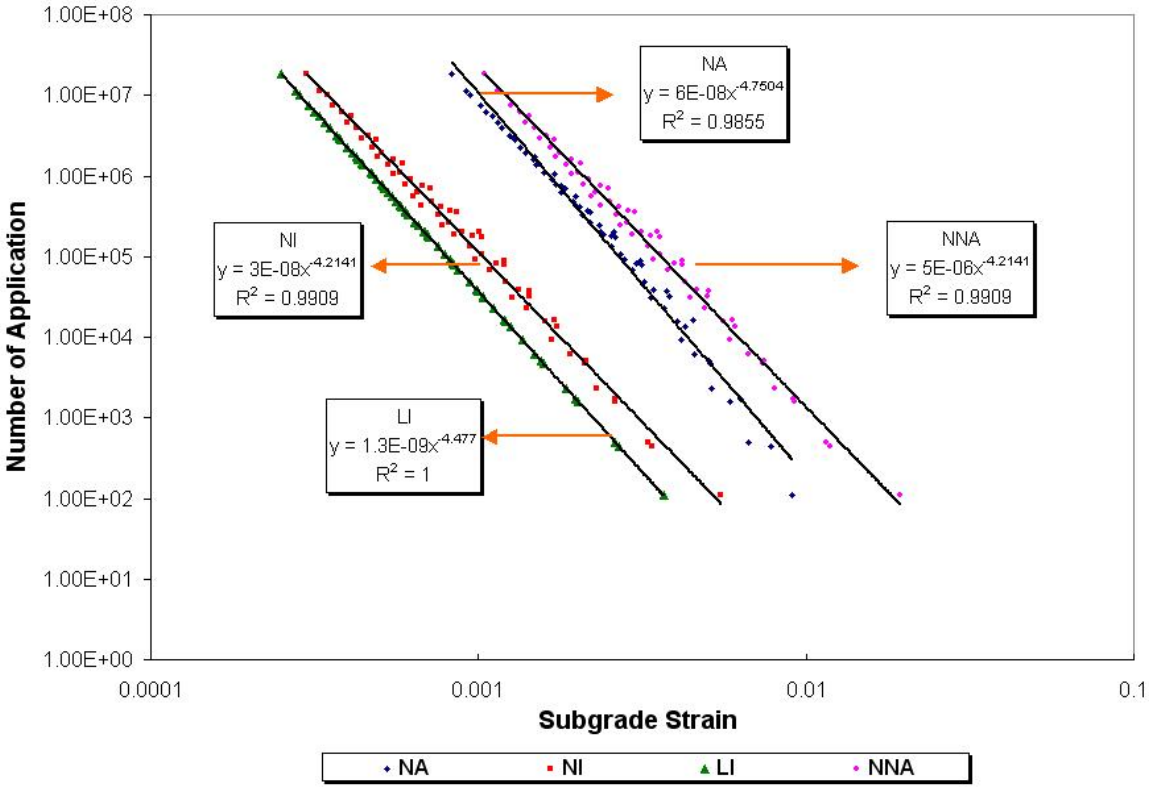

Figure 6.22. Shift of Critical Strain at the Top of the Subgrade in Case 2

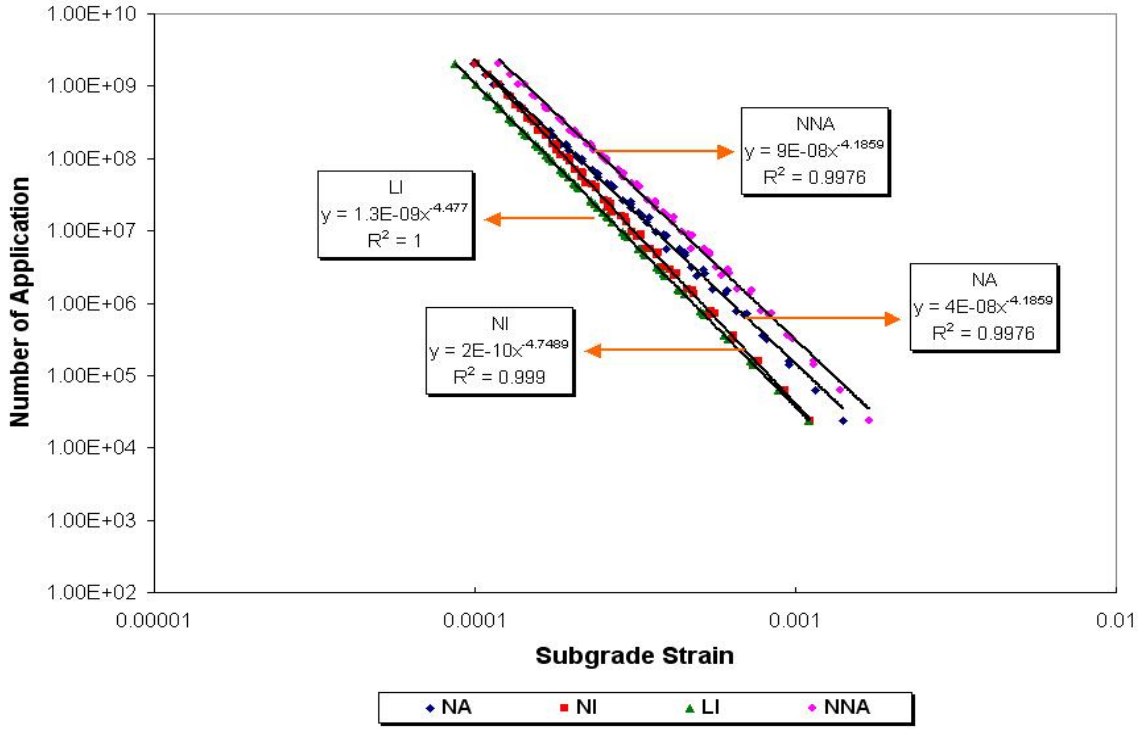

Figure 6.23. Shift of Critical Strain at the Top of the Subgrade in Case 3

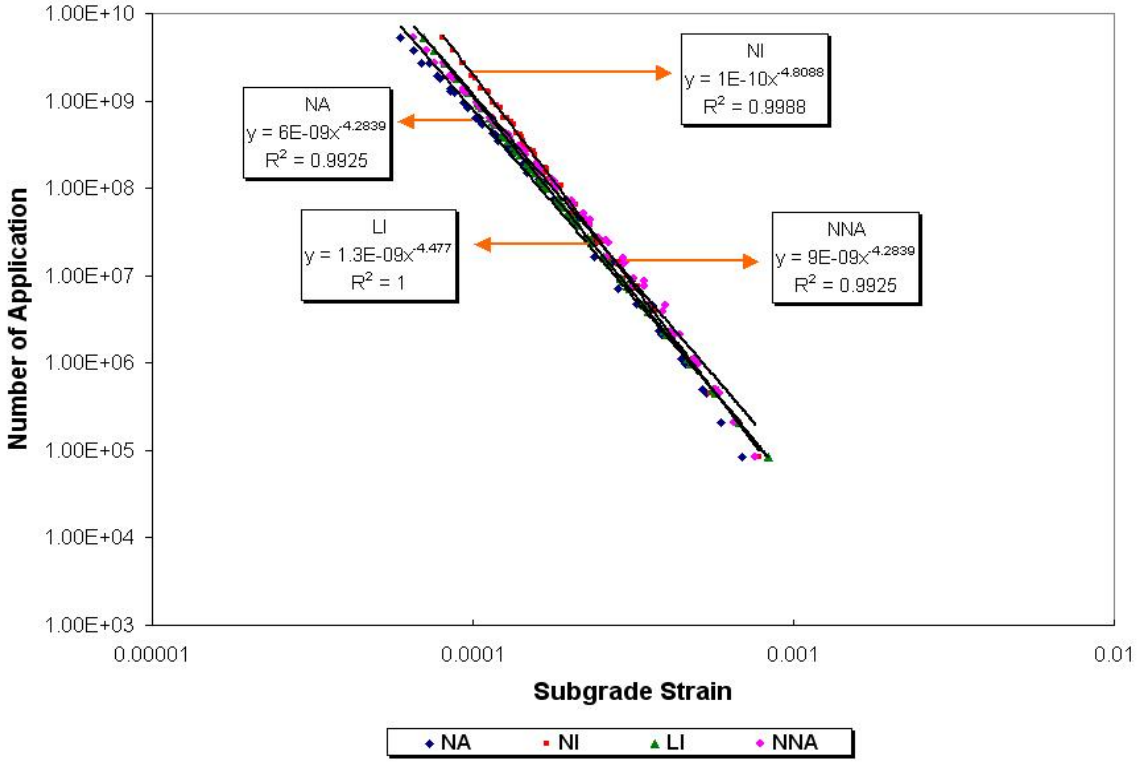

Figure 6.24. Shift of Critical Strain at the Top of the Subgrade in Case 4

An evidence of the shift of the critical strain at the top of the subgrade layer under the center of the loading was detected from this task. As the base layer becomes weaker as in case 1 and case 2, the shift of the strain was much clearer. As expected, the NNA model allowed larger strain due to the reduced horizontal modulus reflecting the characteristic of the cross-anisotropy. However, in cases 3 and 4 where the base layer was stabilized with a high resilient modulus the strain was not significantly influenced by the cross-anisotropic condition. Even all of the strains calculated from the 4 models show a similar trend in case 4 which has a stiff subgrade in which the horizontal modulus is 1.2 times larger than vertical modulus. It is considered that the trend reflects effectively the smaller pavement response due to the enhanced spread of the loading caused by the increased horizontal modulus. From the above, an attempt was made in order to identify the shift factor between the NI and NNA

models. The reason to select the NNA model instead of the NA model is that the NNA model gives larger crucial strains resulting in the conservative performance prediction. The NI model in case 4 can be used without consideration of anisotropy because there is no significant difference between the prediction from the NI model and NNA or NA model. The shift factor was determined by taking the ratio of strains obtained by the NNA model to the NI model. The statistic results are presented in Table 6.5.

Table 6.5. Shift Factor of the Subgrade Strain for Each Case

	N	Mean	Std. Deviation	Variance
Case 1	48	5.07	0.59	0.36
Case 2	48	3.47	0.34	0.12
Case 3	48	1.37	0.11	0.12

After the determination of the above shift factor, the OTRA program was run taking into account the shift factor by following the same procedure described in section 6.2.4. From this, charts are established considering the cross-anisotropic condition and are plotted with the original charts based on the NI model as shown in Figures 6.25 to 6.30. In these figures, the dotted lines present the NI estimation. It was observed that there is an evident shift in the curves. A higher unit service life consumed was generated by adopting cross-anisotropy which will lead to shorter service life.

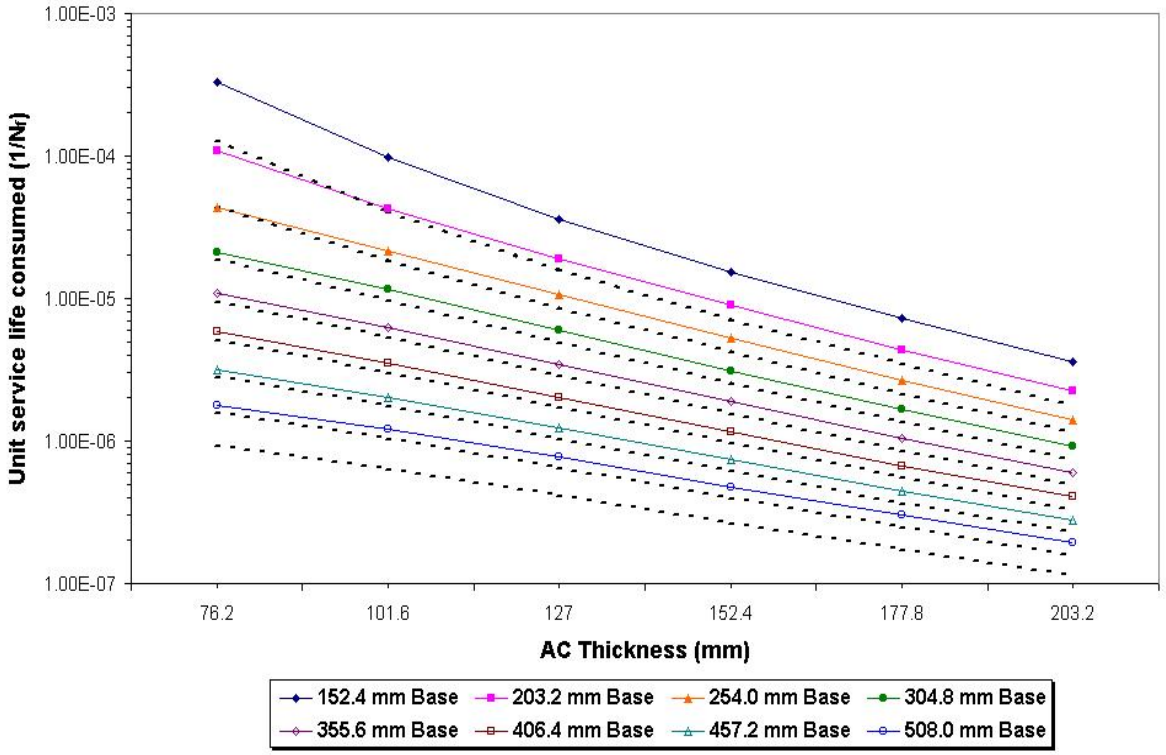

Figure 6.25. Comparison of $1/N_f$ Calculated between the NNA and NI Models for Rutting in Case 1 (80/20)

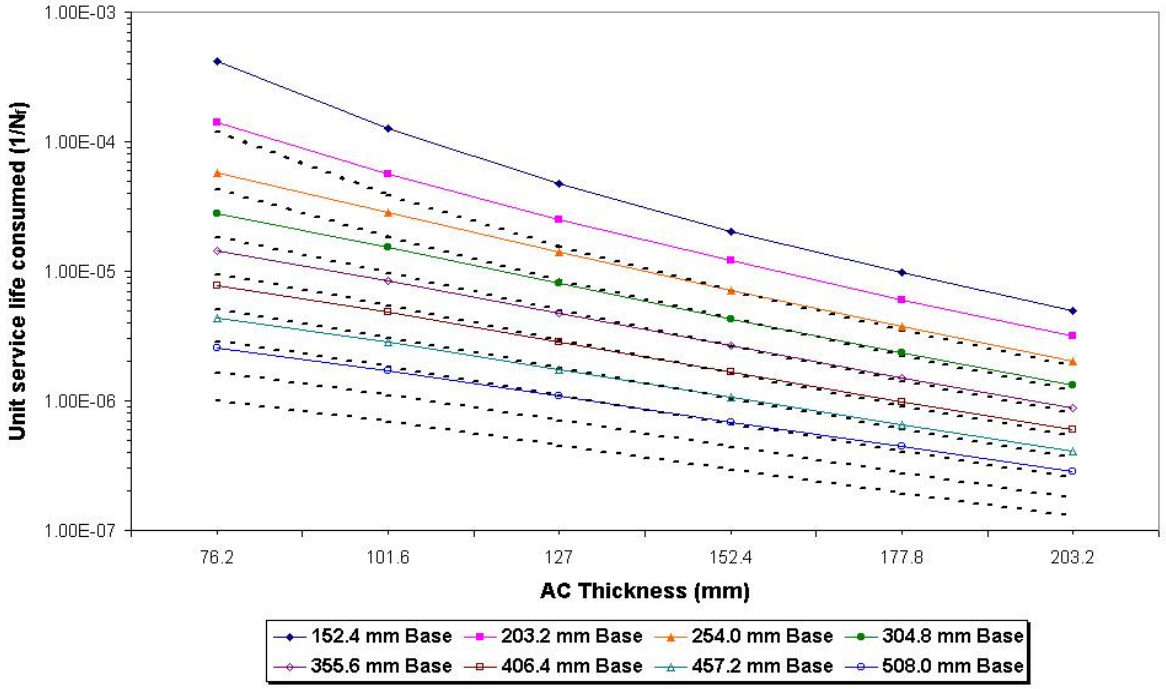

Figure 6.26. Comparison of $1/N_f$ Calculated between the NNA and NI Models for Rutting in Case 1 (50/50)

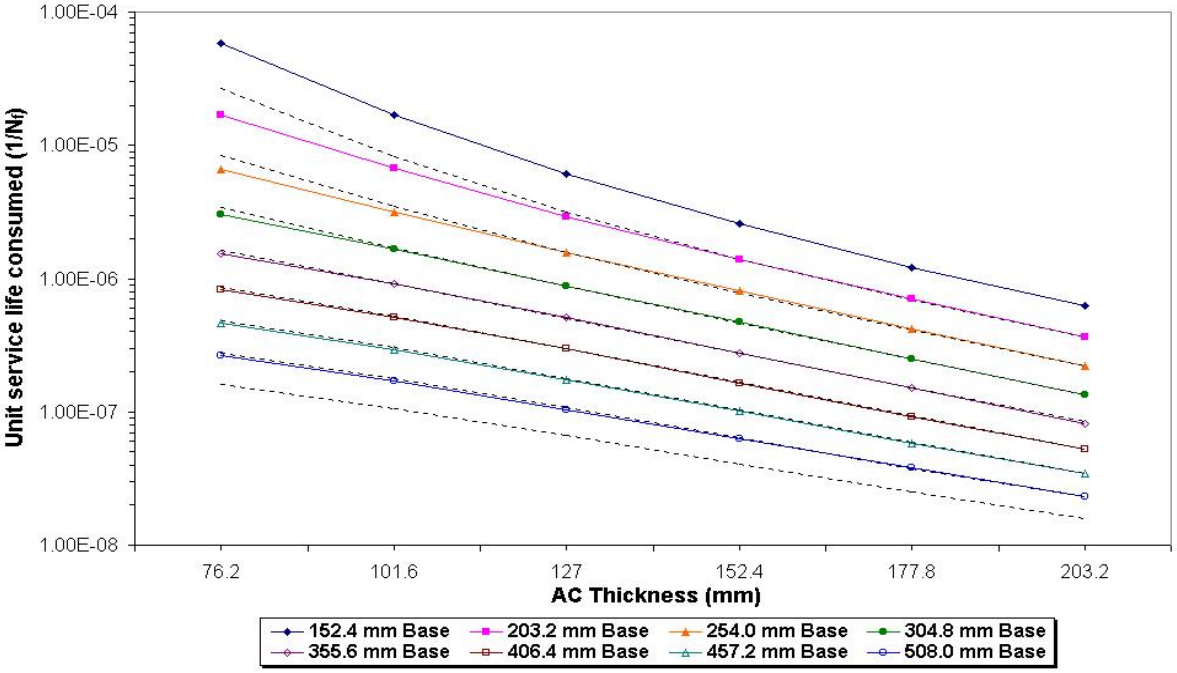

Figure 6.27. Comparison of $1/N_f$ Calculated between the NNA and NI Models for Rutting in Case 2 (80/20)

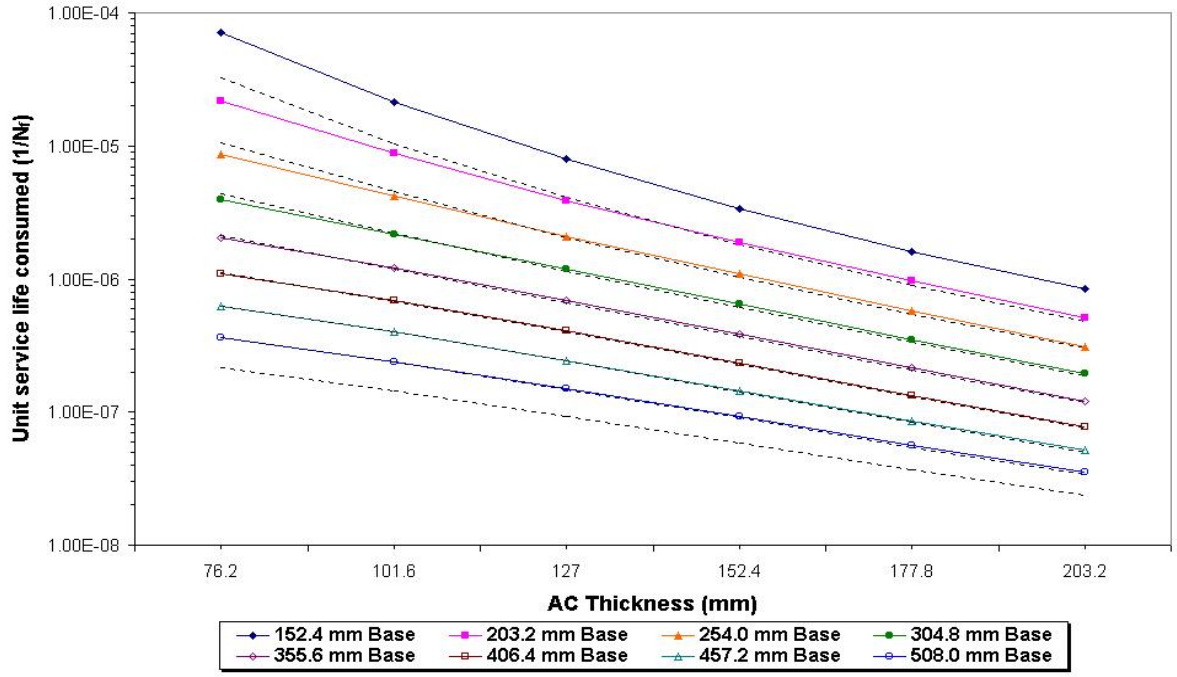

Figure 6.28. Comparison of $1/N_f$ Calculated between the NNA and NI Models for Rutting in Case 2 (50/50)

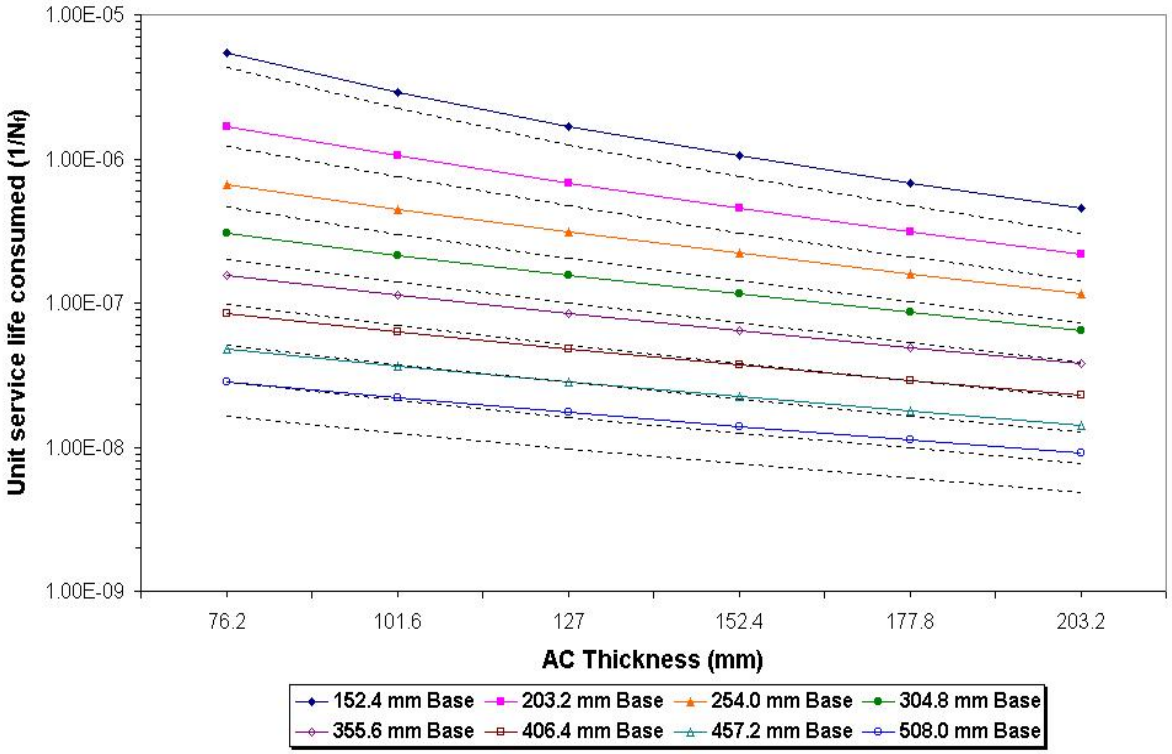

Figure 6.29. Comparison of $1/N_f$ Calculated between the NNA and NI Models for Rutting in Case 3 (80/20)

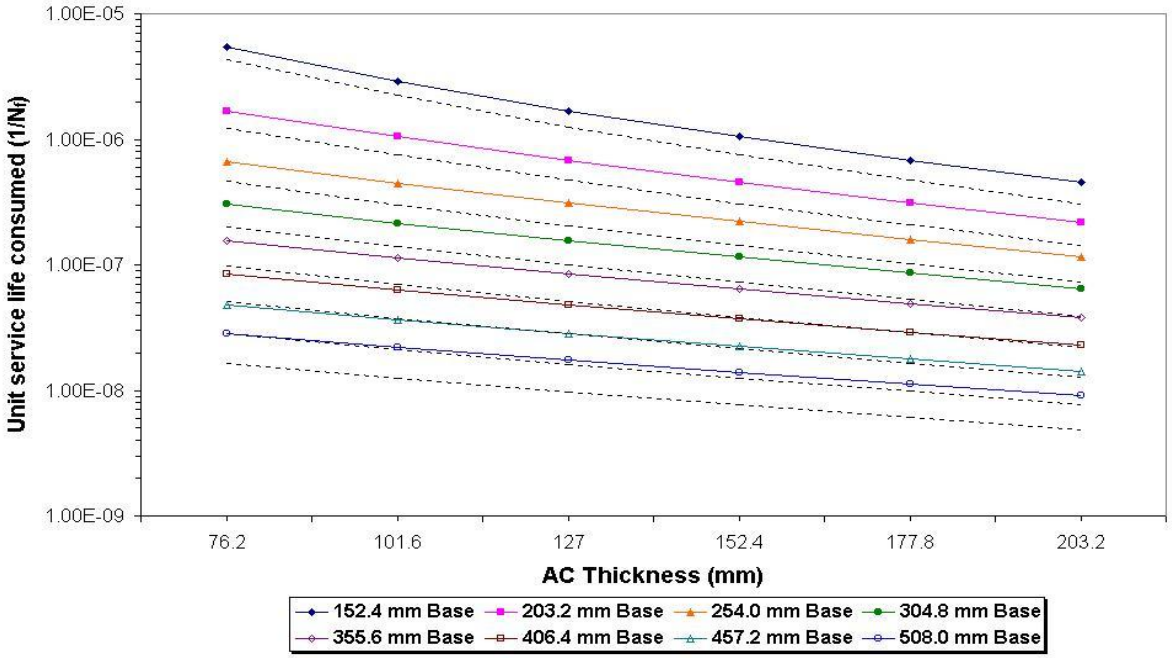

Figure 6.30. Comparison of $1/N_f$ Calculated between the NNA and NI Models for Rutting in Case 3 (50/50)

The same attempt was made to determine the shift factor in the AC strain. The number of load applications at failure for this distress was determined using equation (5.3) based on the LI model. Then the calculated AC strains from the different models were matched with the number of applications obtained by the LI model in order to check the extent of the shift of the AC strain. For the NNA model, two levels of n in the AC material were assumed to be 0.5 and 0.8. The results are presented in Figures 6.31 to 6.34. It was found that the extent of the shift was not as significant as with rutting. The NA model gave the highest AC strain. Thus, additional charts to adopt the NA model were established because it showed the highest AC strain. The AC strain calculated by the NNA with the value of n equal to 0.8 ranged between that of the NI and NNA model while the AC strain with n equal to 0.5 was between the NI and LI model. This confirms the finding, which was mentioned in chapter V, that larger fatigue cracking is expected with the NI model when the n value of the AC is larger than 0.6. Using anisotropic properties in the AC layer predicts a longer fatigue life and a lesser shift factor between the laboratory and field condition. The NI model in case 4 can be used without consideration of anisotropy because there is no significant difference between the prediction from the NI, NNA, or the NA models. The shift factor was determined by taking the ratio of strains obtained by the NA model to those of the NI model. The statistical results are presented in Table 6.6.

Table 6.6. Shift Factor of the AC Strain for Each Case

	N	Mean	Std. Deviation	Variance
Case 1	48	1.35	0.39	0.26
Case 2	48	1.23	0.24	0.11
Case 3	48	1.16	0.15	0.10

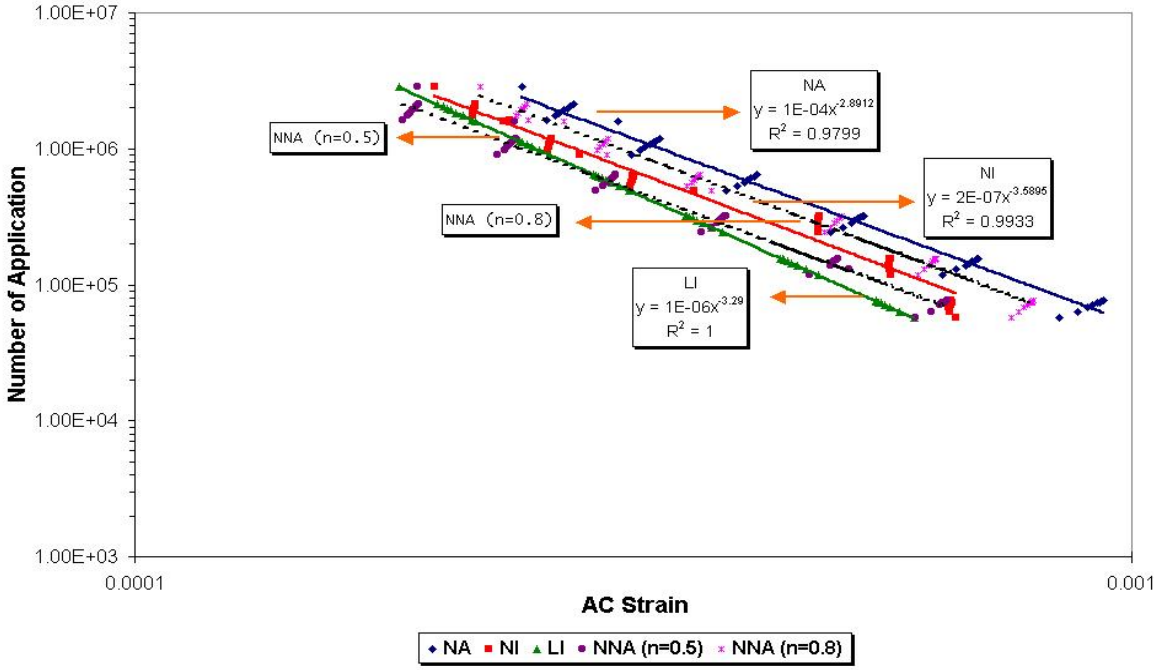

Figure 6.31. Shift of AC Strain at the Bottom of the AC in Case 1

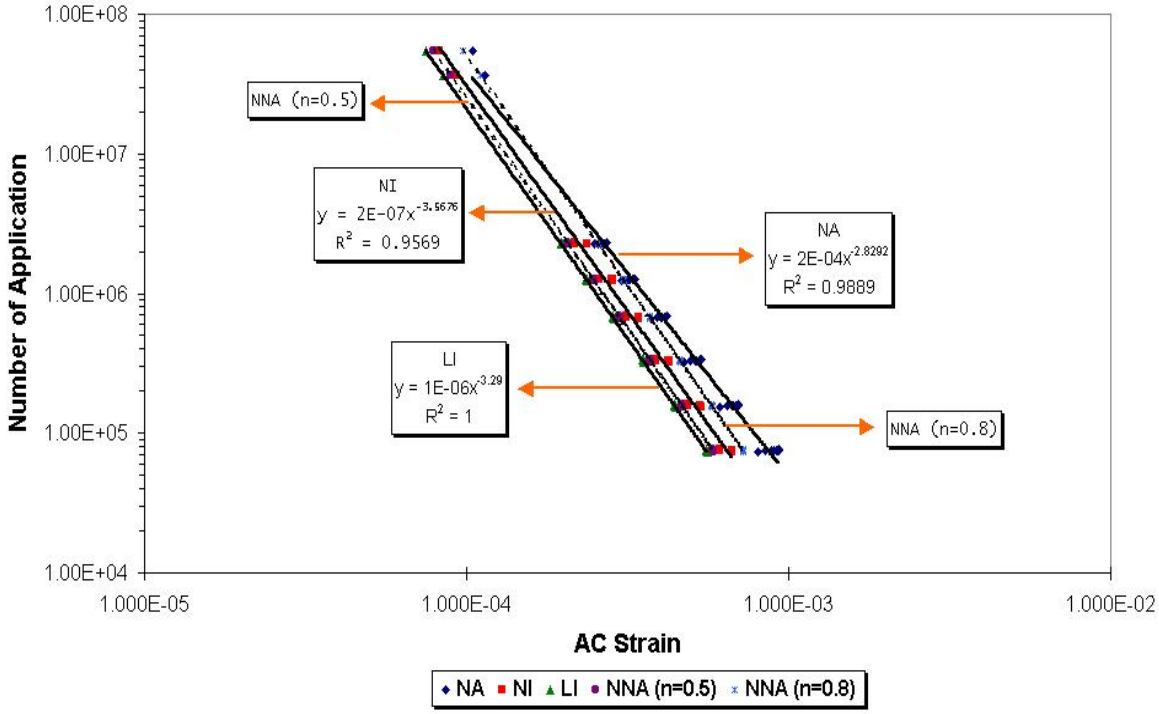

Figure 6.32. Shift of AC Strain at the Bottom of the AC in Case 2

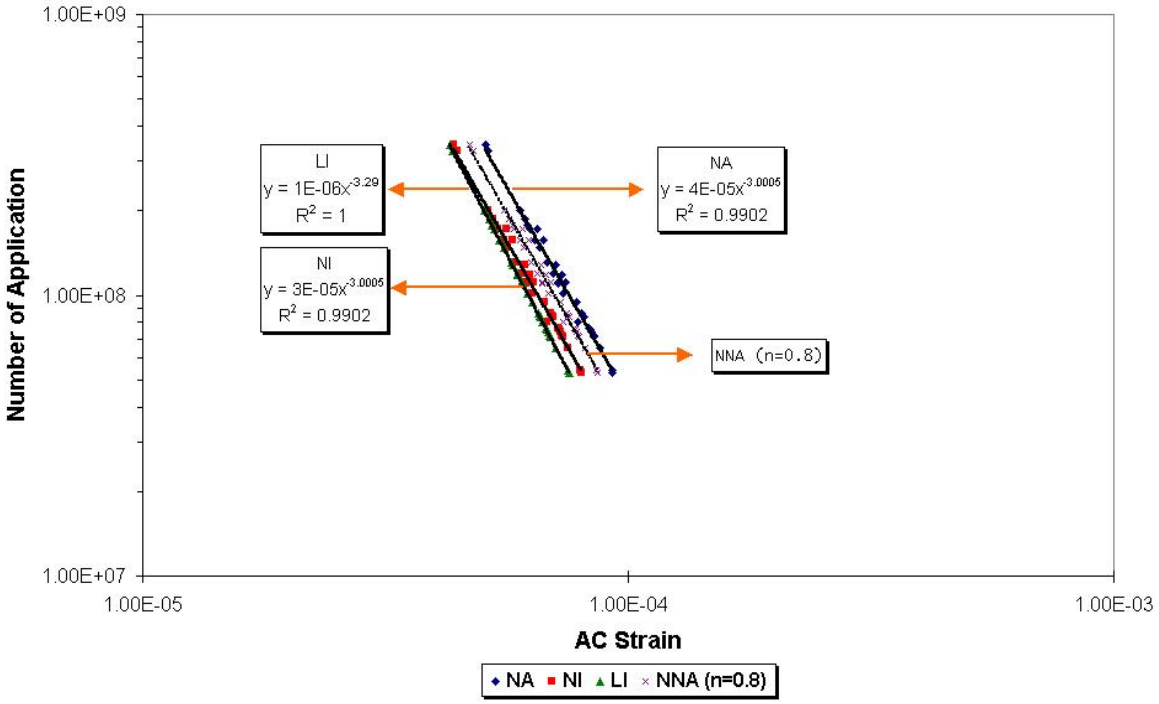

Figure 6.33. Shift of AC Strain at the Bottom of the AC in Case 3

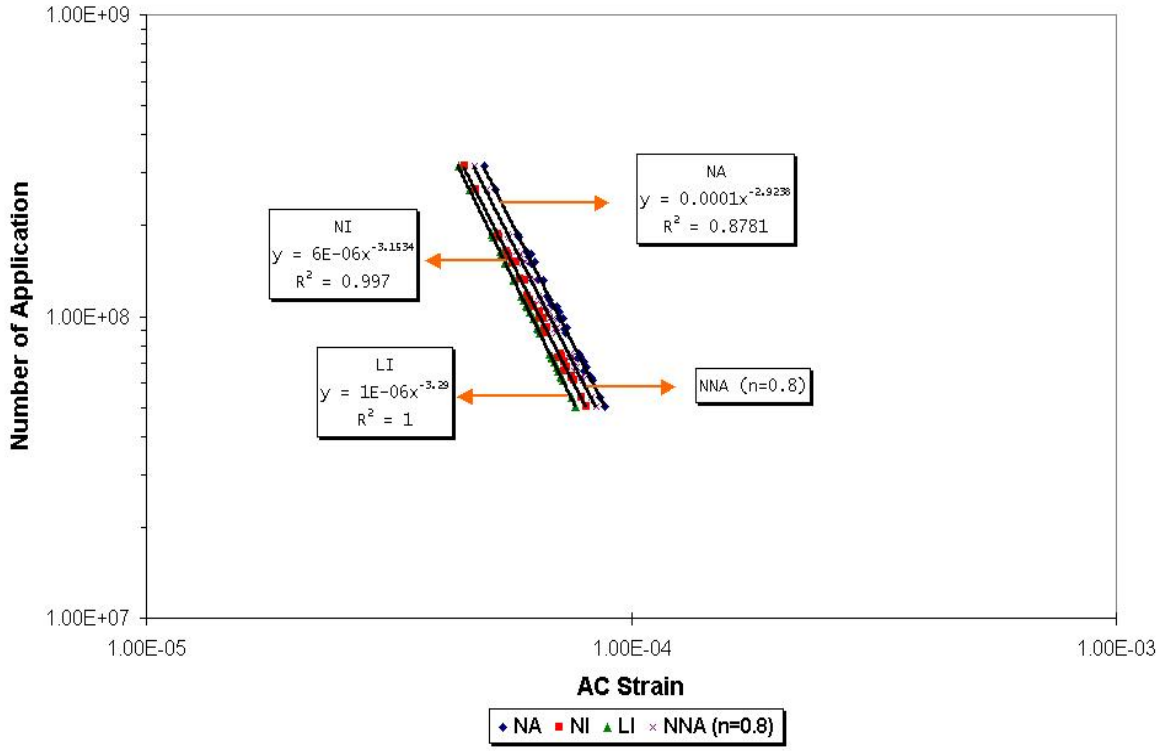

Figure 6.34. Shift of AC Strain at the Bottom of the AC in Case 4

After the determination of the above shift factor, the OTRA program was run taking into account the factor by following the same procedure described in section 6.2.4. From this, charts are established considering the cross-anisotropic condition and plotted with the original charts based on the NI model as shown in Figures 6.35 to 6.37. In these figures, the dotted lines present the NI estimation. It was observed that there is an evident shift in curves. A higher unit service life consumed was generated by adopting cross-anisotropy which will lead to a shorter service life although a relatively smaller shift factor was determined for fatigue cracking as compared to rutting.

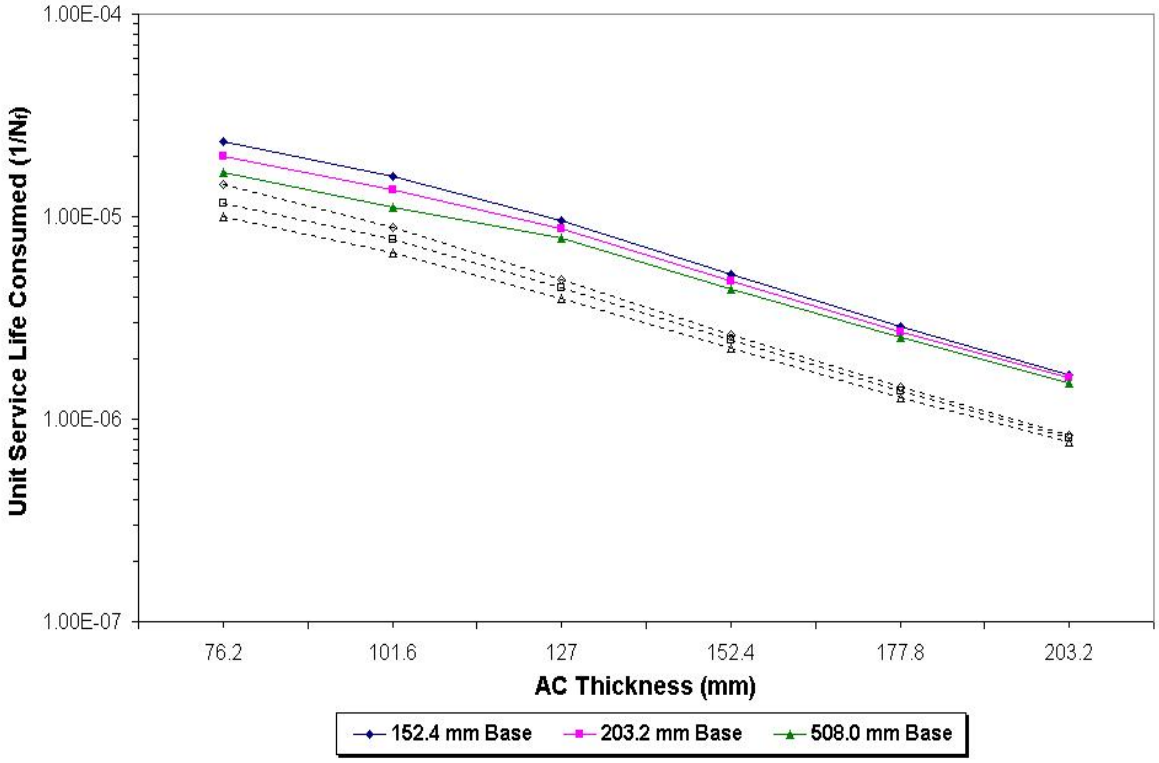

Figure 6.35. Comparison of $1/N_f$ Calculated between the NA and NI Models for Fatigue Cracking in Case 1 (50/50)

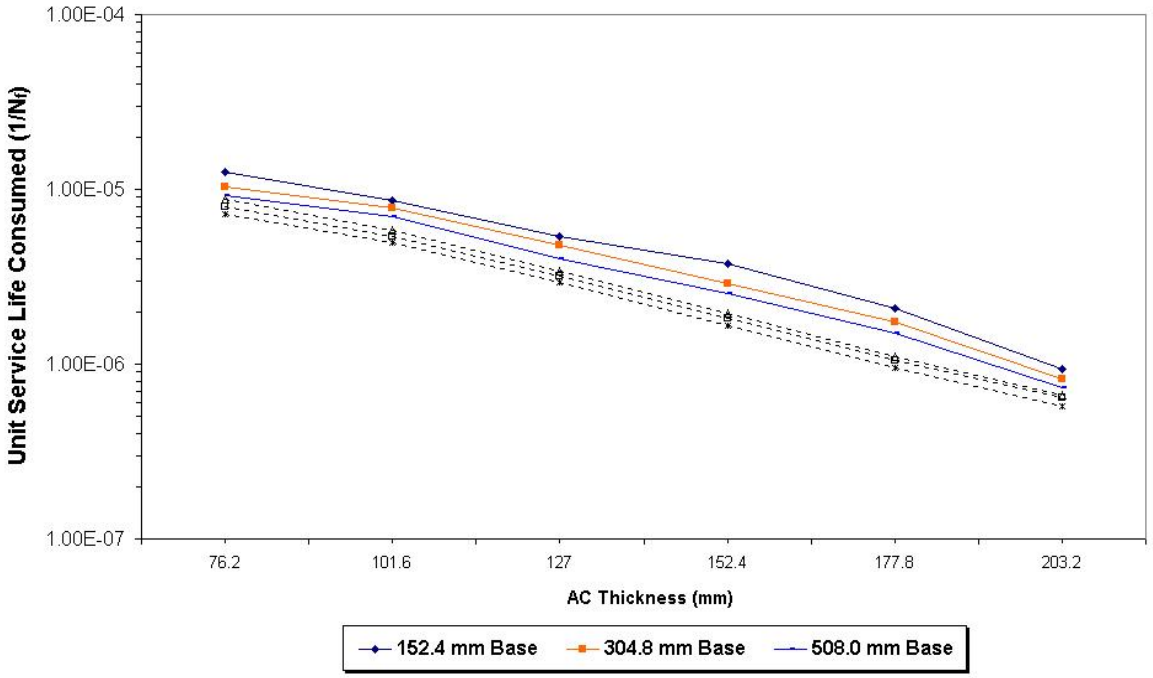

Figure 6.36. Comparison of $1/N_f$ Calculated between the NA and NI Models for Fatigue Cracking in Case 2 (50/50)

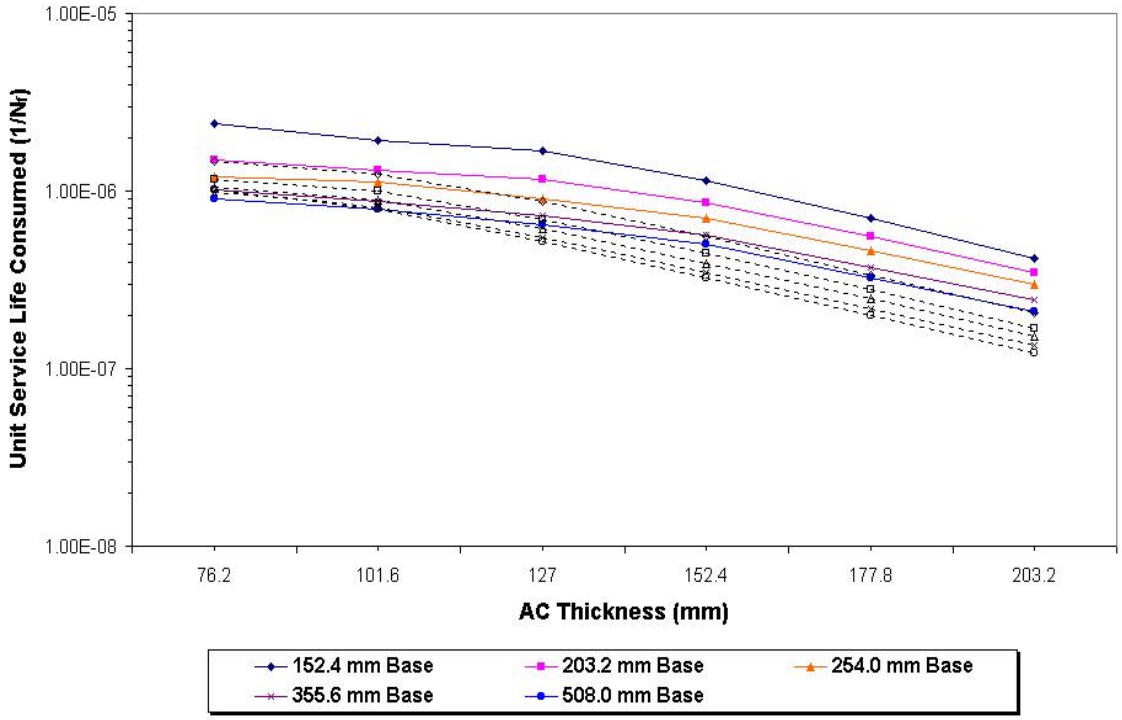

Figure 6.37. Comparison of $1/N_f$ Calculated between the NA and NI Models for Fatigue Cracking in Case 3 (50/50)

6.4. APPLICATION OF CHARTS IN PRACTICE

This section shows an example how to use charts to determine the service life. The pavement structure considered is composed of 152.4 mm AC, 406.4 mm base layer and subgrade is assumed with 120,000 truck passes per year. The portion of trucks is comprised of 30 percent OTTs and 70 percent legal trucks. Based on the results of the DCP and the FWD test, the section is classified as case 1 (AC + Weak Base + Weak Subgrade) in accordance with the case separations. A service life to sustain the expected traffic can be determined in terms of rutting and fatigue cracking. Because the portion of overweight trucks is more than 20 %, charts depicted in Figures 6.28 and 6.36 can be used for the two distresses.

The unit service life consumed was determined to be 2.0 E-06 and 8.5 E-07 for rutting in the NNA and NI conditions, respectively. The unit service life consumed for fatigue cracking was determined to be 6.5 E-06 and 2.0 E-06 in the NA and NI conditions. The service life corresponding to the determined unit service life consumed factor can be found in charts 6.7 and 6.8. The service life with a 60,000 truck traffic rate per year is 2.5 years in the NA condition and 8.5 years in the NI condition for the fatigue cracking. For rutting, 8 years and 20 years in the NNA and NI condition were determined. Therefore, fatigue cracking is more critical and requires improving the quality of the AC material through overlay or material replacement.

The application of cross-anisotropy significantly influences the prediction of the service life by showing much shorter service life.

CHAPTER VII

SUMMARY AND CONCLUSIONS

An area influenced by overweight truck traffic is expected to broaden and deepen into the supporting unbound granular materials and subgrade soils. Thus, it is critical to model the behavior of those materials in the assessment of pavement performance in the long term.

Existing pavement design and analysis methods rely on the linear isotropic theory to represent the relationship between repeated traffic loading and induced deformations due to its simplicity in application. However, it often leads to inadequate estimation of stress and strain because pavement materials in reality do not behave as expected. There is strong evidence in the literature that nonlinear elastic models are superior to linear elastic models in characterizing unbound granular materials.

Apart from modeling stress dependent moduli, the development of particulate mechanics enables many researchers to take into account cross-anisotropy in granular materials which is highly related to the particle orientation, random aggregate placement and compaction during construction. In general, granular materials induced by the cross-anisotropic condition become stiffer in the vertical direction than in the horizontal direction. In order to formulate this in the theoretical approach, five elastic constants, which are three moduli and two Poisson's ratios, are required to describe the directional differences in responses.

In this study, the five cross-anisotropy properties of sampled granular materials and an intact Shelby tube sample subgrade soils, were obtained by using modified triaxial tests in the compression and shear stress states. Seven stress states were used in these test sequences. Once the five properties are determined for each stress state, 9 parameters from K_1 to K_9 are

obtained using multiple regression analysis. Those parameters are used to express the modulus in the direction of vertical, horizontal and shear by employing the Uzan model. The estimated moduli are used to obtain the ratio of the horizontal to the vertical modulus to show the extent of anisotropy. The modular ratios, horizontal to vertical modulus, n, and shear to vertical modulus ratios, m, were fairly constant for a specific material at all stress levels. The obtained values of n and m appear to be reasonable when compared with the previous findings conducted by several other studies. It is interesting to find that some of the intact soils present a reverse anisotropic condition that the horizontal modulus is larger than the vertical modulus. The trend frequently takes place in the overconsolidated clay soils. Such clays possess a greater load spreading capacity than normally consolidated clay and thus it may have a significant influence on the pavement response.

In this study, the nonlinear cross-anisotropic pavement analysis (NCPA) finite element program was developed by modifying previous programs. Three parameters (K_1 ~ K_3) and the Poisson's ratio and moduli ratios (n, m and p) are used to represent the stress dependent cross-anisotropic condition. Once the vertical moduli converge, the horizontal and shear modulus automatically converged by the operation of the n, m, and p values. This removes the necessity to converge each of the three moduli using the 9 parameters (K_1 ~ K_9). The calculation of cross-anisotropy was verified by comparing the results with theoretical solutions and the CIRCLY program. The results are quite comparable and successfully remove the tensile horizontal stress at the bottom of base layer which is typically generated by the isotropic solution. In addition to the nonlinear cross-anisotropy tool, the program is capable of performance prediction with respect to both rutting and fatigue cracking under observed different seasonal conditions. To evaluate the damage due to rutting, permanent deformation tests of sampled materials were performed. Model parameters, which fit the

VESYS and Three-Parameter models, were obtained using nonlinear regression. Two different stress levels were used. The higher deviatoric stress generates the larger plastic strain. It implies that heavy traffic such as OTT can produce larger plastic strain within layers resulting in severe rutting development.

Intensive nondestructive field testing has been conducted at the field test section SH 4/48 located in Brownsville, Texas. The Falling Weigh Deflectometer (FWD) was used to backcalculate layer moduli, the Ground Penetrometer Radar (GPR) was used to identify layer thickness, the Multi-Depth Deflectometer (MDD) was used to measure layer displacements and the Weigh-In Motion (WIM) was used to monitor traffic data. As an experimental trial, the Fiber Fabry-Perot Interferometer (FFPI) optical sensor was used to monitor traffic load data. In this study, it appeared to be a promising tool but it still needs to be calibrated and modified to obtain better results. To characterize seasonal change during the study, the Time Domain Reflectometry (TDR) equipment was used to measure moisture variation and a number of thermocouples were used to investigate the change of temperature. The data were stored in the installed weather station. As a result, measurements were made in three seasonal terms and the data were used for the prediction of pavement performance.

Different material constitutive models such as linear isotropy (LI), linear anisotropy (LA), nonlinear isotropy (NI), and nonlinear anisotropy (NA) were used to predict vertical pavement displacement under load were and compared with values measured by MDD. Both FWD loads and a number of OTTs were imposed at the MDD sensor locations. An improvement of accuracy in analysis was achieved by recording the offset distance between the MDD sensor and the tire positions, the AC temperature, traffic time, and axle weight from a nearby WIM station. As a result, the NA model was considered as the most appropriate model in the assessment of pavement response by exhibiting the least variance

between model predictions and test data. The reduction of the horizontal modulus and elimination of tensile horizontal stress within granular materials and subgrade contributes to larger deformations in the vertical direction. In addition, the reduced horizontal modulus induces self-confinement in the horizontal direction so that the tensile horizontal stress is reduced.

Additional model verification was conducted through an evaluation of rutting and fatigue cracking. Rutting was predicted by integrating the layer strain multiplied by the permanent deformation property, estimating the equivalent single axle load (ESAL), and seasonal variation so as to compare with field measurements taken by a rut-bar. Fatigue cracking was predicted using the result of creep-compliance tests, cracking initiation length and seasonal AC modulus to match with field measurement. In this analysis, the cross-anisotropic characteristic of the AC layer was introduced and applied to predict the performance. It was observed that larger rutting and fatigue cracking were produced when the layers were modeled with the anisotropic condition and the resulting prediction matched field measurement well. Modeling of the AC accounting for the directional modulus can be a promising tool in the assessment of pavement performance.

The sensitivity of stress dependent and cross-anisotropic properties to the displacement and critical strains were investigated. In the stress dependent parameters (K_1 ~ K_3), predicted displacements and critical strains was most sensitive to the parameter K_1. An increase in K_1 results in higher resilient modulus and leads to a decrease of deformations. Among the cross-anisotropy parameters (n, m, and p), an appreciable sensitivity of all deformations to variations in both n and m was revealed. This means that the pavement response depends highly on the ratio of horizontal to vertical modulus. As the three ratios

increase to 30 percent, displacements decrease from 10 to 30 percent. It is apparent that higher level of anisotropy is more critical in its effects on pavement response.

Charts to evaluate the service life of an the existing pavement subjected to OTT loading were established. The unit service life consumed ($1/N_f$) was employed to assess the damage potential under different combinations of pavement thickness, traffic, and material properties which represent both stiff and weak support layers. Basic charts based on the NI model were used as the first level assessment and additional charts accounting for the cross-anisotropy were also developed to be used. There was a specific shift between curves generated from the NI to the NA model curves and the latter provided a more critical result in the prediction of service life with respect to the rutting and fatigue cracking.

REFERENCES

Adu-Osei.(2000). "Characterization of Unbound Granular Layers in Flexible Pavements." *Ph.D. Dissertation*, Texas A&M University, College Station, TX.

Asphalt Institute. (1982). "Research and Development of the Asphalt Institute's Thickness Design Manual (MS-1) Ninth Edition." *Research Report No. 82-2*, Asphalt Institute, Lexington, KY.

Balbissi, A.H. (1983). "A Comparative Analysis of the Fracture and Fatigue Properties of Asphalt Concrete and Sulphlex." *Ph.D. Dissertation*, Texas A&M University, College Station, TX.

Barden, L. (1963). "Stresses and Displacements in a Cross-Anisotropic Soil." *Geotechnique*, 13, 198-210

Bellotti, R., Jamiolkowski, M., Lo Presti, D.C.F., and O'Neill, D.A. (1996). "Anisotropy of Small Strain Stiffness in Ticino Sand". *Geotechnique*, 46, (1), 115-131.

Brown, S.F. (1996). "Soil Mechanics in Pavement Engineering." *Geotechnique*, 46(3), 383-426.

Burmister, D.M. (1943). "The Theory of Stresses and Displacements in Layered Systems and Applications to the Design of Airport Runways." *Proceedings, Highway Research Board*, 23, 126-144.

CIRCLY 4 : User's Manual. MINCAD Systems Pty. Ltd., February 1999.

Cosentino, P.J. and Grossman, B.G. (1997). "Development of Fiber Optic Dynamic Weigh-In-Motion System." *Final Report*, Florida Institute of Technology, Melbourne, FL.

Cunagin, W.D. (1986). "Use of Weigh-In-Motion Systems for Data Collection and Enforcement." *National Cooperative Highway Research Program (NCHRP) Report 124*, Transportation Research Board, Washington, DC.

Dandridge A., Cole, J.H. and Siegel, G.H. Jr. (1984) "Optical Fiber Sensors." *Technical Digest Symposium on Optical Fiber Measurements*, 7, 49-54.

Dolcemascolo, V., Jacob, B., Boutillier, L., and Reversat, B.L.(1998). "Accuracy Assessment of a Low Speed Weigh-In-Motion System." *Second European Conference on WIM of Road Vehicles*, Paris, 345-354.

Duncan, J.M., Monismith, C.L., and Wilson, E.L. (1968). "Finite Element Analysis of Pavements." *Highway Research Record No. 228*, Highway Research Board, Washington DC, 18-33.

Fernando E.G., and Liu W. (1999a). User's Manual for Pavement Dynamic Back-Calculation Procedure with Systems Identification Method (DBSID). *Research Report.* Texas A&M University System. College Station, TX.

Fernando E.G., and Liu, W (1999b). Program for Load-Zoning Analysis (PLZA): User's Guide. *Research Report 2123-1.* Texas Transportation Institute. College Station, TX.

Fernando, E.G., Liu, W., and Ryu, D. (2001). "Development of a Procedure for Temperature Correction of Backcalculated AC Modulus." *Research Report 1863-1.* Texas Transportation Institute. College Station, TX.

Fernando, E.G., and Liu, W. (2004). Program for Overweight Truck Route Analysis (OTRA): User's Guide. *Research Report 4184-2.* Texas Transportation Institute. College Station, TX.

Gazetas, A.M. (1982). "Stresses and Displacements in Cross-Anisotropic Soils." *Journal of Geotechnical Engineering*, 108(4), 532-553.

German, F.P., and Lytton, R.L. (1979). "Methodology for Predicting the Reflection Cracking Life of Asphalt Concrete Overlays." *Report No. TTI-2-8-75-207-5*, Texas A&M University, College Station, TX.

Heukelom, W., and A.J.G. Klomp. (1962). "Dynamic Testing as a Means of Controlling Pavements During and After Construction." *Proceedings, (1st) International Conference on the Structural Design of Asphalt Pavements*, Boston, 667-685.

Hicks, R.G. (1970). "Factors Influencing the Resilient Properties of Granular Materials." *Ph.D. Dissertation*, University of California, Berkeley.

Hicks, R.G. and Monismith, C.L. (1971). "Factors Influencing the Resilient Properties of Granular Materials." *Transportation Research Record No. 345*, Transportation Research Board, National Research Council, Washington, DC, 15-31.

Huang, Y.H. (1993). *Pavement Analysis and Design*. 1st Edition, Prentice Hall, Englewood Cliffs, NJ.

Jacob, B. (1999). "WAVE- European Research Project on Weigh-In-Motion." *Proceedings of the Final Symposium of the Project WAVE (1996-1999)*, Paris, 15-29.

Jahaes, S. (1999). "Tests of WIM Systems in Cold Climates." *Proceedings of the Final Symposium of the Project WAVE (1996-1999)*, Paris, 285-296.

Jooste, F.J., and Fernando, E.G. (1994). "Modeling of Pavement Response Under Superheavy Loads." *Transportation Research Record 1448*, TRB, National Research Council, Washington, DC. 69-74.

Jooste, F.J., and Fernando, E.G. (1995). “Development of a Procedure for the Structural Evaluation of Superheavy Load Routes.” *Research Report 1335-3F*. Texas Transportation Institute. College Station, TX.

Kenis, W.J. (1978). “Predictive Design Procedure, VESYS User’s Manual: An Interim Design Method for Flexible Pavement Using the VESYS Structural Subsystem.” *Final Report No. FHWA-RD-77-154*, Federal Highway Administration, Department of Transportation, Washington, DC.

Kirkpatric, W.M., and Rennie, I.A. (1972). ”Directional Properties of a Consolidated Kaoline”. *Geotechnique,* 22(1), 166-169.

Klemunes, J.J. (1998) “Determining Soil Volumetric Moisture Content Using Time Domain Reflectometry.” *FHWA Report No FHWA-RD-97-139*, Federal Highway Administration, Washington, DC.

Kleyn, E.G. and Savage, P.F. (1982). “The Application of the Pavement DCP to Determine the Bearing Properties and Performance of Road Pavements.” *Proc. of the First International Conference on Bearing Capacity of Roads and Airfields*, Trondheim, Norway. 130-136.

Lee, C.E. and Garner, J.E. (1996). “Collection and Analysis of Augmented Weigh-In-Motion Data.” *Research Report 987-8*, Center for Transportation Research, The University of Texas at Austin.

Leknitskii S. G. (1963) *Theory of Elasticity of an Anisotropic Elastic Body*. Holden-Day, San Franscisco, CA.

Little, D.N. (1987). *Fundamentals of the Stabilization of Soil with Lime*. National Lime Association, Arlington, VA.

Little, D.N. (1994). *Handbook for Stabilization of Pavement Subgrades and Base Courses with Lime (Final Draft)*. National Lime Association, Arlington, VA.

Livneh, M., Ishai, I., and Livneh, N.A. (1995). “Effect of Vertical Confinement on Dynamic Cone Penetrometer Strength Values in Pavement and Subgrade Evaluations.” *Transportation Research Record 1473*, TRB, National Research Council, Washington, DC. 1–8.

Lytton, R.L., Germann, F.P., Chou, Y.J., and Stoffels, S.M. (1989). “Determining Asphaltic Concrete Pavement Structural Properties by Nondestructive Testing.” *National Cooperative Highway Research Program (NCHRP) Report 327*, Transportation Research Board, Washington, DC.

Lytton, R.L. (1983). “System Design of Pavement.” Class notes, CVEN 616, Texas A&M University, College Station, TX.

Lytton, R.L., Pufahl, D.E., Michalak, C.H., Liang, H.S., and Dempsey, B.J. (1990). "An Integrated Model of the Climates Effects on Pavements." *FHWA Report No. FHWA-RD-90-033*, Federal Highway Administration, Washington, DC.

Lytton, R.L. (2000). "Characterizing Asphalt Pavements for Performance." *Transportation Research Record 1723*, TRB, National Research Council, Washington, DC. 5–16.

Lytton, R.L. (2004). Personal Communications, Department of Civil Engineering, Texas A&M University, College Station, TX.

McCall, B. and Vodrazka, W.C. (1997). *State's Successful Practice Weigh-In-Motion Handbook*. Center for Transportation Research and Education, Iowa State University, Ames, IA.

Miner, M.A. (1945). "Cumulative Damage in Fatigue." *Transactions of the ASME*, 67, A159-A164.

MODULUS: User's Manual-Version 6.0. Texas Transportation Institute, Texas A&M University, College Station, TX.

Molenaar, J.M.M., and Molenaar, A.A.A. (2000). "Fracture Toughness of Asphalt in the Semi-Circular Bend Test." Eurasphalt and Eurobitume Congress, September, Barcelona.

Owen, D.R.J., and Hinton, E. (1980). *Finite Elements in Plasticity: Theory and Practice*. Pineridge Press, Swansea, UK.

Park, S.W. (2000). "Evaluation of Accelerated Rut Development in Unbound Pavement Foundations and Load Lmits on Load-Zoned Pavements." *Ph.D. Dissertation*, Texas A&M University, College Station, TX.

Pavement Management Information System Rater's Manual (2002). Texas Department of Transportation, Austin, TX.

Pocket Facts. Field Analytic Technologies Encyclopedia: Ground Penetrating Radar. (http://fate.clu-in.org/gpr.asp?techtypeid=41) Accessed March 23, 2003.

Pocket Facts. Dynatest Consulting Inc., Multi Depth Deflectometer. (http://www.dynatest.com/hardware/CSIR/mdd.htm) Accessed March 20, 2003.

Pocket Facts. Time Domain Reflectometers (TDR). (http://www.sowacs.com/sensors/tdr.html) Accessed March 30, 2003.

Porter, D.W. (1992). Technical Basis of the 1992 Austroads Pavement Design Guide (Flexibel Pavements), *ARRB Transport Research No. RC7095-2*, Melbourne, Austrailia.

Raad, L. and Figueroa, J.L. (1980). "Load Response of Transportation Support Systems." *Journal of Transportation Engineering*, ASCE, 16(TE1), 111-128.

Ramos, S. (2003). “Study of the Asphalt Pavement Damage through Nondestructive Testing on Overweight Truck Routes.” *M.S.* Thesis, Texas A&M University, College Station, TX.

Roesset, J. (2002). MEMA 647 Course Notes. Texas A&M University, College Station, TX.

Sayers M.W., Gillespie, T.D., and Queiroz, C.A.V. (1986). *International Experiment to Establish Correlation and Standard Calibration Methods for Road Roughness Measurements*. The World Bank, Washington DC.

Schapery, R.A. (1973). “A Theory of Crack Growth in Visco-Elastic Media.” *Report NM 2764-73-1*. Mechanics and Materials Research Center, Texas A&M University, College Station, TX.

Scott, M.G., Phang, W.A., and Patterson, D.E. (1983). *Developments in Situ Monitoring of Moisture in Pavement Structures by Time Domain Reflectometry (TDR),* The Transportation Technology and Energy Branch, Ontario Ministry of Transportation and Communications.

Selig, E.T. (1987). “Tensile Zone Effects on Performance of Layered Systems.” *Geotechnique*, 37(3). 247-254.

Sirkis, J.S. (1999). “ Optical Fiber Strain Sensing in Engineering Mechanics.” Short course notes, SPIE’s International Symposium on Smart Structures, Newport Beach, CA.

Soil Survey of Cameron County, Texas. (1977). United States Department of Agriculture in cooperation with Texas Agricultural Experiment Station.

SPSS (2001). The SPSS System for Windows Version 11.0.1. SPSS Inc., Chicago.

Topp, G.C., Davis, J.L., and Annnan, A.P. (1980). “Electromagnetic Determination of Soil Water Content: Measurements in Coaxial Transmission Lines.” *Water Resources Research*, 16(3), 574-582.

Tseng, K-H. (1988). “A Finite Element Methods for the Performance Analysis of Pavement.” *Ph.D. Dissertation*, Texas A&M University, College Station, TX.

Tseng, K-H., and Lytton, R.L. (1989). “Prediction of Permanent Deformation in Flexible Pavement Materials.” *Implication of Aggregates in the Design, Construction, and, Performance of Flexible Pavements, ASTM STP 1016*, ASTM, Philadelphia, PA, 154-172.

Tseng, K-H., and Lytton, R.L. (1990). “Fatigue Damage Properties of Asphaltic Concrete Pavements.” *Transportation Research Record No. 1022*, TRB, National Research Council, Washington, DC, 52-59.

Tutumluer, E. (1995). “Predicting Behavior of Fexible Pavements with Granular Bases.” *Ph.D. Dissertation*, Georgia Institute of Technology, Atlanta, GA.

Tutumluer, E. and Thompson, M.R. (1997) "Anisotropic Modeling of Granular Bases in Flexible Pavements." *Transportation Research Record No. 1577*, TRB, National Research Council, Washington, DC, 18-26.

U.S. Army Engineer Waterways Experiment Station (1960). *The Unified Soil Classification System*. Technical Memorandum No. 3-357, Appendix A, Characteristics of Soil Groups Pertaining to Embankments and Foundations, 1953; Appendix B, Characteristics of Soil Groups Pertaining to Roads and Airfields, 1957.

Uzan, J. (1985). "Characterization of Granular Material." *Transportation Research Record No. 1022*, TRB, National Research Council, Washington, DC, 52-59.

Uzan, J. (1992). "Resilient Characterization of Pavement Materials." *International Journal for Numerical and Analytical Methods in Geomechanics,* 16, 435-459.

Van Til, C.J., McCullough, B.F., Vallerga, B.A., and Hicks, R.G. (1972). "Evaluation of AASHTO Interim Guides for Design of Pavement Structures." *NCHRP 128*, Highway Research Board

Ward, W.H., Samuels, S.G., and Gutler, M.E. (1959). "Further Studies of the Properties of London Clay". *Geotechnique*, 9(2), 321-344.

Weaver, J.W., and Johnston, P.R. (1984) *Finite Elements for Structural Analysis*. Prentice-Hall, Inc., New Jersey.

Webster, S.L., Grau, R.H. and Williams, T.P. (1992). "Description and Application of Dual Mass Dynamic Cone Penetrometer." *Instruction Report GL-92-3*. U.S. Army Engineers Waterways Experimental Staion,Vicksburg, MS.

Zienkiewicz, O.C., Valliappan, S., and King, I.P. (1968). "Stress Analysis of Rock as a No Tension Material." *Geotechnique*, 18, 56-66.

Zienkiewicz, O.C. and Taylor, R.L. (1989). *The Finite Element Method. Volume 1, Basic Formulation and Linear Problems*, 4th Edition, McGraw Hill Book Co., New York.

APPENDIX A

DEVELOPMENT OF FIBER OPTIC BASED WIM SYSTEM

A.1 INTRODUCTION

The objective of this study is to investigate the feasibility of a weigh-in-motion (WIM) measurement system utilizing the fiber Fabry-Perot interferometer (FFPI) optical sensors. This is the first investigation of this unique sensor as an alternative to piezoelectric sensors for the WIM application. Disadvantages of present-day piezoelectric-based WIM systems include: maintenance difficulties, susceptibility to corrosion, occurrence of erroneous readings and damage due to power surges, signal crosstalk from adjacent traffic lanes, and high cost. The fiber optic Fabry-Perot sensor is more durable, immune from electromagnetic interference and crosstalk, electrically isolated from the monitoring equipment, free from corrosion effects, suitable for remote monitoring with multi-km separation between the signal conditioning unit (SCU) and sensors, and potentially cost-effective when many sensors are operated from a single SCU.

A.2 BASIC PRINCIPLE OF FIBER OPTIC SENSOR

Fiber optic cable is a sort of pipe that transmits light. Most cables are glass, with plastic cables used in some limited applications. The structure of a fiber optic cable is shown in Figure A1. The core carries the optical signal and the core size varies, depending on cable types. Single mode cable, used for range transmission of light and high bandwidth systems, has a core size of 8 to 10 μm. Multi-mode cable, used for shorter range, has a core size of 62.5 μm.

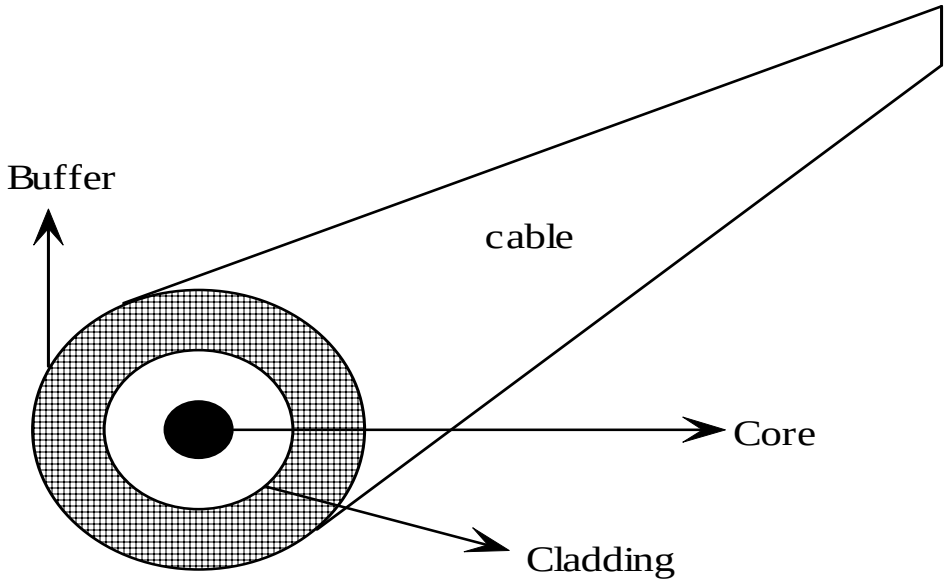

Figure A1. Components of Fiber Optic Cable

The cladding, 125 μm in diameter, is glass similar to the core, but with a slightly different composition. This layer keeps the light within the core, and prevents external light from entering the core. Surrounding the cladding is a buffer layer that protects the inner glass. The buffer diameter is 900μm. made of ceramic of plastic (Dandridge et. al 1984).

Fiber optic sensors may be divided into two broad categories, intensiometric and interferometric sensors. The principle of intensiometric sensors is simply based on the amount of light detected through the fiber. In its simplest form, damage may be detected by a fiber breaking and transmission going from on to off. Strain sensors based on intensity variation due to microbending have also been developed; however, they are relatively insensitive, inaccurate and have a limited range of detection. Interferometric sensors have been developed for high-sensitivity applications, such as acoustic sensors and magnetic field sensors, and are usually based on a single-mode fiber (Sirkis, 1999).

A.3 FFPI AND MONITORING SYSTEM

The fiber optic sensor that was tested is the Fiber Fabry-Perot Interferometer (FFPI) developed by the Fiber Optic Laboratory of Texas A&M University. The FFPI consists of two mirrors in a single mode optical fiber, separated by a distance L as depicted in Figure A2. The dielectric mirrors are formed by vacuum deposition of a 1000 nm-thick film of TiO_2 on the surface of a cleaved fiber end, followed by arc fusion splicing of the coated fiber to an uncoated fiber. The reflectivity of an internal mirror is controlled by varying the splicing parameters to achieve a desired value of about 5 percent.

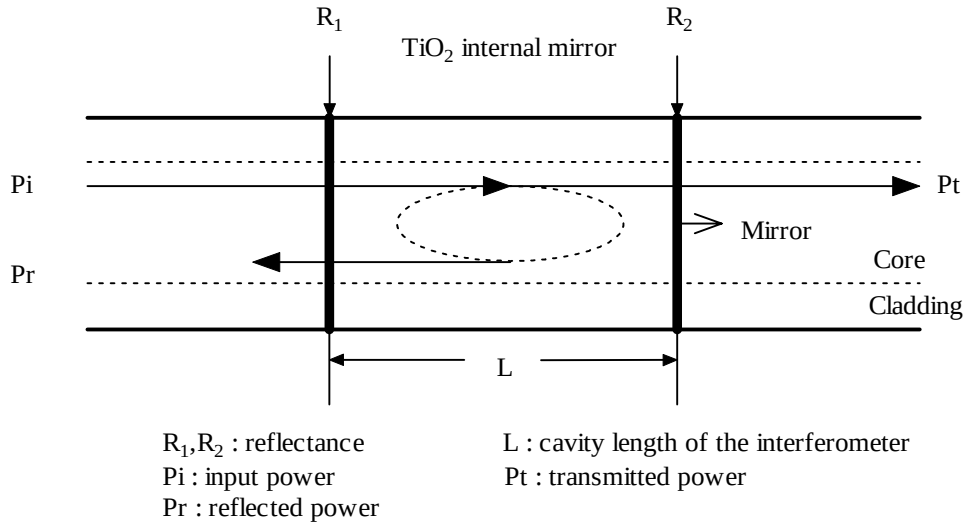

Figure A2. Fiber Fabry-Perot Interferometer

Light from a source is launched into cable, which directs the light to an in-fiber Fabry-Perot cavity formed by two thin film mirrors inserted into the optical fiber. Part of the light is reflected from the first partial mirror and part of it is transmitted into the Fabry-Perot cavity. The light entering the Fabry-Perot cavity is reflected at the second internal mirror into the lead-in/out fiber. The two light components reflected back into the lead-in/out fiber interfere coherently; the resulting intensity function is recorded by a photo detector at the

output lead of the coupler. The two light components have an optical phase change of ϕ. The effect on ϕ of variations in length ΔL, frequency $\Delta\nu$ and temperature ΔT can be expressed as

$$\phi = \phi_0 + \Delta\phi_L + \Delta\phi_\nu + \Delta\phi_T \tag{A.1}$$

with

$$\Delta\phi_L = \frac{4\pi n}{\lambda}\Delta L \tag{A.2}$$

$$\Delta\phi_\nu = \frac{4\pi L}{c}\left(n + \nu\frac{dn}{d\nu}\right)\Delta\nu \tag{A.3}$$

$$\Delta\phi_T = \frac{4\pi}{\lambda}\left(L\frac{d\nu}{dT} + n\frac{dL}{dT}\right)\Delta T \tag{A.4}$$

where ϕ_0 is the initial phase shift and n is the refractive index of the fiber and λ is the wavelength of the light.

The sensor is bonded with polyamide in a 6.35×3.175 mm groove in a metal bar with cross-sectional dimensions of 25.4×25.4 mm. The groove is then filled with high temperature red silicone. Sensors were embedded in both steel and aluminum bars. Lengths of the bars were 30.48 cm (1 ft) for lab calibration and 121.92 cm (4 ft) for road tests.

The Signal Conditioning Unit (SCU) consists of four parts: the laser light source, the signal processor, the photo detector, and the hand-held controller. The SCU in this experiment is capable of monitoring as many as 16 FFPI sensors with a single 1310 nm distributed feedback laser and a digital signal processor. The laser is modulated at 2400 Hz with a periodic saw-tooth waveform so that the frequency of the emitted light varies linearly with time during the modulation cycle. Optical star couplers distribute the laser light to individual FFPI sensors and direct the reflected signal to an array of PIN photodetectors. The interference fringe data produced by reflected waves from the two mirrors in each sensor are

processed with a microprocessor to determine the phase shift in each fiber interferometer, and produce voltage outputs proportional to the phase shifts. The upper limit of 1200 Hz frequency response (half the sampling rate) is more than adequate for the WIM application.

The output data from the SCU is collected by a personal computer using a LabView data acquisition system and processed by a C++ program specifically designed for this research. The sampling rate can be varied, so that memory storage space can be saved by utilizing the minimum required sampling rate.

A.4 LABORATORY TESTING AND RESULTS

Initial tests on the performance of the embedded FFPI sensors were performed in the Texas Transportation Institute (TTI) Material Testing System (MTS) laboratory. The test samples were 30.48 cm long aluminum and steel bars, with an FFPI sensor embedded in the center of each bar. In each case the axis of the FFPI sensing fiber was parallel to the axis of the metal bar. During each test sequence, the MTS machine strikes the bar five times at a 5 Hz frequency. The maximum applied force can be varied from 0.89 to 20 kN, with a minimum of 0.22 kN exerted every strike to eliminate the bounce of the bar.

The response of the sensors embedded in steel and in aluminum with a maximum MTS striking force of 8.9 kN (2 kip) is shown in Figures A3 and A4. The signal for the sensor embedded in the steel bar showed a single peak in response to an MTS strike, while the aluminum bar exhibited a pronounced ringing effect with two strain peaks for each strike.

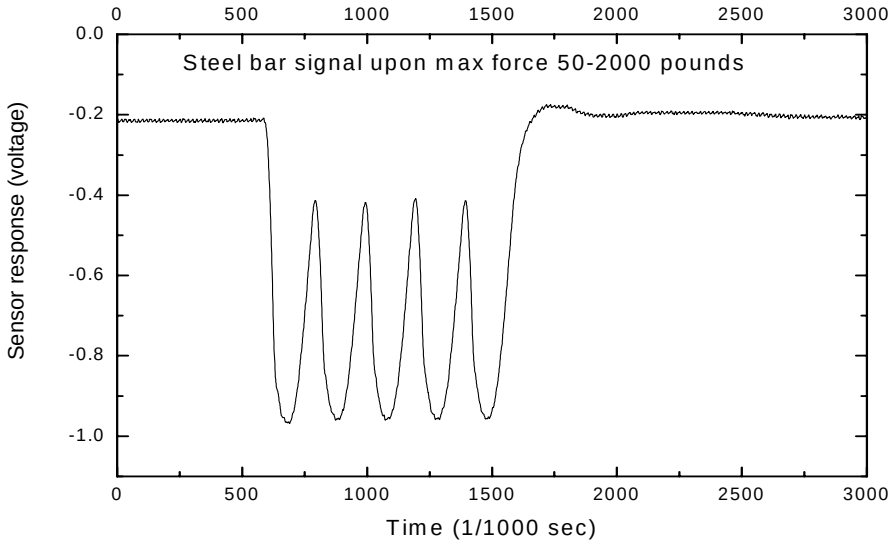

Figure A3. Steel Bar Response of MTS

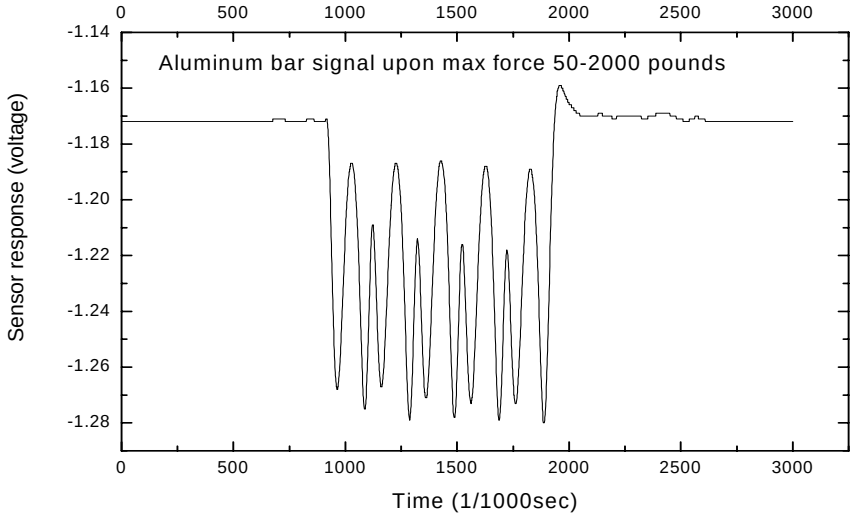

Figure A4. Aluminum Bar Response of MTS

Figure A5 shows the fiber optic sensor response is a fairly linear function of the axial displacement, indicating that this sensor is promising for measuring strain in the WIM application.

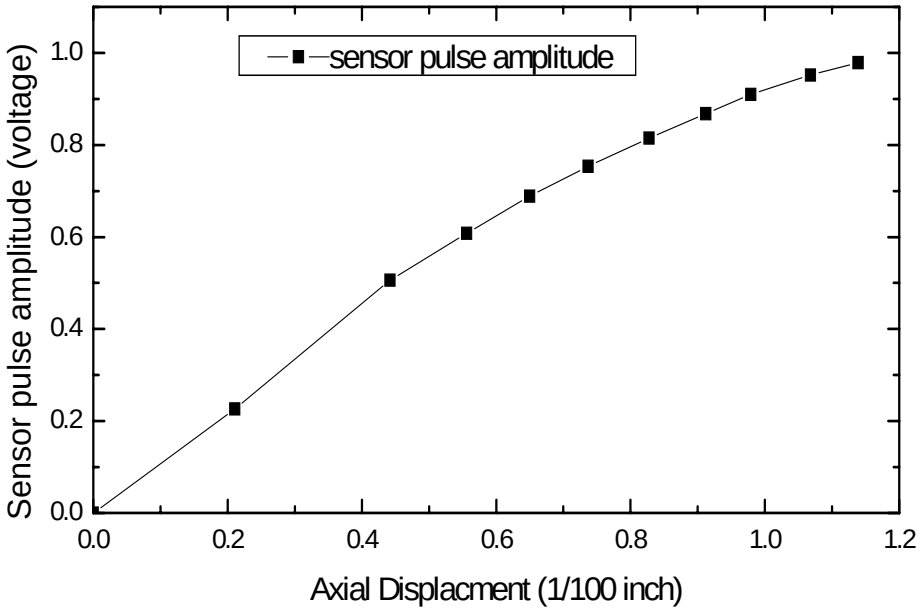

Figure A5. Dependence of Peak Response on Axial Displacement

A.5 FIELD TESTING AND RESULTS

The sensor was installed in an outer wheel path of the field test section where most of the permitted trucks move. As in the laboratory tests, the sensors were embedded in steel and aluminum bars with cross-sectional dimensions of 25.4 x 25.4 mm. In the road tests, the bars were 121.92 cm (4 ft) long, and 5 sensors were embedded in each bar. The procedure to install the FFPI sensor is illustrated by the following figures with comments.

Step 1 : Align FFPI sensor straight along a groove made on steel bar and coat the fiber using adhesive then put on the protection cover at each sensor location.

Step 2 : Make two grooves on pavement surface with 25.4 mm wide and 50.8 mm depth.

Step 3 : Put the bar along a groove in the pavement and fill with hot bituminous sealant and then use solid hot mix Epoxy to fill in the grooves evenly to the level of the road surface, so that the sensors will measure the strain experienced by the surrounding pavement.

Figure A6. FFPI Installation Procedure

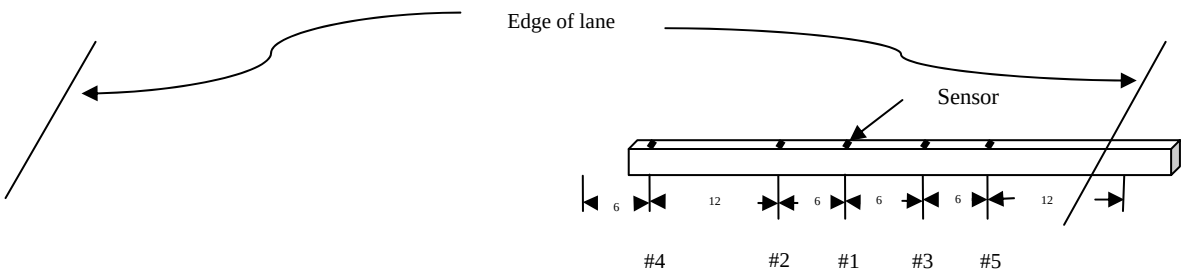

Figure A7. Location of Sensors

Representative data are shown in Figure A8. Because the signal amplitude is affected by the position of the wheels relative to the sensor, the relative amplitudes are an indication of the position of the truck in the lane. Sensor 5 produces a larger signal than other sensors, indicating that the truck is in the right-hand portion of the lane. After a truck passes by, the signal from each sensor resumes its starting value quickly, thus allowing for the collection of data from a continuous line of trucks. Note that the sensor captured the response the truck traffic effectively because its peak represents the axle configuration corresponding to the class similar to the response of the MDD.

A total of 30 trucks were monitored with sensors in the aluminum bar and another 30 trucks with sensors in the steel bar. An effort to correlate the fiber optic sensor data with static weights of these trucks supplied by TTI was not successful due to the lack of the data primarily. The other factor which probably contributed to the discrepancy was the fact that the limited distance (2 ½ feet) over which the FFPI sensors were distributed made it possible to monitor only one wheel of each truck, so that uneven lateral distribution of weight leads to erroneous readings.

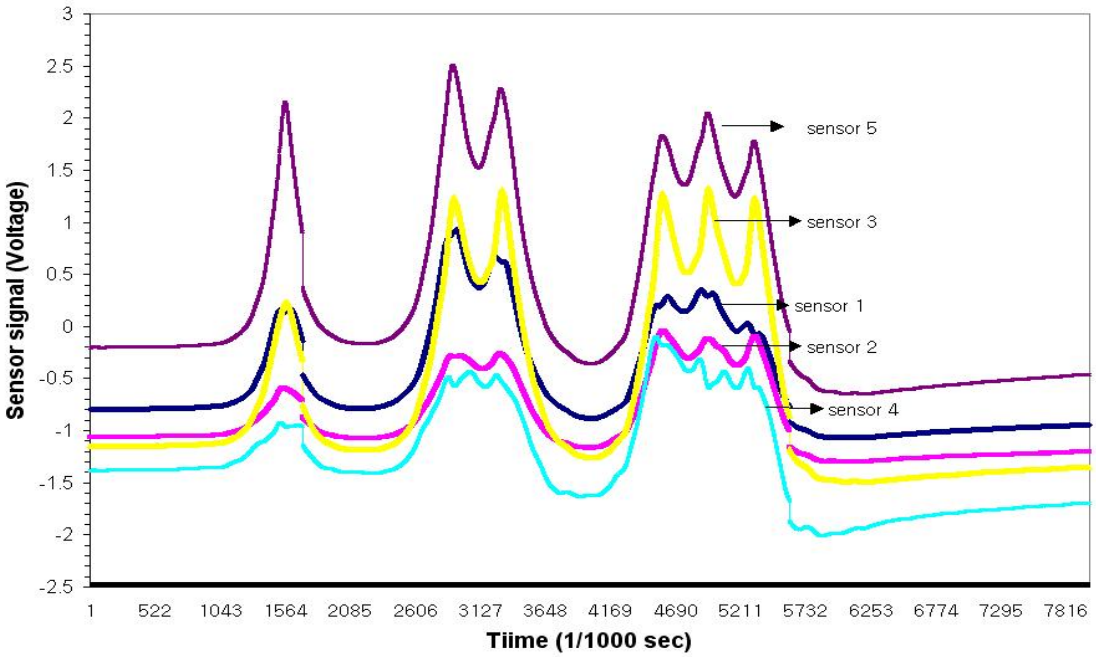

Figure A8. Response of Five FFPI Sensors Embedded in a Steel Bar on a Class 10 Truck

A.6 CONCLUSIONS

The application of FFPI sensors for WIM has been investigated for the first time. The impulse response of sensors embedded in steel and aluminum bars was examined using the MTS. The aluminum bar showed a significant ringing following striking by the MTS machine, an effect which was absent in the steel bar response. The peak response of strain from the FFPI sensor in the steel bar showed a fairly linear dependence on axial displacement. Field tests were conducted with steel and aluminum bars containing FFPI sensors which were embedded in the highway. The FFPI sensors showed strong response and consistently reproduced the expected characteristics of truck wheel crossings. However, the correlation between peak fiber optic sensor response and truck static weight data was not matched well due to the lack of data. Calibration methods to relate the response of multiple sensors to

actual truck weights needs to be investigated before the FFPI sensor can be a viable candidate for a practical WIM system.

APPENDIX B

MATERIAL PROPERTY OF INTACT SOILS

Table B1. Physical Soil Property of BE Clay

FWD Station	Soil Type	LL (%)	PL (%)	PI (%)
K7-11	BE (CH*)	66	22	44

(Note: * referred to Table 3.1.)

Table B2. Cross-Anisotropy Test Result of BE Clay

Stress state	Axial Stress (kPa)	Radial Stress (kPa)	M_R^V (MPa)	M_R^H (MPa)	ν_{VH}	ν_{HH}	G_{HV} (MPa)	n	m	p
1	114.29	13.47	107.45	120.88	0.24	0.48	71.86	1.12	0.67	1.97
2	142.14	16.50	145.83	151.92	0.44	0.87	101.90	1.04	0.70	1.97
3	202.14	24.58	161.71	173.69	0.53	1.04	100.88	1.07	0.62	1.97
4	229.29	27.27	170.20	169.71	0.37	0.73	103.07	1.00	0.61	1.97
5	289.29	35.36	192.72	199.37	0.42	0.83	84.49	1.03	0.44	1.97
6	344.29	41.08	202.19	203.02	0.46	0.93	154.67	1.00	0.76	2.03
7	391.43	43.10	216.84	224.83	0.42	0.85	156.29	1.04	0.72	2.03

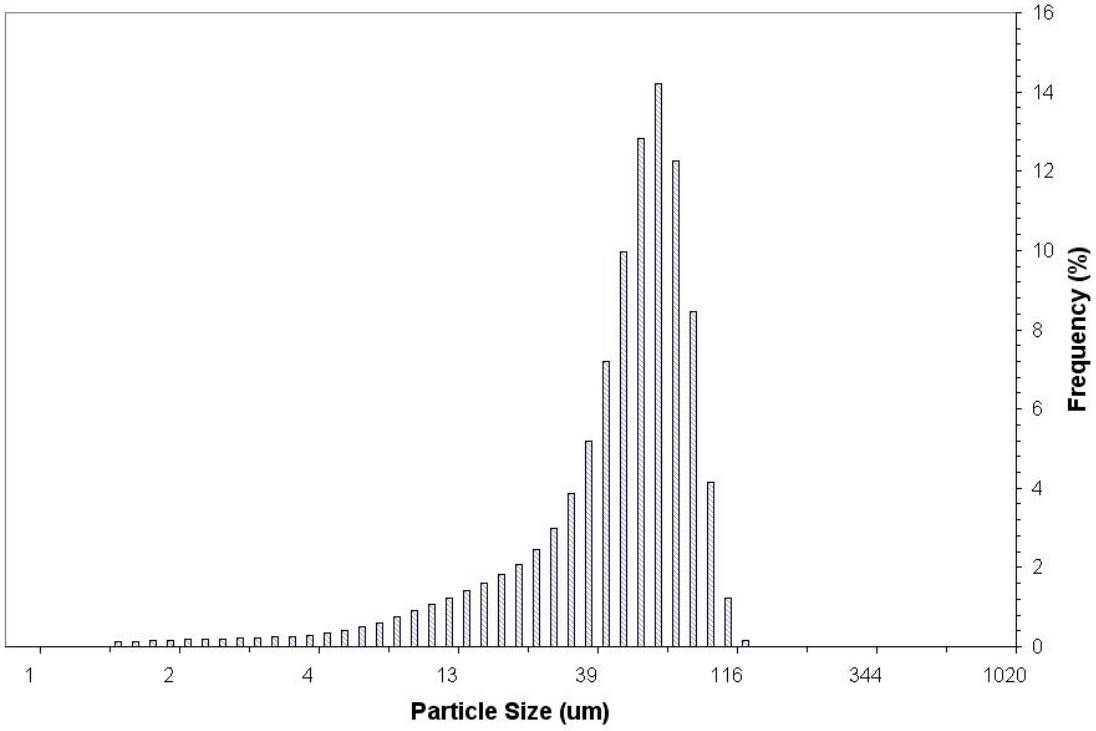

Figure B1. Particle Size Distribution Curve of BE Clay

Table B3. Physical Soil Property of BU Clay

FWD Station	Soil Type	LL (%)	PL (%)	PI (%)
K6-23, 29 K7-12, 15, 20	BU (CH*)	73	27	46

(Note: * referred to Table 3.1.)

Table B4. Cross-Anisotropy Test Result of BU Clay

Stress state	Axial Stress (kPa)	Radial Stress (kPa)	M_R^V (MPa)	M_R^H (MPa)	ν_{VH}	ν_{HH}	G_{HV} (MPa)	n	m	p
1	114.29	13.47	83.85	72.01	0.24	0.48	43.22	0.86	0.52	1.97
2	142.14	16.50	99.35	85.29	0.44	0.87	52.83	0.86	0.53	1.97
3	202.14	24.58	89.96	90.20	0.53	1.04	53.04	1.00	0.59	1.97
4	229.29	27.27	116.82	112.40	0.37	0.73	67.98	0.96	0.58	1.97
5	289.29	35.36	130.75	114.28	0.42	0.83	80.30	0.87	0.61	1.97
6	344.29	41.08	154.70	133.61	0.46	0.93	115.99	0.86	0.75	2.03
7	391.43	43.10	136.06	134.02	0.42	0.85	84.58	0.98	0.62	2.03

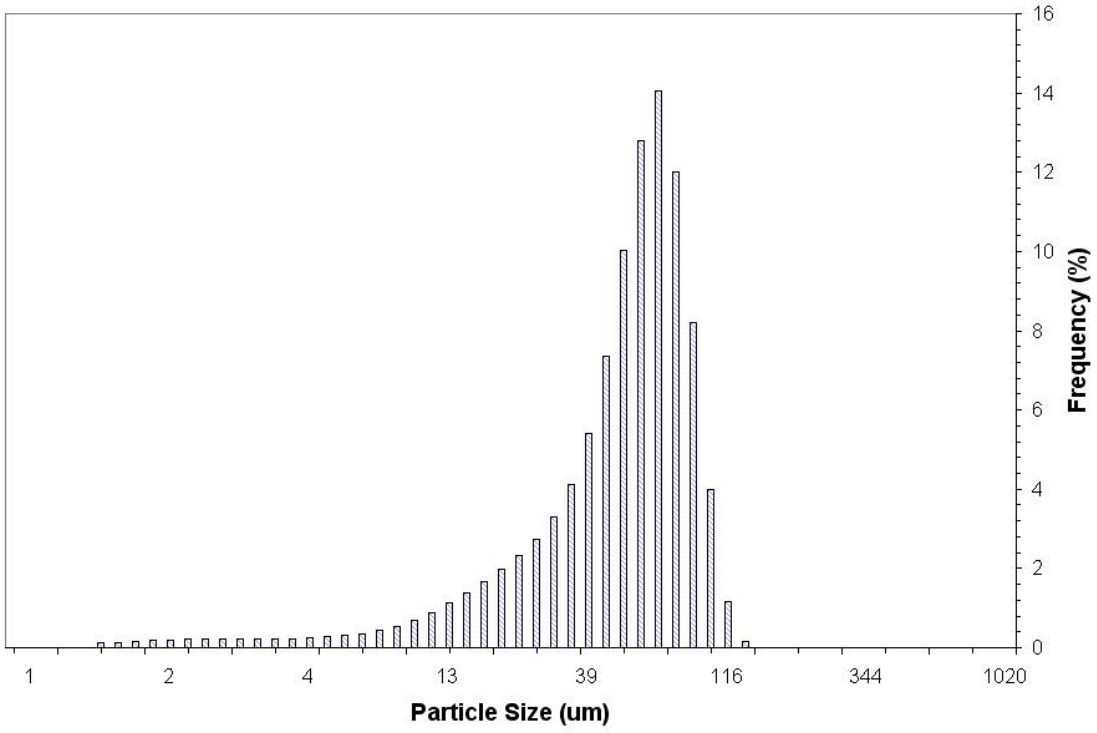

Figure B2. Particle Size Distribution Curve of BU Clay

Table B5. Physical Soil Property of HA Clay

FWD Station	Soil Type	LL (%)	PL (%)	PI (%)
K6-11, 45 K7-9	HA(CH*)	68	23	45

(Note: * referred to Table 3.1.)

Table B6. Cross-Anisotropy Test Result of HA Clay

Stress state	Axial Stress (kPa)	Radial Stress (kPa)	M_R^V (MPa)	M_R^H (MPa)	ν_{VH}	ν_{HH}	G_{HV} (MPa)	n	m	p
1	114.29	13.47	91.53	51.31	0.25	0.49	47.29	0.56	0.52	1.97
2	142.14	16.50	89.05	64.36	0.25	0.49	49.24	0.72	0.55	1.97
3	202.14	24.58	137.32	80.12	0.31	0.62	77.79	0.58	0.57	1.97
4	229.29	27.27	144.66	85.90	0.27	0.52	77.49	0.59	0.54	1.97
5	289.29	35.36	161.06	75.58	0.24	0.47	77.38	0.47	0.48	1.97
6	344.29	41.08	186.24	125.00	0.16	0.33	93.33	0.67	0.50	2.03
7	391.43	43.10	194.42	105.49	0.25	0.51	100.73	0.54	0.52	2.03

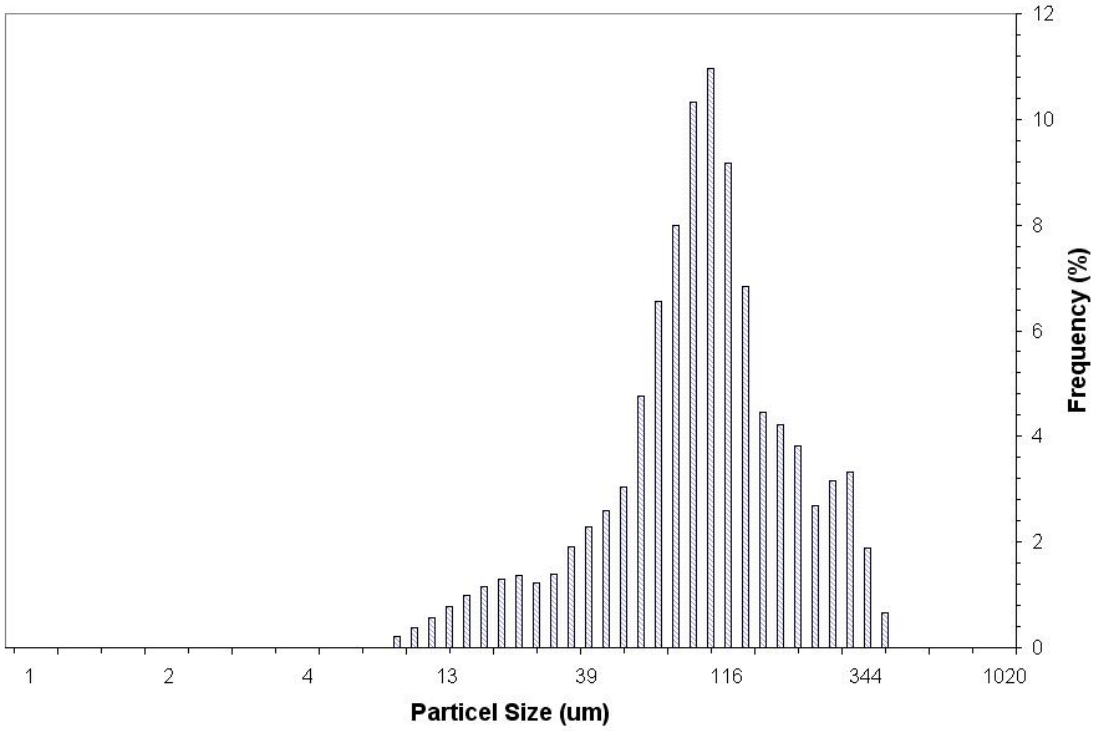

Figure B3. Particle Size Distribution Curve of HA Clay

Table B7. Physical Soil Property of HE Clay

FWD Station	Soil Type	LL (%)	PL (%)	PI (%)
K6-50, 53 K7-40, 46	HE(CH*)	65	23	42

(Note: * referred to Table 3.1.)

Table B8. Cross-Anisotropy Test Result of HE Clay

Stress state	Axial Stress (kPa)	Radial Stress (kPa)	M_R^V (MPa)	M_R^H (MPa)	ν_{VH}	ν_{HH}	G_{HV} (MPa)	n	m	p
1	114.29	13.47	102.98	120.16	0.24	0.48	46.88	1.17	0.46	1.97
2	142.14	16.50	112.19	100.14	0.44	0.87	51.21	0.89	0.46	1.97
3	202.14	24.58	131.84	117.75	0.53	1.04	82.40	0.89	0.63	1.97
4	229.29	27.27	149.07	141.61	0.37	0.73	69.49	0.95	0.47	1.97
5	289.29	35.36	157.89	139.68	0.42	0.83	80.71	0.88	0.51	1.97
6	344.29	41.08	172.03	165.69	0.46	0.93	102.96	0.96	0.60	2.03
7	391.43	43.10	189.23	186.81	0.42	0.85	80.89	0.99	0.43	2.03

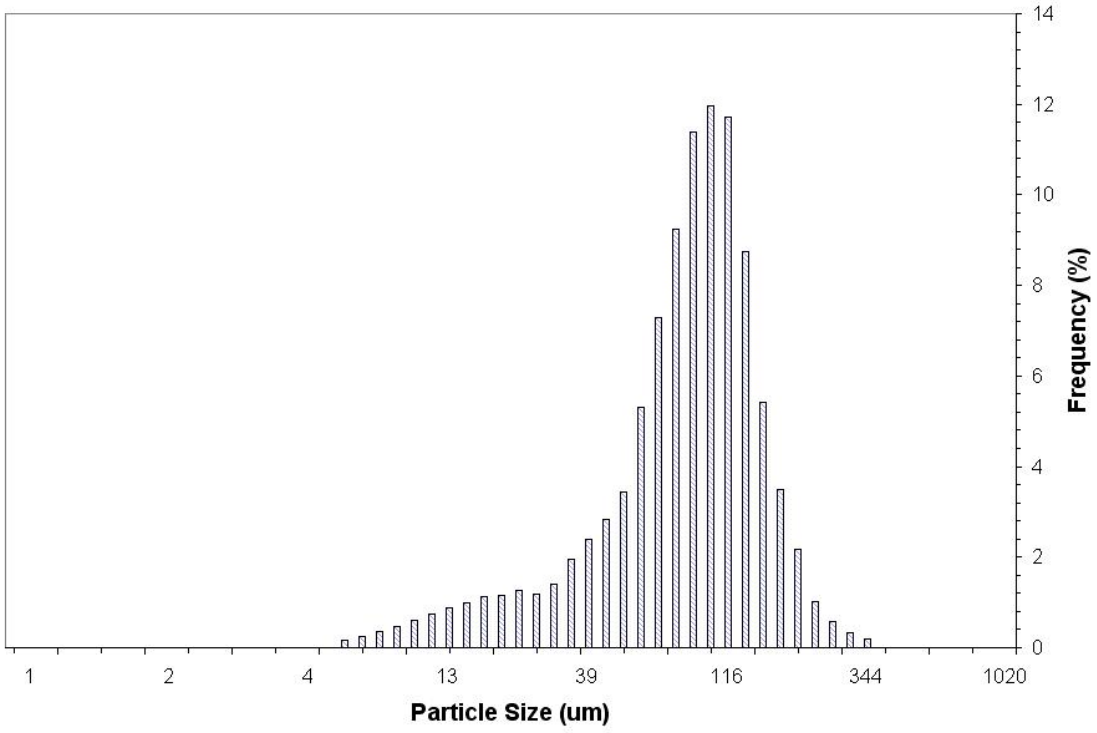

Figure B4. Particle Size Distribution Curve of HE Clay

Table B9. Physical Soil Property of OM Clay

FWD Station	Soil Type	LL (%)	PL (%)	PI (%)
K6-1, 4 K7-3	OM(CL*)	45	21	24

(Note: * referred to Table 3.1.)

Table B10. Cross-Anisotropy Test Result of OM Clay

Stress state	Axial Stress (kPa)	Radial Stress (kPa)	M_R^V (MPa)	M_R^H (MPa)	ν_{VH}	ν_{HH}	G_{HV} (MPa)	n	m	p
1	114.29	13.47	91.53	51.31	0.25	0.49	47.29	0.56	0.52	1.97
2	142.14	16.50	89.05	64.36	0.25	0.49	49.24	0.72	0.55	1.97
3	202.14	24.58	137.32	80.12	0.31	0.62	77.79	0.58	0.57	1.97
4	229.29	27.27	144.66	85.90	0.27	0.52	77.49	0.59	0.54	1.97
5	289.29	35.36	161.06	75.58	0.24	0.47	77.38	0.47	0.48	1.97
6	344.29	41.08	186.24	125.00	0.16	0.33	93.33	0.67	0.50	2.03
7	391.43	43.10	194.42	105.49	0.25	0.51	100.73	0.54	0.52	2.03

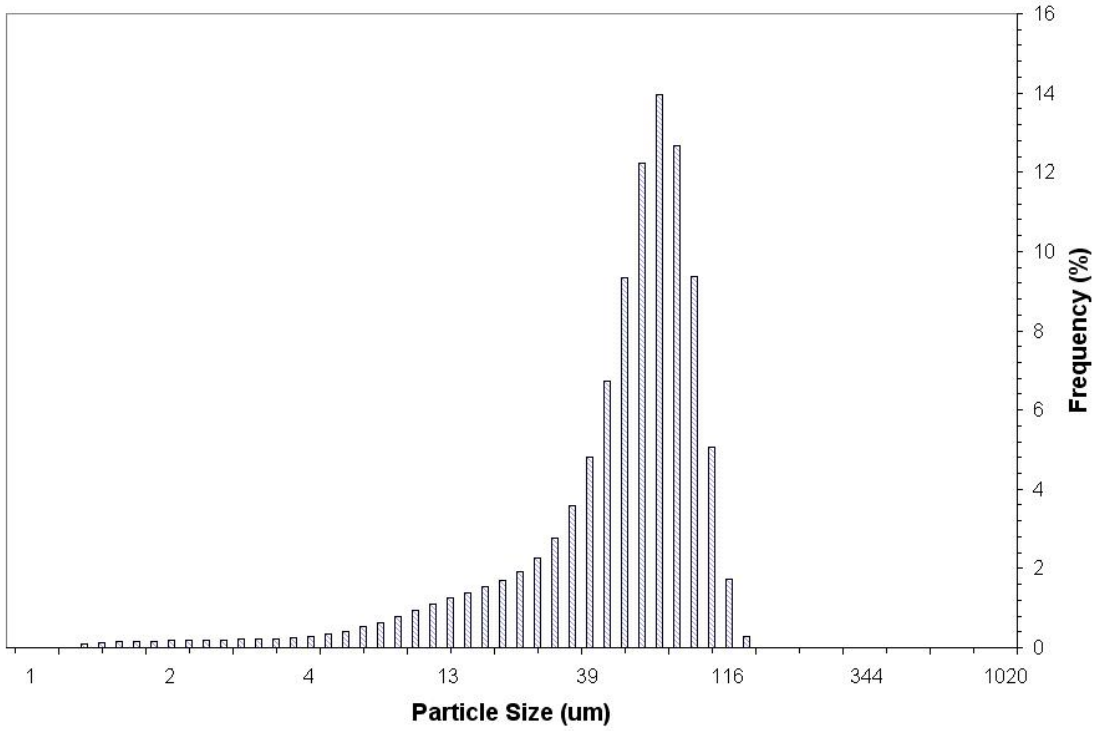

Figure B5. Particle Size Distribution Curve of OM Clay

Table B11. Physical Soil Property of ON Clay

FWD Station	Soil Type	LL (%)	PL (%)	PI (%)
K6-35, 42 K7-31, 37	ON(CH*)	51	22	29

(Note: * referred to Table 3.1.)

Table B12. Cross-Anisotropy Test Result of ON Clay

Stress state	Axial Stress (kPa)	Radial Stress (kPa)	M_R^V (MPa)	M_R^H (MPa)	ν_{VH}	ν_{HH}	G_{HV} (MPa)	n	m	p
1	114.29	13.47	70.97	60.14	0.44	0.86	49.45	0.85	0.70	1.97
2	142.14	16.50	73.86	57.41	0.44	0.87	39.15	0.78	0.53	1.97
3	202.14	24.58	113.35	98.36	0.53	1.04	60.86	0.87	0.54	1.97
4	229.29	27.27	106.54	80.28	0.37	0.73	81.97	0.75	0.77	1.97
5	289.29	35.36	114.19	103.68	0.42	0.83	49.44	0.91	0.43	1.97
6	344.29	41.08	130.87	96.39	0.46	0.93	86.56	0.74	0.66	2.03
7	391.43	43.10	160.22	132.21	0.42	0.85	97.91	0.83	0.61	2.03

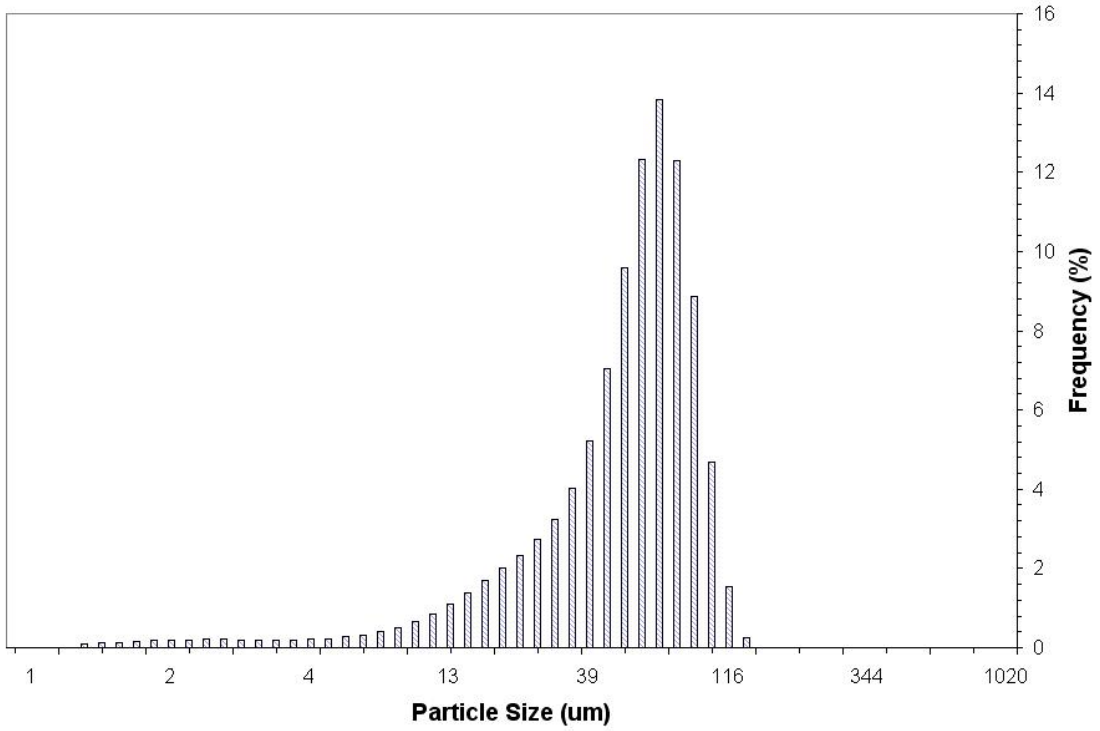

Figure B6. Particle Size Distribution Curve of ON Clay

APPENDIX C

PLOTS OF VARIATION IN FATIGUE CRACKING AND PAVEMENT SCORE FROM VISUAL SURVEY

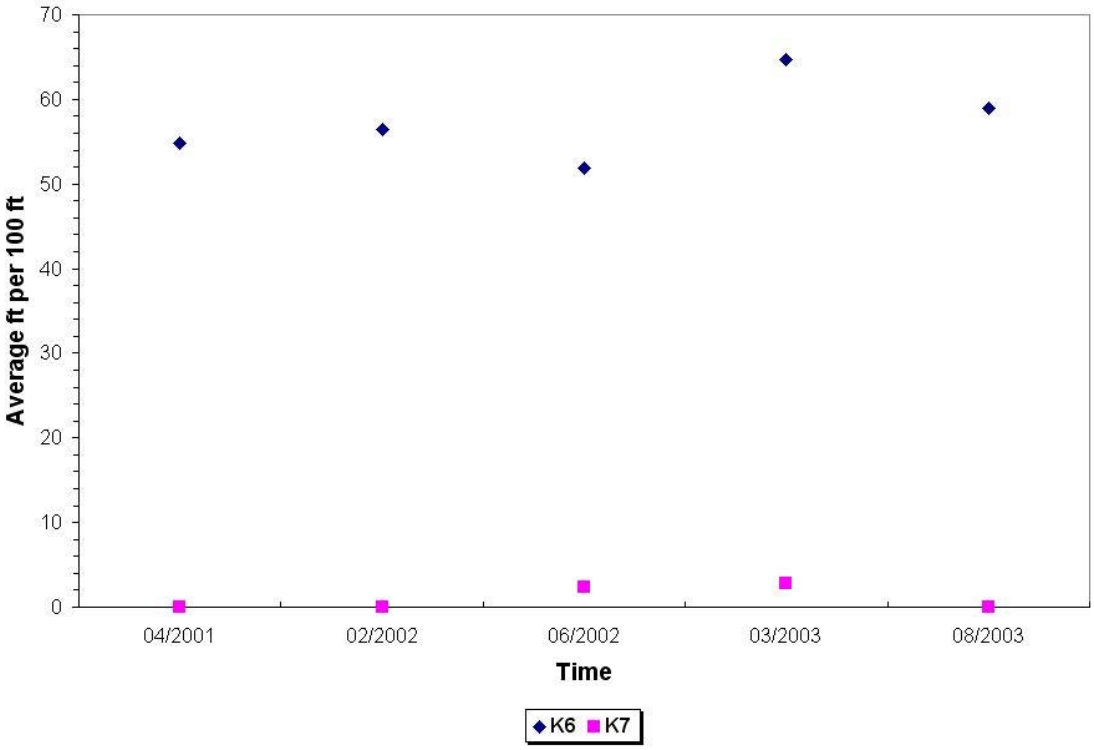

Figure C1. Variation of Longitudinal Crack in Group 1A

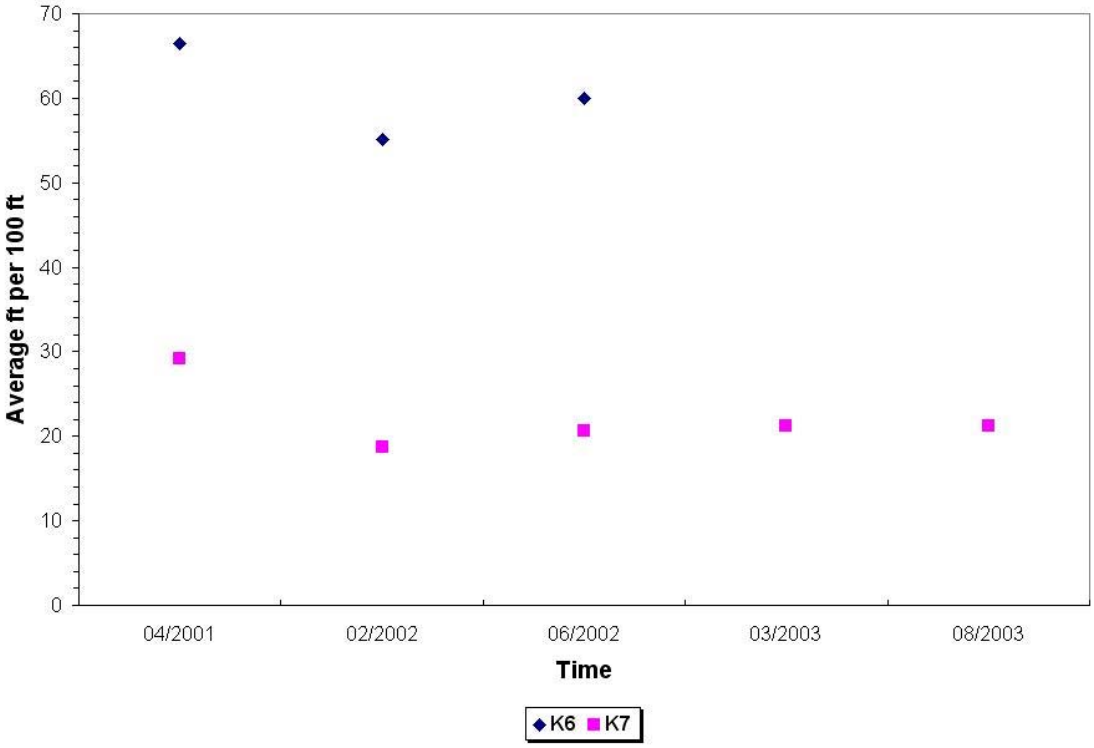

Figure C2. Variation of Longitudinal Crack in Group 1

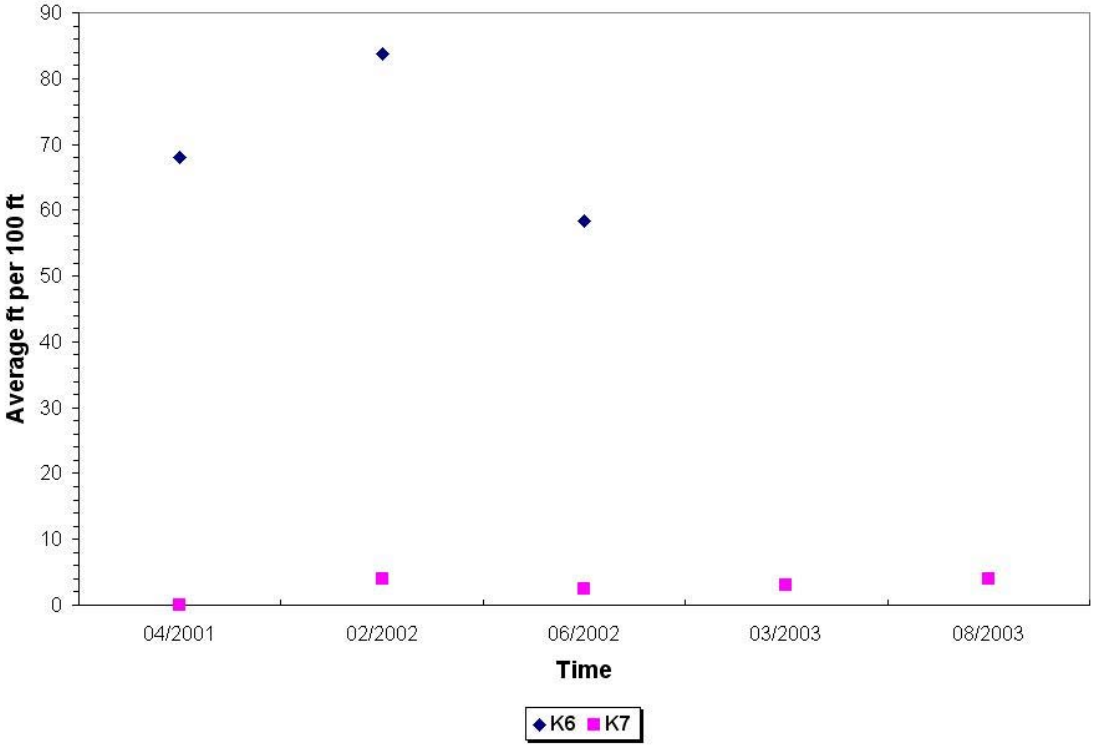

Figure C3. Variation of Longitudinal Crack in Group 2

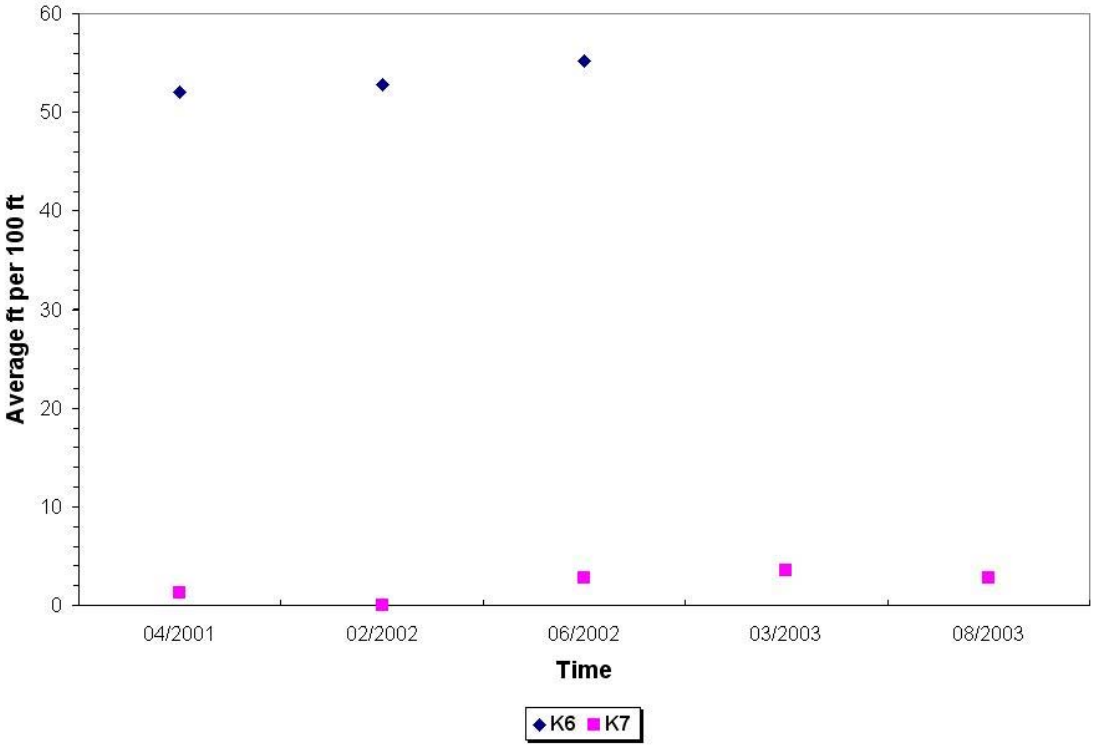

Figure C4. Variation of Longitudinal Crack in Group 3

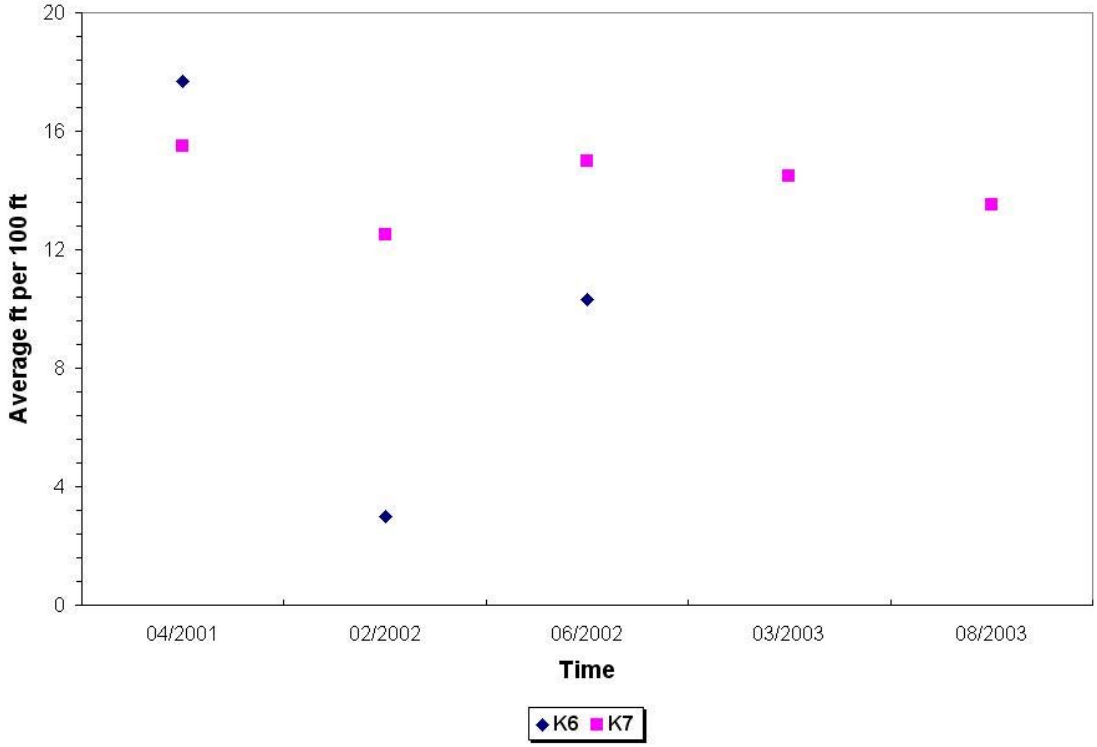

Figure C5. Variation of Longitudinal Crack in Group 4

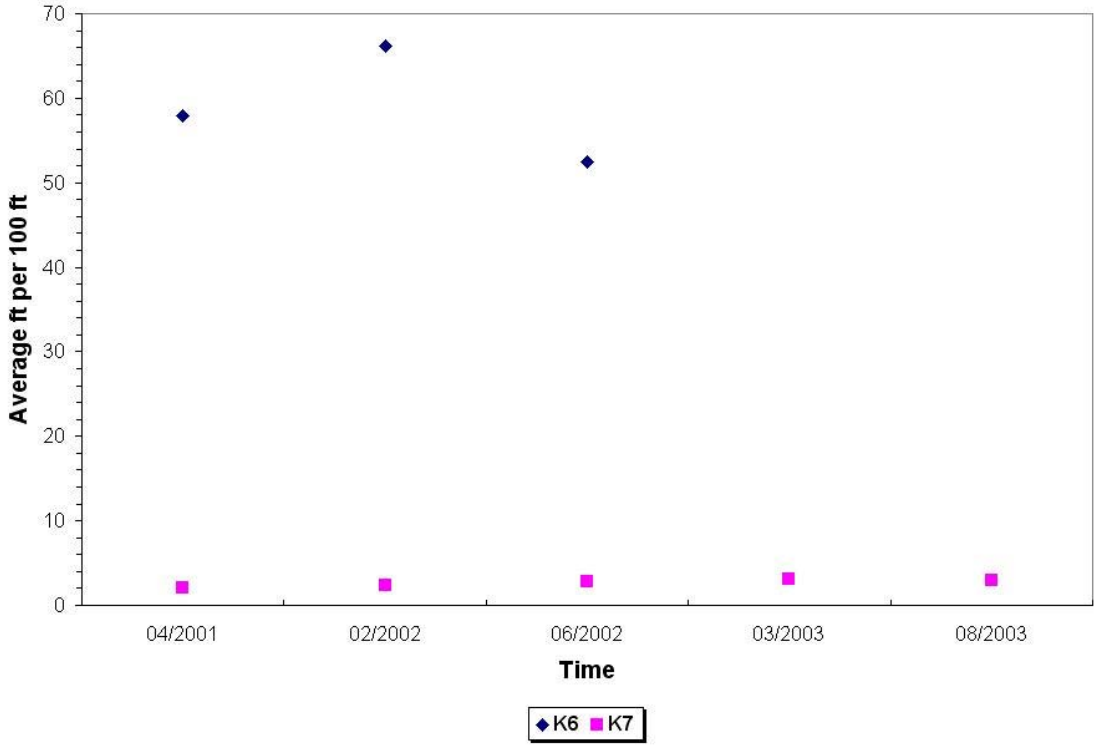

Figure C6. Variation of Longitudinal Crack in Group 5

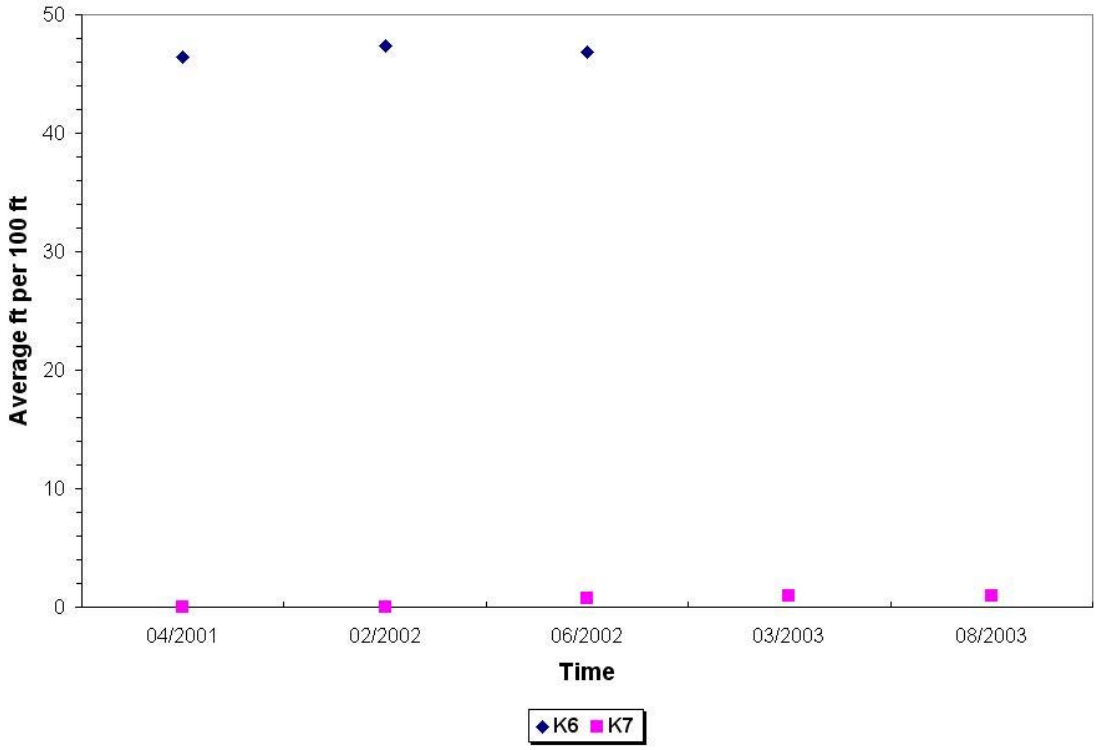

Figure C7. Variation of Longitudinal Crack in Group 6

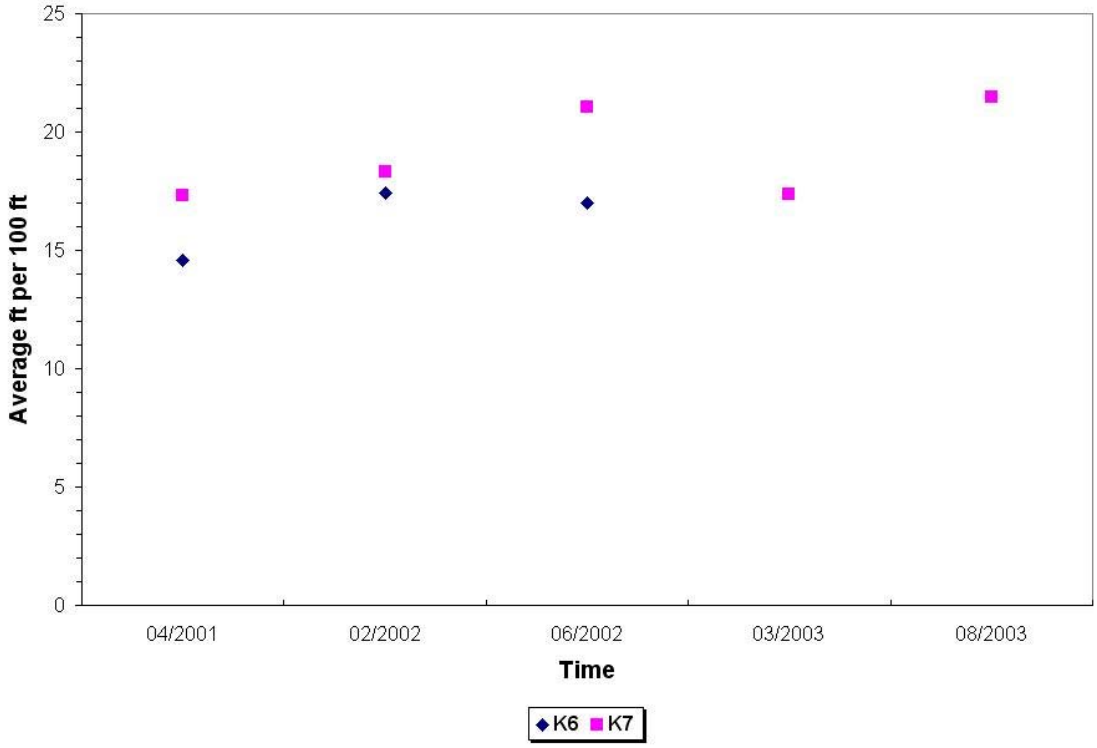

Figure C8. Variation of Longitudinal Crack in Group 7

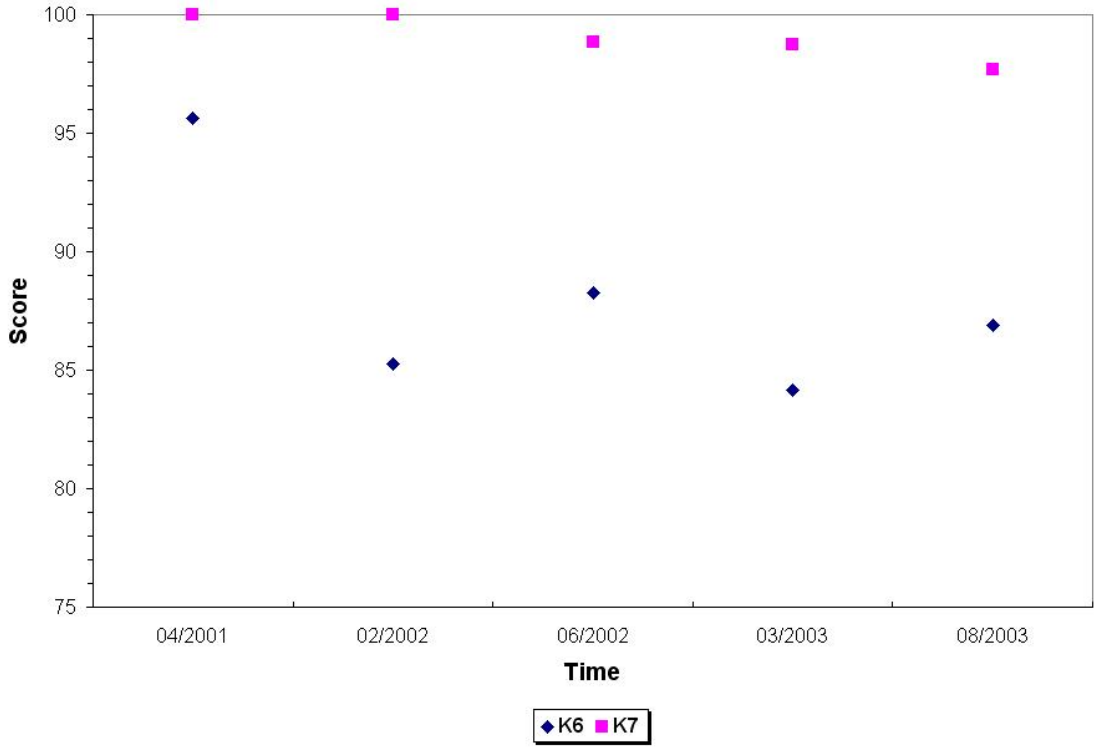

Figure C9. Variation of Pavement Score in Group 1A

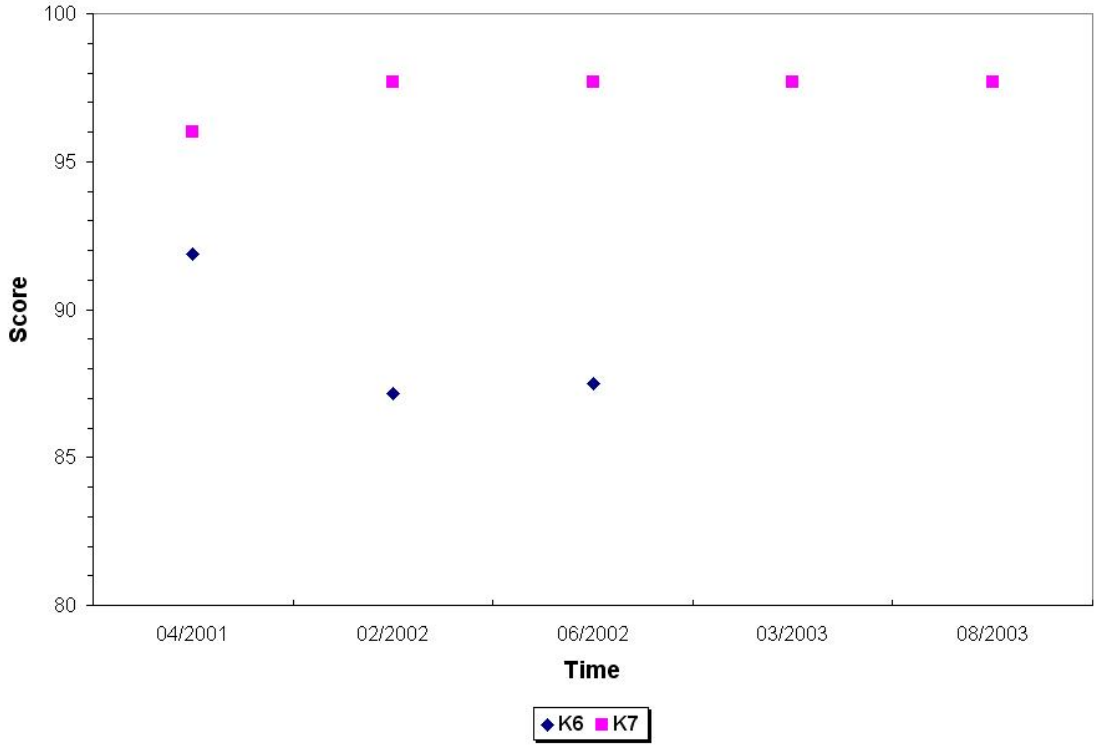

Figure C10. Variation of Pavement Score in Group 1

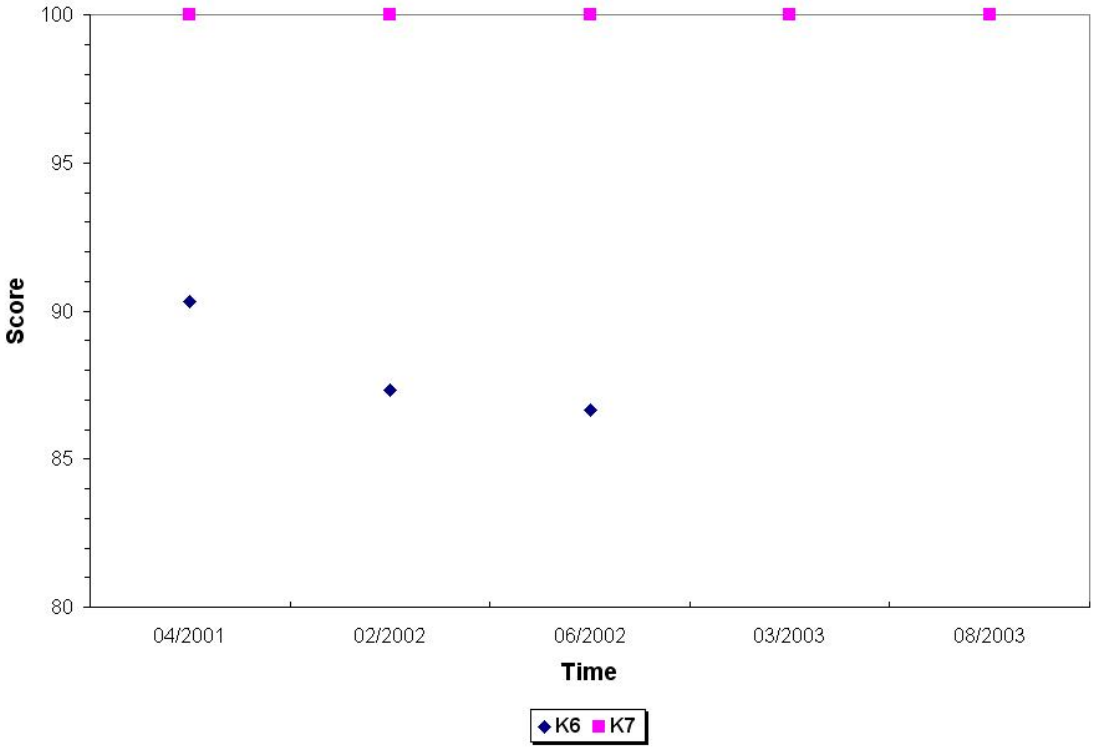

Figure C11. Variation of Pavement Score in Group 2

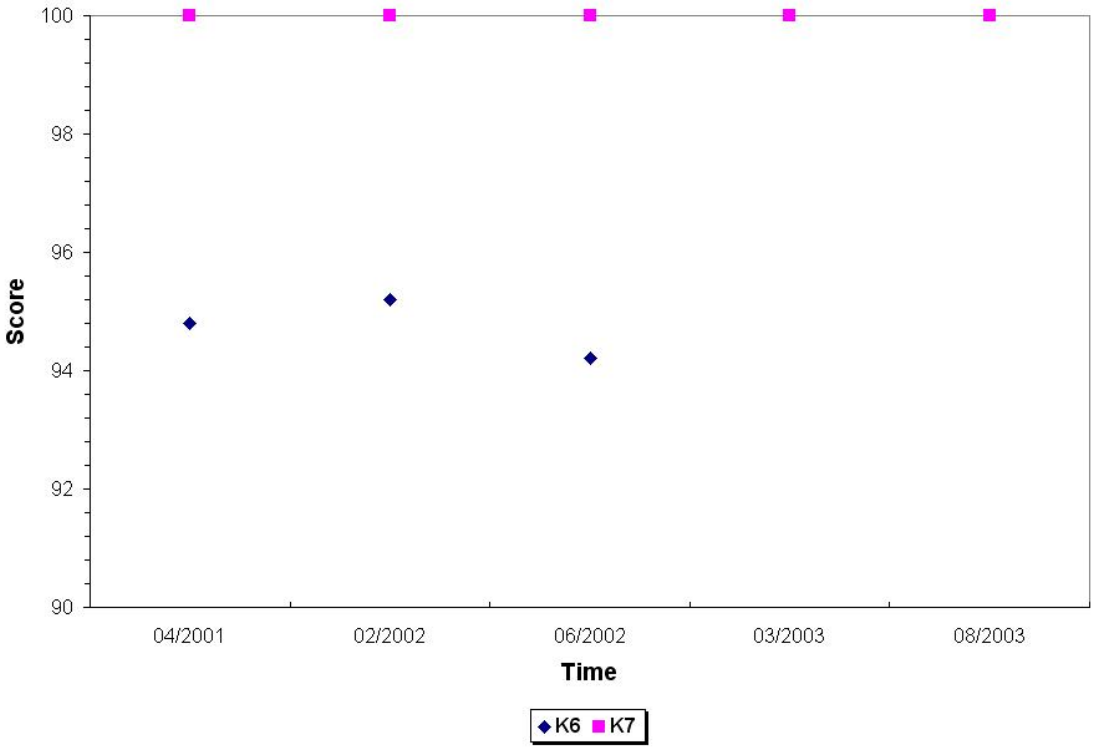

Figure C12. Variation of Pavement Score in Group 3

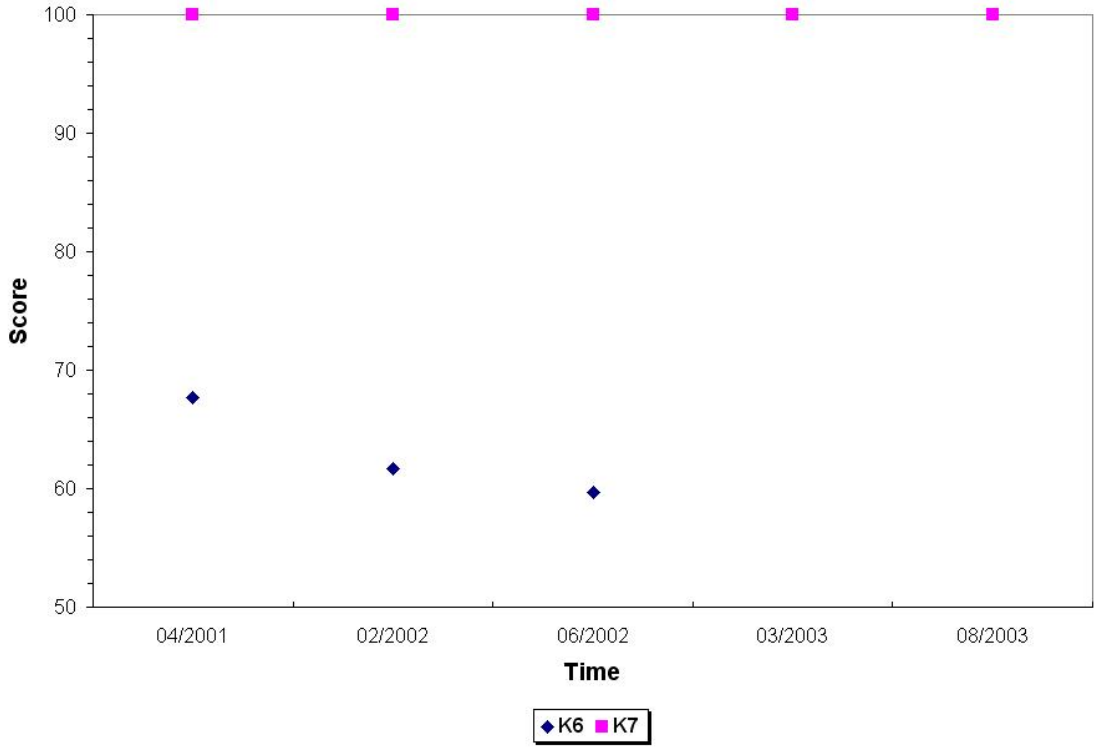

Figure C13. Variation of Pavement Score in Group 4

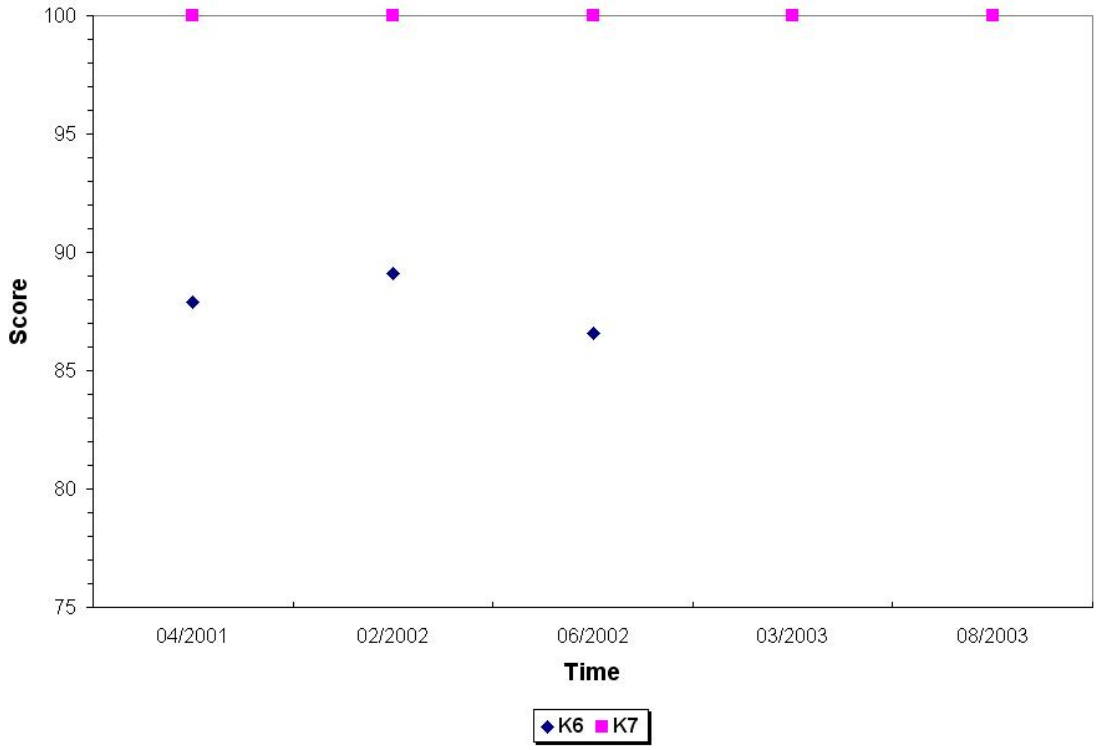

Figure C14. Variation of Pavement Score in Group 5

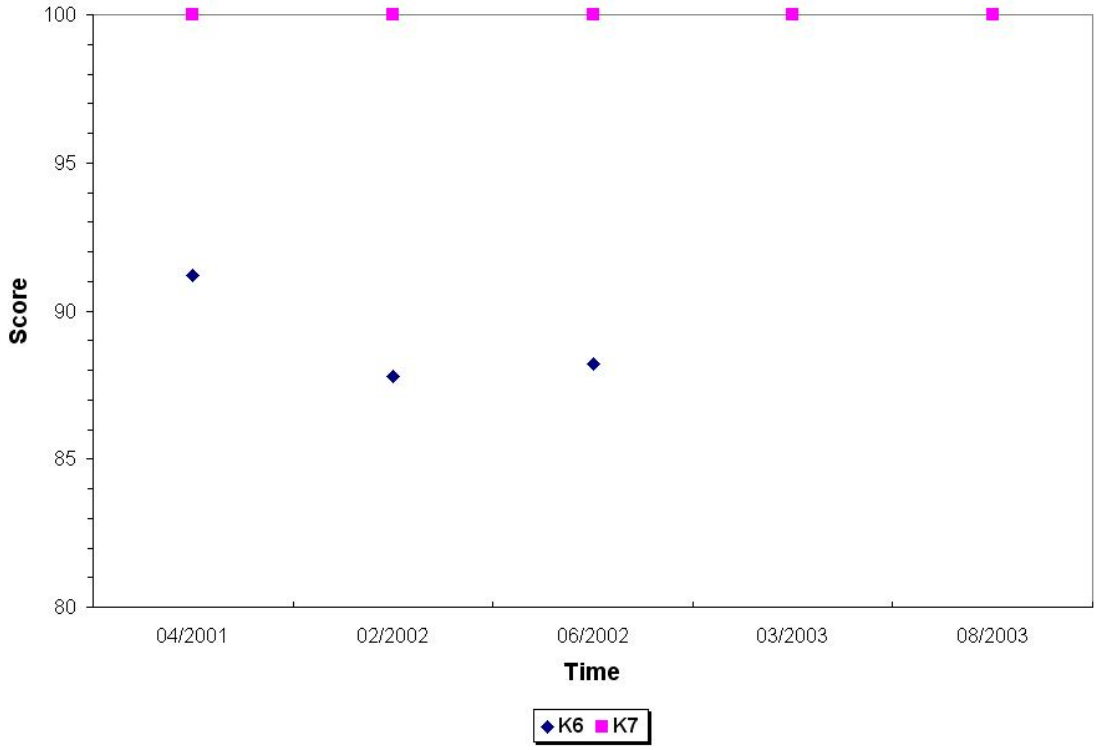

Figure C15. Variation of Pavement Score in Group 6

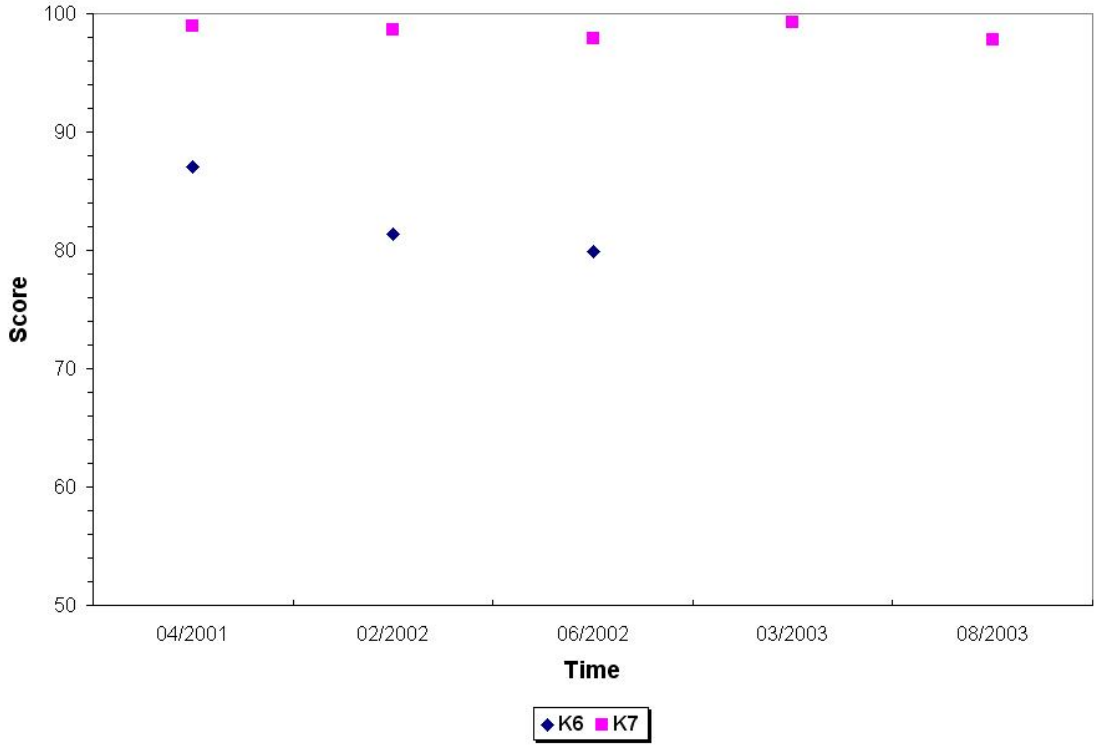

Figure C16. Variation of Pavement Score in Group 7

VITA

Jeong Ho Oh was born on November 8, 1972 in Korea. He enrolled at Korea University, in Seoul, South Korea, where he received a Bachelor of Engineering degree in civil engineering in 1997. During 1993-1994 he served his country in the Korean Air Force. In the fall of 1997, he enrolled in the School of Civil and Environmental Engineering at Korea University and received a Master of Science degree in civil engineering in 1999. He worked under the supervision of Dr. Woo-Jin Lee with a thesis topic "Measurement of Pile Load Transfer Using Fiber Bragg Grating Sensor." Since then, he has worked as a research assistant in the Texas Transportation Institute of the Texas A&M University from September 2000 to August 2004 in order to pursue Ph.D. dealing with a specific area in pavement and geotechnical engineering. He received his Ph.D. in August 2004. He has co-authored several papers and research reports. He is interested in foundation designs and constitutive modeling pavement materials.

His permanent mailing address is:

11-306 Sam-Ho Apartment
Bangbae-Dong, Seocho-Gu
Seoul, Korea 137-060